The impact of volcanism on trace metal biogeochemistry in the Southern Ocean

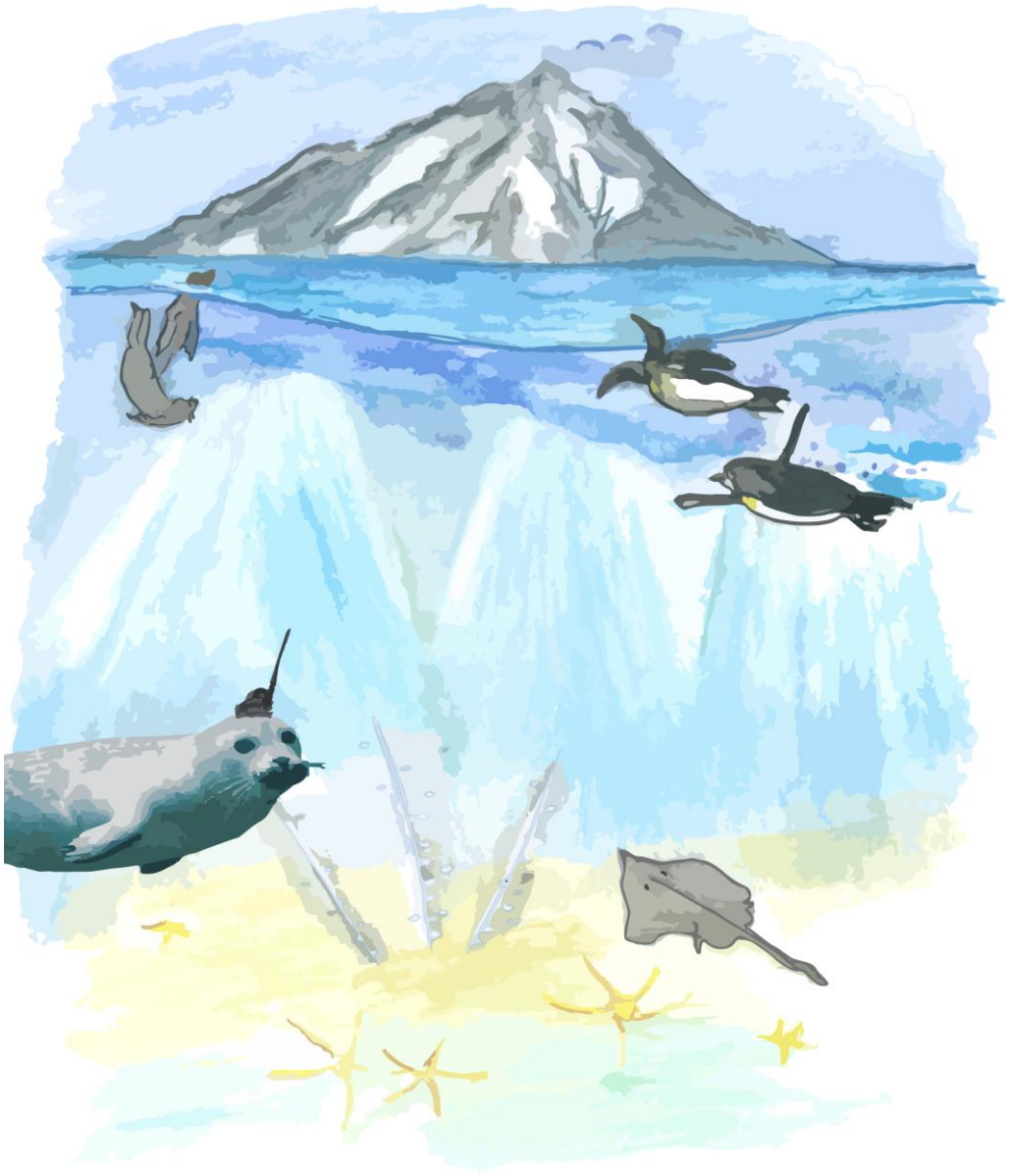

By Thomas M Holmes, B.App.Sci. (Env.Sci., Hon)

Under the supervision of Andrew Bowie, Zanna Chase, Pier van der Merwe and Ashley Townsend

Submitted in partial fulfilment of the requirements for the degree of

Doctor of Philosophy

September 2018

ACE CRC ANTARCTIC CLIMATE & ECOSYSTEMS COOPERATIVE RESEARCH CENTRE

UNIVERSITY of TASMANIA

IMAS INSTITUTE FOR MARINE & ANTARCTIC STUDIES

The impact of volcanism on trace metal biogeochemistry in the Southern Ocean

By

Thomas M Holmes

Abstract

Iron (Fe) is now recognised as a limiting, or co-limiting, micronutrient for biological production in the ocean. Areas of the ocean that are high in the macronutrients nitrogen (N) and phosphorous (P) but low in chlorophyll producing organisms are known as HNLC regions and cover approximately one third of the world's oceans, the largest of which is the Southern Ocean (SO). When coupled with the inhibition of nitrogen fixation by microbes under low Fe conditions in low-latitude regions, this means that Fe regulates biological productivity in as much as half the world's oceans. As such, Fe plays a key role in biogeochemical cycling and the drawdown of carbon from the atmosphere.

Sources of Fe to the SO include resuspension of coastal and shallow sediments, glacial and iceberg melt, seasonal sea ice retreat, island wakes, vertical diffusive flux, interaction between bathymetry and currents, dust deposition and hydrothermal inputs. Hydrothermal inputs, in particular, have gained increasing recognition in recent years as a previously overlooked source of Fe to the deep ocean that may potentially affect surface productivity in some ocean basins. Furthermore, shallow hydrothermal vents and subaerial volcanic islands, while less common than deep mid-ocean ridge vents, may supply Fe directly to the surface mixed layer. This dissertation explores the impact of both hydrothermal and subaerial aspects of volcanism on Fe biogeochemistry in the SO.

First, the impact of hydrothermalism on Fe cycling in the SO is explored through an extensive compilation of global hydrothermal studies and hydrothermal Fe measurements. This review

highlights a dearth of hydrothermal studies conducted in the SO, with only 72 of the 631 vents discovered located south of 30° at the time of writing. A total of 31 of the 72 SO vents are located in the upper 2000 m of the water column, with 16 located in the upper 1000 m, increasing the probability of hydrothermal Fe reaching surface waters transported in upwelling SO meridional circulation. However, with only a small fraction of the ~20,000 km of tectonic plate boundaries located in the SO surveyed to date, many more observations at hydrothermal vent sites and further investigation of Fe transport mechanisms are required in order to constrain the impact of hydrothermalism on the SO and global ocean Fe cycles.

Within the Indian sector of the SO lies an oasis of relatively Fe rich waters overlaying the Kerguelen Plateau. At the southern part of the central Kerguelen plateau is an active volcanic hotspot, hosting two subaerial volcanically active islands, Heard and McDonald (HIMI), the former of which is largely covered by glaciers. Waters in the region are subject to an intense mixing regime, caused by shallow bathymetry and the location of the plateau in the path of strong currents associated with the polar front. Fed by the Fe rich waters formed on the plateau, a phytoplankton bloom on the order of thousands of square kilometres forms in the lee of the plateau annually each summer. Few studies to date have focused on HIMI due to its extreme isolation. As such, the role of HIMI in the region's biogeochemical cycling is relatively unknown.

In order to examine the impact of these subaerial volcanoes on biogeochemical cycling in the area, dissolved iron (DFe) and macronutrient (NO_3^-, PO_4^{3-} and Si) data from waters surrounding HIMI was collected on the RV Investigator during the Heard Earth-Ocean-Biosphere Interactions (HEOBI) voyage (GEOTRACES process study GIpr05) in January to February 2016. Results show that DFe availability drives macronutrient uptake on the plateau. In late summer the majority of the plateau to the north of HIMI contains a deficit of DFe relative to macronutrients with respect to phytoplankton requirements, although dissolution of particulate Fe is expected to fulfil at least some of the Fe demand. Comparison of Fe:N and Fe:P drawdown

ratios with the Redfield ratio indicate that recycling of Fe decreases near HIMI, indicating that Fe limitation is alleviated close to the islands. Comparison with data from the only previous study in the area shows that DFe distribution varies between years due to the complex oceanographic conditions on the plateau, with greatest variability observed over the rough bathymetry and strongly tidally influenced region closest to HIMI. Together these data highlight the central role of Fe and the complexity of biogeochemical cycling in the HIMI region of the Kerguelen plateau.

Finally, processes supplying DFe around HIMI are further constrained by examining the DFe redox speciation and hydrogen peroxide (H_2O_2) chemistry in the region, analysed during the HEOBI voyage. Dissolved iron(II) (DFe(II)) is the reduced, short lived, potentially more bioavailable oxidation state of Fe in the ocean. Concentrations of DFe(II) in the surface ocean are inversely correlated to the concentration of reactive oxygen species such as H_2O_2, which decrease DFe(II) half-life. Surface DFe(II) concentrations at the open ocean reference station were very low (<0.09 nmol L^{-1}), while stations near HIMI showed elevated concentrations over the entire water column (mean 0.24 nmol L^{-1} and 0.36 nmol L^{-1}, respectively). At Heard Island, the greatest DFe(II) concentrations (max 0.57 nmol L^{-1}) were detected north of the island, and an inverse correlation of DFe(II) concentrations with salinity suggest the origin is from a marine-terminating glacier on the island. At McDonald Islands, the greatest DFe(II) concentrations (1.01 nmol L^{-1}) were detected east of the island which, based on water column profiles from five targeted stations and observed excess ^{3}He concentrations, appears likely to originate from shallow diffuse hydrothermalism. DFe(II):DFe(total) ratios at the sites of high DFe(II) concentrations at Heard and McDonald Islands (25% and 37%, respectively) adds further evidence that strong, but different sources of reduced Fe exist at each of the islands. Furthermore, lack of correlation with H_2O_2 and irradiance data suggest that over the plateau near HIMI, DFe(II) concentrations are more strongly governed by strong DFe(II) sources rather than by H_2O_2 and irradiance.

The findings presented in this thesis highlight the importance and sparse knowledge of the impact of hydrothermalism to Fe cycling in the SO, and significantly improve understanding of how the subaerial HIMI volcanoes influence biogeochemical cycling at a biological and volcanic hotspot in the SO.

Declaration and statements

Declaration of originality

This thesis contains no material which has been accepted for a degree or diploma by the University or any other institution, except by way of background information and duly acknowledged in the thesis, and to the best of my knowledge and belief no material previously published or written by another person except where due acknowledgement is made in the text of the thesis, nor does the thesis contain any material that infringes copyright.

Authority of access and statement regarding published work contained in the thesis

The publishers of the papers comprising Chapter 2 and Chapter 3 hold the copyright for that content, and access to the material should be sought from the respective journal. The remaining non published content of the thesis may be made available for loan and limited copying and communication in accordance with the Copyright Act 1968.

Signed:

Thomas M Holmes

PhD Candidate

6th of September 2018

Statement of co-authorship

The following people and institutions contributed to the publication of work undertaken as part of this thesis:

(1) Thomas M. Holmes (candidate) – Antarctic Climate and Ecosystems Cooperative Research Centre (ACE CRC), University of Tasmania, Hobart, Australia; Institute for Marine and Antarctic Studies (IMAS), University of Tasmania, Hobart, Australia.

(2) Andrew R. Bowie – Antarctic Climate and Ecosystems Cooperative Research Centre (ACE CRC), University of Tasmania, Hobart, Australia; Institute for Marine and Antarctic Studies (IMAS), University of Tasmania, Hobart, Australia.

(3) Zanna Chase – Institute for Marine and Antarctic Studies (IMAS), University of Tasmania, Hobart, Australia.

(4) Pier van der Merwe – Antarctic Climate and Ecosystems Cooperative Research Centre (ACE CRC), University of Tasmania, Hobart, Australia.

(5) Ashley T. Townsend – Central Science Laboratory (CSL), University of Tasmania, Hobart, Australia.

(6) Kathrin Wuttig – Antarctic Climate and Ecosystems Cooperative Research Centre (ACE CRC), University of Tasmania, Hobart, Australia.

(7) Christina Schallenberg – Antarctic Climate and Ecosystems Cooperative Research Centre (ACE CRC), University of Tasmania, Hobart, Australia.

(8) Manon Tonnard – Antarctic Climate and Ecosystems Cooperative Research Centre (ACE CRC), University of Tasmania, Hobart, Australia; Institute for Marine and Antarctic Studies (IMAS), University of Tasmania, Hobart, Australia; Laboratoire des sciences de l'Environnement MARin (LEMAR) – CNRS UMR 6539 - Institut Universitaire Européen de la Mer (IUEM), Université de Bretagne Occidentale, Technopôle Brest-Iroise, Plouzané, France.

Author's contributions

Chapters 2, 3, and 4 of this thesis have been prepared as manuscripts for submission to peer-reviewed journals. In all cases the design and implementation of the research, data analysis, interpretation of the results, and preparation of the manuscripts were the responsibility of the candidate but were carried out in consultation with supervisors and with the input of specialist contributors. These contributions are highlighted for each of these manuscripts below.

Chapter 2 (Paper 1): Detection, dispersal and biogeochemical contribution of hydrothermal iron in the ocean.

T. M. Holmes (first author): data compilation, data processing and analysis, manuscript writing.

Z. Chase (author 2): data analysis, manuscript writing.

P. van der Merwe (author 3): data analysis, manuscript writing.

A. T. Townsend (author 4): data analysis, manuscript writing.

A. R. Bowie (author 5): data analysis, manuscript writing.

Chapter 3 (Paper 2): Iron availability influences nutrient drawdown in the Heard and McDonald Islands region, Southern Ocean.

T. M. Holmes (first author): field work, laboratory work, data processing and analysis, manuscript writing.

K. Wuttig (author 2): field work, laboratory work, data processing and analysis, manuscript writing.

Z. Chase (author 3): field work, laboratory work, data processing and analysis, manuscript writing.

P. van der Merwe (author 4): field work, laboratory work, data processing and analysis, manuscript writing.

A. T. Townsend (author 5): laboratory work, data processing and analysis, manuscript writing.

C. Schallenberg (author 6): data processing and analysis, manuscript writing.

M. Tonnard (author 7): field work, laboratory work, data processing and analysis, manuscript writing.

A. R. Bowie (author 8): field work, laboratory work, data processing and analysis, manuscript writing.

Chapter 4 (Paper 3): Glacial and hydrothermal sources of dissolved iron(II) in Southern Ocean waters surrounding Heard and McDonald Islands.

T. M. Holmes (first author): field work, laboratory work, data processing and analysis, manuscript writing.

K. Wuttig (author 2): field work, laboratory work, data processing and analysis, manuscript writing.

Z. Chase (author 3): field work, laboratory work, data processing and analysis, manuscript writing.

C. Schallenberg (author 4): data processing and analysis, manuscript writing.

P. van der Merwe (author 5): field work, laboratory work, data processing and analysis, manuscript writing.

A. T. Townsend (author 6): data processing and analysis, manuscript writing.

A. R. Bowie (author 7): field work, laboratory work, data processing and analysis, manuscript writing.

We the undersigned agree with the above stated `proportion of work undertaken' for each of the above manuscripts contributing to this thesis:

Signed:

A/Prof. Andrew Bowie
Supervisor
Antarctic Climate and Ecosystems Cooperative Research Centre (ACECRC)
Institute for Marine and Antarctic Studies (IMAS)
University of Tasmania

Date: 12/09/2018

Signed:

Dr Delphine Lannuzel
Deputy Centre Head - Oceans & Cryosphere
Institute for Marine and Antarctic Studies (IMAS)
University of Tasmania

Date: 14/09/2018

Acknowledgements

My first thanks need to go to Andy, you took a risk in taking me on, as someone who'd been out of academia for almost seven years and with a background outside of oceanography. Four years, two voyages and a thesis later, look how far I've come! Thanks mate.

Zanna, thank you for being such an inspiration! Your lightning-fast running speed is surpassed only by your mental agility. Your ideas and the time you spent shaping my manuscripts really was instrumental in getting me here and taught me a great deal.

Pier, your unwavering patience and technical prowess is the reason why I know what I do about clean lab techniques, clean sampling protocols and basically all the practicalities of being a trace metal scientist. Without your expertise I think that either the FIA may have destroyed my sanity, or I might have destroyed it. Thank you!

Ash, apart from your obviously first class ICP-MS skills, which were instrumental in putting together my DFe chapter, I want to thank you for your constant positivity, your sharp editing eye and your positive reinforcement. I know it's your natural state, but your positive attitude really made a huge difference in getting through all the edits, iterations and challenging times.

To all four of you I'd like you to know that I feel really lucky to have a supervisory team comprised of such down to earth, friendly, supportive, patient and competent scientists. You all really set a great example and without all of you I'm certain my PhD wouldn't have been such a success. Thank you!

Others outside of my supervisory team also contributed a great deal to my thesis and to my development as a scientist. Kathrin, thank you for being so much more than just a co-author. You took on a mentoring role and taught me a great deal over the last few years. Your support was extremely helpful and greatly appreciated. Christina, your input into the structuring of my papers and your expertise in Fe(II) really sped up my writing process, thank you. Mel, your

advice at key points over the last few years was invaluable, thank you. Lavy, your advice and prowess at navigating through the wilderness of university bureaucracy while also winning grants and funding taught me a lot about being a successful academic, thanks!

I'd also like to thank the broader team at ACECRC. You have constantly been a great support and given me opportunities I never would have had elsewhere, including conference funding, a top-up scholarship and the opportunity to participate in Southern Ocean voyages. I feel lucky to be associated with such a great organisation.

Finally, I of course need to thank my partner and my family, because when you do a PhD all those around you also kind of have to do it too. Without their support, I couldn't have achieved what I have, or at least, not with some semblance of my sanity left intact. Christine especially, thank you so much for your huge support throughout, but most of all at the latter stages, of my PhD. You inspired me and gave me the drive to keep going, all while tackling your own thesis.

Contents

List of Figures

List of Tables

Chapter 1

1 Introduction

The ocean contains roughly 60 times more carbon than the atmosphere and exerts a dominant control on atmospheric carbon dioxide (CO_2) concentrations (Sarmiento and Gruber, 2006). Through photosynthesis, marine phytoplankton consume roughly an equal amount of CO_2 annually as terrestrial photosynthetic organisms (Field, 1998). This drives drawdown of CO_2 from the atmosphere into the surface ocean and subsequently converts carbon into particulate form, some of which sinks and is sequestered within deep ocean water or sediments (Sarmiento and Gruber, 2006). Phytoplankton, like terrestrial plants, require nutrients (e.g. nitrate, phosphorous, silicate and trace elements), sunlight and carbon to survive.

The trace element iron (Fe) is now recognised as a key limiting micronutrient, regulating primary productivity in as much as half the world's oceans (Moore et al., 2009, 2001). Areas of the ocean that are high in the macronutrients nitrogen (N) and phosphorous (P) but low in chlorophyll producing organisms are known as high-nutrient low-chlorophyll (HNLC) regions. Given that Fe plays such an important role in phytoplankton productivity and distribution in the ocean, Fe observations and knowledge of the processes governing Fe distribution are still relatively sparse in comparison to macronutrient observations. This is mostly due to the difficulties involved in sampling the picomolar (10^{-12} mole L^{-1}) to nanomolar (10^{-9} mole L^{-1}) concentrations present in low-Fe seawater while keeping samples free from Fe contamination, which is abundant on the ships from which samples are taken. The development of trace-metal-clean sampling techniques (Cutter et al., 2017) and analytical methods with sufficiently low detection limits (Worsfold et al., 2014), coupled with the internationally collaborative sampling program GEOTRACES (Schlitzer et al., 2018) and inter-laboratory calibration efforts (Johnson et al., 2007) has allowed a recent

rapid expansion of Fe observations and insights into processes controlling the distribution of Fe in the ocean (Mawji et al., 2015; Schlitzer et al., 2018; Tagliabue et al., 2017).

Though great progress has been made in resolving the ocean Fe cycle in the last 30 years, many questions remain unresolved, including the distribution and cycling of Fe in remote regions of the Southern Ocean (Tagliabue et al., 2017). The Southern Ocean is of particular importance, in terms of biogeochemical cycling and CO_2 drawdown, as this region of the ocean is responsible for 20 – 25% of global ocean CO_2 uptake, while representing only 10% of the total area of the ocean (Takahashi et al., 2002). It is also the largest HNLC region (Boyd et al., 2012). Therefore, understanding the biogeochemistry of the Southern Ocean is vital to understanding our current climate system and accurately predicting future climate scenarios.

Iron in the ocean is redox sensitive and is found in two forms, Fe(II), the reduced form that is highly soluble but highly unstable in oxygenated waters, and Fe(III), the oxidised form that is stable in oxygenated waters but highly insoluble, and which precipitates out of solution (Millero et al., 1995). The low concentration of Fe found in much of the ocean is largely due to the low solubility of Fe(III) in oxygenated waters, coupled with biological demand for the essential nutrient (Boyd and Ellwood, 2010; Tagliabue et al., 2017). However, dissolved Fe(III) (DFe) is found in higher concentrations in the ocean than predicted by thermodynamic considerations due to stabilisation by organic complexing molecules, known as ligands (Gledhill and Buck, 2012), which are actively produced by microbes and passively by organic matter. Dissolved Fe concentrations are greatest near sources such as mid-ocean ridge hydrothermal vents and continental margins (Figure 1.1).

Sources of Fe to the ocean include resuspension of coastal and shallow sediments (Blain et al., 2007; Johnson et al., 1999; Moore and Braucher, 2008; Pollard et al., 2009; Tagliabue et al., 2009), glacial and iceberg melt (Hawkings et al., 2018; Hopwood et al., 2014; Smith et al., 2007), seasonal sea ice retreat (Lannuzel et al., 2008; Schallenberg et al., 2016; Sedwick and DiTullio,

1997; van der Merwe et al., 2011), island wakes (Blain et al., 2007, 2001; Doty and Oguri, 1956), vertical diffusive flux (Boyd et al., 2005; Law et al., 2003), interaction between bathymetry and currents (Sokolov and Rintoul, 2007), dust deposition (Duce and Tindale, 1991; Gaiero et al.,

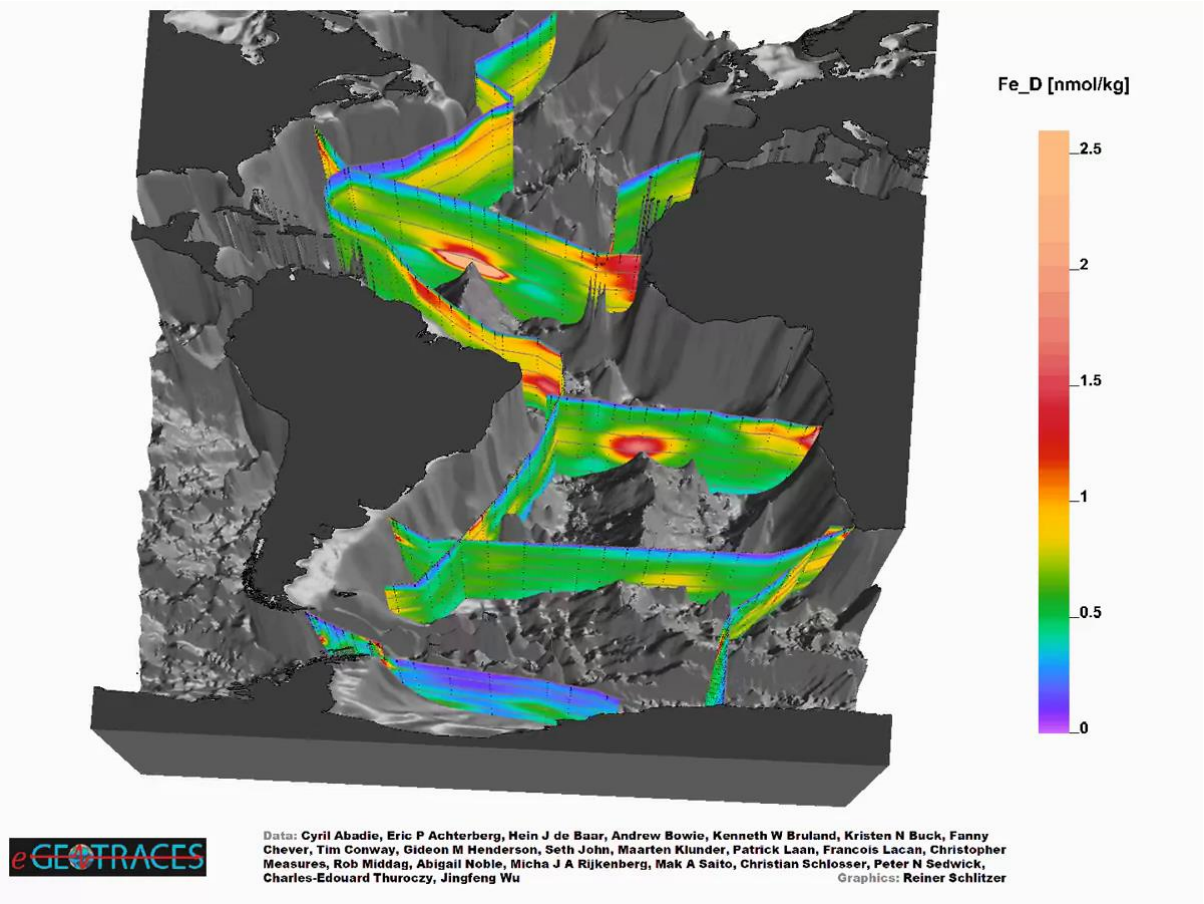

Figure 1.1. Three dimensional GEOTRACES scene of DFe concentrations in the Atlantic Ocean. The greatest DFe concentrations are found over the mid-ocean ridges from hydrothermal input and near continental shelves from sedimentary, dust and riverine input. Concentrations are lowest in the Southern Ocean. Courtesy of Schlitzer, Reiner, eGEOTRACES - Electronic Atlas of GEOTRACES Sections and Animated 3D Scenes, http://www.egeotraces.org, 2018. Data contributors are cited in figure.

2003; Tagliabue et al., 2009; Winton et al., 2015) and hydrothermal inputs (Hawkes et al., 2013; Klunder et al., 2011; Mackey et al., 2002). Major processes of the ocean Fe cycle are shown in Figure 1.2. Hydrothermal inputs, in particular, have gained increasing recognition in recent years as a previously overlooked source of Fe to the deep ocean that may potentially affect surface productivity in some regions of the ocean (Holmes et al., 2017). Furthermore, shallow hydrothermal vents, while less common than mid-ocean ridge vents, may supply Fe directly to the surface mixed layer (defined as the oceanic surface layer within which salinity, temperature

and density are almost vertically uniform; e.g. de Boyer Montégut et al., 2004). Subaerial volcanic islands are also sources of Fe, potentially through multiple processes including shallow hydrothermalism (Fitzsimons et al., 1997; Kleint et al., 2017), sediments (Charette et al., 2007), volcanic ash and dust (Olgun et al., 2011) and island mass effects (Blain et al., 2001).

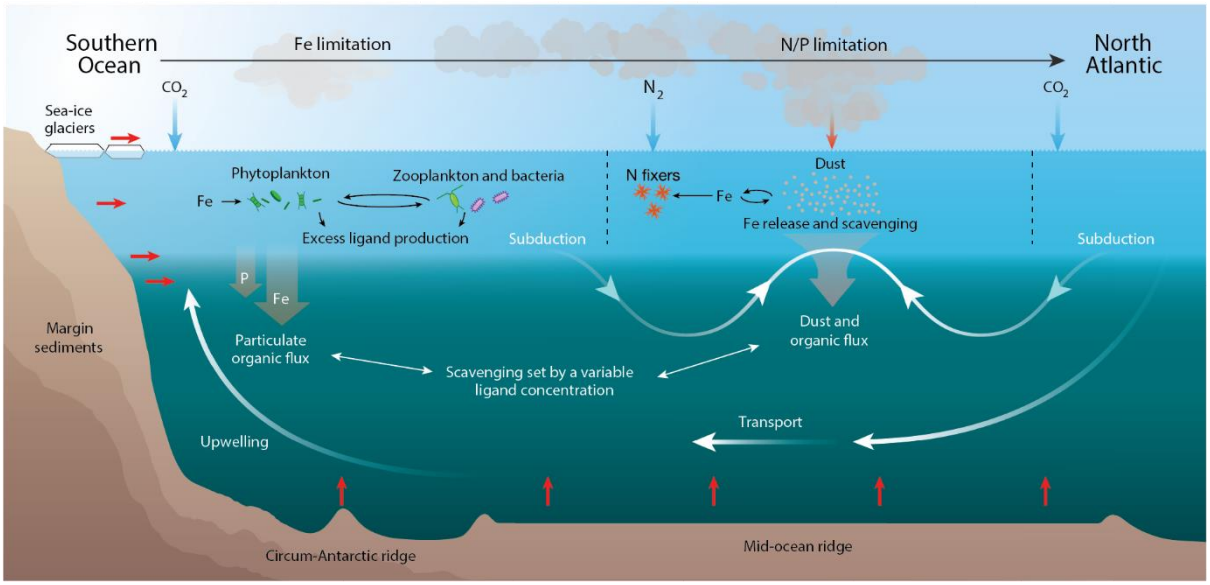

Figure 1.2. Schematic of major processes in the ocean iron cycle, with the Atlantic Ocean used as example (Figure from Tagliabue et al., 2017).

Heard and McDonald Islands (HIMI) are volcanically active subaerial islands (Figure 1.3.) located on the central Kerguelen Plateau in the Indian sector of the Southern Ocean (Figure 1.4.). Glacier-covered Heard Island is highly active and has erupted regularly in recent times (Duncan et al., 2016); most recently observed in January 2016, during the research voyage used to collect data for this study (Figure 3; Coffin, 2016). Unglaciated McDonald Islands is a relatively new island (Quilty and Wheller, 2000) and is also recently active, almost doubling in size around 1997 (Stephenson et al., 2005). The northern Kerguelen plateau is relatively shallow (Beaman and O'Brien, 2011) and lies in the path of strong currents associated with the Antarctic Circumpolar Current. The north of the northern plateau lies in the path of strong currents associated with the Polar Front and the central plateau lies in the path of strong currents associated with the Fawn Trough (Figure 1.4.). In the midst of the HNLC Southern Ocean, a

large phytoplankton plume forms over the plateau to the north of HIMI and in the lee of the plateau on the order of thousands of square kilometres (Blain et al., 2007). This bloom is fed by Fe derived from the plateau (Blain et al., 2008; Bowie et al., 2015); however, the sources of Fe require further investigation and prior to this research there have been no studies directly focusing on the biogeochemical cycling of Fe around HIMI.

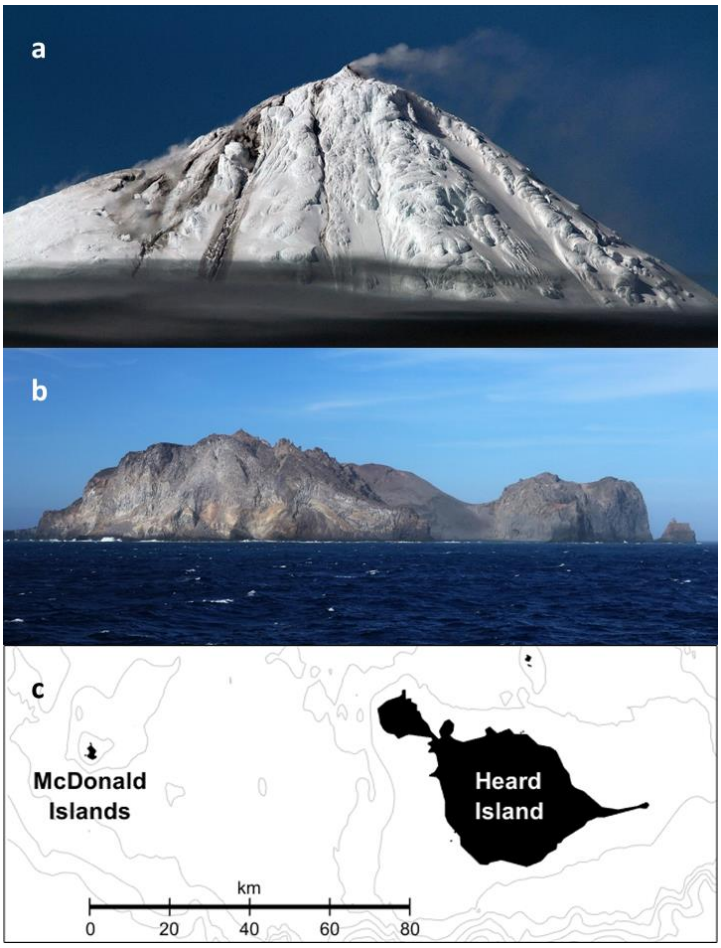

Figure 1.3. **a.** Mawson Peak, Heard Island, eruption observed during the HEOBI voyage. Photo courtesy of Pete Harmsen. **b.** McDonald Islands, as observed during the HEOBI voyage. Photo courtesy of Richard Arculus. **c.** Heard and McDonald Islands. Bathymetric isobaths are shown at every 100 m depth.

Based on the high primary productivity observed in previous in situ and satellite studies of the region just to the north of HIMI (Blain et al., 2008; Bowie et al., 2015; Mongin et al., 2008) we hypothesise in this thesis that supply of Fe from volcanic activity at HIMI is an important source of bioavailable Fe to the northern region of the Kerguelen Plateau. In January – February 2016 samples were collected during the Heard Earth-Ocean-Biosphere Interactions (HEOBI) voyage

to test this hypothesis. Data collected during this voyage aboard the Australian CSIRO research vessel *Investigator*, in conjunction with a global compilation of hydrothermal Fe data, is used in this thesis to investigate the role that volcanism plays in Fe biogeochemical cycling at the basin scale in the Southern Ocean, at the regional scale at the central Kerguelen Plateau and at the local scale around Heard and McDonald Islands.

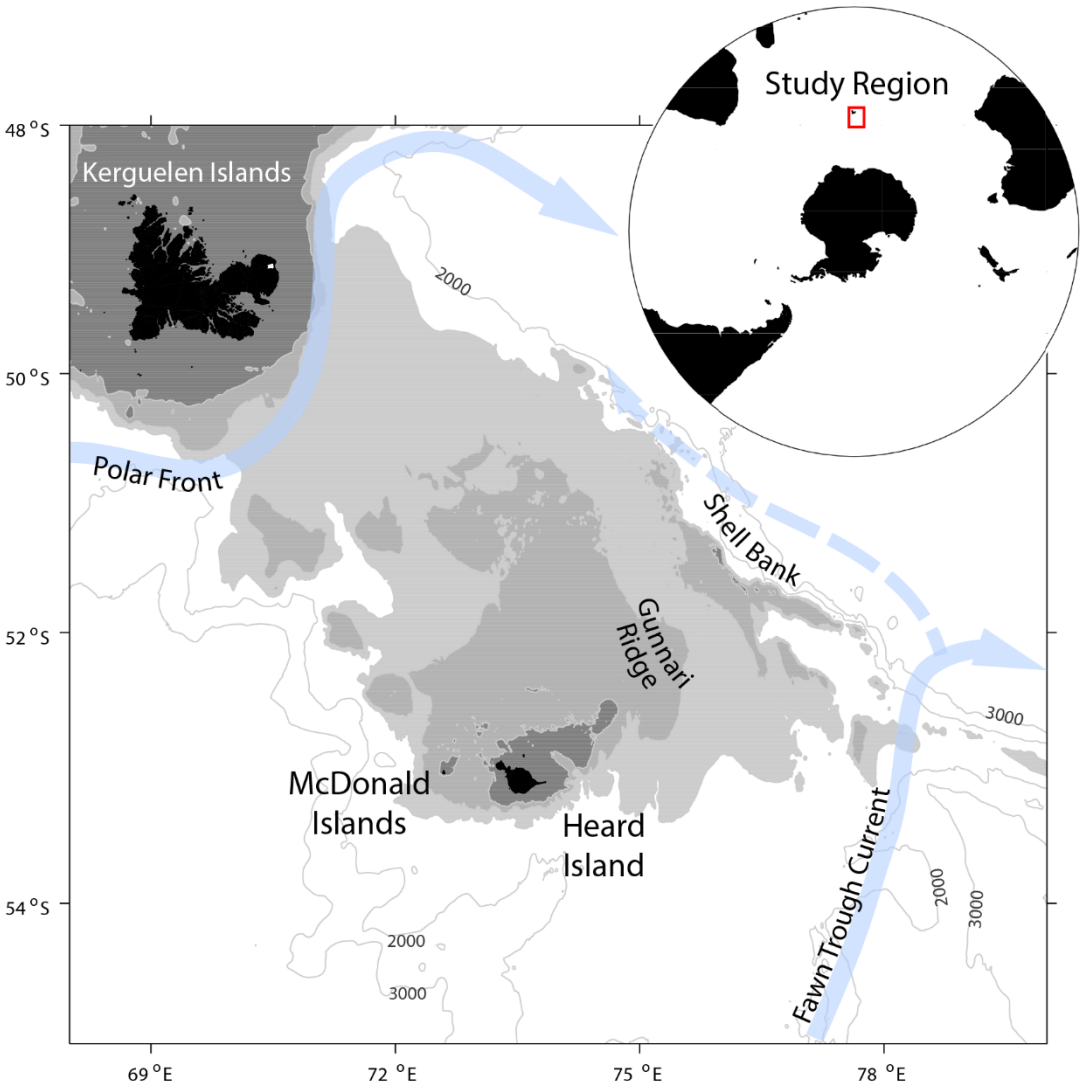

Figure 1.4. Northern Kerguelen Plateau. Location of the plateau is shown in top inset. Bathymetric isobaths are shown, with seabed <200 m depth shaded dark grey, <500 m shaded lighter grey and <1000 m shaded lightest grey. Major currents are shown in light blue arrows, adapted from Park et al., (2014).

The impact of volcanism on Fe biogeochemistry in the Southern Ocean is addressed by first broadly examining the impact of hydrothermalism on Fe cycling in the Southern Ocean through

an extensive compilation of hydrothermal end-member Fe measurements and literature review in **chapter 2** (manuscript published in Marine and Freshwater Research, 2017). The focus is then drawn to the volcanically active HIMI region, a biological hotspot in the Indian sector of the Southern Ocean. Laboratory and shipboard methods used for the biogeochemical investigation of HIMI are presented in **chapter 3**. Dissolved Fe and macronutrient data collected during HEOBI from the HIMI region and further north and east on the plateau is utilised to examine how DFe availability influences nutrient drawdown in the region in **chapter 4** (manuscript submitted to Marine Chemistry, 2018). The focus is then drawn in closer to HIMI, and the distribution and processes of Fe redox speciation are examined at each of the islands to gain insight into Fe supply mechanisms around these unique hotspot volcanoes in **chapter 5** (manuscript in preparation for Earth and Planetary Science Letters, 2018). Finally, **chapter 6** summarises the broad conclusions of this work and outlines some recommended directions for future research.

1.1 References

Beaman, R., O'Brien, P., 2011. Kerguelen Plateau Bathymetric Grid, November 2010.

Blain, S., Quéguiner, B., Armand, L., Belviso, S., Bombled, B., Bopp, L., Bowie, A., Brunet, C., Brussaard, C., Carlotti, F., Christaki, U., Corbière, A., Durand, I., Ebersbach, F., Fuda, J.-L., Garcia, N., Gerringa, L., Griffiths, B., Guigue, C., Guillerm, C., Jacquet, S., Jeandel, C., Laan, P., Lefèvre, D., Lo Monaco, C., Malits, A., Mosseri, J., Obernosterer, I., Park, Y.-H., Picheral, M., Pondaven, P., Remenyi, T., Sandroni, V., Sarthou, G., Savoye, N., Scouarnec, L., Souhaut, M., Thuiller, D., Timmermans, K., Trull, T., Uitz, J., van Beek, P., Veldhuis, M., Vincent, D., Viollier, E., Vong, L., Wagener, T., 2007. Effect of natural iron fertilization on carbon sequestration in the Southern Ocean. Nature 446, 1070–4. doi:10.1038/nature05700

Blain, S., Sarthou, G., Laan, P., 2008. Distribution of dissolved iron during the natural iron-fertilization experiment KEOPS (Kerguelen Plateau, Southern Ocean). Deep Sea Res. Part II Top. Stud. Oceanogr. 55, 594–605. doi:10.1016/j.dsr2.2007.12.028

Blain, S., Tréguer, P., Belviso, S., Bucciarelli, E., Denis, M., Desabre, S., Fiala, M., Martin Jézéquel, V., Le Fèvre, J., Mayzaud, P., Marty, J.-C., Razouls, S., 2001. A biogeochemical study of the island mass effect in the context of the iron hypothesis: Kerguelen Islands, Southern Ocean. Deep Sea Res. Part I Oceanogr. Res. Pap. 48, 163–187. doi:10.1016/S0967-0637(00)00047-9

Bowie, A.R., van der Merwe, P., Quéroué, F., Trull, T., Fourquez, M., Planchon, F., Sarthou, G., Chever, F., Townsend, A.T., Obernosterer, I., Sallée, J.-B., Blain, S., 2015. Iron budgets for three distinct biogeochemical sites around the Kerguelen archipelago (Southern Ocean) during the natural fertilisation experiment KEOPS-2. Biogeosciences Discuss. 11, 17861–17923. doi:10.5194/bgd-11-17861-2014

Boyd, P.W., Arrigo, K.R., Strzepek, R., van Dijken, G.L., 2012. Mapping phytoplankton iron utilization: Insights into Southern Ocean supply mechanisms. J. Geophys. Res. 117, C06009. doi:10.1029/2011JC007726

Boyd, P.W., Ellwood, M.J., 2010. The biogeochemical cycle of iron in the ocean. Nat. Geosci. doi:10.1038/ngeo964

Boyd, P.W., Law, C.S., Hutchins, D. a., Abraham, E.R., Croot, P.L., Ellwood, M., Frew, R.D., Hadfield, M., Hall, J., Handy, S., Hare, C., Higgins, J., Hill, P., Hunter, K. a., LeBlanc, K., Maldonado, M.T., McKay, R.M., Mioni, C., Oliver, M., Pickmere, S., Pinkerton, M., Safi, K., Sander, S., Sanudo-Wilhelmy, S. a., Smith, M., Strzepek, R., Tovar-Sanchez, a., Wilhelm, S.W., 2005. FeCycle: Attempting an iron biogeochemical budget from a mesoscale SF6 tracer experiment in unperturbed low iron waters. Global Biogeochem. Cycles 19, 1–13.

doi:10.1029/2005GB002494

Charette, M.A., Gonneea, M.E., Morris, P.J., Statham, P., Fones, G., Planquette, H., Salter, I., Garabato, A.N., 2007. Radium isotopes as tracers of iron sources fueling a Southern Ocean phytoplankton bloom. Deep. Res. Part II Top. Stud. Oceanogr. 54, 1989–1998. doi:10.1016/j.dsr2.2007.06.003

Coffin, M., 2016. HEOBI: Heard Earth-Ocean-Biosphere Interactions voyage summary. Hobart, Australia.

Cutter, G., Casciotti, K., Croot, P., Geibert, W., Heimbürger, L.-E., Lohan, M., Planquette, H., van de Flierdt, T., 2017. Sampling and Sample-handling Protocols for GEOTRACES Cruises. Version 3, August 2017. Toulouse, France. doi:http://dx.doi.org/10.25607/OBP-2

de Boyer Montégut, C., Madec, G., Fischer, A.S., Lazar, A., Iudicone, D., 2004. Mixed layer depth over the global ocean: An examination of profile data and a profile-based climatology. J. Geophys. Res. C Ocean. 109, 1–20. doi:10.1029/2004JC002378

Doty, M.S., Oguri, M., 1956. The island mass effect. ICES J. Mar. Sci. 22, 33–37. doi:10.1093/icesjms/22.1.33

Duce, R. a., Tindale, N.W., 1991. Atmospheric transport of iron and its deposition in the ocean. Limnol. Oceanogr. 36, 1715–1726. doi:10.4319/lo.1991.36.8.1715

Duncan, R.A., Quilty, P.G., Barling, J., Fox, J.M., 2016. Geological development of Heard Island, Central Kerguelen Plateau. Aust. J. Earth Sci. 63, 81–89. doi:10.1080/08120099.2016.1139000

Field, C.B., 1998. Primary Production of the Biosphere: Integrating Terrestrial and Oceanic Components. Science (80-.). 281, 237–240. doi:10.1126/science.281.5374.237

Fitzsimons, M.F., Dando, P.R., Hughes, J.A., Thiermann, F., Akoumianaki, I., Pratt, S.M., 1997.

Submarine hydrothermal brine seeps off Milos, Greece: Observations and geochemistry. Mar. Chem. 57, 325–340. doi:10.1016/S0304-4203(97)00021-2

Gaiero, D.M., Probst, J.L., Depetris, P.J., Bidart, S.M., Leleyter, L., 2003. Iron and other transition metals in Patagonian riverborne and windborne materials: Geochemical control and transport to the southern South Atlantic Ocean. Geochim. Cosmochim. Acta 67, 3603–3623. doi:10.1016/S0016-7037(03)00211-4

Gledhill, M., Buck, K.N., 2012. The organic complexation of iron in the marine environment: a review. Front. Microbiol. 3, 69. doi:10.3389/fmicb.2012.00069

Hawkes, J.A., Connelly, D.P., Gledhill, M., Achterberg, E.P., 2013. The stabilisation and transportation of dissolved iron from high temperature hydrothermal vent systems. Earth Planet. Sci. Lett. 375, 280–290. doi:10.1016/j.epsl.2013.05.047

Hawkings, J.R., Benning, L.G., Raiswell, R., Kaulich, B., Araki, T., Abyaneh, M., Stockdale, A., Koch-müller, M., Wadham, J.L., Tranter, M., 2018. Biolabile ferrous iron bearing nanoparticles in glacial sediments. Earth Planet. Sci. Lett. 493, 92–101. doi:10.1016/j.epsl.2018.04.022

Holmes, T.M., Chase, Z., Van Der Merwe, P., Townsend, A.T., Bowie, A.R., 2017. Detection, dispersal and biogeochemical contribution of hydrothermal iron in the ocean. Mar. Freshw. Res. 68, 2184–2204. doi:10.1071/MF16335

Hopwood, M.J., Statham, P.J., Tranter, M., Wadham, J.L., 2014. Glacial flours as a potential source of Fe(II) and Fe(III) to polar waters. Biogeochemistry 118, 443–452. doi:10.1007/s10533-013-9945-y

Johnson, K.S., Chavez, F.P., Friederich, G.E., 1999. Continental-shelf sediment as a primary source of iron for coastal phytoplankton. Nature 398, 697–700. doi:10.1038/19511

Johnson, K., Elrod, V., Fitzwater, S., 2007. Developing standards for dissolved iron in seawater. Eos (Washington. DC). 88, 131–132.

Kleint, C., Pichler, T., Koschinsky, A., 2017. Geochemical characteristics, speciation and size-fractionation of iron (Fe) in two marine shallow-water hydrothermal systems, Dominica, Lesser Antilles. Chem. Geol. 454, 44–53. doi:10.1016/j.chemgeo.2017.02.021

Klunder, M.B., Laan, P., Middag, R., De Baar, H.J.W., van Ooijen, J.C., 2011. Dissolved iron in the Southern Ocean (Atlantic sector). Deep Sea Res. Part II Top. Stud. Oceanogr. 58, 2678–2694. doi:10.1016/j.dsr2.2010.10.042

Lannuzel, D., Schoemann, V., de Jong, J., Chou, L., Delille, B., Becquevort, S., Tison, J.L., 2008. Iron study during a time series in the western Weddell pack ice. Mar. Chem. 108, 85–95. doi:10.1016/j.marchem.2007.10.006

Law, C.S., Abraham, E.R., Watson, A.J., Liddicoat, M.I., 2003. Vertical eddy diffusion and nutrient supply to the surface mixed layer of the Antarctic Circumpolar Current. J. Geophys. Res. 108, 3272. doi:10.1029/2002JC001604

Mackey, D.J., O'Sullivan, J.E.Os., Watson, R.J., 2002. Iron in the western Pacific: a riverine or hydrothermal source for iron in the Equatorial Undercurrent? Deep Sea Res. Part I Oceanogr. Res. Pap. 49, 877–893. doi:10.1016/S0967-0637(01)00075-9

Mawji, E., Schlitzer, R., Masferrer, E., Abadie, C., Abouchami, W., Anderson, R.F., Baars, O., Bakker, K., Baskaran, M., Bates, N.R., Bluhm, K., Bowie, A., Bown, J., Boye, M., Boyle, E.A., Branellec, P., Bruland, K.W., Brzezinski, M.A., Bucciarelli, E., Buesseler, K., Butler, E., Cai, P., Cardinal, D., Casciotti, K., Chaves, J., Cheng, H., Chever, F., Church, T.M., Colman, A.S., Conway, T.M., Croot, P.L., Cutter, G.A., Baar, H.J.W. De, Souza, G.F. De, Dehairs, F., Deng, F., Thi, H., Dulaquais, G., Echegoyen-sanz, Y., Edwards, R.L., Fahrbach, E., Fitzsimmons, J., Fleisher, M., Frank, M., Friedrich, J., Fripiat, F., Galer,

S.J.G., Gamo, T., Garcia, E., Gerringa, L.J.A., Marcus, J., Gonzalez, S., Grossteffan, E., Hatta, M., Hayes, C.T., Iris, M., Henderson, G., Huang, K., Jeandel, C., Jenkins, W.J., John, S., Kenna, T.C., Klunder, M., Kretschmer, S., Kumamoto, Y., Laan, P., Labatut, M., Lacan, F., Lam, P.J., Lannuzel, D., Lechtenfeld, O.J., Lohan, M.C., Lu, Y., Masqué, P., Mcclain, C.R., Measures, C., Middag, R., Moffett, J., Navidad, A., Nishioka, J., Noble, A., Obata, H., Ohnemus, D.C., Owens, S., Planchon, F., Pradoux, C., Puigcorbé, V., Quay, P., Radic, A., Rehkämper, M., Remenyi, T., Rijkenberg, M.J.A., Rintoul, S., Robinson, L.F., Roeske, T., Rosenberg, M., Rutgers, M., Loeff, V. Der, Ryabenko, E., Saito, M.A., Roshan, S., Salt, L., Sarthou, G., Schauer, U., Scott, P., Sedwick, P.N., Sha, L., Shiller, A.M., Sigman, D.M., Smethie, W., Smith, G.J., Sohrin, Y., Speich, S., Stichel, T., Stutsman, J., Swift, J.H., Tagliabue, A., Thomas, A., Tsunogai, U., Twining, B.S., Aken, H.M. Van, Heuven, S. Van, Ooijen, J. Van, Weerlee, E. Van, Venchiarutti, C., Voelker, A.H.L., Wake, B., Warner, M.J., Woodward, E.M.S., Wu, J., Wyatt, N., Yoshikawa, H., Zheng, X., Xue, Z., Zieringer, M., Zimmer, L.A., 2015. The GEOTRACES Intermediate Data Product 2014. Mar. Chem. 1–8. doi:10.1016/j.marchem.2015.04.005

Millero, F.J., Yao, W., Aicher, J., 1995. The speciation of Fe(II) and Fe(III) in natural waters. Mar. Chem. 50, 21–39. doi:10.1016/0304-4203(95)00024-L

Mongin, M., Molina, E., Trull, T.W., 2008. Seasonality and scale of the Kerguelen plateau phytoplankton bloom: A remote sensing and modeling analysis of the influence of natural iron fertilization in the Southern Ocean. Deep Sea Res. Part II Top. Stud. Oceanogr. 55, 880–892. doi:10.1016/j.dsr2.2007.12.039

Moore, C.M., Mills, M.M., Achterberg, E.P., Geider, R.J., LaRoche, J., Lucas, M.I., McDonagh, E.L., Pan, X., Poulton, A.J., Rijkenberg, M.J. a., Suggett, D.J., Ussher, S.J., Woodward, E.M.S., 2009. Large-scale distribution of Atlantic nitrogen fixation controlled by iron availability. Nat. Geosci. 2, 867–871. doi:10.1038/ngeo667

Moore, J.K., Braucher, O., 2008. Sedimentary and mineral dust sources of dissolved iron to the world ocean. Biogeosciences 5, 631–656.

Moore, J.K., Doney, S.C., Glover, D.M., Fung, I.Y., 2001. Iron cycling and nutrient-limitation patterns in surface waters of the world ocean. Deep. Res. Part II Top. Stud. Oceanogr. 49, 463–507. doi:10.1016/S0967-0645(01)00109-6

Olgun, N., Duggen, S., Croot, P.L., Delmelle, P., Dietze, H., Schacht, U., Óskarsson, N., Siebe, C., Auer, A., Garbe-Schönberg, D., 2011. Surface ocean iron fertilization: The role of airborne volcanic ash from subduction zone and hot spot volcanoes and related iron fluxes into the Pacific Ocean. Global Biogeochem. Cycles 25, 1–15. doi:10.1029/2009GB003761

Pollard, R.T., Salter, I., Sanders, R.J., Lucas, M.I., Moore, C.M., Mills, R. a, Statham, P.J., Allen, J.T., Baker, A.R., Bakker, D.C.E., Charette, M. a, Fielding, S., Fones, G.R., French, M., Hickman, A.E., Holland, R.J., Hughes, J.A., Jickells, T.D., Lampitt, R.S., Morris, P.J., Nédélec, F.H., Nielsdóttir, M., Planquette, H., Popova, E.E., Poulton, A.J., Read, J.F., Seeyave, S., Smith, T., Stinchcombe, M., Taylor, S., Thomalla, S., Venables, H.J., Williamson, R., Zubkov, M. V, 2009. Southern Ocean deep-water carbon export enhanced by natural iron fertilization. Nature 457, 577–80. doi:10.1038/nature07716

Quilty, P.G., Wheller, G., 2000. Heard Island and the McDonald Islands: a window into the Kerguelen Plateau. Pap. Proc. R. Soc. Tasmania 133, 1–12.

Sarmiento, J.L., Gruber, N., 2006. Ocean biogeochemical dynamics. Princeton : Princeton University Press, Princeton, New Jersey. USA.

Schallenberg, C., van der Merwe, P., Chever, F., Cullen, J.T., Lannuzel, D., Bowie, A.R., 2016. Dissolved iron and iron(II) distributions beneath the pack ice in the East Antarctic (120°E) during the winter/spring transition. Deep Sea Res. Part II Top. Stud. Oceanogr. 131, 96–110. doi:10.1016/j.dsr2.2015.02.019

Schlitzer, R., Anderson, R.F., Dodas, E.M., Lohan, M., Geibert, W., Tagliabue, A., Bowie, A., Jeandel, C., Maldonado, M.T., Landing, W.M., Cockwell, D., Abadie, C., Abouchami, W., Achterberg, E.P., Agather, A., Aguliar-Islas, A., van Aken, H.M., Andersen, M., Archer, C., Auro, M., de Baar, H.J., Baars, O., Baker, A.R., Bakker, K., Basak, C., Baskaran, M., Bates, N.R., Bauch, D., van Beek, P., Behrens, M.K., Black, E., Bluhm, K., Bopp, L., Bouman, H., Bowman, K., Bown, J., Boyd, P., Boye, M., Boyle, E.A., Branellec, P., Bridgestock, L., Brissebrat, G., Browning, T., Bruland, K.W., Brumsack, H.-J., Brzezinski, M., Buck, C.S., Buck, K.N., Buesseler, K., Bull, A., Butler, E., Cai, P., Mor, P.C., Cardinal, D., Carlson, C., Carrasco, G., Casacuberta, N., Casciotti, K.L., Castrillejo, M., Chamizo, E., Chance, R., Charette, M.A., Chaves, J.E., Cheng, H., Chever, F., Christl, M., Church, T.M., Closset, I., Colman, A., Conway, T.M., Cossa, D., Croot, P., Cullen, J.T., Cutter, G.A., Daniels, C., Dehairs, F., Deng, F., Dieu, H.T., Duggan, B., Dulaquais, G., Dumousseaud, C., Echegoyen-Sanz, Y., Edwards, R.L., Ellwood, M., Fahrbach, E., Fitzsimmons, J.N., Russell Flegal, A., Fleisher, M.Q., van de Flierdt, T., Frank, M., Friedrich, J., Fripiat, F., Fröllje, H., Galer, S.J.G., Gamo, T., Ganeshram, R.S., Garcia-Orellana, J., Garcia-Solsona, E., Gault-Ringold, M., George, E., Gerringa, L.J.A., Gilbert, M., Godoy, J.M., Goldstein, S.L., Gonzalez, S.R., Grissom, K., Hammerschmidt, C., Hartman, A., Hassler, C.S., Hathorne, E.C., Hatta, M., Hawco, N., Hayes, C.T., Heimbürger, L.-E., Helgoe, J., Heller, M., Henderson, G.M., Henderson, P.B., van Heuven, S., Ho, P., Horner, T.J., Hsieh, Y.-T., Huang, K.-F., Humphreys, M.P., Isshiki, K., Jacquot, J.E., Janssen, D.J., Jenkins, W.J., John, S., Jones, E.M., Jones, J.L., Kadko, D.C., Kayser, R., Kenna, T.C., Khondoker, R., Kim, T., Kipp, L., Klar, J.K., Klunder, M., Kretschmer, S., Kumamoto, Y., Laan, P., Labatut, M., Lacan, F., Lam, P.J., Lambelet, M., Lamborg, C.H., Le Moigne, F.A.C., Le Roy, E., Lechtenfeld, O.J., Lee, J.-M., Lherminier, P., Little, S., López-Lora, M., Lu, Y., Masque, P., Mawji, E., Mcclain, C.R., Measures, C., Mehic, S., Barraqueta, J.-L.M., van der Merwe, P., Middag, R., Mieruch, S., Milne, A., Minami, T., Moffett, J.W., Moncoiffe, G., Moore, W.S.,

Morris, P.J., Morton, P.L., Nakaguchi, Y., Nakayama, N., Niedermiller, J., Nishioka, J., Nishiuchi, A., Noble, A., Obata, H., Ober, S., Ohnemus, D.C., van Ooijen, J., O'Sullivan, J., Owens, S., Pahnke, K., Paul, M., Pavia, F., Pena, L.D., Peters, B., Planchon, F., Planquette, H., Pradoux, C., Puigcorbé, V., Quay, P., Queroue, F., Radic, A., Rauschenberg, S., Rehkämper, M., Rember, R., Remenyi, T., Resing, J.A., Rickli, J., Rigaud, S., Rijkenberg, M.J.A., Rintoul, S., Robinson, L.F., Roca-Martí, M., Rodellas, V., Roeske, T., Rolison, J.M., Rosenberg, M., Roshan, S., Rutgers van der Loeff, M.M., Ryabenko, E., Saito, M.A., Salt, L.A., Sanial, V., Sarthou, G., Schallenberg, C., Schauer, U., Scher, H., Schlosser, C., Schnetger, B., Scott, P., Sedwick, P.N., Semiletov, I., Shelley, R., Sherrell, R.M., Shiller, A.M., Sigman, D.M., Singh, S.K., Slagter, H.A., Slater, E., Smethie, W.M., Snaith, H., Sohrin, Y., Sohst, B., Sonke, J.E., Speich, S., Steinfeldt, R., Stewart, G., Stichel, T., Stirling, C.H., Stutsman, J., Swarr, G.J., Swift, J.H., Thomas, A., Thorne, K., Till, C.P., Till, R., Townsend, A.T., Townsend, E., Tuerena, R., Twining, B.S., Vance, D., Velazquez, S., Venchiarutti, C., Villa-Alfageme, M., Vivancos, S.M., Voelker, A.H.L., Wake, B., Warner, M.J., Watson, R., van Weerlee, E., Alexandra Weigand, M., Weinstein, Y., Weiss, D., Wisotzki, A., Woodward, E.M.S., Wu, J., Wu, Y., Wuttig, K., Wyatt, N., Xiang, Y., Xie, R.C., Xue, Z., Yoshikawa, H., Zhang, J., Zhang, P., Zhao, Y., Zheng, L., Zheng, X.-Y., Zieringer, M., Zimmer, L.A., Ziveri, P., Zunino, P., Zurbrick, C., 2018. The GEOTRACES Intermediate Data Product 2017. Chem. Geol. doi:10.1016/j.chemgeo.2018.05.040

Sedwick, P.N., DiTullio, G.R., 1997. Regulation of algal blooms in Antarctic Shelf Waters by the release of iron from melting sea ice. Geophys. Res. Lett. 24, 2515–2518. doi:10.1029/97GL02596

Smith, K.L., Robison, B.H., Helly, J.J., Kaufmann, R.S., Ruhl, H. a, Shaw, T.J., Twining, B.S., Vernet, M., 2007. Free-drifting icebergs: hot spots of chemical and biological enrichment in the Weddell Sea. Science 317, 478–82. doi:10.1126/science.1142834

Sokolov, S., Rintoul, S.R., 2007. On the relationship between fronts of the Antarctic Circumpolar Current and surface chlorophyll concentrations in the Southern Ocean. J. Geophys. Res. 112, C07030. doi:10.1029/2006JC004072

Stephenson, J., Budd, G.M., Manning, J., Hansbro, P., 2005. Major eruption-induced changes to the McDonald Islands, southern Indian Ocean. Antarct. Sci. 17, 259–266. doi:10.1017/S095410200500266X

Tagliabue, A., Bopp, L., Aumont, O., 2009. Evaluating the importance of atmospheric and sedimentary iron sources to Southern Ocean biogeochemistry. Geophys. Res. Lett. 36, L13601. doi:10.1029/2009GL038914

Tagliabue, A., Bowie, A.R., Boyd, P.W., Buck, K.N., Johnson, K.S., Saito, M.A., 2017. The integral role of iron in ocean biogeochemistry. Nature 543, 51–59. doi:10.1038/nature21058

Takahashi, T., Sutherland, S.C., Sweeney, C., Poisson, A., Metzl, N., Tilbrook, B., Bates, N., Wanninkhof, R., Feely, R.A., Sabine, C., Olafsson, J., Nojiri, Y., 2002. Global sea–air CO_2 flux based on climatological surface ocean pCO2, and seasonal biological and temperature effects. Deep Sea Res. Part II Top. Stud. Oceanogr. 49, 1601–1622. doi:10.1016/S0967-0645(02)00003-6

van der Merwe, P., Lannuzel, D., Bowie, a. R., Mancuso Nichols, C. a., Meiners, K.M., 2011. Iron fractionation in pack and fast ice in East Antarctica: Temporal decoupling between the release of dissolved and particulate iron during spring melt. Deep. Res. Part II Top. Stud. Oceanogr. 58, 1222–1236. doi:10.1016/j.dsr2.2010.10.036

Winton, V.H.L., Bowie, A.R., Edwards, R., Keywood, M., Townsend, A.T., van der Merwe, P., Bollhöfer, A., 2015. Fractional iron solubility of atmospheric iron inputs to the Southern Ocean. Mar. Chem. 177, 20–32. doi:10.1016/j.marchem.2015.06.006

Worsfold, P., Lohan, M., Ussher, S., Bowie, A., 2014. Determination of dissolved iron in

seawater: A historical review. Mar. Chem. doi:10.1016/j.marchem.2014.08.009

Chapter 2

2 Detection, dispersal and biogeochemical contribution of hydrothermal iron in the ocean

This chapter was published as an article under the same title in Marine and Freshwater Research, 2017, by CSIRO Publishing, DOI: 10.1071/MF16335

Thomas M. Holmes[1,2], Zanna Chase[2], Pier van der Merwe[1], Ashley T. Townsend[3] and Andrew R. Bowie[1,2].

[1]Antarctic Climate and Ecosystems Cooperative Research Centre (ACE CRC), University of Tasmania, Hobart, Australia
[2]Institute for Marine and Antarctic Studies (IMAS), University of Tasmania, Hobart, Australia
[3]Central Science Laboratory (CSL), University of Tasmania, Hobart, Australia.

2.1 Abstract

This review aims to bring into focus the current understanding of hydrothermal systems and plume dynamics, tracers of hydrothermalism and the contribution of iron from hydrothermal vents to the global oceanic iron budget. The review then explores hydrothermal effect on surface ocean productivity. It is now well documented that scarcity of iron limits the production of chlorophyll-producing organisms in many regions of the ocean that are high in macronutrients. However, it is only recently that hydrothermal inputs have gained recognition as a source of Fe to the deep oceans that may potentially affect surface ocean productivity in some regions. A compilation of iron measurements from hydrothermal vents reveals that although hydrothermal studies measuring iron have increased significantly in recent years, there is still a dearth of data below 40°S. New analytical approaches for tracing iron sources, coupled with increasing sampling coverage of the oceans, is quickly improving knowledge of the effect of hydrothermal sources on biogeochemical cycles, a vital component in predicting future climate scenarios.

2.2 Introduction

The role of iron (Fe) as a limiting nutrient in regions of the oceans has been widely recognised since the publication of a seminal paper by oceanographer John Martin (1990), although the notion was first suggested in the 1930s (Ruud 1930; Gran 1931; Hart 1934). It is now well documented that the scarcity of this micronutrient limits the growth of chlorophyll-producing organisms in regions of the ocean that are high in macronutrients. These areas, covering approximately one-third of the ocean surface (Boyd et al. 2007), are known as high-nutrient, low-chlorophyll (HNLC) regions, where the growth of CO_2-consuming organisms, and thus potential CO_2 sequestration from the atmosphere, is inhibited by low Fe concentrations (Martin et al. 1990; de Baar et al. 2005; Boyd et al. 2007). Links between iron and nitrogen fixation by microbes in low-latitude regions of the oceans have also been demonstrated, which, together

with HNLC waters, may mean that Fe regulates biological productivity in as much as half the world's oceans (Moore et al. 2001, 2009).

Quantifying the relative importance and effect of different sources of Fe to the ocean will aid in predicting the response of biological productivity to future changing climate and oceanic conditions. Sources of Fe include resuspension of coastal and shallow sediments, glacial and iceberg melt, seasonal sea ice retreat, eddy-sediment interactions, island wakes, vertical diffusive flux, interaction between bathymetry and currents, dust deposition close to continents and discrete hydrothermal vent sources (Boyd and Ellwood 2010; Tagliabue et al. 2017; Figure 2.1). Hydrothermal inputs, in particular, have gained increasing recognition in recent years as a previously overlooked source of Fe to the deep oceans that may potentially affect surface productivity in some regions of the world's oceans (Tagliabue et al. 2010; Carazzo et al. 2013; Conway and John 2014; Fitzsimmons et al. 2014; Hawkes et al. 2014; Resing et al. 2015; Sander and Koschinsky 2016)

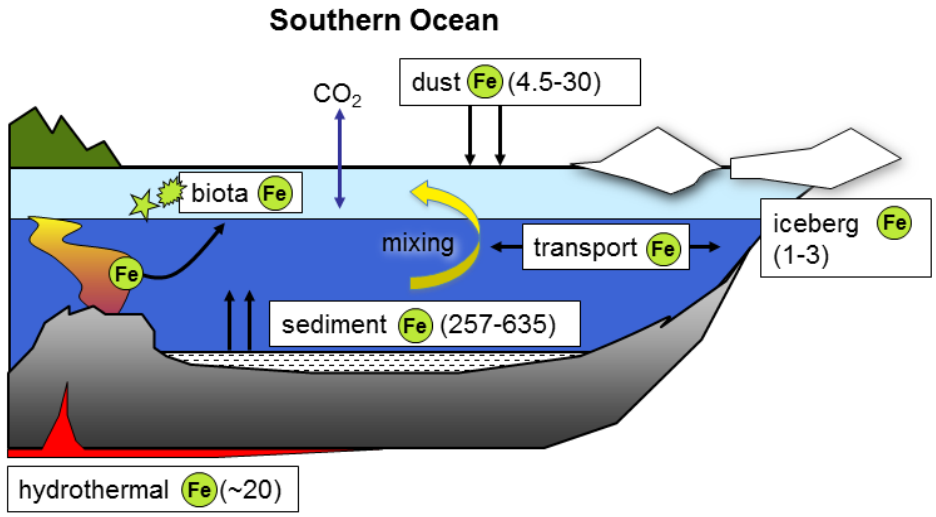

Figure 2.1 Schematic representation of the oceanic dissolved (D) Fe cycle in the Southern Ocean, including the range of estimates (in parentheses) of the total annual inputs of DFe ($\times 10^9$ g) of each of the source mechanisms to the overall Southern Ocean Fe budget (south of 35°S). The hydrothermal contribution is modelled by Tagliabue et al. (2010) from a compilation of 20 hydrothermal ^{3}He and DFe measurements. (Figure courtesy of Bernadette Proemse; adapted from Tagliabue et al. (2010))

Increasing hydrothermal observations, coupled with growing understanding of the complex mechanisms that stabilise dissolved Fe (DFe) in the ocean (see below), mean our understanding

of the importance of hydrothermal inputs to the global iron budget is evolving rapidly. In a recent review, German and Seyfried (2014) provide a comprehensive overview of hydrothermal systems with a focus on geological processes, including sub-seafloor hydrothermalism and formation of metalliferous sediments, as well as an overview of hydrothermal plume dynamics. The present review provides a summary of hydrothermal processes and methods for identifying plumes in oceanographic studies and expands on German and Seyfried's (2014) summary of processes affecting the dispersion of plumes into the ocean. Current knowledge of the contribution of Fe from hydrothermal vents to the global oceanic Fe budget and surface ocean productivity is brought into focus, including a discussion of hydrothermal Fe in the Southern Ocean and a global compilation of Fe measurements from hydrothermal vents (see Table S1, available as Supplementary Material to this paper). The data presented in Table S1 were compiled using the InterRidge Vents Database (Beaulieu 2015) to identify known vents, followed by an extensive search of scientific journal databases to identify studies that had measured Fe for each vent. At the time of writing, Table S1 was current with the latest data recorded in the InterRidge database. This review also aims to highlight key areas requiring further investigation in order to fully define the role of hydrothermal Fe in ocean biogeochemistry.

2.3 Hydrothermal vents: occurrence and geological settings

Close to sites of hydrothermal activity, fractures in the sea floor allow ocean water to infiltrate the Earth's crust (Lister 1972; Edmond et al. 1982; Von Damm 1995). In regions where hot, upwelling mantle rises close to the seafloor, seawater reaching hot lithospheric substrate (basaltic rock, ultramafic rock or magmatic fluid) is heated and returns to the seafloor, where it is released through hydrothermal vents, either as high-temperature fluids (i.e. 'black smokers' or 'white smokers') or as more diffuse, lower-temperature fluids that mix with ambient seawater intrusions upon ascent (Kadko et al. 1995; Von Damm 1995; German and Seyfried 2014; Figure 2.2). High-

temperature fluids not yet diluted with abyssal seawater are known as end-member fluids, which, upon mixing with ambient seawater, become known as hydrothermal plumes.

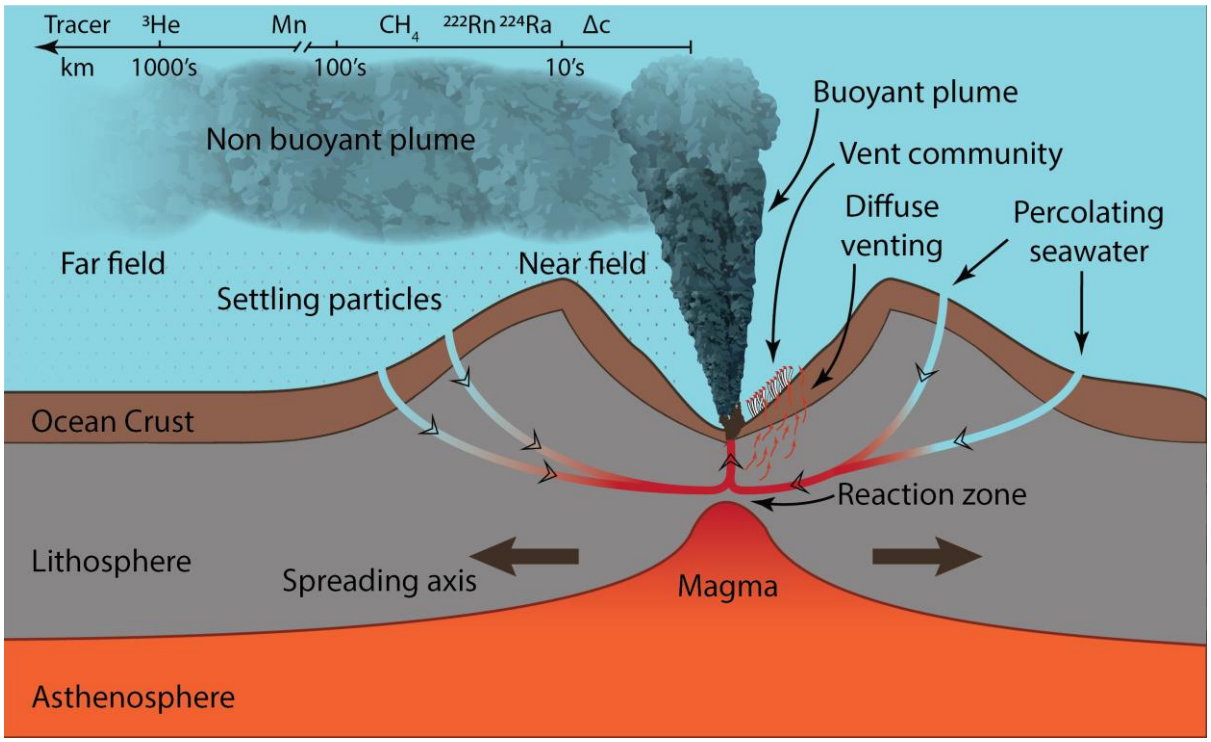

Figure 2.2 Schematic of a hydrothermal system showing abyssal seawater percolating through fractures in the sea floor to the reaction zone. In the reaction zone, seawater is super heated by hot lithospheric substrate (superheated rock or magmatic fluid), where it becomes buoyant and rapidly returns to the sea floor to be ejected through a focused vent structure ('smoker') or percolating through more fractures, diluting with seawater and being released as diffuse hydrothermal fluid. Areas around high-temperature vents and where diffuse flow escapes the sea floor commonly host rich hydrothermally fed ecosystems. High-temperature fluid rapidly rises to a point of neutral buoyancy, where it spreads laterally along density gradients. Close to the vent, particles rapidly precipitate and settle to the sea floor (near field), whereas in the neutrally buoyant plume particles also aggregate and settle to the sea floor at increasing distance (far field). The scale in the top left corner shows a representation of the spatial scales of tracers discussed in the text, namely Helium-3 (^{3}He), manganese (Mn), methane (CH_4), radon-222 (^{222}Rn), radium-224 (^{224}Ra) and particle concentration (Δc; giving light absorbance anomalies).

Hydrothermal vents exist in many geological settings containing shoaled mantle sources, including on mid-ocean ridges (plate spreading), back-arc spreading centres and volcanic arcs (plate subduction) and hotspots (intraplate; Figure 2.3, 2.4; Beaulieu et al. 2013; German and Seyfried, 2014). Mid-ocean ridges have historically been the most studied, although arc volcanoes and back-arc spreading centres have steadily been drawing more attention in recent years (Baker and German 2004; Beaulieu et al. 2013). Total vents described in the InterRidge Vents Database (Beaulieu 2015), median depths, median maximum fluid temperatures and end-member DFe

concentrations are presented in Table 2-1 and Figure 2.4. Because these vents only represent what has been discovered to date, these statistics may include sampling biases.

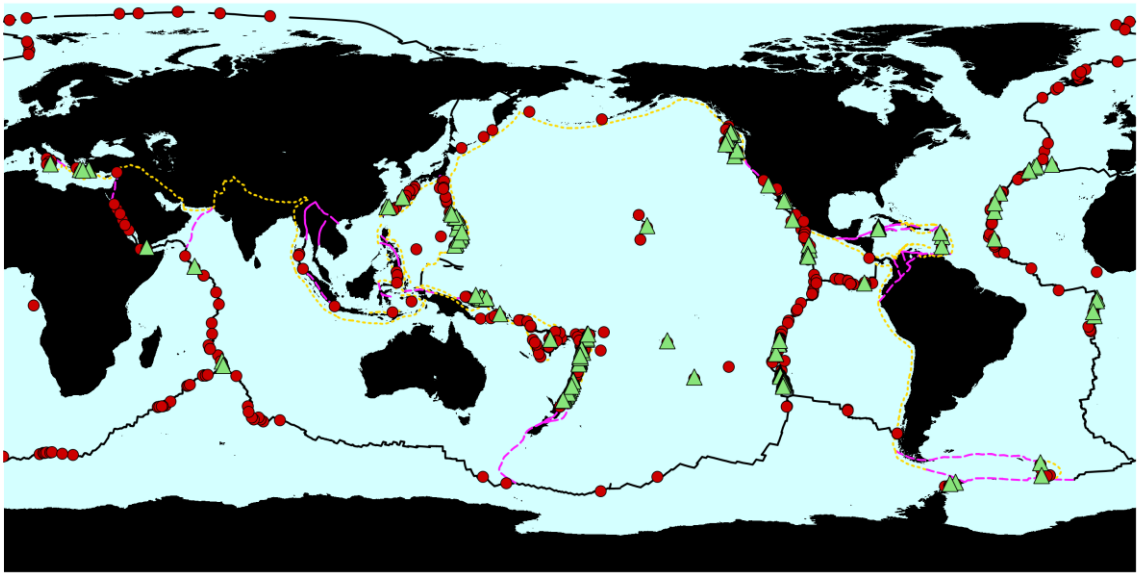

Figure 2.3 Map of hydrothermal vent locations. Dots indicate vents either visually confirmed or inferred from plume observations. Triangles indicate studies measuring Fe in hydrothermal fluids as listed in Table S1. Mid-ocean ridges (solid black line), trenches (dotted line) and transform faults (dashed line) are also shown. Vent data are from the InterRidge database (http://vents-data.interridge.org/ventfields, accessed 5 April 2017). Plate boundaries are from University of Texas PLATES project shapefiles (Coffin et al. 1998).

Table 2-1 Overview of hydrothermal vent characteristics based on end-member vent fluid observations. Depth and temperature measurements are taken from the InterRidge Vents Database (Beaulieu 2015). See Table S1 for the full compilation of end-member and non-end-member Fe observations. No end-member dissolved (d) Fe data were available for intraplate or 'other' volcanos. The 'other' geological category includes coastal faults and offshore extensions of above-water level geothermal systems

Geological setting	Total number (%) of vents described	Median depth (m)	Median maximum temperature (°C)	Number of measurements	Median DFe (µmol kg–1)	Number of measurements
Arc volcano	143 (23)	600	133	45	19	22
Back-arc spreading centre	122 (19)	2000	297	34	261	50
Mid-ocean ridge	350 (55)	2621	328	80	1720	173
Intraplate volcano	7 (~1)	420	35	5	–	–
Other	10 (~2)	12.5	85	7	–	–

Only a decade ago, the total known active vent fields numbered ~280 (Baker and German 2004), whereas today 631 active (visually observed) or inferred active (based on water column

indicators, such as chemical anomalies) vent sites have been documented globally (Beaulieu 2015; Figure 2.3). Baker and German (2004) estimated the total global number of hydrothermal vent fields at divergent plate boundaries (i.e. mid-ocean ridges and back-arc spreading centres) to be around 1000 based on their calculated ratio of vent frequency to ridge spreading rate (for a discussion of ridge spreading rates, see below). The most recent estimate by Beaulieu et al. (2015) has increased this number to around 1300 vent sites.

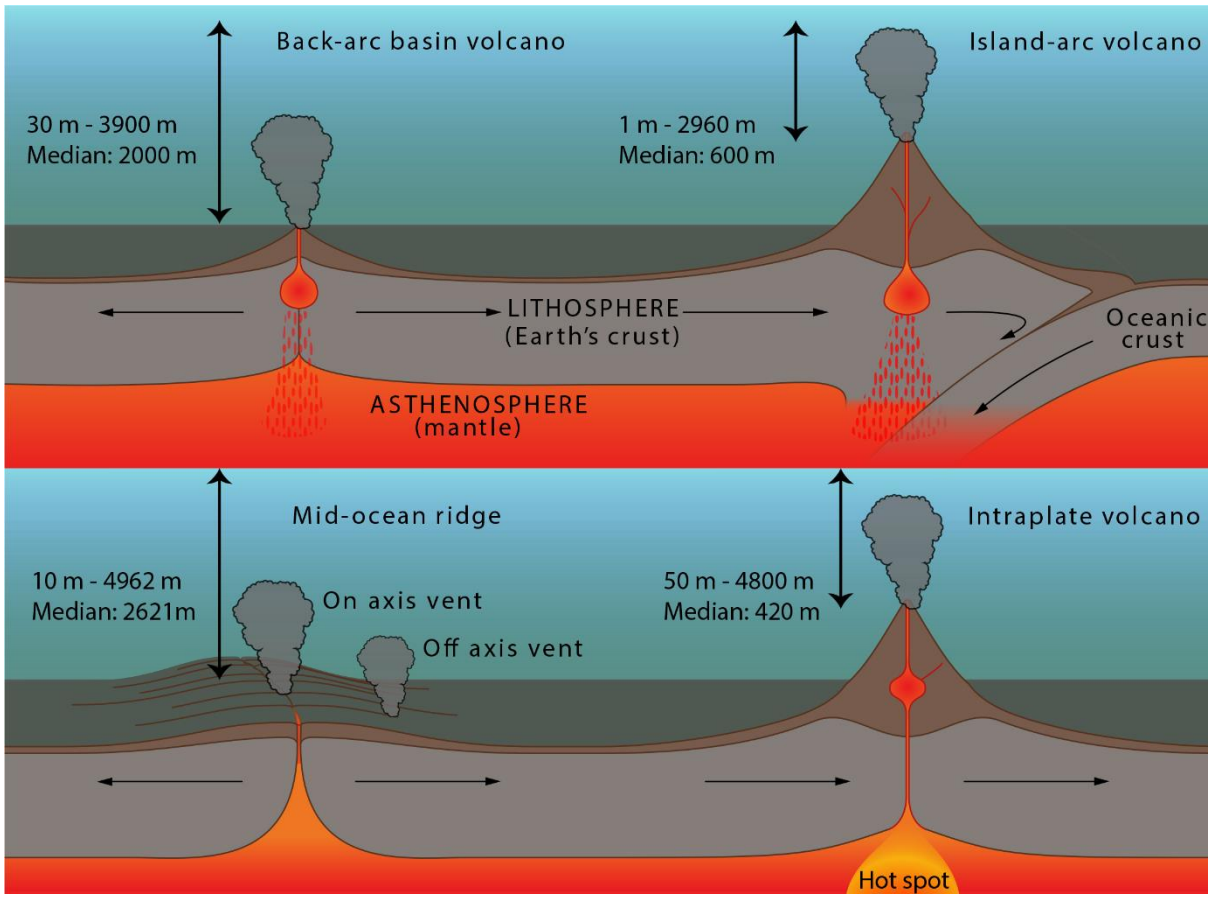

Figure 2.4 Schematic representation of the geological settings of hydrothermal vents, with ranges and median depths of vents discovered to date in each setting.

Although the number of discovered vents has more than doubled in the past decade, there is no question that many more have yet to be discovered. Only one-third of the ~60 000 km of mid-ocean ridges has been surveyed to date (Beaulieu et al. 2015). As of 2011, 57% of the ~6900 km of intraoceanic arcs had been systematically surveyed for hydrothermal vents (de Ronde 2011), and most of the ~14 800 km of other non-continental arcs were yet to undergo detailed

examination (Baker et al. 2008; Lupton et al. 2011). For example, studies measuring hydrothermal Fe have only been undertaken at a small subset of discovered vents (Figure 2.5a).

Observations in certain key regions of the oceans remain sparse. Large regions of the Arctic and Southern oceans (e.g. the South Pacific, South-east Indian Ridge and Kerguelen-Heard Island hot spot regions) remain under-surveyed. Further observations of hydrothermal vents at slow-spreading ridges (discussed below), further analysis of Fe from hydrothermal vents at high latitudes (Figure 2.5b) and further study of the effects of diffuse flow systems on long-range Fe flux are required in order to account for discrepancies in Fe emissions shown in recent models (see below; Tagliabue et al. 2010, 2012; Saito et al. 2013; German et al. 2015).

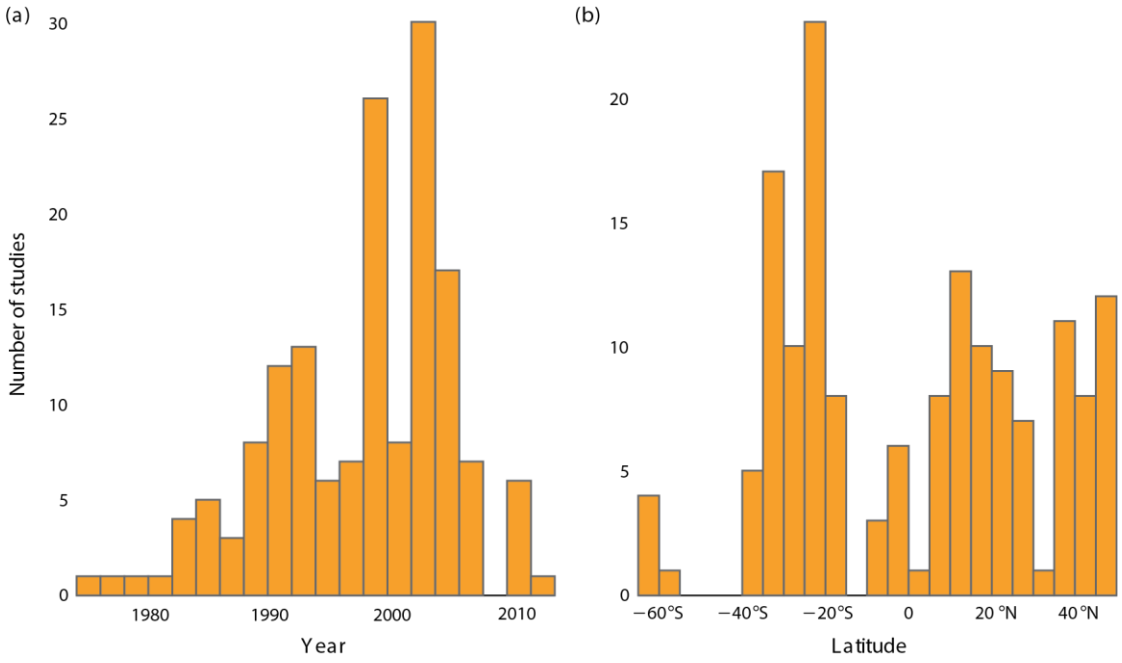

Figure 2.5 Number of studies measuring hydrothermal Fe at unique vent sites by (a) year and (b) latitude (compiled from Table S1).

2.3.1 Vent fluid composition

Hydrothermal vent fluid composition varies from one hydrothermal vent to the next (Von Damm 1995), and may also vary temporally on time scales from minutes to years (Massoth et al. 1994; German and Seyfried 2014). There are few common vent fluid characteristics to enable

categorisation based on vent type or location; however, they may be loosely categorised by temperature and geological setting (German and Seyfried 2014). Black or white 'smoker' chimneys emit undiluted high temperature fluids (may exceed 400°C; Koschinsky et al. 2008) that generally contain high concentrations of metals (Figure 2.6; Sander and Koschinsky 2011). These vents are generally observed along ridge axes at mid-ocean plate boundaries, but have also been observed off-axis (e.g. on ridge flanks; for a diagram of on and off axis vents, see Figure 2.4; Von Damm and Lilley 2004; Haase et al. 2009). In contrast, low-temperature vents emit fluids less than 50°C that have either undergone mixing with cool seawater before emission from the vent or have only circulated through cooler parts of the oceanic crust. These vents generally emit fluids containing low metal concentrations (Figure 2.6), but exhibit higher biological activity (German and Seyfried 2014; German et al. 2015) and are found both on- and off-axis (Von Damm and Lilley 2004; Schmidt et al. 2011). Both high- and low-temperature vents are also observed on island arc chains (Massoth et al. 2003; de Ronde 2011). Median vent fluid temperatures taken from the InterRidge Vents Database (Beaulieu 2015) are given in Table 2-1.

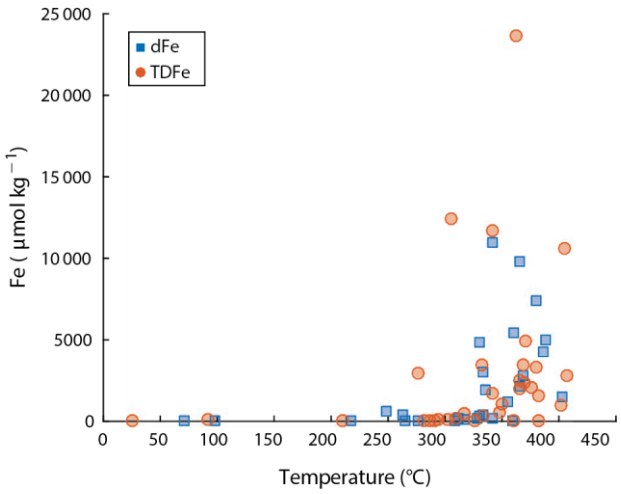

Figure 2.6 Dissolved (d) and total dissolvable (TD) Fe concentrations plotted against temperature at unique vent sites (compiled from Table S1).

The chemistry of hydrothermal fluids is controlled by seawater interactions with minerals contained within the rock substrate at high temperature and pressure, and thus vent fluid chemical composition varies widely with vent type and site-specific geochemical characteristics

(Von Damm 1990; Shock 1992). Phase separation is common in hydrothermal systems and is one of the processes responsible for much of the fluid chemistry variability observed (German and Seyfried 2014; de Ronde and Stucker 2015). Phase separation is the separation of seawater into higher and lower chlorinity phases. This occurs when seawater reaches a critical point of pressure–temperature conditions and may involve boiling or condensing processes depending on the pressure and temperature reached in the system (German and Seyfried 2014). Hydrothermal fluid components (such as Fe) may be more concentrated in one of the phases or trapped subsurface (de Ronde and Stucker 2015). Phase separation is covered extensively in recent reviews (see German and Seyfried 2014; de Ronde and Stucker 2015) and so will not be discussed further here.

Notably, dissolved Mn and Fe concentrations at the vent source may be a million-fold higher than surrounding waters (e.g. Baker et al. 1995; Von Damm 1995; Bruland et al. 2014). Figure 2.7 summarises the element composition of hydrothermal vent fluids.

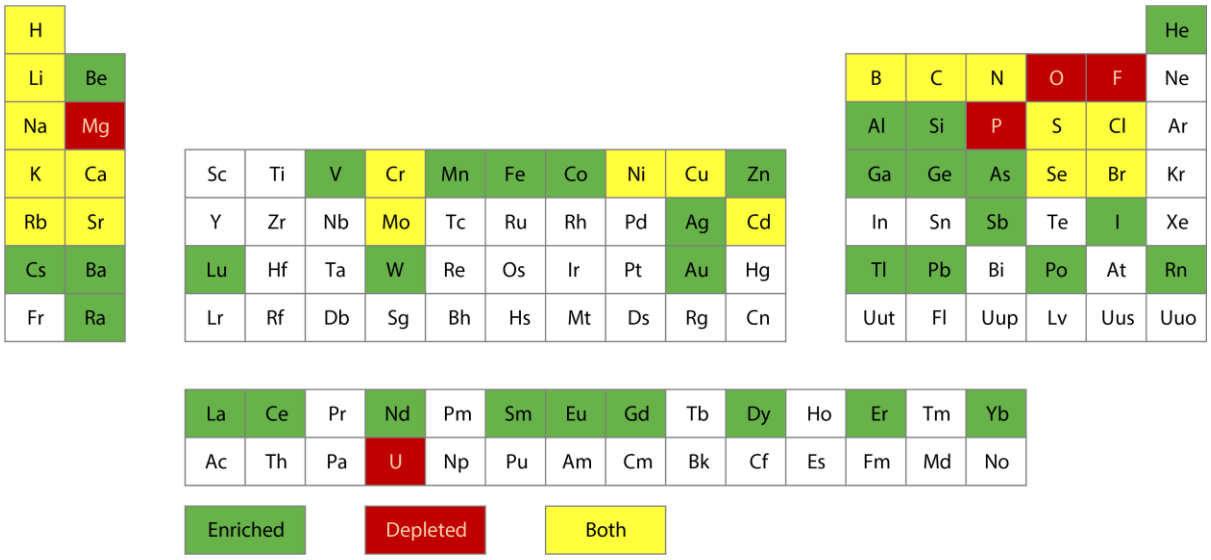

Figure 2.7 Periodic table of elements enriched in end-member hydrothermal fluids, elements depleted in end-member hydrothermal fluids and elements enriched in some end-member vent fluids and depleted in other end-member vent fluids all in relation to seawater Cl concentration to enable for true measure of gain or loss. Adapted from German and Seyfried (2014).

2.4 Hydrothermal Plumes

Hydrothermal plumes transfer fluids emitted from hydrothermal vents into the global oceans where they are dispersed. At the vent opening, end-member fluids rise rapidly because their temperature may range between ~2°C (diffuse vent) to >400°C (undiluted or 'smoker' vent; Figure 2.2) above ambient deep ocean temperatures (Von Damm 1995). This stage is known as the buoyant plume, where fluids undergo dilution by a factor of 104–105 (Lupton et al. 1985; Elderfield and Schultz 1996). Dilution occurs by way of turbulent eddies, formed by friction at the boundary between swiftly rising buoyant fluid and ambient ocean water (Lupton 1995). These eddies entrap surrounding ambient ocean water and transport it into the plume, often referred to as 'entrainment'.

On leaving the vent orifice, hot vent fluids mix with seawater, forming an anhydrite ($CaSO_4$) framework upon which sulfide minerals precipitate forming chimney structures (German and Seyfried 2014). As vent fluid escapes these chimneys, the plume rises and entrains ambient seawater, precipitating metal sulfides and sulfates as a result of oxidation (Figure 2.2; Lilley et al. 1995). Some elements are scavenged by these particles upon mixing with ambient seawater, effectively turning hydrothermal plumes into sinks for oceanic phosphate, V, Cr, As, Be, Y, Th, Pa and rare earth elements (REE), among others (German et al. 1991; Lilley et al. 1995; Elderfield and Schultz 1996; German and Seyfried 2014).

In the space of tens to hundreds of metres, these fluids reach a point of neutral buoyancy, the stage at which the plume ceases vertical ascent and commences lateral dispersion (Baker and Massoth 1987; Speer and Rona 1989). Lateral dispersion has been shown to reach distances of tens to thousands of kilometres based on temperature (Reid 1982; Baker and Massoth 1987), ^3He (Lupton and Craig 1981; Lupton 1996; Fitzsimmons et al. 2014) and dissolved Mn (DMn) and DFe anomalies (Resing et al. 2015), allowing for far-field dispersal of some hydrothermal fluid end-member components.

It has become apparent that this distal transport may not only apply to 'conservative' tracers, such as ^{3}He, but also to other chemical constituents, such as Fe, that were originally thought to quickly precipitate out of plumes close to the vent site (Fitzsimmons et al. 2014; Resing et al. 2015). This review shows that these species may be preserved within plumes at above-ambient concentrations through certain mechanisms (e.g. complexation) for great distances (see below). As discussed below, recent studies emphasise the importance of understanding the local geological and topographic setting, deep-water temperature and salinity and local and regional current regimes, as well as the ability to model these processes on local scales in order to understand the transport and dispersion of hydrothermal plumes (Wu et al. 2011; Saito et al. 2013; Conway and John 2014; Fitzsimmons et al. 2014; Resing et al. 2015).

2.4.1 Methods for identifying hydrothermal plumes

The physical and chemical properties of fluids emanating from hydrothermal vents vary significantly from typical oceanic water properties and may be used as tracers of hydrothermal activity. These tracers exhibit varying degrees of reactivity, with their lifetime in the plume ranging from hours and days (e.g. Ra) to ~1000 years (i.e. ^{3}He; Clarke et al. 1969; Kadko et al. 1990; Farley et al. 1995). In the context of this discussion, 'conservative' refers to conservation of a tracer through time.

With the exception of ^{3}He, water column residence times of hydrothermal tracers have been shown to vary depending on vent and ambient seawater chemistry. However, the residence time of various passive tracers can been generalised as: light transmission < ^{224}Ra < ^{222}Rn < CH_4 < Mn < ^{3}He (Figure 2.2; Kadko et al. 1990). This sequence has proven useful while surveying fast-spreading ridges, because background levels of conservative tracers such as ^{3}He may be elevated because of multiple hydrothermal vents in the region, which can confound efforts to locate discrete hydrothermal sources. The non-conservative tracers (e.g. Ra) that have a shorter

residence time in the plume have very low background levels, giving a greater signal-to-noise ratio (Lupton 1995), ultimately making detection less problematic. Each of these tracers may be used individually to identify hydrothermal plumes, or may be used as part of a suite of tracers to provide valuable information on geological settings, plume chemistry, age and provenance (Jenkins 2014). Importantly in the context of this discussion, these tracers also provide clues as to whether Fe in the ocean may come from a hydrothermal origin.

2.4.1.1 Hydrographic tracers

Salinity, temperature and density anomalies relative to ambient seawater are telling indicators of hydrothermal emissions. Potential temperature has been used as a conservative tracer in plume studies (Reid 1982). However, as discussed below, the use of these parameters as hydrothermal plume tracers may be complicated by ocean basin hydrographic differences, such as in the Atlantic, where hydrothermal plumes can be cooler and less saline than ambient conditions. Hence, most hydrothermal plume studies in the Atlantic have instead used optical or chemical tracers to identify hydrothermal plumes (Baker et al. 1995).

Transmissometers or nephelometers, commonly deployed with CTD (conductivity, temperature and depth) packages, measure light absorbance or particle reflectance within a water sample and are both methods of optically measuring suspended particulates. Optical anomalies are a non-conservative tracer of hydrothermal plumes because transmissometers or nephelometers are more sensitive to larger organic particles found in the near-field plume as opposed to the fine metallic particles often associated with plumes further from the vent source. This tracer is more sensitive and less complicated to interpret than temperature and salinity anomalies, and thus provides an effective near-field tracer (Baker et al. 1995).

2.4.1.2 Helium

Helium derived from deep crustal or primordial gases, which degas at hydrothermal sites, is easily distinguishable from atmospheric or radioactive decay sources in the deep ocean because it

has a distinct isotopic ratio, enriched in ^{3}He in relation to ^{4}He (Lupton and Craig 1981; Belviso et al. 1987; Lupton 1998; German and Seyfried 2014). ^{3}He is also inert and thus conserved in the ocean (German and Seyfried 2014), making it an excellent dilution tracer of hydrothermal plumes. As discussed below, low ^{3}He:heat ratio signatures in the water column are a distinguishing feature of event plumes (Baker et al. 2011). Ratios of chemical constituents in hydrothermal plumes may be compared to ^{3}He in order to estimate rates of oxidation or scavenging (e.g. CH_4 : ^{3}He, Mn : ^{3}He and DFe : ^{3}He) and fluxes from individual vents or at a global scale (Baker et al. 1989; Jean-Baptiste et al. 1991; Boyle and Jenkins 2008; German et al. 2010; Fitzsimmons et al. 2014).

2.4.1.3 Radon and Radium

Radon-222 (^{222}Rn) is enriched in hydrothermal fluids as a product of decay from radium (Ra), which is supplied to the hydrothermal system by high temperature alteration of basalt (Dymond et al. 1983; Kadko and Moore 1988; Rudnicki and Elderfield 1993). The ratio of ^{222}Rn to ^{3}He (both of which are chemically inert) in a hydrothermal plume provides a useful tool for determining the age of a plume and may also be used to determine rates of uptake or removal of non-conservative chemical constituents (e.g. H_2, CH_4 and Mn) and particles (Kadko et al. 1990).

Ra is released into hydrothermal fluids as seawater interacts with basalt at high temperatures and low pH (Dymond et al. 1983; Kadko and Moore 1988). The concentration of Ra in the hydrothermal fluids is dependent on the fluid residence time, circulation depth and composition of the host rock (Dymond et al. 1983; Kadko and Moore 1988). Ra has several isotopes, some of which have relatively short half-lives (e.g. ^{223}Ra $t_{1/2}$ = 11.4 days; ^{224}Ra: $t_{1/2}$ = 3.66 days), whereas others are longer lived (e.g. ^{228}Ra: $t_{1/2}$ = 5.75 years). Kipp et al. (2017) have recently used ^{223}Ra and ^{224}Ra isotopes to successfully determine plume ages of neutrally buoyant plumes from sites on the East Pacific Rise (EPR) and Mid Atlantic Ridge (MAR) of ~1 month and ~2 days respectively, and were then able to use ^{228}Ra to identify plumes of different origins further afield

from the EPR and to estimate the residence time of hydrothermal DFe within the plume (9.3–14 years).

2.4.1.4 Manganese

Mn in hydrothermal end-member fluids ranges from 4 to 7100 μmol kg–1 (total dissolvable Mn (TDMn); Table S1), whereas background levels in the deep ocean are observed in the nano- to picomolar range (Martin et al. 1985; Bruland et al. 2014). Although redox active, abiotic manganese oxidation is kinetically inhibited in seawater (Cowen et al. 1998; German and Seyfried 2014), its oxidation is controlled predominantly by bacterial processes in the non-buoyant plume (Cowen et al. 1986, 1990; Cowen and Hui Li 1991). The oxidation rate of Mn is slow relative to the rate of plume dispersal (Cowen et al. 1990, 1998). Hence, Mn may persist in greater concentrations than Fe in hydrothermal plumes (at least in the range of hundreds of kilometres). This enables its use as an effective although non-conservative tracer for hydrothermal emissions. Ratios of Fe : Mn and Cl : Mn in hydrothermal fluids have also been used to trace magma intrusions in hydrothermal systems (Pester et al. 2014). In the basin-scale EPR plume, Resing et al. (2015) traced Fe further than Mn, highlighting the complexity of hydrothermal plume chemistry. Indeed, the relationship between integrated Mn and ^{3}He presented by Resing et al. (2015, fig. 3d), showing a slight non-linearity, suggests Mn may behave non-conservatively in distal hydrothermal plumes, contrary to earlier conclusions.

Enhancing its suitability as a tracer, Mn may be measured while at sea with relative ease and precision using flow injection analysis (FIA), based on chemiluminescence or colourimetry reactions catalysed by Mn (Chapin et al. 1991; von Langen et al. 1997; Chase et al. 2005; Middag et al. 2011). In addition, several in situ Mn detection methods have been developed that have proven effective as real-time hydrothermal plume detectors. These devices are all based on automated FIA methods. Examples include the submersible chemical analyser (Scanner; Coale et

al. 1991; Chin et al. 1994), the zero-angle photon spectrometer (ZAPS; Klinkhammer 1994) and the geochemical anomaly monitoring system (GAMOS; Okamura et al. 2001; Gamo et al. 2015).

2.4.1.5 Methane

Methane (CH_4) is released from both high- and low-temperature vents through various organic and inorganic processes, such as thermal breakdown of complex hydrocarbons (>100°C), biological production (<120°C) and serpentinisation (hydration and metamorphic transformation) of ultramafic rocks (Welhan 1988; Lilley et al. 1995; Charlou et al. 1998; Love et al. 2008). Background ocean concentrations of CH_4 are <5 nmol kg^{-1}, whereas concentrations in vent fluids have been measured in the micromole per kilogram to millimole per kilogram range (Von Damm 1995; Charlou et al. 2002; German and Seyfried 2014). These characteristics make CH_4 a valuable tracer of hydrothermal fluids.

The ability to analyse CH_4 at sea makes this gas especially useful as a tracer of hydrothermal activity. However, the varying nature of CH_4 concentrations at different vent sites, coupled with varying residence times depending on local conditions, means that CH_4 may only prove a useful hydrothermal tracer in some cases. There have been some instances of CH_4 detection in the absence of both ^3He and Mn (Horibe et al. 1986; Belviso et al. 1987; Jean-Baptiste et al. 1990), indicating a source of CH_4 unrelated to hydrothermal venting. Conversely, the absence of CH_4 does not necessarily preclude hydrothermal activity and may provide clues to site-specific geological setting, sub-seafloor hydrology and plume dynamics.

2.4.2 Dispersion of hydrothermal plumes

2.4.2.1 Geological setting

The geological and topographic setting in which a hydrothermal vent is located has a major effect on plume dispersion. At slow (20–55 mm $year^{-1}$)-spreading and ultra-slow (<20 mm $year^{-1}$)-spreading ridges such as the Mid-Atlantic, South-west Indian, Central Indian and Gakkel

ridges, rift valley walls are often 1–3 km high, far above average neutrally buoyant plume height, constraining lateral advection of plumes along ridge axis trajectories. At faster-spreading ridges (>55 mm year^{-1}), such as the EPR, South-east Indian Ridge, Chile Ridge and Juan de Fuca Ridge, neutrally buoyant plumes often rise above the ~100 m ridge walls, allowing off-axis dispersion to occur more readily (Chen and Morgan 1990; Baker et al. 1995; German and Seyfried 2014).

Hydrothermal plumes from vents at shallower depths are more likely to be dispersed by surface-generated eddies and deep winter surface mixed layers (Adams et al. 2011; Hawkes et al. 2014). Volcanic arc hydrothermal vents are often found at much shallower depths than those of mid-ocean ridges (the median depth of vents discovered at volcanic arcs to date is 600 m; Beaulieu 2015), which may lead to greater dispersion of hydrothermal plumes to surface waters (de Ronde et al. 2001; Massoth et al. 2003; Hawkes et al. 2014). However, some vents in these settings are located within confining calderas, limiting plume dispersion (Hawkes et al. 2014). Although the depth of hot spot-related hydrothermal vents discovered to date ranges considerably (50–4800 m, median 420 m; Beaulieu 2015), these vents may also be found at depths conducive to dispersion into the surface mixed layer. Dispersion of hydrothermal plumes into the surface mixed layer is also of great interest in the context of directly affecting surface biological productivity through, for example, stimulation of phytoplankton growth by essential nutrients and micronutrients in the hydrothermal plume, as discussed below.

2.4.2.2 Deep water temperature and salinity

Temperature and salinity differences in the world's oceans affect the dispersion of hydrothermal plumes. The Pacific Ocean's deep waters are warmer and saltier than its overlying waters (Lupton et al. 1985; Broecker 1991; Lupton 1995; Marshall and Speer 2012). This means that hydrothermal plumes in this ocean are saltier and warmer than surrounding water as they rise. The salinity increases the density, whereas the elevated temperature decreases the density of the plume, somewhat offsetting each effect (Lupton et al. 1985). Hence, buoyant plumes in the deep

Pacific reach neutral buoyancy (when plume density equals ambient density) while the plume is still warmer and saltier than surrounding water (Lupton 1995).

In the Atlantic Ocean, where deep waters are colder and fresher than overlying waters, hydrothermal plumes are both warmer and less saline than surrounding waters on ascent (Speer and Rona 1989). This means plumes in the Atlantic ascend higher than those in the Pacific before reaching a point of neutral buoyancy. These differing oceanic water column properties, together with the hydrothermal vent source heat flux, determine the height above the vent at which the neutrally buoyant plume is found in different ocean basins (Table 2-2; Speer and Rona 1989; Rudnicki and Elderfield 1993; Carazzo et al. 2013). The depth of the hydrothermal vent coupled with the height of neutrally buoyant plume emplacement controls which isopycnal (constant density) gradient the plume will disperse along, and thus affects plume dispersal to the greater ocean (Bennett et al. 2008).

Table 2-2 Hydrothermal plume rise heights observed in different ocean basins

Ocean basin	Plume height (m)	References
Pacific	200–400	Baker (1994), Feely et al. (1994), Lupton et al. (1985)
Atlantic	300–700	Jean-Baptiste et al. (1991), Langmuir et al. (1997), Speer and Rona (1989)
Indian	100–400	Ray et al. (2012), Rudnicki and German (2002), Scheirer et al. (1998)
Arctic	300–600	Baker et al. (2004), Stranne et al. (2010)
Southern	100–500	Baker et al. (2004), Hawkes et al. (2013), Tyler (2011)

2.4.2.3 Local and regional current regimes

In the deep ocean at the basin scale, mid-ocean ridges exert strong control on circulation, with currents flowing in the direction of ridges for hundreds of kilometres (Speer et al. 2003). These along-axis currents are broken up by across-axis currents, generated from surface wind stress and thermohaline forcing (heat and salinity gradients), which leave the ridge and flow into the interior of ocean basins dispersing hydrothermal plumes away from mid-ocean ridges (Speer et al. 2003). A recent study of hydrothermal vent community larval dispersal mechanisms has shown that basin-scale currents also disperse hydrothermal plumes from arc and back-arc volcano settings in

the western Pacific (Mitarai et al. 2016). Not only are hydrothermal fluids advected by these deep currents, but in certain regions of the mid-ocean ridge the buoyancy flux caused by hydrothermalism may even drive oceanic circulation and thus aid in the dispersion of plumes (Stommel 1982; Joyce and Speer 1987; Hautala and Riser 1989; Speer 1989; Helfrich and Speer 1995; Adcroft et al. 2001). Another recent study on the northern EPR demonstrated that surface-generated mesoscale eddies may, in fact, reach sufficient depths to affect the dispersal of hydrothermal plumes at mid-ocean ridges (2350 m at the study site; Adams et al. 2011).

There are several means by which hydrothermal fluids may escape the confines of slow-spreading ridges with large rift valleys, such as the MAR, where currents generally drive hydrothermal plumes along-axis within the rift valley (German et al. 2010). Fracture zones allow fluids confined within the rift valley to escape in some locations, such as near the equator at the Romanche and Chain fracture zones on the MAR (Mercier and Speer 1998). Turbulence generated by uneven topography and narrow passages along the MAR have been shown to drive upward mixing, allowing overflow of rift valley-confined waters and increasing mixing rates throughout the water column above the MAR (Polzin et al. 1997; Ledwell et al. 2000; St Laurent and Thurnherr 2007). Dissolved Fe data from the 2010 North Atlantic zonal GEOTRACES cruise (GA03) suggest that hydrothermal Fe must escape the MAR rift valley for transport hundreds of kilometres to the west (Conway and John 2014; Fitzsimmons et al. 2015; Hatta et al. 2015). Finally, event plumes may also allow escape of hydrothermal plumes above confining rift valley walls, as discussed in the following section.

2.4.2.4 Event plumes

In addition to the 'chronic' plumes (i.e. hydrothermal venting that occurs over time scales in the range of 10–10 000 years) discussed above, large 'event' plumes have been observed to occur sporadically at both plate boundary and intraplate hydrothermal settings (Baker et al. 1987, 2012; Kadko et al. 1995; German and Lin 2004). Between 1986 and 2012, evidence of 22 eruption

events were reported (Baker et al. 2012). Some examples include the first discovery of a 'megaplume' at the Juan de Fuca ridge (Baker et al. 1987), 'EP96A' at Gorda Ridge (Kelley et al. 1998) and 'EP08A-H' at the Northeast Lau Spreading Centre (Baker et al. 2011). These plumes persist in the water column for 0.5–2 years on average (Carazzo et al. 2013) and are associated with massive heat fluxes and greater-than-average metal concentrations (Massoth et al. 1994). As a consequence of these large heat fluxes, metal-enriched hydrothermal emissions can rise up to 1000 m above the sea floor before reaching neutral buoyancy (Baker et al. 1987, 1989; Massoth et al. 1994). Lupton (1995) argued that event plumes are probably not a significant source of hydrothermal input based on lack of observed ^{3}He anomalies at event plume depths. Koski et al. (2003) also argued that event plumes are not a significant source of hydrothermal input based on observations that an event plume at the Co-Axial vent field, North Pacific Ocean, contributed less than 10% of the total (chronic and event) heat and chemical flux at this site over its 3-year lifespan (Baker et al. 1998). However, Carazzo et al. (2013) recently conducted a study suggesting that internal layering within event plumes driven by the differential diffusion of heat and small mineral precipitates extends the longevity of plumes in the water column, greatly enhancing probability of distal transport. The extreme plume buoyancy and chemical fluxes associated with event plumes means their potential to affect ocean chemistry warrants further study (Baker et al. 2012).

2.5 Iron in hydrothermal plumes

Early studies of end-member hydrothermal vent fluids inferred that all Fe rapidly formed Fe oxide and Fe sulfide precipitates, which then quickly settled to the sea floor (e.g. Mottl and McConachy 1990; German et al. 1991; Rudnicki and Elderfield 1993), rendering Fe contribution from hydrothermal sources insufficient to provide a significant contribution to the oceanic DFe budget. More recently, the 'leaky vent hypothesis' (Toner et al. 2012) has gained momentum, with work showing that Fe in more stable forms, such as nanoparticulate minerals and Fe

complexed by organic ligands, has a water column residence half-life (i.e. the time it takes for half the Fe-rich nanoparticles or Fe–ligand complexes to undergo oxidative dissolution or aggregation and precipitate out of the plume) long enough to greatly increase the probability of reaching surface waters (Field and Sherrell 2000; Wu et al. 2011; Carazzo et al. 2013; Fitzsimmons et al. 2014). Such findings have led to a paradigm shift in our understanding of hydrothermal Fe input to the global oceanic Fe budget, with studies tending towards greater estimates of hydrothermal contribution in more recent years (Tagliabue et al. 2010; Sander and Koschinsky 2011; Carazzo et al. 2013; Resing et al. 2015), as discussed below.

Concentrations of Fe in hydrothermal vent fluids vary widely depending on geological setting, temperature and pressure, among other factors (Von Damm 1995; Table 2-1; Table S1). Iron concentrations of end-member fluids are often generalised as enriched by 106 : 1, or greater, over open ocean concentrations (Von Damm and Bischoff 1987; Chin et al. 1994; Sharma et al. 2001; Sands et al. 2012; German and Seyfried 2014), with observed concentration ranges from <2 to 26 000 μM at mid-ocean ridges (e.g. Rudnicki and Elderfield 1993; Elderfield and Schultz 1996; Douville et al. 2002; Gallant and Von Damm 2006; Table 2-1; Figure 2.6, 2.8, 2.9a; Table S1). Note that Fe concentrations may be reported as total dissolvable Fe (TDFe; measured using unfiltered acidified samples giving dissolved plus dissolvable particles) or as DFe (measured using samples filtered through 0.2- or 0.4-μm filters).

An analysis of variance (ANOVA) of end-member Fe data from Table S1 found a significant difference between DFe concentrations from different geological settings ($P < 0.001$; Figure 2.9a). A Games–Howell post hoc test revealed that DFe concentrations measured in arc volcano settings ($n = 22$) are significantly lower than concentrations in back-arc spreading centre ($P < 0.001$; $n = 50$) or mid-ocean ridge ($P < 0.001$; $n = 173$) settings. There were no significant differences between back-arc spreading centre and mid-ocean ridge settings. The lower DFe concentrations in arc volcano settings is consistent with their cooler temperatures (Table 2-1),

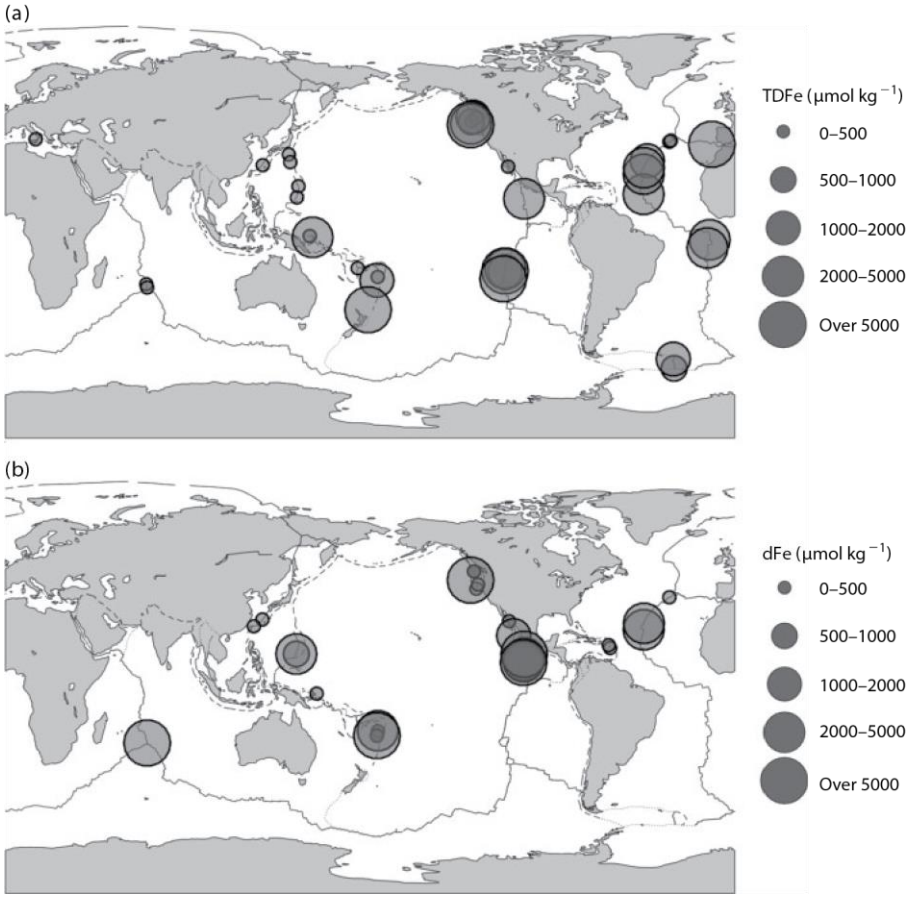

Figure 2.8 Reported vent fluid end-member concentrations of (a) total dissolvable Fe (μmol kg–1) and (b) dissolved Fe (μmol kg–1). Only measurements taken directly at the vent orifice and calculated back to undiluted vent fluid (end-member) data are shown. Where multiple measurements have been collected at a single hydrothermal site, mean values are shown. (Data compiled in Table S1.)

which is often a characteristic of more diffuse, lower-concentration vent fluid (de Ronde and Stucker 2015). TDFe showed no significant differences between geological settings. However, it must be noted that this analysis is based on very different group sizes of TDFe observations (n = 13, 45 and 125 for arc, back-arc and mid-ocean ridge settings respectively).

There is also a significant difference between end-member DFe concentrations at different mid-ocean ridge spreading rate categories ($P < 0.001$; Figure 2.9b). A Games–Howell post hoc test revealed that end-member DFe concentrations measured at slow-spreading rate ridges are significantly lower than at fast-spreading rate ridges ($P < 0.001$), but not significantly lower than at intermediate-spreading rate ridges. End-member DFe concentrations at intermediate- and fast-spreading rate ridges are also not significantly different from each other. There were not enough

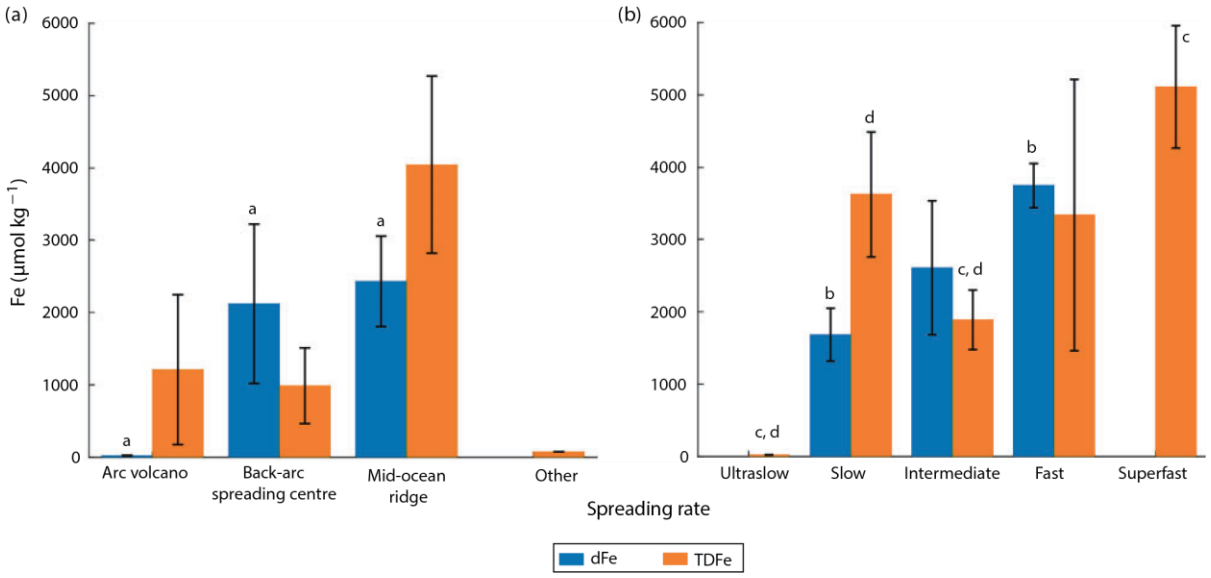

Figure 2.9 (a) Mean (±s.e.m.) dissolved Fe (DFe) and total dissolvable Fe (TDFe) end-member concentrations of unique hydrothermal vent sites by geological setting. Columns with different letters differ significantly ($P < 0.05$). For arc volcano, back-arc spreading centre, mid-ocean ridge and other settings n = 8, 17, 38 and 1 respectively. (b) Mean (±s.e.m.) DFe and TDFe end-member concentrations of unique hydrothermal vent sites by spreading rate category. For ultraslow, slow, intermediate, fast and superfast ridges n = 5, 134, 113, 120 and 26 respectively. (Compiled from Table S1. Error bars show standard error of mean.)

end-member measurements at ultraslow- or superfast-spreading ridges to perform statistical analyses. TDFe also showed a statistically significant difference between spreading rate categories ($P < 0.001$). A Games–Howell post hoc test revealed that end-member TDFe concentrations measured at superfast-spreading rate ridges are significantly higher than at intermediate ($P < 0.05$) and ultraslow ($P < 0.001$) ridges, but not significantly higher than at slow-spreading ridges. Concentrations at intermediate ridges are significantly higher than at ultraslow ridges ($P < 0.001$), but not significantly different to slow-spreading ridges. Concentrations at slow ridges are significantly higher than at ultraslow ridges ($P < 0.05$).

These results are consistent with observations that at intermediate- to ultrafast-spreading ridges hydrothermal activity is observed to increase with spreading rate (the 'magmatic budget hypothesis'; Baker and German 2004). More recent observations at slow-spreading ridges show a departure from this trend, with more frequent hydrothermal activity discovered than expected (Saito et al. 2013). This departure from the expected trend has been attributed to tectonic

processes controlling a large proportion of hydrothermal activity at slow-spreading ridges, in contrast with the predominantly magmatic processes observed at faster-spreading ridges (Rona et al. 2010; Saito et al. 2013; Beaulieu et al. 2015; German et al. 2016). It should be noted that there is a lack of end-member Fe data for fast- (n = 3; from one site) and ultraslow-spreading ridges (n = 4; from one site), which may have skewed the data for these tectonic settings. The remainder of this section examines how some of this Fe may be stabilised and thus distributed into the wider ocean.

2.5.1 Stabilisation of hydrothermal iron

There is a growing list of studies showing evidence of stabilisation of hydrothermal Fe over long distances in the ocean (Wu et al. 2011; Nishioka et al. 2013; Conway and John 2014; Fitzsimmons et al. 2014; Hatta et al. 2015; Resing et al. 2015; Sedwick et al. 2015; Sander and Koschinsky 2016), which may eventually lead to revisions of estimated hydrothermal plume Fe lifetime, with potential ramifications for our understanding of Fe biogeochemical cycling. The furthest distance from source at which elevated DFe has been detected within a hydrothermal plume to date is estimated at ~6000 km (Fitzsimmons et al. 2014), with several other studies also identifying hydrothermal Fe plumes in the range of thousands of kilometres (e.g. Wu et al. 2011; Saito et al. 2013; Resing et al. 2015). Conway and John (2014) recently tracked sources of DFe using stable Fe isotope ratios (δ^{56}Fe) in the North Atlantic Ocean and traced hydrothermally derived Fe transported laterally ~1000 km to the west of the Trans-Atlantic Geotraverse (TAG) hydrothermal field. Stabilisation of dissolved and particulate Fe has been attributed to complexation by organic ligands, nanoparticulate processes and DFe(II) oxidation kinetic processes, as discussed in detail in the following sections.

2.5.1.1 Organic ligands

Over 99% of dissolved Fe in the ocean is bound in ligand complexes (Gledhill and van den Berg 1994; Rue and Bruland 1995; Tian et al. 2006; Ibisanmi et al. 2011). In non-buoyant hydrothermal plumes, 4–8% of DFe may be complexed by Fe-binding ligands (Bennett et al. 2008; Sander and Koschinsky 2011; Hawkes et al. 2013; Fitzsimmons et al. 2017). In high-temperature end-member vent fluids, complex organics are broken down and it is unlikely this fluid is the source of ligands in buoyant or non-buoyant plumes (Shock and Schulte 1998). Studies have pointed towards low-temperature diffuse vent fluids in the vicinity of high-temperature vents as a major source of organic ligands, or of organic carbon that may react with high-temperature vent fluid constituents to produce ligands (Lang et al. 2006; Bennett et al. 2008; Toner et al. 2009; Hawkes et al. 2013). Hawkes et al. (2013) showed that these ligands are most likely of the L_2 category bond strength (thought to be the more bioavailable form; Boyd et al. 2010; Poorvin et al. 2011; Gledhill and Buck 2012) in concentrations ranging from 2 to 18 nM within the neutrally buoyant plume, and calculated at up to 260 nM in 'near-vent' fluids. Mean background concentrations of ligands in this region of the deep Southern Ocean are reported at around 1 nM (Caprara et al. 2016). Diffuse hydrothermal systems, as a major contributor of ligands to buoyant hydrothermal plumes, have also been implicated as an important source of stabilised Fe to hydrothermal plumes in recent modelling and observational studies (German et al. 2015; Kleint et al. 2016).

Background concentrations of ligands in the deep ocean (often referred to as the 'ligand soup') are produced by bacterial remineralisation of sinking biogenic particles (Boyd et al. 2010; Gledhill and Buck 2012) and may also be entrained into the buoyant plume on ascent. There is some question as to whether higher concentrations (10 – 100 nM) of ligands too weak to be detected by widely used cathodic stripping voltammetry techniques exist in deep ocean water (Hawkes et al. 2013), which may contribute to entrained ligands within buoyant hydrothermal plumes.

Plume-dwelling microbes have also been suggested as a source of Fe-complexing ligands (Dick et al. 2013; Hawkes et al. 2013; Li et al. 2014); however, this mechanism has yet to be proven. Importantly, ligand concentrations likely play a greater role than end-member trace metal concentrations in governing persistence and transport in the ocean (Resing et al. 2015; Völker and Tagliabue 2015).

2.5.1.2 Nanoparticles

Nanoparticulate minerals are solids ranging in size from a few nanometres to 200 nm in diameter (Yücel et al. 2011; Gartman et al. 2014). These particles are thought to form within hydrothermal fluid before discharge at the sea floor (Yücel et al. 2011). All minerals enter a nanoparticulate stage during formation, and although this stage is often transitionary, in certain systems the rate of ion production is far higher than the rate of ion or particle aggregation, allowing nanoparticles to exist in relative equilibrium (Hochella et al. 2008; Mullaugh and Luther 2011). The mechanisms by which these nanoparticles are stabilised are still an area of discovery, because nanoparticles behave unexpectedly compared with larger particles in relation to surface area and oxidation state (Hochella et al. 2008; Yücel et al. 2011; Gartman et al. 2014).

Nanoparticles can account for a significant fraction of the Fe within the operationally defined dissolved size class (<0.2 μm) in hydrothermal fluids (Yücel et al. 2011; Gartman et al. 2014). Nanopyrite was observed to compose 5–25% of the DFe at the Rainbow, TAG and Snakepit hydrothermal sites (Gartman et al. 2014), and nanoparticulate oxyhydroxide particles have been implicated as a significant component of DFe from the southern EPR (Fitzsimmons et al. 2017).

Iron has predominantly been described as existing as a nanoparticulate in oxyhydroxide or pyrite (FeS_2) form, but has recently been found to exist in several other nanoparticulate forms, such as silicates and chalcopyrite ($CuFeS_2$; Gartman et al. 2014; Fitzsimmons et al. 2017). Although the complex physical and chemical processes involved in nanoparticle behaviour in the environment are currently under investigation, it has been shown that these particles may also persist for great

distances from hydrothermal sources (Yücel et al. 2011; Gartman et al. 2014). For example, Gartman (2013) showed that at a deep-water oxygen concentration of ~200 μM and temperature of 2°C, the half-life of pyrite nanoparticles is ~200 days. At an upwelling rate of 2.2 m day^{-1} (Kadko and Johns 2011), these nanoparticles would travel ~1.3 km vertically in three half lives, and ~3 km in seven half lives, lending credibility to the possibility of hydrothermally derived Fe nanoparticles reaching surface waters (Gartman et al. 2014). By the same token, based on average lateral ocean currents over the EPR of ~5 cm s^{-1}, and a maximum measured rate of ~15 cm s^{-1} (Adams et al. 2011), pyrite nanoparticles could travel ~2600–6000 km in three to seven half lives or, at the maximum current, ~7800–18 200 km in three to seven half lives.

In addition to the stabilisation of Fe by formation of nanoparticulates and organic complexes as separate processes, some recent studies have focused on the interaction between these two processes (Toner et al. 2009; Fitzsimmons et al. 2017). It is now becoming clearer that nanoparticulates and organic ligands may work in concert, because inorganic nanoparticles eventually undergo oxidative dissolution and are subsequently stabilised by ligand complexation (Yücel et al. 2011; Fitzsimmons et al. 2014). In proximity to a vent source, colloidal (0.02–0.4 μm) Fe is often the dominant fraction, whereas the further Fe travels from a vent source, the higher the likelihood that Fe will exist within the soluble (<0.02 μm) fraction, tending towards a 50 : 50 ratio of soluble to colloidal size fractions (Fitzsimmons et al. 2014). Both nanoparticulate (inorganic) and complexed (organic) Fe may be found in either of these fractions, and organics have also been found covering the surface of some nanoparticulates, further stabilising them (Hochella et al. 2008; Toner et al. 2009; Sander and Koschinsky 2011; Yücel et al. 2011; Gartman et al. 2014). Fitzsimmons et al. (2017) have recently provided further evidence of these interactions tracing nanoparticulate–ligand exchanges in the hydrothermal plume extending over 4000 km from the EPR.

2.5.1.3 Fe(II) oxidation times influenced by ocean chemistry

Iron, in the form of Fe(II), is often the most abundant component in high-temperature end-member fluids, with maximum concentrations found up to millimolar ranges (Von Damm 1995). The majority of Fe(II) in hydrothermal fluids is quickly oxidized upon mixing with ambient seawater (German et al. 1991; Rudnicki and Elderfield 1993). Fe(II) may even oxidise below the seafloor, resulting in Fe(III) emissions from some plumes and vast FeS deposits below the seafloor in some regions (German et al. 2016). Varying properties of seawater in different ocean basins and regions affect the longevity of Fe in plumes. Fe(II) lifetimes in low-oxygen waters, such as those found in the South Pacific, are among the longest, potentially enhancing distal transport (Field and Sherrell 2000; Fitzsimmons et al. 2014). Inter-basin differences in pH and O_2 levels, as well as local currents affecting plume dilution, have been shown to affect Fe particulate and dissolved phase distribution in hydrothermal plumes to a greater extent than variations in vent fluid composition (Field and Sherrell 2000). Reported Fe(II) oxidation half-lives vary from 2.1 min in some areas of the Atlantic (Rudnicki and Elderfield 1993; Sedwick et al. 2015) to as long as 32–42 h in some areas of the Pacific (Chin et al. 1994). Binding of Fe(II) by organic ligands and incorporation into nanoparticulates has also been shown to increase Fe(II) oxidation time scales (Toner et al. 2009; Gartman et al. 2014). Field and Sherrell (2000) reported that an oxidation half-life of 3.3 h was long enough for Fe(III) colloid production and aggregation to occur in the neutrally buoyant plume where vent fluid is relatively dilute (as opposed to the buoyant plume, where vent fluid is highly concentrated), thus reducing the aggregation of particulates and increasing the likelihood of Fe persisting in suspended form.

2.5.2 Iron isotopes

Iron stable isotope analysis compares isotopic ratios of $^{56}Fe/^{54}Fe$ or $^{57}Fe/^{54}Fe$ (Dauphas and Rouxel 2006; Johnson et al. 2008). These isotopes are quantified in per mille (‰) deviation relative to a standard reference, which, in this context, is bulk silicate earth (Dauphas and Rouxel

2006; Bennett et al. 2009). Different sources of Fe produce unique isotope signatures, which can be traced throughout the water column (Conway and John 2014; German and Seyfried 2014). Processes within hydrothermal systems that affect Fe isotope ratios include biological and abiotic redox processes with either kinetic or equilibrium fractionation effects (Rouxel et al. 2008; Lough et al. 2017).

Initial isotope studies observed Fe isotope signatures of end-member vent fluids that were lighter compared with igneous rocks, falling in the range of –0.67 to –0.09‰ (Rouxel et al. 2004, 2008; Dauphas and Rouxel 2006; Bennett et al. 2009; German and Seyfried 2014). Isotopically heavy (from +0.1 to +1.7‰; Ellwood et al. 2015; Fitzsimmons et al. 2016) and very light (–1.35‰; Conway and John 2014) δ^{56}Fe signatures have now been observed in hydrothermal plumes, highlighting the diversity of hydrothermal processes involved in fractionation. Increasing δ^{56}Fe observations in different hydrothermal settings and within different stages of hydrothermal systems and plumes in recent years have further defined the processes giving rise to various isotopic signatures (Rouxel et al. 2008, 2016; Lough et al. 2017).

Mechanisms identified leading to Fe fractionation in subsurface hydrothermal systems include the formation of chimney structures (increase in fluid δ^{56}Fe values if the chimney structure is pyrite, but little effect if the structure is chalcopyrite; Rouxel et al. 2008); sub-surface mixing of unaltered seawater with hydrothermal fluids causing sulfide precipitation (increase in fluid δ^{56}Fe values) or basalt alteration and partial Fe oxidation (both decrease fluid δ^{56}Fe values; Rouxel et al. 2008). Once hydrothermal fluid leaves the vent, processes that lead to further Fe fractionation include precipitation of sulfide in the first tens of metres (increase in fluid δ^{56}Fe; Mottl and McConachy 1990; Bennett et al. 2009; Rouxel et al. 2016; Lough et al. 2017), followed by Fe oxyhydroxide formation in the first hundreds of metres (decrease in fluid δ^{56}Fe; Severmann et al. 2004; Lough et al. 2017), formation of pyrite nanoparticles (decrease in fluid δ^{56}Fe because these isotopically light particles fall within the operationally defined 0.4-μm dissolved fraction;

Fitzsimmons et al. 2016; Lough et al. 2017) and binding with organic ligands (increase in fluid δ^{56}Fe; Dideriksen et al. 2008; Morgan et al. 2010; Fitzsimmons et al. 2016).

The ratio of Fe to sulfide, determined by the geological setting of a hydrothermal system, has a marked effect on the δ^{56}Fe signature, because the formation of sulfide particles and the formation of oxyhydroxide particles exert opposing controls on the isotopic signature of the hydrothermal fluid (Rouxel et al. 2016; Lough et al. 2017). In geological settings that produce low sulfide concentrations, such as ultramafic-hosted systems, Fe precipitates primarily as Fe oxyhydroxides in the buoyant plume, shifting dissolved δ^{56}Fe towards light values (Severmann et al. 2004). In basaltic-hosted hydrothermal systems that have much higher sulfide concentrations, the opposite effect is observed (Fitzsimmons et al. 2016). The rate of oxidation of Fe(II) in hydrothermal fluid also exerts an effect on fractionation. If precipitation is rapid, the dissolved phase can be driven towards heavier δ^{56}Fe values, whereas if precipitation proceeds at a slower rate dissolved phase δ^{56}Fe will be lighter (Fitzsimmons et al. 2016). Because Fe(II) oxidation rate varies by ocean basin, as discussed above, Fe fractionation in the non-buoyant plume depends on the abyssal seawater properties in addition to hydrothermal system geological setting. Although there is a need to further constrain processes affecting Fe isotope fractionation in distal hydrothermal plumes, δ^{56}Fe signatures have proven to be a valuable tool for investigating hydrothermal processes and should prove valuable in tracing hydrothermal plumes in future investigations (Fitzsimmons et al. 2016; Rouxel et al. 2016; Lough et al. 2017).

2.6 Biogeochemical contribution of hydrothermal iron in the ocean

2.6.1 Effect of hydrothermalism on the global iron budget

Hydrothermal Fe, assumed to be a quasi-constant source, may act to buffer the world's oceans against fluctuations of other major sources of Fe, such as ice melt, dust and sediments, over

longer time scales (Tagliabue et al. 2010). A large portion of deep-ocean Fe is contributed by hydrothermal activity at mid-ocean ridges throughout the world's oceans (estimates range from 5 to 75%; Tagliabue et al. 2010; Carazzo et al. 2013; Saito et al. 2013; Conway and John 2014), with more effect in some ocean basins (such as the Pacific) than others (Tagliabue et al. 2014c).

In the past two decades, several models have been developed attempting to define the biogeochemical cycle of Fe in the ocean (Johnson et al. 1997; Archer and Johnson 2000; Moore et al. 2001; Parekh 2004; Weber et al. 2005; Aumont and Bopp 2006; Moore and Braucher 2008). Aeolian inputs of Fe (i.e. dust) were initially given the most attention by modelling studies until the importance of sedimentary sources was recognised (Tagliabue et al. 2009). The first global model to incorporate Fe from hydrothermal sources did not emerge until 2010, in response to growing evidence of stable hydrothermal Fe (Tagliabue et al. 2010).

Prior to the global model of Tagliabue et al. (2010), Bennett et al. (2008) postulated that 11–22% of the global deep-ocean DFe budget may originate from hydrothermal sources. This estimate was based on their calculations that ~4% of the total Fe released from one vent site was stabilised by Fe-complexing ligands (assuming that the concentrations found at the studied vent site were representative of all hydrothermal systems). Tagliabue et al. (2010) used the results obtained by Bennett et al. (2008) and observations of DFe : ^{3}He ratios coupled with observed relationships between spreading rate and ^{3}He flux to calculate a global annual hydrothermal Fe flux of 9 × 108 mol. This flux was input into a state-of-the-art biogeochemical–ocean circulation model (NEMO-PISCES) to assess the effect of the hydrothermal flux on world ocean biogeochemistry. The model showed that the biogeochemical response to hydrothermal DFe input is greatest in the Southern Ocean, and that observations of DFe in the Southern Ocean could only be replicated with a hydrothermal flux of Fe included in the model. In addition, Tagliabue et al. (2010) found that surface DFe is only weakly modified by hydrothermalism, whereas deep waters are affected to a much greater degree, particularly in the Southern Ocean.

The contribution of hydrothermalism to total Southern Ocean carbon export was found to be 5–15%, with a contribution to some regions of the Southern Ocean of up to 30%.

Hawkes et al. (2013) used reverse titration–competitive ligand exchange–adsorptive cathodic stripping voltammetry to show that 30% of the DFe in a hydrothermal plume in the Southern Ocean was stabilised by organic ligands. Extrapolating from this finding, the authors put forward that ~7.5% of total Fe within hydrothermal vent fluids is stabilised, but refrained from equating that figure to a fraction of the global budget, noting that hydrothermal fluids vary in Fe composition by up to five orders of magnitude. Subsequently, Carazzo et al. (2013) used laboratory experiments and observations of event plumes over different ocean ridges to develop a model suggesting that with the addition of 'particle diffusive convection' of nanoparticles in certain types of hydrothermal plumes (a process of thermal layering, prolonging large 'event' plumes for extended periods of time), Fe from hydrothermal vents may contribute up to 75% of the global deep-ocean DFe budget.

However, it is important to note that although Fe flux estimates and models have significantly improved our understanding of hydrothermally derived Fe in the global biogeochemical cycle, there are still uncertainties that may affect the modelled effect of hydrothermal Fe on the global oceanic Fe budget. For example, Fe : ^{3}He ratios on slow-spreading ridges have been observed 80-fold higher than those used to constrain current hydrothermal flux models (Saito et al. 2013). The effect of this discrepancy between current biogeochemical models and real processes is still under investigation (Tagliabue and Resing 2016). Another factor, suggested by Baker et al. (1993) over two decades ago, is that based on the differences of chemical fluxes between vents of high temperature and diffuse low temperature emanations, global Fe flux estimates may vary by a factor of 20. German et al. (2015) show evidence that adds support to the importance of diffuse sources of DFe and ligands. Tagliabue et al. (2014a) noted that uncertainties in the Fe-binding ligand pool may significantly affect model outputs, with variations in modelled ligand

concentrations affecting Fe-mediated changes to atmospheric CO_2 by up to 25%. A recent study modelling Fe-binding ligands in a three-dimensional biogeochemical ocean model has further constrained ligand processes in global oceans and more accurately reproduces Fe distribution compared with previous models that assume a uniform ligand distribution (Völker and Tagliabue 2015). Although producing more accurate oceanic Fe profiles overall, the model still produced some inconsistencies with observations in certain ocean regions, highlighting the complexity of Fe–ligand systems and a need to refine global models further. Resing et al. (2015) used their observations of a hydrothermal Fe plume from the southern EPR, coupled with the latest global model used by Völker and Tagliabue (2015), to estimate a mean (± s.d.) global DFe hydrothermal flux of 4 ± 1 Gmol $year^{-1}$. This estimate is fourfold higher than previous estimates and translates to ~15–30% of modelled export production south of the Polar Front. Most recently, Fitzsimmons et al. (2017) provided evidence that within the plume Resing et al. (2015) studied, both dissolved and particulate Fe sink in relation to ^3He, crossing isopycnals. These new results may need to be incorporated into existing models to accurately predict distal transport of hydrothermal Fe.

2.6.2 Hydrothermal vents as a source of iron in the Southern Ocean

The Southern Ocean is a region of great importance in controlling the global air–sea balance of CO_2 (Martin et al. 1990; Richardson 2008; Tagliabue et al. 2012, 2014a). Therefore, understanding supply mechanisms of Fe to the Southern Ocean is pivotal to understanding the global carbon cycle (Boyd et al. 2012). Upwelling carries excess macronutrients to surface waters of the Southern Ocean (de Baar et al. 1995; Tagliabue et al. 2012, 2014b), which contains the largest unused nutrient inventory of any ocean (Boyd et al. 2012).

Upwelling also delivers deep-ocean Fe to the surface in the Southern Ocean (Figure 2.10a; Tagliabue et al. 2012; Resing et al. 2015). These deep waters are enriched in Fe (~0.5–0.7 nM) by

both remineralisation and hydrothermalism. The InterRidge Vents Database (Beaulieu 2015) cites 72 hydrothermal vent sites that have been discovered south of 30°S to date (Figure 2.10a, b). Thirty-one of the 72 vents are located in the upper 2000 m of the water column, with 16 located in the upper 1000 m (Figure 2.10a), greatly increasing the probability of hydrothermal Fe reaching the surface mixed layer, as discussed earlier.

The network of ridges, back-arc spreading centres, arc volcanoes and transform faults south of 30°S cover a linear distance of ~20 000 km, large regions of which have not yet been surveyed for hydrothermal activity. The Kerguelen–Heard hot spot is also a region of active volcanism that has the potential for hydrothermal activity (Coffin et al. 1986; Ramsay et al. 1986; Weis et al. 2002; Figure 2.10b). It is within reason to assume that areas of hydrothermal activity are yet to be discovered along these ridges and hot spots. In support of this assumption, hydrothermal activity was recently confirmed on the KR1 and KR2 segments of the Australian–Antarctic Ridge south of New Zealand between 59 and 63°S (Hahm et al. 2015).

2.6.3 Moving forward: determining the effect of hydrothermalism on surface ocean productivity

Although the overall contribution of discrete sources of hydrothermal Fe to the Southern and global oceans remains to be seen, the effect of hydrothermalism on the overall deep oceanic Fe budget may affect productivity in regions of the ocean where upwelling of deep waters occurs. Direct links between hydrothermalism and surface ocean biological productivity are rare in the published literature. This highlights the difficulty of tracing hydrothermal inputs. However, emerging techniques, such as δ^{56}Fe isotope analysis and advanced modelling efforts, may provide new insights. Just as the effect of hydrothermal Fe on a global scale is an area of research in relative infancy, the effect of hydrothermal Fe on surface biogeochemistry at regional scales requires further investigation. Examples of regions where such links have been suggested include

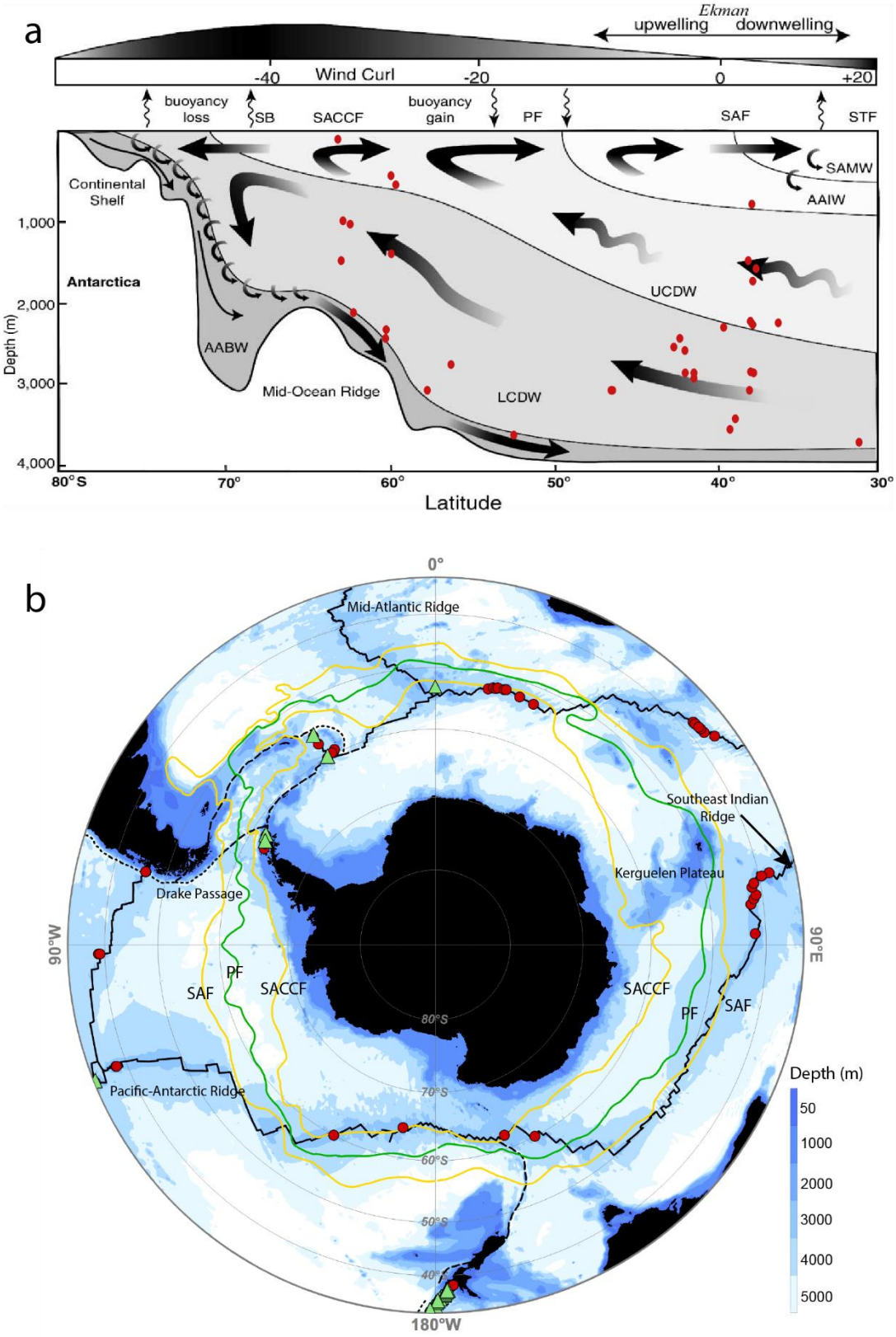

Figure 2.10 . (a) Schematic of meridional overturning circulation, depicting upwelling and downwelling ocean cells in the Southern Ocean. Dots indicate latitudes and depths of hydrothermal vents in the Southern Ocean (vent data from the InterRidge database; http://vents-data.interridge.org/ventfields, accessed 5 April 2017). The southern boundary of the Antarctic Circumpolar Current (SB), southern ACC front (SACCF), Polar Front (PF), Subantarctic Front (SAF), Subtropical Front (STF), Subantarctic

Mode Water (SAMW), Antarctic Intermediate Water (AAIW), Antarctic Bottom Water (AABW) and the Upper and Lower Circumpolar Deep Water (UCDW and LCDW respectively) are shown. Modified from (Speer et al. 2000) and (Trull et al. 2001). Note that the locations of the water parcels are approximate and vary at different longitudes around Antarctica. (b) South polar orthographic view of the Southern Ocean showing hydrothermal vents discovered (dots) and Fe studies at hydrothermal sites (triangles) with shaded bathymetry. Mid-ocean ridges (solid black line), trenches (dotted line) and transform faults (dashed line) are also shown along with the SAF, PF and SACCF. Main topographic features are also labelled. Adapted from Marshall and Speer (2012).

the equatorial Pacific (Wells et al. 1999; Mackey et al. 2002), the South-west Pacific arc volcanoes (Massoth et al. 2007; Boyle and Jenkins 2008) and the Southern Ocean (Hawkes et al. 2013, 2014). In addition, Hawkes et al. (2014) suggested that shallow hydrothermal sources, such as those often found in island arc chains, supply Fe directly to the surface. Hawkes et al. (2014) also suggested that a significant portion of this Fe is present in bioavailable colloidal particles, increasing their relative effect on fertilisation. Discovering such links between hydrothermal systems and surface ocean productivity is important, because this information could affect current Fe cycle models.

Key areas of research requiring further investigation in order to better constrain the role of hydrothermal Fe on global export production are:

• further observations at hydrothermal vents, in hydrothermal plumes and at ocean basin scales using analytical techniques that unequivocally trace hydrothermally derived Fe

• quantification of the fraction of DFe in ligand-bound versus nanoparticulate form in distal hydrothermal plumes and the bioavailable contribution of these fractions

• the global distribution of ligands in the ocean and how that may change under changing environmental conditions

• the relationship between ^{3}He and Fe at different ridge spreading rates and geological settings

• the mechanics of Fe-containing nanoparticles in hydrothermal plumes and their interaction with ligands and particles.

As these areas of research are addressed, modelling estimates of global flux and effects on the surface mixed layer will continue to evolve (Gartman et al. 2014; Tagliabue et al. 2010, 2014c). Recent models, such as those designed by Völker and Tagliabue (2015) and Resing et al. (2015), coupled with an increasing database of oceanic observations made through programs such as GEOTRACES and the release of the second GEOTRACES Intermediate Data Product in 2017 are key to further defining the processes controlling Fe concentrations and thus biogeochemical cycling in the world's oceans.

2.7 Acknowledgements

The authors thank the Australian Research Council (DP150100345; FT130100037) and the Australian Government Cooperative Research Centres Program through the Antarctic Climate and Ecosystems Cooperative Research Centre (ACE CRC), both of which provided project funding and PhD scholarship support. The authors thank the three anonymous reviewers for their time and attention to detail, which greatly improved this manuscript. The authors also thank Stace Beaulieu for assistance in locating previously compiled data and Stephanie Downes for her comments and suggestions during development of the manuscript.

2.8 Appendix

Table S1, a global compilation of Fe measurements from hydrothermal vents, created for this chapter can be found at: http://www.publish.csiro.au/mf/acc/MF16335/MF16335_AC.zip

2.9 References

Adams, D. K., McGillicuddy, D. J., Zamudio, L., Thurnherr, A. M., Liang, X., Rouxel, O., German, C. R., and Mullineaux, L. S. (2011). Surface-generated mesoscale eddies transport

deep-sea products from hydrothermal vents. Science 332, 580–583 doi:10.1126/science.1201066.

Adcroft, A., Scott, J. R., and Marotzke, J. (2001). Impact of geothermal heating on the global ocean circulation. Geophysical Research Letters 28, 1735–1738 doi:10.1029/2000GL012182.

Archer, D. E., and Johnson, K. (2000). A model of the iron cycle in the ocean. Global Biogeochemical Cycles 14, 269-279 doi:10.1029/1999GB900053.

Aumont, O., and Bopp, L. (2006). Globalizing results from ocean in situ iron fertilization studies. Global Biogeochemical Cycles 20, GB2017. doi:10.1029/2005GB002591

Baker, E. T. (1994). A 6-year time series of hydrothermal plumes over the Cleft segment of the Juan de Fuca Ridge. Journal of Geophysical Research 99, 4889-4904 doi:10.1029/93JB01030.

Baker, E. T. E., and German, C. C. R. (2004). On the global distribution of hydrothermal vent fields. Mid-Ocean Ridges 148, 1–18. 10.1029/148GM10

Baker, E. T., and Massoth, G. J. (1987). Characteristics of hydrothermal plumes from two vent fields on the Juan de Fuca Ridge, northeast Pacific Ocean. Earth and Planetary Science Letters 85, 59–73 doi:10.1016/0012-821X(87)90021-5.

Baker, E. T., Massoth, G. J., and Feely, R. a. (1987). Cataclysmic hydrothermal venting on the Juan de Fuca Ridge. Nature 329, 149–151 doi:10.1038/329149a0.

Baker, E. T., Lavelle, J. W., Feely, R. A., Massoth, G. J., Walker, S. L., and Lupton, J. E. (1989). Episodic venting of hydrothermal fluids from the Juan de Fuca Ridge. Journal of Geophysical Research 94, 9237-9250doi:10.1029/JB094iB07p09237.

Baker, E. T., Massoth, G. J., Walker, S. L., and Embley, R. W. (1993). A method for quantitatively estimating diffuse and discrete hydrothermal discharge. Earth and Planetary Science Letters 118, 235–249 doi:10.1016/0012-821X(93)90170-E.

Baker, E. T., German, C. R., and Elderfield, H. (1995). Hydrothermal plumes over spreading-centre axes: global distributions and geological inferences. In 'Seafloor Hydrothermal Systems: Physical, Chemical, Biological, and Geological Interactions'. (Eds S. E. Humphris, R. A. Zierenberg, L. S. Mullineaux, and R. E. Thomson.) Geophysical Monograph Series, pp. 47–71. (American Geophysical Union: Washington, DC, USA.) doi:10.1029/GM091

Baker, E. T., Massoth, G. J., Feely, R. a., Cannon, G. a., and Thomson, R. E. (1998). The rise and fall of the Coaxial hydrothermal site, 1993–1996. Journal of Geophysical Research 103, 9791-9806 doi:10.1029/97JB03112.

Baker, E. T., Edmonds, H. N., Michael, P. J., Bach, W., Dick, H. J. B., Snow, J. E., Walker, S. L., Banerjee, N. R., and Langmuir, C. H. (2004). Hydrothermal venting in magma deserts: the ultraslow-spreading Gakkel and Southwest Indian ridges. Geochemistry Geophysics Geosystems 5, 1–29 doi:10.1029/2004GC000712.

Baker, E. T., Embley, R. W., Walker, S. L., Resing, J. a., Lupton, J. E., Nakamura, K., de Ronde, C. E. J., and Massoth, G. J. (2008). Hydrothermal activity and volcano distribution along the Mariana arc. Journal of Geophysical Research 113, B08S09 doi:10.1029/2007JB005423.

Baker, E. T., Lupton, J. E., Resing, J. A., Baumberger, T., Lilley, M. D., Walker, S. L., and Rubin, K. H. (2011). Unique event plumes from a 2008 eruption on the Northeast Lau Spreading Center. Geochemistry Geophysics Geosystems 12, doi:10.1029/2011GC003725.

Baker, E., Chadwick, W., Cowen, J., Dziak, R., Rubin, K., and Fornari, D. (2012). Hydrothermal discharge during submarine eruptions: the importance of detection, response, and new technology. Oceanography 25, 128–141 doi:10.5670/oceanog.2012.11.

Beaulieu, S. E. (2015). InterRidge global database of active submarine hydrothermal vent fields: prepared for InterRidge, Version 3.4. Available at http://vents-data.interridge.org [Verified 5 April 2017].

Beaulieu, S. E., Baker, E. T., German, C. R., and Maffei, A. (2013). An authoritative global database for active submarine hydrothermal vent fields. Geochemistry Geophysics Geosystems 14, 4892–4905 doi:10.1002/2013GC004998.

Beaulieu, S. E., Baker, E. T., and German, C. R. (2015). Where are the undiscovered hydrothermal vents on oceanic spreading ridges? Deep-Sea Research – II. Topical Studies in Oceanography 121, 202–212 doi:10.1016/j.dsr2.2015.05.001.

Belviso, S., Jean-Baptiste, P., Nguyen, B. C., Merlivat, L., Labeyrie, L., and Merliva, L. (1987). Deep methane maxima and ^{3}He anomalies across the Pacific entrance to the Celebes Basin. Geochimica et Cosmochimica Acta 51, 2673–2680 doi:10.1016/0016-7037(87)90148-7.

Bennett, S. A., Achterberg, E. P., Connelly, D. P., Statham, P. J., Fones, G. R., and German, C. R. (2008). The distribution and stabilisation of dissolved Fe in deep-sea hydrothermal plumes. Earth and Planetary Science Letters 270, 157–167 doi:10.1016/j.epsl.2008.01.048.

Bennett, S. A., Rouxel, O., Schmidt, K., Garbe-Schönberg, D., Statham, P. J., and German, C. R. (2009). Iron isotope fractionation in a buoyant hydrothermal plume, 5°S Mid-Atlantic Ridge. Geochimica et Cosmochimica Acta 73, 5619–5634 doi:10.1016/j.gca.2009.06.027.

Boyd, P. W., Jickells, T., Law, C. S., Blain, S., Boyle, E. A., Buesseler, K. O., Coale, K. H., Cullen, J. J., de Baar, H. J. W., Follows, M., Harvey, M., Lancelot, C., Levasseur, M., Owens, N. P. J., Pollard, R., Rivkin, R. B., Sarmiento, J., Schoemann, V., Smetacek, V., Takeda, S., Tsuda, A., Turner, S., and Watson, A. J. (2007). Mesoscale iron enrichment experiments 1993–2005: synthesis and future directions. Science 315, 612–617 doi:10.1126/science.1131669.

Boyd, P. W., and Ellwood, M. J. (2010). The biogeochemical cycle of iron in the ocean. Nature Geoscience 3, 675–682. doi:10.1038/ngeo964

Boyd, P. W., Ibisanmi, E., Sander, S. G., Hunter, K. A., and Jackson, G. A. (2010). Remineralization of upper ocean particles: implications for iron biogeochemistry. Limnology and Oceanography 55, 1271–1288 doi:10.4319/lo.2010.55.3.1271.

Boyd, P. W., Arrigo, K. R., Strzepek, R., and van Dijken, G. L. (2012). Mapping phytoplankton iron utilization: insights into Southern Ocean supply mechanisms. Journal of Geophysical Research 117, C06009 doi:10.1029/2011JC007726.

Boyle, E., and Jenkins, W. (2008). Hydrothermal iron in the deep western South Pacific. Geochimica et Cosmochimica Acta Supplement 72, 107. [Abstract]

Broecker, W. S. (1991). The great ocean conveyor. Oceanography 4, 79–89 doi:10.5670/oceanog.1991.07.

Bruland, K. W., Middag, R., and Lohan, M. C. (2014). Controls of trace metals in seawater. In 'Treatise on Geochemistry'. (Eds H. Holland and K. Turekian.) pp. 19–51. (Elsevier: Amsterdam, Netherlands.) doi:10.1016/B978-0-08-095975-7.00602-1

Caprara, S., Buck, K. N., Gerringa, L. J. A., Rijkenberg, M. J. A., and Monticelli, D. (2016). A compilation of iron speciation data for open oceanic waters. Frontiers in Marine Science 3, 221 doi:10.3389/fmars.2016.00221.

Carazzo, G., Jellinek, A. M., and Turchyn, A. V. (2013). The remarkable longevity of submarine plumes: implications for the hydrothermal input of iron to the deep-ocean. Earth and Planetary Science Letters 382, 66–76 doi:10.1016/j.epsl.2013.09.008.

Chapin, T. P., Johnson, K. S., and Coale, K. H. (1991). Rapid determination of manganese in sea water by flow-injection analysis with chemiluminescence detection. Analytica Chimica Acta 249, 469–478 doi:10.1016/S0003-2670(00)83021-4.

Charlou, J., Fouquet, Y., Bougault, H., Donval, J. P., Etoubleau, J., Jean-Baptiste, P., Dapoigny, A., Appriou, P., and Rona, P. A. (1998). Intense CH_4 plumes generated by serpentinization of ultramafic rocks at the intersection of the 15°20□ N fracture zone and the Mid-Atlantic Ridge. Geochimica et Cosmochimica Acta 62, 2323–2333 doi:10.1016/S0016-7037(98)00138-0.

Charlou, J., Donval, J., Fouquet, Y., Jean-Baptiste, P., and Holm, N. (2002). Geochemistry of high H_2 and CH_4 vent fluids issuing from ultramafic rocks at the Rainbow hydrothermal field (36°14□ N, MAR). Chemical Geology 191, 345–359 doi:10.1016/S0009-2541(02)00134-1.

Chase, Z., Johnson, K. S., Elrod, V. A., Plant, J. N., Fitzwater, S. E., Pickell, L., and Sakamoto, C. M. (2005). Manganese and iron distributions off central California influenced by upwelling and shelf width. Marine Chemistry 95, 235–254 doi:10.1016/j.marchem.2004.09.006.

Chen, Y., and Morgan, W. J. (1990). Rift valley/no rift valley transition at mid-ocean ridges. Journal of Geophysical Research 95, 17571-17581 doi:10.1029/JB095iB11p17571.

Chin, C. S., Coale, K. H., Elrod, V. A., Johnson, K. S., Massoth, G. J., and Baker, E. T. (1994). In situ observations of dissolved iron and manganese in hydrothermal vent plumes, Juan de Fuca Ridge. Journal of Geophysical Research 99, 4969–4984 doi:10.1029/93JB02036.

Clarke, W. B., Beg, M. A., and Craig, H. (1969). Excess ^3He in the sea: evidence for terrestrial primordial helium. Earth and Planetary Science Letters 6, 213–220 doi:10.1016/0012-821X(69)90093-4.

Coale, K. K. H., Chin, C. C. S., Massoth, G. G. J., Johnson, K. S., and Baker, E. T. (1991). In situ chemical mapping of dissolved iron and manganese in hydrothermal plumes. Nature 352, 325–328 doi:10.1038/352325a0.

Coffin, M., Davies, H., and Haxby, W. (1986). Structure of the Kerguelen Plateau province from SEASAT altimetry and seismic reflection data. Nature 324, 134–136. doi:10.1038/324134a0

Coffin, M. F., Gahagan, L. M., & Lawver, L. A. (1998). Present-day plate boundary digital data compilation. University of Texas Institute for Geophysics technical report (Vol. 174). Austin, TX.

Conway, T., and John, S. (2014). Quantification of dissolved iron sources to the North Atlantic Ocean. Nature 511, 212–215 doi:10.1038/nature13482.

Cowen, J. P., and Hui Li, Y. (1991). The influence of a changing bacterial community on trace metal scavenging in a deep-sea particle plume. Journal of Marine Research 49, 517–542 doi:10.1357/002224091784995800.

Cowen, J. P., Massoth, G. J., and Baker, E. T. (1986). Bacterial scavenging of Mn and Fe in a mid- to far-field hydrothermal particle plume. Nature 322, 169–171 doi:10.1038/322169a0.

Cowen, J. P., Massoth, G. J., and Feely, R. A. (1990). Scavenging rates of dissolved manganese in a hydrothermal vent plume. Deep-Sea Research – A. Oceanographic Research Papers 37, 1619–1637 doi:10.1016/0198-0149(90)90065-4.

Cowen, J. P., Bertram, M. A., Baker, E. T., Feely, R. A., Massoth, G. J., and Summit, M. (1998). Geomicrobial transformation of manganese in Gorda Ridge event plumes. Deep-Sea Research – II. Topical Studies in Oceanography 45, 2713–2737 doi:10.1016/S0967-0645(98)00090-3.

Dauphas, N., and Rouxel, O. (2006). Mass spectrometry and natural variations of iron isotopes. Mass Spectrometry Reviews 25, 515–550 doi:10.1002/mas.20078.

de Baar, H. J. W., de Jong, J. T. M., Bakker, D. C. E., Löscher, B. M., Veth, C., Bathmann, U., and Smetacek, V. (1995). Importance of iron for plankton blooms and carbon dioxide drawdown in the Southern Ocean. Nature 373, 412–415 doi:10.1038/373412a0.

de Baar, H. J. W., Boyd, P. W., Coale, K. H., Landry, M. R., Tsuda, A., Assmy, P., Bakker, D. C. E., Bozec, Y., Barber, R. T., Brzezinski, M. a., Buesseler, K. O., Boyé, M., Croot, P. L., Gervais, F., Gorbunov, M. Y., Harrison, P. J., Hiscock, W. T., Laan, P., Lancelot, C., Law, C. S., Levasseur, M., Marchetti, A., Millero, F. J., Nishioka, J., Nojiri, Y., van Oijen, T., Riebesell, U., Rijkenberg, M. J., Saito, H., Takeda, S., Timmermans, K. R., Veldhuis, M. J. W., Waite, A. M., and Wong, C. S. (2005). Synthesis of iron fertilization experiments: from the iron age in the age of enlightenment. Journal of Geophysical Research – C. Oceans 110, 1–24 10.1029/2004JC002601.

de Ronde, C. E. J. (2011). Seafloor hydrothermal systems of intraoceanic arcs. Oceans 2011, 12–14.

de Ronde, C. E. J., and Stucker, V. K. (2015). Seafloor hydrothermal venting at volcanic arcs and backarcs. In 'The Encyclopedia of Volcanoes'. (Eds H. Sigurdsson, B. Houghton, S. R. McNutt, H. Rymer, and J. Stix..) pp. 823–849. (Academic Press: London..) doi:10.1016/B978-0-12-385938-9.00047-X

de Ronde, C. E. J., Baker, E. T., Massoth, G. J., Lupton, J. E., Wright, I. C., Feely, R. A., and Greene, R. R. (2001). Intra-oceanic subduction-related hydrothermal venting, Kermadec volcanic arc, New Zealand. Earth and Planetary Science Letters 193, 359–369 doi:10.1016/S0012-821X(01)00534-9.

Dick, G. J., Anantharaman, K., Baker, B. J., Li, M., Reed, D. C., and Sheik, C. S. (2013). The microbiology of deep-sea hydrothermal vent plumes: ecological and biogeographic linkages to seafloor and water column habitats. Frontiers in Microbiology 4, 1–16 doi:10.3389/fmicb.2013.00124.

Dideriksen, K., Baker, J. A., and Stipp, S. L. S. (2008). Equilibrium Fe isotope fractionation between inorganic aqueous Fe(III) and the siderophore complex, Fe(III)-desferrioxamine B. Earth and Planetary Science Letters 269, 280–290 doi:10.1016/j.epsl.2008.02.022.

Douville, E., Charlou, J. L., Oelkers, E. H., Bienvenu, P., Jove Colon, C., Donval, J., Fouquet, Y., Prieur, D., Appriou, P., and Colon, C. F. J. (2002). The Rainbow vent fluids (36°14□ N, MAR): the influence of ultramafic rocks and phase separation on trace metal content in Mid-Atlantic Ridge hydrothermal fluids. Chemical Geology 184, 37–48 doi:10.1016/S0009-2541(01)00351-5.

Dymond, J., Cobler, K., Gordon, L., Biscayne, P. E., and Mathieu, G. (1983). ^{226}Ra and ^{222}Rn contents of Galapagos Rift hydrothermal waters: the importance of low-temperature interactions with crustal rocks. Earth and Planetary Science Letters 64, 417–429 doi:10.1016/0012-821X(83)90102-4.

Edmond, J. M., Von Damm, K. L., McDuff, R. E., Measures, C. I., and Group, N. P. (1982). Chemistry of hot springs on the East Pacific Rise and their effluent dispersal. Nature 297, 187–191 doi:10.1038/297187a0.

Elderfield, H., and Schultz, A. (1996). Mid-ocean ridge hydrothermal fluxes and the chemical composition of the ocean. Annual Review of Earth and Planetary Sciences 24, 191–224 doi:10.1146/annurev.earth.24.1.191.

Ellwood, M. J., Hutchins, D. A., Lohan, M. C., Milne, A., Nasemann, P., Nodder, S. D., Sander, S. G., Strzepek, R., Wilhelm, S. W., and Boyd, P. W. (2015). Iron stable isotopes track

pelagic iron cycling during a subtropical phytoplankton bloom. Proceedings of the National Academy of Sciences of the United States of America 112, E15–E20 doi:10.1073/pnas.1421576112.

Farley, K. A., Maier-Reimer, E., Maier-Reimer, E., Schlosser, P., and Broecker, W. S. (1995). Constraints on mantle ^{3}He fluxes and deep-sea circulation from an oceanic general circulation model. Journal of Geophysical Research 100, 3829-3839 doi:10.1029/94JB02913.

Feely, R. A., Massoth, G. J., Trefry, J. H., Baker, E. T., Paulson, A. J., and Lebon, G. T. (1994). Composition and sedimentation of hydrothermal plume particles from north Cleft segment, Juan de Fuca Ridge. Journal of Geophysical Research 99, 4985–5006 doi:10.1029/93JB02509.

Field, M. P., and Sherrell, R. M. (2000). Dissolved and particulate Fe in a hydrothermal plume at 9°45□ N, East Pacific Rise: slow Fe(II) oxidation kinetics in Pacific plumes. Geochimica et Cosmochimica Acta 64, 619–628. doi:10.1016/S0016-7037(99)00333-6

Fitzsimmons, J. N., Boyle, E. a., and Jenkins, W. J. (2014). Distal transport of dissolved hydrothermal iron in the deep South Pacific Ocean. Proceedings of the National Academy of Sciences of the United States of America 111, 16654–16661. doi:10.1073/pnas.1418778111

Fitzsimmons, J. N., Carrasco, G. G., Wu, J., Roshan, S., Hatta, M., Measures, C. I., Conway, T. M., John, S. G., and Boyle, E. A. (2015). Partitioning of dissolved iron and iron isotopes into soluble and colloidal phases along the GA03 GEOTRACES North Atlantic Transect. Deep-Sea Research – II. Topical Studies in Oceanography 116, 130–151 doi:10.1016/j.dsr2.2014.11.014.

Fitzsimmons, J. N., Conway, T. M., Lee, J.-M., Kayser, R., Thyng, K. M., John, S. G., and Boyle, E. A. (2016). Dissolved iron and iron isotopes in the southeastern Pacific Ocean. Global Biogeochemical Cycles 30, 1372–1395 doi:10.1002/2015GB005357.

Fitzsimmons, J. N., John, S. G., Marsay, C. M., Hoffman, C. L., Nicholas, S. L., Toner, B. M., German, C. R., Sherrell, R. M., Ho, C. L., Nicholas, S. L., Toner, B. M., German, C. R., and Sherrell, R. M. (2017). Iron persistence in a distal hydrothermal plume supported by dissolved-particulate exchange. Nature Geoscience 10, 195–201 doi:10.1038/ngeo2900.

Gallant, R. M., and Von Damm, K. L. (2006). Geochemical controls on hydrothermal fluids from the Kairei and Edmond Vent Fields, 23°–25°S, Central Indian Ridge. Geochemistry, Geophysics, Geosystems 7, Q06018. doi:10.1029/2005GC001067

Gamo, T., Okamura, K., Hatanaka, H., Hasumoto, H., Komatsu, D., Chinen, M., Mori, M., Tanaka, J., Hirota, A., Tsunogai, U., and Tamaki, K. (2015). Hydrothermal plumes in the Gulf of Aden, as characterized by light transmission, Mn, Fe, CH_4 and $\delta^{13}C$–CH_4 anomalies. Deep-Sea Research – II. Topical Studies in Oceanography 121, 62–70 doi:10.1016/j.dsr2.2015.06.004.

Gartman, A. (2013). The formation, oxidation and distribution of pyrite nanoparticles emitted from hydrothermal vents: a laboratory and field based approach. Ph.D. Thesis, University of Delaware, Newark, DE, USA.

Gartman, A., Findlay, A. J., and Luther, G. W. (2014). Nanoparticulate pyrite and other nanoparticles are a widespread component of hydrothermal vent black smoker emissions. Chemical Geology 366, 32–41 doi:10.1016/j.chemgeo.2013.12.013.

German, C. R., and Lin, J. (2004). The thermal structure of the oceanic crust, ridge-spreading and hydrothermal circulation: how well do we understand their inter-connections? In 'Mid-

Ocean Ridges'. (Eds C. R. German, J. Lin, and L. . M. Parson..) pp. 1–18. (American Geophysical Union: Washington, D. C..) doi:10.1029/148GM01

German, C. R., and Seyfried, W. E. (2014). Hydrothermal processes. In 'Treatise on Geochemistry'. (Eds H. Holland and K. Turekian.) pp. 191–233. (Elsevier: Amsterdam.) doi:10.1016/B978-0-08-095975-7.00607-0

German, C., Campbell, A., and Edmond, J. (1991). Hydrothermal scavenging at the Mid-Atlantic Ridge: modification of trace element dissolved fluxes. Earth and Planetary Science Letters 107, 101–114. doi:10.1016/0012-821X(91)90047-L

German, C. R., Thurnherr, A. M., Knoery, J., Charlou, J.-L., Jean-Baptiste, P., and Edmonds, H. N. (2010). Heat, volume and chemical fluxes from submarine venting: a synthesis of results from the Rainbow hydrothermal field, 36°N MAR. Deep-Sea Research – I. Oceanographic Research Papers 57, 518–527 doi:10.1016/j.dsr.2009.12.011.

German, C. R., Legendre, L. L., Sander, S. G., Niquil, N., Luther, G. W., Bharati, L., Han, X., and Le Bris, N. (2015). Hydrothermal Fe cycling and deep ocean organic carbon scavenging: model-based evidence for significant POC supply to seafloor sediments. Earth and Planetary Science Letters 419, 143–153 doi:10.1016/j.epsl.2015.03.012.

German, C. R., Petersen, S., and Hannington, M. D. (2016). Hydrothermal exploration of mid-ocean ridges: where might the largest sulfide deposits be forming? Chemical Geology 420, 114–126 doi:10.1016/j.chemgeo.2015.11.006.

Gledhill, M., and Buck, K. N. (2012). The organic complexation of iron in the marine environment: a review. Frontiers in Microbiology 3, 69 doi:10.3389/fmicb.2012.00069.

Gledhill, M., and van den Berg, C. M. G. (1994). Determination of complexation of iron(III) with natural organic complexing ligands in seawater using cathodic stripping voltammetry. Marine Chemistry 47, 41–54. doi:10.1016/0304-4203(94)90012-4

Gran, H. H. (1931). On the conditions for the production of plankton in the sea. Rapports et Proces verbaux des Reunions,Conseil International pour l'exploration de la Mer 75, 37–46.

Haase, K. M., Koschinsky, A., Petersen, S., Devey, C. W., German, C., Lackschewitz, K. S., Melchert, B., Seifert, R., Borowski, C., Giere, O., and Paulick, H. (2009). Diking, young volcanism and diffuse hydrothermal activity on the southern Mid-Atlantic Ridge: the Lilliput field at 9°33□ S. Marine Geology 266, 52–64 doi:10.1016/j.margeo.2009.07.012.

Hahm, D., Baker, E. T., Rhee, T. S., Won, Y.-J., Resing, J. A., Lupton, J. E., Lee, W.-K., Kim, M., and Park, S.-H. (2015). First hydrothermal discoveries on the Australian–Antarctic Ridge: discharge sites, plume chemistry, and vent organisms. Geochemistry, Geophysics, Geosystems 16, 3061–3075. doi:10.1002/2015GC005926

Hart, T. J. (1934). On the phytoplankton of the Southwest Atlantic and the Bellinghausen Sea, 1929–1931. Discovery Reports 8, 1–268.

Hatta, M., Measures, C. I., Wu, J., Roshan, S., Fitzsimmons, J. N., Sedwick, P., and Morton, P. (2015). An overview of dissolved Fe and Mn distributions during the 2010–2011 U.S. GEOTRACES north Atlantic cruises: GEOTRACES GA03. Deep-Sea Research – II. Topical Studies in Oceanography 116, 117–129 doi:10.1016/j.dsr2.2014.07.005.

Hautala, S. L., and Riser, S. C. (1989). A simple model of abyssal circulation, including effects of wind, buoyancy and topography. Journal of Physical Oceanography 19, 596–611 doi:10.1175/1520-0485(1989)019<0596:ASMOAC>2.0.CO;2.

Hawkes, J. A., Connelly, D. P., Gledhill, M., and Achterberg, E. P. (2013). The stabilisation and transportation of dissolved iron from high temperature hydrothermal vent systems. Earth and Planetary Science Letters 375, 280–290 doi:10.1016/j.epsl.2013.05.047.

Hawkes, J. J. A., Connelly, D. P., Rijkenberg, M. J. A., and Achterberg, E. P. (2014). The importance of shallow hydrothermal island arc systems in ocean biogeochemistry. Geophysical Research Letters 41, 942–947. doi:10.1002/2013GL058817

Helfrich, K. R., and Speer, K. G. (1995). Oceanic Hydrothermal Circulation: Mesoscale and Basin-Scale Flow. In 'Seafloor Hydrothermal Systems: Physical, Chemical, Biological, and Geological Interactions'. (Eds S. E. Humphris, R. A. Zierenberg, L. S. Mullineaux, and R. E. Thomson.) pp. 347–356. (American Geophysical Union: Washington, DC, USA.) doi: 10.1029/GM091p0347

Hochella, M. M. F., Lower, S. S. K., Maurice, P. A., Penn, R. L., Sahai, N., Sparks, D. L., and Twining, B. S. (2008). Nanominerals, mineral nanoparticles, and earth systems. Science 319, 1631–1635 doi:10.1126/science.1141134.

Horibe, Y., Kim, K.-R., and Craig, H. (1986). Hydrothermal methane plumes in the Mariana back-arc spreading centre. Nature 324, 131–133 doi:10.1038/324131a0.

Ibisanmi, E., Sander, S. G., Boyd, P. W., Bowie, A. R., and Hunter, K. a. (2011). Vertical distributions of iron-(III) complexing ligands in the Southern Ocean. Deep Sea Research Part II: Topical Studies in Oceanography 58, 2113–2125. doi:10.1016/j.dsr2.2011.05.028

Jean-Baptiste, P., Belviso, S., Alaux, G., Nguyen, B. C., and Mihalopoulos, N. (1990). ^{3}He and methane in the Gulf of Aden. Geochimica et Cosmochimica Acta 54, 111–116 doi:10.1016/0016-7037(90)90199-U.

Jean-Baptiste, P., Charlou, J. L., Stievenard, M., Donval, J. P., Bougault, H., and Mevel, C. (1991). Helium and methane measurements in hydrothermal fluids from the Mid-Atlantic Ridge: the Snake Pit site at 23°N. Earth and Planetary Science Letters 106, 17–28 doi:10.1016/0012-821X(91)90060-U.

Jenkins, W. J. 2014. Tracers of ocean mixing. In 'Treatise on Geochemistry'. (Eds H. Holland and K. Turekian.) pp. 235–257. (Elsevier: Amsterdam.) doi:10.1016/B978-0-08-095975-7.00608-2

Johnson, K. S., Gordon, R. M., and Coale, K. H. (1997). What controls dissolved iron concentrations in the world ocean? Marine Chemistry 57, 137–161 doi:10.1016/S0304-4203(97)00043-1.

Johnson, C. M., Beard, B. L., and Roden, E. E. (2008). The iron isotope fingerprints of redox and biogeochemical cycling in Modern and Ancient Earth. Annual Review of Earth and Planetary Sciences 36, 457–493 doi:10.1146/annurev.earth.36.031207.124139.

Joyce, T. M., and Speer, K. G. (1987). Modeling the large-scale influence of geothermal sources on abyssal flow. Journal of Geophysical Research 92, 2843–2850 doi:10.1029/JC092iC03p02843.

Kadko, D., and Johns, W. (2011). Inferring upwelling rates in the equatorial Atlantic using 7Be measurements in the upper ocean. Deep-Sea Research – I. Oceanographic Research Papers 58, 647–657 doi:10.1016/j.dsr.2011.03.004.

Kadko, D., and Moore, W. (1988). Radiochemical constraints on the crustal residence time of submarine hydrothermal fluids: Endeavour Ridge. Geochimica et Cosmochimica Acta 52, 659–668 doi:10.1016/0016-7037(88)90328-6.

Kadko, D. C., Rosenberg, N. D., Lupton, J. E., Collier, R. W., and Lilley, M. D. (1990). Chemical reaction rates and entrainment within the Endeavour Ridge hydrothermal plume. Earth and Planetary Science Letters 99, 315–335 doi:10.1016/0012-821X(90)90137-M.

Kadko, D., Baross, J., and Alt, J. (1995). The magnitude and global implications of hydrothermal flux. In 'Seafloor Hydrothermal Systems: Physical, Chemical, Biological, and Geological Interactions'. (Eds S. E. Humphris, R. A. Zierenberg, L. S. Mullineaux, and R. E. Thomson.)

Geophysical Monograph Series, pp. 446–466. (American Geophysical Union: Washington, DC, USA.) doi:10.1029/GM091

Kelley, D. S., Lilley, M. D., Lupton, J. E., and Olson, E. J. (1998). Enriched H_2, CH_4, and ^3He concentrations in hydrothermal plumes associated with the 1996 Gorda Ridge eruptive event. Deep Sea Research Part II: Topical Studies in Oceanography 45, 2665–2682.Kleint, C., Hawkes, J. A., Sander, S. G., and Koschinsky, A. (2016). Voltammetric investigation of hydrothermal iron speciation. Frontiers in Marine Science 3, 1–11 doi:10.3389/fmars.2016.00075.

Kipp, L. E., Sanial, V., Henderson, P. B., van Beek, P., Reyss, J.-L., Hammond, D. E., Moore, W. S., and Charette, M. A. (2017). Radium isotopes as tracers of hydrothermal inputs and neutrally buoyant plume dynamics in the deep ocean. Marine Chemistry. [Published online early 30 June 2017]. doi:10.1016/j.marchem.2017.06.011

Kleint, C., Hawkes, J. A., Sander, S. G., and Koschinsky, A. (2016). Voltammetric investigation of hydrothermal iron speciation. Frontiers in Marine Science 3, 1–11. doi:10.3389/FMARS.2016.00075

Klinkhammer, G. P. (1994). Fiber optic spectrometers for in situ measurements in the oceans: the ZAPS probe. Marine Chemistry 47, 13–20 doi:10.1016/0304-4203(94)90010-8.

Koschinsky, A., Garbe-Schönberg, D., Sander, S., Schmidt, K., Gennerich, H.-H., and Strauss, H. (2008). Hydrothermal venting at pressure-temperature conditions above the critical point of seawater, 5°S on the Mid-Atlantic Ridge. Geology 36, 615-618 doi:10.1130/G24726A.1.

Koski, R. A., German, C. R., and Hein, J. R. (2003). Fate of hydrothermal products from mid-ocean ridge hydrothermal systems: near-field to global perspectives. In 'Energy and Mass Transfer in Marine Hydrothermal Systems'. (Eds P. E. Halbach, V. Tunnicliffe, and J. R. Hein.) pp. 317–335. (Dahlem University Press: Berlin, Germany.)

Lang, S. Q., Butterfield, D. A., Lilley, M. D., Paul Johnson, H., and Hedges, J. I. (2006). Dissolved organic carbon in ridge-axis and ridge-flank hydrothermal systems. Geochimica et Cosmochimica Acta 70, 3830–3842 doi:10.1016/j.gca.2006.04.031.

Langmuir, C., Humphris, S., Fornari, D., Van Dover, C., Von Damm, K., Tivey, M. K., Colodner, D., Charlou, J.-L., Desonie, D., Wilson, C., Fouquet, Y., Klinkhammer, G., and Bougault, H. (1997). Hydrothermal vents near a mantle hot spot: the Lucky Strike vent field at 37°N on the Mid-Atlantic Ridge. Earth and Planetary Science Letters 148, 69–91 doi:10.1016/S0012-821X(97)00027-7.

Ledwell, J. R., Ledwell, J. R., Montgomery, E. T., Montgomery, E. T., Polzin, K. L., Polzin, K. L., St Laurent, L. C., St Laurent, L. C., Schmitt, R. W., Schmitt, R. W., Toole, J. M., and Toole, J. M. (2000). Evidence for enhanced mixing over rough topography in the abyssal ocean. Nature 403, 179–182 doi:10.1038/35003164.

Li, M., Toner, B. M., Baker, B. J., Breier, J. A., Sheik, C. S., and Dick, G. J. (2014). Microbial iron uptake as a mechanism for dispersing iron from deep-sea hydrothermal vents. Nature Communications 5, 3192 doi:10.1038/ncomms4192.

Lilley, M. D., Feely, R. A., and Trefry, J. H. (1995). Chemical and biochemical transformations in hydrothermal plumes. In 'Seafloor Hydrothermal Systems: Physical, Chemical, Biological, and Geological Interactions'. (Eds S. E. Humphris, R. A. Zierenberg, L. S. Mullineaux, and R. E. Thomson.) Geophysical Monograph Series, pp. 369–391. (American Geophysical Union: Washington, DC, USA.) doi:10.1029/GM091

Lister, C. R. B. (1972). On the thermal balance of a mid-ocean ridge. Geophysical Journal International 26, 515–535 doi:10.1111/j.1365-246X.1972.tb05766.x.

Lough, A. J. M., Klar, J. K., Homoky, W. B., Comer-Warner, S. A., Milton, J. A., Connelly, D. P., James, R. H., and Mills, R. A. (2017). Opposing authigenic controls on the isotopic signature

of dissolved iron in hydrothermal plumes. Geochimica et Cosmochimica Acta202, 1-20.. doi:10.1016/j.gca.2016.12.022.

Love, B. A., Resing, J. A., Cowen, J. P., Lupton, J. E., Fornari, D. J., Shank, T. M., and Biller, D. (2008). Methane, manganese, and helium in hydrothermal plumes following volcanic eruptions on the East Pacific Rise near 9°50□ N. Geochemistry, Geophysics, Geosystems 9, Q06T01. doi:10.1029/2008GC002104

Lupton, J. E. (1995). Hydrothermal plumes: near and far field. In 'Seafloor Hydrothermal Systems: Physical, Chemical, Biological, and Geological Interactions'. (Eds S. E. Humphris, R. A. Zierenberg, L. S. Mullineaux, and R. E. Thomson.) Geophysical Monograph Series, pp. 317–346. (American Geophysical Union: Washington, DC, USA.) doi:10.1029/GM091

Lupton, J. E. (1996). A far-field hydrothermal plume from Loihi Seamount. Science 272, 976–979 doi:10.1126/science.272.5264.976.

Lupton, J. (1998). Hydrothermal helium plumes in the Pacific Ocean. Journal of Geophysical Research 103, 15853–15868 doi:10.1029/98JC00146.

Lupton, J. E., and Craig, H. (1981). A major helium-3 source at 15°S on the East Pacific Rise. Science 214, 13–18 doi:10.1126/science.214.4516.13.

Lupton, J. E., Delaney, J. R., Johnson, H. P., and Tivey, M. K. (1985). Entrainment and vertical transport of deep-ocean water by buoyant hydrothermal plumes. Nature 316, 621–623 doi:10.1038/316621a0.

Lupton, J., de Ronde, C., Sprovieri, M., Baker, E. T., Bruno, P. P., Italiano, F., Walker, S., Faure, K., Leybourne, M., Britten, K., and Greene, R. (2011). Active hydrothermal discharge on the submarine Aeolian Arc. Journal of Geophysical Research 116, B02102 10.1029/2010JB007738.

Mackey, D. J., O'Sullivan, J. E., and Watson, R. J. (2002). Iron in the western Pacific: a riverine or hydrothermal source for iron in the Equatorial Undercurrent? Deep-Sea Research – I. Oceanographic Research Papers 49, 877–893 doi:10.1016/S0967-0637(01)00075-9.

Marshall, J., and Speer, K. (2012). Closure of the meridional overturning circulation through Southern Ocean upwelling. Nature Geoscience 5, 171–180 doi:10.1038/ngeo1391.

Martin, J. (1990). Glacial-interglacial CO_2 change: the iron hypothesis. Paleoceanography 5, 1–13. doi:10.1029/PA005i001p00001

Martin, J. H., Knauer, G. A., and Broenkow, W. W. (1985). VERTEX: the lateral transport of manganese in the northeast Pacific. Deep-Sea Research – A. Oceanographic Research Papers 32, 1405–1427 doi:10.1016/0198-0149(85)90056-1.

Martin, J. H., Gordon, R. M., and Fitzwater, S. E. (1990). Iron in Antarctic waters. Nature 345, 156–158 doi:10.1038/345156a0.

Massoth, G. J., Baker, E. T., Lupton, J. E., Feely, R. A., Butterfield, D. A., Von Damm, K. L., Roe, K. K., Lebon, G. T., Massoth, J., Baker, T., Lupton, E., Feely, A., Von Damm, L., and Lebon, T. (1994). Temporal and spatial variability of hydrothermal manganese and iron at Cleft segment, Juan de Fuca Ridge. Journal of Geophysical Research 99, 4905–4923 doi:10.1029/93JB02799.

Massoth, G. J., De Ronde, C. E. J., Lupton, J. E., Feely, R. A., Baker, E. T., Lebon, G. T., and Maenner, S. M. (2003). Chemically rich and diverse submarine hydrothermal plumes of the southern Kermadec volcanic arc (New Zealand). Geological Society of London, Special Publications 219, 119–139 doi:10.1144/GSL.SP.2003.219.01.06.

Massoth, G., Baker, E., Worthington, T., Lupton, J., de Ronde, C., Arculus, R., Walker, S., Nakamura, K., Ishibashi, J., Stoffers, P., Resing, J., Greene, R., and Lebon, G. (2007).

Multiple hydrothermal sources along the south Tonga arc and Valu Fa Ridge. Geochemistry, Geophysics, Geosystems 8, Q11008. doi:10.1029/2007GC001675

Mercier, H., and Speer, K. G. (1998). Transport of bottom water in the Romanche Fracture Zone and the Chain Fracture Zone. Journal of Physical Oceanography 28, 779–790 doi:10.1175/1520-0485(1998)028<0779:TOBWIT>2.0.CO;2.

Middag, R., de Baar, H. J. W., Laan, P., Cai, P. H., and van Ooijen, J. C. (2011). Dissolved manganese in the Atlantic sector of the Southern Ocean. Deep-Sea Research – II. Topical Studies in Oceanography 58, 2661–2677 doi:10.1016/j.dsr2.2010.10.043.

Mitarai, S., Watanabe, H., Nakajima, Y., Shchepetkin, A. F., and McWilliams, J. C. (2016). Quantifying dispersal from hydrothermal vent fields in the western Pacific Ocean. Proceedings of the National Academy of Sciences of the United States of America 113, 2976–2981 doi:10.1073/pnas.1518395113.

Moore, J. K., and Braucher, O. (2008). Sedimentary and mineral dust sources of dissolved iron to the world ocean. Biogeosciences 5, 631–656. doi:10.5194/bg-5-631-2008

Moore, J. K., Doney, S. C., Glover, D. M., and Fung, I. Y. (2001). Iron cycling and nutrient-limitation patterns in surface waters of the world ocean. Deep-Sea Research – II. Topical Studies in Oceanography 49, 463–507 doi:10.1016/S0967-0645(01)00109-6.

Moore, C. M., Mills, M. M., Achterberg, E. P., Geider, R. J., LaRoche, J., Lucas, M. I., McDonagh, E. L., Pan, X., Poulton, A. J., Rijkenberg, M. J. a., Suggett, D. J., Ussher, S. J., and Woodward, E. M. S. (2009). Large-scale distribution of Atlantic nitrogen fixation controlled by iron availability. Nature Geoscience 2, 867–871 doi:10.1038/ngeo667.

Morgan, J. L. L., Wasylenki, L. E., Nuester, J., and Anbar, A. D. (2010). Fe isotope fractionation during equilibration of Fe–organic complexes. Environmental Science & Technology 44, 6095–6101 doi:10.1021/es100906z.

Mottl, M. J., and McConachy, T. F. (1990). Chemical processes in buoyant hydrothermal plumes on the East Pacific Rise near 21°N. Geochimica et Cosmochimica Acta 54, 1911–1927 doi:10.1016/0016-7037(90)90261-I.

Mullaugh, K. M., and Luther, G. W. (2011). Growth kinetics and long-term stability of CdS nanoparticles in aqueous solution under ambient conditions. Journal of Nanoparticle Research 13, 393–404 doi:10.1007/s11051-010-0045-9.

Nishioka, J., Obata, H., and Tsumune, D. (2013). Evidence of an extensive spread of hydrothermal dissolved iron in the Indian Ocean. Earth and Planetary Science Letters 361, 26–33 doi:10.1016/j.epsl.2012.11.040.

Okamura, K., Kimoto, H., Saeki, K., Ishibashi, J., Obata, H., Maruo, M., Gamo, T., Nakayama, E., and Nozaki, Y. (2001). Development of a deep-sea in situ Mn analyzer and its application for hydrothermal plume observation. Marine Chemistry 76, 17–26. doi:10.1016/S0304-4203(01)00043-3

Parekh, P. (2004). Modeling the global ocean iron cycle. Global Biogeochemical Cycles 18, GB1002 doi:10.1029/2003GB002061.

Pester, N. J., Ding, K., and Seyfried, W. E. (2014). Magmatic eruptions and iron volatility in deep-sea hydrothermal fluids. Geology 42, 255–258 doi:10.1130/G35079.1.

Polzin, K. L., Toole, J. M., Ledwell, J. R., and Schmitt, R. (1997). Spatial variability of turbulent mixing in the spatial variability abyssal ocean. Science 276, 93–96 doi:10.1126/science.276.5309.93.

Poorvin, L., Sander, S. G., Velasquez, I., Ibisanmi, E., LeCleir, G. R., and Wilhelm, S. W. (2011). A comparison of Fe bioavailability and binding of a catecholate siderophore with virus-mediated lysates from the marine bacterium Vibrio alginolyticus PWH3a. Journal of Experimental Marine Biology and Ecology 399, 43–47 doi:10.1016/j.jembe.2011.01.016.

Ramsay, D. C. D., Colwell, J. B. J., Coffin, M. F., Davies, H. L., Hill, P. J., Pigram, C. J., and Stagg, H. M. J. (1986). New findings from the Kerguelen Plateau. Geology 14, 589–593. doi:10.1130/0091-7613(1986)14<589:NFFTKP>2.0.CO;2

Ray, D., Kamesh Raju, K. a., Baker, E. T., Srinivas Rao, A., Mudholkar, A. V., Lupton, J. E., Surya Prakash, L., Gawas, R. B., and Vijaya Kumar, T. (2012). Hydrothermal plumes over the Carlsberg Ridge, Indian Ocean. Geochemistry Geophysics Geosystems 13, Q01009 doi:10.1029/2011GC003888.

Reid, J. L. (1982). Evidence of an effect of heat flux from the East Pacific Rise upon the characteristics of the mid-depth waters. Geophysical Research Letters 9, 381–384 doi:10.1029/GL009i004p00381.

Resing, J. a., Sedwick, P. N., German, C. R., Jenkins, W. J., Moffett, J. W., Sohst, B. M., and Tagliabue, A. (2015). Basin-scale transport of hydrothermal dissolved metals across the South Pacific Ocean. Nature 523, 200–203 doi:10.1038/nature14577.

Richardson, P. L. (2008). On the history of meridional overturning circulation schematic diagrams. Progress in Oceanography 76, 466–486 doi:10.1016/j.pocean.2008.01.005.

Rona, P. A., Devey, C. W., Dyment, J., and Murton, B. J. (2010). 'Diversity of Hydrothermal Systems on Slow Spreading Ocean Ridges.' Geophysical Monograph Series 188. (American Geophysical Union: Washington, DC, USA.)Rouxel, O., Fouquet, Y., and Ludden, J. N. (2004). Subsurface processes at the lucky strike hydrothermal field, Mid-Atlantic Ridge: evidence from sulfur, selenium, and iron isotopes. Geochimica et Cosmochimica Acta 68, 2295–2311 doi:10.1016/j.gca.2003.11.029.

Rouxel, O., Shanks, W. C., III, Bach, W., and Edwards, K. (2008). Integrated Fe- and S-isotope study of seafloor hydrothermal vents at East Pacific Rise 9–10°N. Chemical Geology 252, 214–227 doi:10.1016/j.chemgeo.2008.03.009.

Rouxel, O., Toner, B. M., Manganini, S. J., and German, C. R. (2016). Geochemistry and iron isotope systematics of hydrothermal plume fall-out at East Pacific Rise 9°50□ N. Chemical Geology 441, 212–234 doi:10.1016/j.chemgeo.2016.08.027.

Rudnicki, M. D., and Elderfield, H. (1993). A chemical model of the buoyant and neutrally buoyant plume above the TAG vent field, 26 degrees N, Mid-Atlantic Ridge. Geochimica et Cosmochimica Acta 57, 2939–2957 doi:10.1016/0016-7037(93)90285-5.

Rudnicki, M. D., and German, C. R. (2002). Temporal variability of the hydrothermal plume above the Kairei vent field, 25°S, Central Indian Ridge. Geochemistry Geophysics Geosystems 3(2), 000–000 doi:10.1029/2001GC000240.

Rue, E. E. L., and Bruland, K. K. W. (1995). Complexation of iron (III) by natural organic ligands in the Central North Pacific as determined by a new competitive ligand equilibration/adsorptive cathodic stripping. Marine Chemistry 50, 117–138. doi:10.1016/0304-4203(95)00031-L

Ruud, J. T. (1930). Nitrates and phosphates in the southern seas. Rapports et Proces Verbaux des Réunions , Conseil International pour l'Exploration de la Mer 5, 347–360 doi:10.1093/icesjms/5.3.347.

Saito, M. A., Noble, A. E., Tagliabue, A., Goepfert, T. J., Lamborg, C. H., and Jenkins, W. J. (2013). Slow-spreading submarine ridges in the South Atlantic as a significant oceanic iron source. Nature Geoscience 6, 775–779 doi:10.1038/ngeo1893.

Sander, S. G., and Koschinsky, A. (2011). Metal flux from hydrothermal vents increased by organic complexation. Nature Geoscience 4, 145–150 doi:10.1038/ngeo1088.

Sander, S. G., and Koschinsky, A. (2016). The export of iron and other trace metals from hydrothermal vents and the impact on their marine biogeochemical cycle. In 'Trace Metal Biogeochemistry and Ecology of Deep-Sea Hydrothermal Vent Systems'. (Eds L. L. Demina

and S. V. Galkin..) pp. 9–24. (Springer International Publishing: Cham, Switzerland..) doi:10.1007/698_2016_4

Sands, C. M., Connelly, D. P., Statham, P. J., and German, C. R. (2012). Size fractionation of trace metals in the Edmond hydrothermal plume, central Indian Ocean. Earth and Planetary Science Letters 319–320, 15–22 doi:10.1016/j.epsl.2011.12.031.

Scheirer, D. S., Baker, E. T., and Johnson, K. T. M. (1998). Detection of hydrothermal plumes along the Southeast Indian Ridge near the Amsterdam–St. Paul Plateau. Geophysical Research Letters 25, 97-100 doi:10.1029/97GL03443.

Schmidt, K., Garbe-Schönberg, D., Koschinsky, A., Strauss, H., Jost, C. L., Klevenz, V., and Königer, P. (2011). Fluid elemental and stable isotope composition of the Nibelungen hydrothermal field (8°18□ S, Mid-Atlantic Ridge): constraints on fluid–rock interaction in heterogeneous lithosphere. Chemical Geology 280, 1–18 doi:10.1016/j.chemgeo.2010.07.008.

Sedwick, P., Sohst, B. M., Ussher, S. J., and Bowie, A. R. (2015). A zonal picture of the water column distribution of dissolved iron(II) during the US GEOTRACES North Atlantic transect cruise (GEOTRACES GA03). Deep-Sea Research – II. Topical Studies in Oceanography 116, 166–175 doi:10.1016/j.dsr2.2014.11.004.

Severmann, S., Johnson, C. M., Beard, B. L., German, C. R., Edmonds, H. N., Chiba, H., and Green, D. R. H. (2004). The effect of plume processes on the Fe isotope composition of hydrothermally derived Fe in the deep ocean as inferred from the Rainbow vent site, Mid-Atlantic Ridge, 36°14□ N. Earth and Planetary Science Letters 225, 63–76 doi:10.1016/j.epsl.2004.06.001.

Sharma, M. Y. Y., Polizzotto, M., and Anbar, A. D. D. Y. (2001). Iron isotopes in hot springs along the Juan de Fuca Ridge. Earth and Planetary Science Letters 194, 39–51 doi:10.1016/S0012-821X(01)00538-6.

Shock, E. L. (1992). Chemical Environments of Submarine Hydrothermal Systems. In 'Marine Hydrothermal Systems and the Origin of Life'. (Ed N. G. Holm.) pp. 67–107. (Springer: Dordrecht, Netherlands..) doi: 10.1007/978-94-011-2741-7_5

Shock, E. L., and Schulte, M. D. (1998). Organic synthesis during fluid mixing in hydrothermal systems. Journal of Geophysical Research 103, 28513–28527 doi:10.1029/98JE02142.

Speer, K. G. (1989). The Stommel and Arons model and geothermal heating in the South Pacific. Earth and Planetary Science Letters 95, 359–366 doi:10.1016/0012-821X(89)90110-6.

Speer, K. G., and Rona, P. a. (1989). A model of an Atlantic and Pacific hydrothermal plume. Journal of Geophysical Research 94, 6213 –6220 doi:10.1029/JC094iC05p06213.

Speer, K. G., Maltrud, M., and Thurberr, A. (2003). A global view of dispersion above the mid-ocean ridge. In 'Energy and mass transfer in marine hydrothermal systems'. (Eds P. E. Halbach, V. Tunnicliffe, and J. R. Hein.) pp. 287–302. (Dahlem University Press: Berlin, Germany.).)

Speer, K., Rintoul, S. R., and Sloyan, B. (2000). The Diabatic Deacon Cell*. Journal of Physical Oceanography 30, 3212–3222. doi:10.1175/1520-0485(2000)030<3212:TDDC>2.0.CO;2

St Laurent, L. C., and Thurnherr, A. M. (2007). Intense mixing of lower thermocline water on the crest of the Mid-Atlantic Ridge. Nature 448, 680–683 doi:10.1038/nature06043.

Stommel, H. (1982). Is the South Pacific helium-3 plume dynamically active? Earth and Planetary Science Letters 61, 63–67. doi:10.1016/0012-821X(82)90038-3

Stranne, C., Sohn, R. a., Liljebladh, B., and Nakamura, K. I. (2010). Analysis and modeling of hydrothermal plume data acquired from the 85°E segment of the Gakkel Ridge. Journal of Geophysical Research – Oceans 115, 1–17 10.1029/2009JC005776.

Tagliabue, A., and Resing, J. (2016). Impact of hydrothermalism on the ocean iron cycle. Philosophical Transactions of the Royal Society of London – A. Mathematical, Physical and Engineering Sciences 374, doi:10.1098/rsta.2015.0291.

Tagliabue, A., Bopp, L., and Aumont, O. (2009). Evaluating the importance of atmospheric and sedimentary iron sources to Southern Ocean biogeochemistry. Geophysical Research Letters 36, L13601 doi:10.1029/2009GL038914.

Tagliabue, A., Bopp, L., Dutay, J.-C., Bowie, A. R., Chever, F., Jean-Baptiste, P., Bucciarelli, E., Lannuzel, D., Remenyi, T., Sarthou, G., Aumont, O., Gehlen, M., and Jeandel, C. (2010). Hydrothermal contribution to the oceanic dissolved iron inventory. Nature Geoscience 3, 252–256 doi:10.1038/ngeo818.

Tagliabue, A., Mtshali, T., Aumont, O., Bowie, R., Klunder, M. B., Roychoudhury, N., and Swart, S. (2012). A global compilation of dissolved iron measurements: focus on distributions and processes in the Southern Ocean. Biogeosciences 9, 2333–2349 doi:10.5194/bg-9-2333-2012.

Tagliabue, A., Aumont, O., and Bopp, L. (2014a). The impact of different external sources of iron on the global carbon cycle. Geophysical Research Letters 41, doi:10.1002/2013GL059059.

Tagliabue, A., Sallée, J.-B., Bowie, A. R., Lévy, M., Swart, S., and Boyd, P. W. (2014b). Surface-water iron supplies in the Southern Ocean sustained by deep winter mixing. Nature Geoscience 7, 314–320 doi:10.1038/ngeo2101.

Tagliabue, A., Williams, R. G., Rogan, N., Achterberg, E. P., and Boyd, P. W. (2014c). A ventilation-based framework to explain the regeneration–scavenging balance of iron in the ocean. Geophysical Research Letters 41, 7227–7236 doi:10.1002/2014GL061066.

Tagliabue, A., Bowie, A. R., Boyd, P. W., Buck, K. N., Johnson, K. S., and Saito, M. A. (2017). The integral role of iron in ocean biogeochemistry. Nature 543, 51–59 doi:10.1038/nature21058.

Tian, F., Frew, R. D., Sander, S., Hunter, K. A., and Ellwood, M. J. (2006). Organic iron(III) speciation in surface transects across a frontal zone: the Chatham Rise, New Zealand. Marine and Freshwater Research 57, 533. doi:10.1071/MF05209

Toner, B. M., Fakra, S. C., Manganini, S. J., Santelli, C. M., Marcus, M. a., Moffett, J. W., Rouxel, O., German, C. R., and Edwards, K. J. (2009). Preservation of iron(II) by carbon-rich matrices in a hydrothermal plume. Nature Geoscience 2, 197–201 doi:10.1038/ngeo433.

Toner, B., Marcus, M., Edwards, K., Rouxel, O., and German, C. (2012). Measuring the form of iron in hydrothermal plume particles. Oceanography 25, 209–212 doi:10.5670/oceanog.2012.19.

Trull, T., Rintoul, S. R., Hadfield, M., and Abraham, E. R. (2001). Circulation and seasonal evolution of polar waters south of Australia: implications for iron fertilization of the Southern Ocean. Deep Sea Research Part II: Topical Studies in Oceanography 48, 2439–2466. doi:10.1016/S0967-0645(01)00003-0

Tyler, P. A. (2011). RRS James Cook Cruise JC55, 13 Jan–22 Feb 2011. Bransfield Strait, the East Scotia Ridge and the Kemp Seamount Calderas, Cruise 3 of the NERC Consortium Grant 'Chemosynthetically-driven ecosystems in the Southern Ocean: Ecology and Biogeography'(ChEsSo). National Oceanography Centre Cruise Report 05, 74, National Oceanography Centre, Southampton, UK.

Völker, C., and Tagliabue, A. (2015). Modeling organic iron-binding ligands in a three-dimensional biogeochemical ocean model. Marine Chemistry 173, 67–77 doi:10.1016/j.marchem.2014.11.008.

Von Damm, K. (1990). Seafloor hydrothermal activity: black smoker chemistry and chimneys. Annual Review of Earth and Planetary Sciences 18, 173–204 doi:10.1146/annurev.ea.18.050190.001133.

Von Damm, K. L. (1995). Controls on the chemistry and temporal variability of seafloor hyrdrothermal fluids. In 'Seafloor Hydrothermal Systems: Physical, Chemical, Biological, and Geological Interactions'. (Eds S. E. Humphris, R. A. Zierenberg, L. S. Mullineaux, and R. E. Thomson.) Geophysical Monograph Series, pp. 222–247. (American Geophysical Union: Washington, DC, USA.) doi:10.1029/GM091

Von Damm, K. L., and Bischoff, J. L. (1987). Chemistry of hydrothermal solutions from the southern Juan de Fuca Ridge. Journal of Geophysical Research 92, 11334 doi:10.1029/JB092iB11p11334.

Von Damm, K., and Lilley, M. (2004). Diffuse flow hydrothermal fluids from 9°50' N East Pacific Rise: Origin, evolution and biogeochemical controls. In 'The Subseafloor Biosphere at Mid-Ocean Ridges'. (Eds W. S. D. Wilcock, E. F. DeLong, D. S. Kelley, J. A. Baross, and S. Craig Cary.) pp. 245–268. (American Geophysical Union: Washington, DC, USA.) doi:10.1029/GM144

von Langen, P. J., Johnson, K. S., Coale, K. H., and Elrod, V. A. (1997). Oxidation kinetics of manganese(II) in seawater at nanomolar concentrations. Geochimica et Cosmochimica Acta 61, 4945–4954 doi:10.1016/S0016-7037(97)00355-4.

Weber, L., Völker, C., Schartau, M., and Wolf-Gladrow, D. a. (2005). Modeling the speciation and biogeochemistry of iron at the Bermuda Atlantic time-series study site. Global Biogeochemical Cycles 19, 1–23 doi:10.1029/2004GB002340.

Weis, D., Frey, F. a., Schlich, R., Schaming, M., Montigny, R., Damasceno, D., Mattielli, N., Nicolaysen, K. E., and Scoates, J. S. (2002). Trace of the Kerguelen mantle plume: evidence from seamounts between the Kerguelen Archipelago and Heard Island, Indian Ocean. Geochemistry Geophysics Geosystems 3, 1–27 doi:10.1029/2001GC000251.

Welhan, J. A. (1988). Origins of methane in hydrothermal systems. Chemical Geology 71, 183–198 doi:10.1016/0009-2541(88)90114-3.

Wells, M., Vallis, G., and Silver, E. (1999). Tectonic processes in Papua New Guinea and past productivity in the eastern equatorial Pacific Ocean. Nature 398, 601–604. doi:10.1038/19281

Wu, J., Wells, M. L., and Rember, R. (2011). Dissolved iron anomaly in the deep tropical–subtropical Pacific: evidence for long-range transport of hydrothermal iron. Geochimica et Cosmochimica Acta 75, 460–468 doi:10.1016/j.gca.2010.10.024.

Yücel, M., Gartman, A., Chan, C. S., and Luther, G. W. (2011). Hydrothermal vents as a kinetically stable source of iron-sulphide-bearing nanoparticles to the ocean. Nature Geoscience 4, 367–371 doi:10.1038/ngeo1148.

Chapter 3

3 Methodology

The following chapters consider data generated from samples collected during the Heard Earth-Ocean-Biosphere Interactions (HEOBI) voyage on the Australian Marine National Facility research vessel *Investigator* to the remote Heard and McDonald Islands region of the Southern Ocean (January 8th to February 27th 2016). Avoiding contamination of samples that contain minute concentrations of Fe, while on-board a ship made almost entirely of Fe-containing metals and producing exhaust fumes extremely high in labile Fe, poses many challenges to trace metal scientists and is part of the reason why this field of research is so difficult and relatively young. This chapter presents methodology for the sampling and analysis of Fe in collected seawater samples, both on-board and in the laboratory.

3.1 Locating sampling stations

The HEOBI voyage was in large part an exploratory voyage, with a major focus to locate hydrothermal activity – a proposed source of Fe to the region. For this reason, the majority of sampling stations (21 of 36 trace metal stations) were located based on potential signs of hydrothermal activity. The tracers used to identify hydrothermal activity were bathymetric features, plumes of bubbles emanating from the seafloor, and on-board analysis of dissolved Fe (DFe) and dissolved Fe(II) (DFe(II); explained in further detail below). Two reference sites were sampled to the west and south of Heard Island (Figure 3.1). Station 11, ~80 km to the west of McDonald Islands, was expected to be located in HNLC waters, but observed shipboard underway fluorescence and chlorophyll biomass was relatively high (up to 2.1 mg m^{-3} Chl*a* in upper 200 m; Wojtasiewicz et al., in prep.). Station 18, ~100 km to the south of Heard Island, was located in waters more representative of HNLC conditions (max 0.81 mg m^{-3} Chl*a* in upper

200 m; Wojtasiewicz et al., in prep.). The remainder of the sampling stations were located on two northeast-southwest transects, which repeated transects 'B' and 'C' of the previous Kerguelen Ocean and Plateau Compared Study voyage (KEOPS-1, 2005), allowing for comparison of off-plateau and on-plateau conditions, and over time.

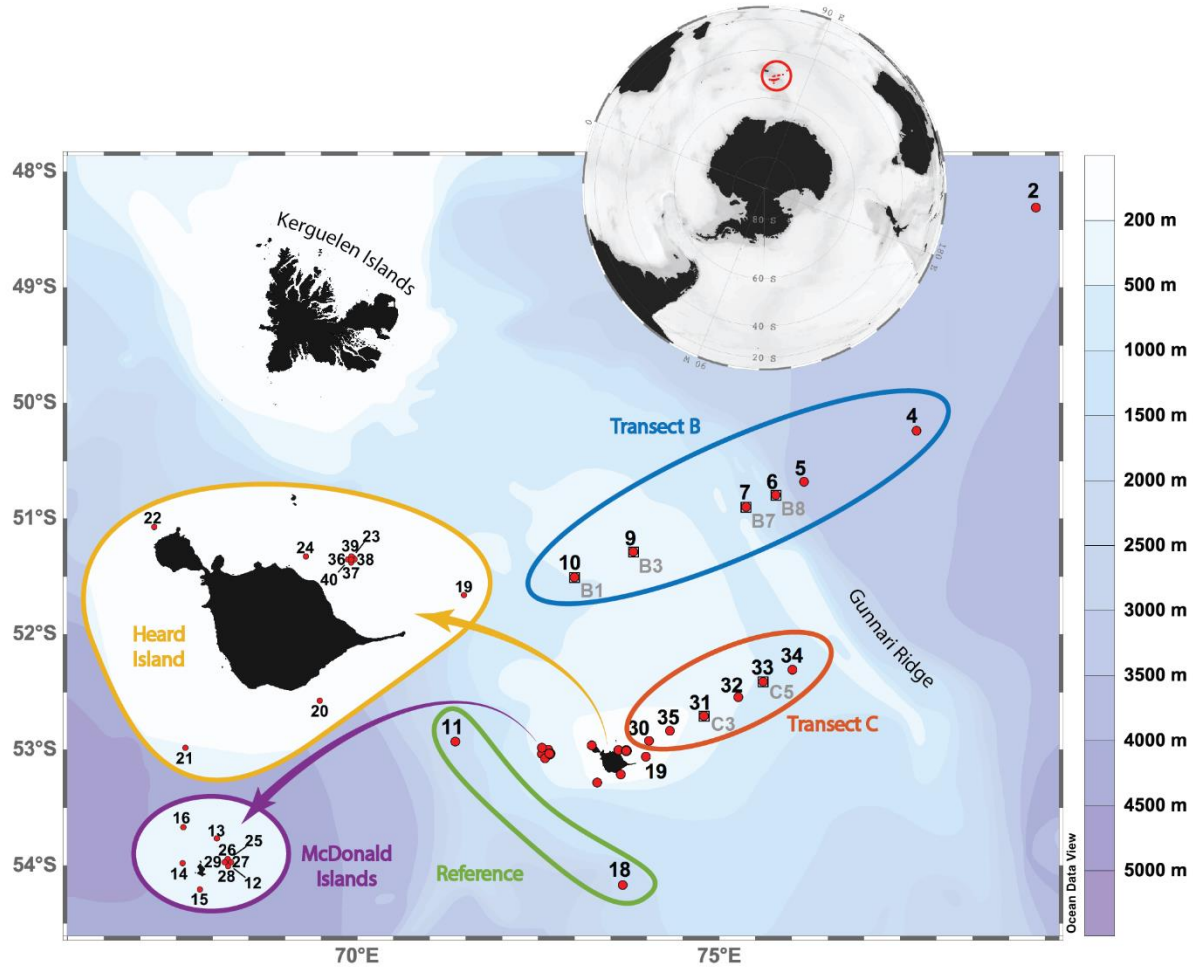

Figure 3.1 Sampling area with station locations. Heard and McDonald Islands are shown zoomed in inset. Transect B (blue) follows Kerguelen Ocean and Plateau Compared Study (KEOPS-1) transect B. Transect C (orange) follows the first 150 km of KEOPS-1 transect C. Heard Island (yellow) and McDonald Islands (purple) station locations were selected based on bathymetric features (Watson et al., 2016) and acoustic flares detected by shipboard echosounder (Spain et al., 2018). Reference stations (green) were located to the west and south of HIMI. Station 11 had higher than expected Fe and chl-a concentrations, but station 18 was located in HNLC waters.

The HIMI region of the Kerguelen Plateau is characterised by numerous sea knolls (Beaman and O'Brien, 2011), interpreted as volcanic edifices, and previously unmapped knolls were discovered near both Heard and McDonald Islands (Figure 3.2; Coffin, 2016). The water column around

HIMI was very well mixed due to shallow bathymetry, strong wind-mixing events that reached to the sea floor, and tidal currents. As such, initial approaches used in the search for hydrothermalism were seafloor bathymetric mapping and marking acoustic 'flares' acquired by an on-board multi-frequency echosounder.

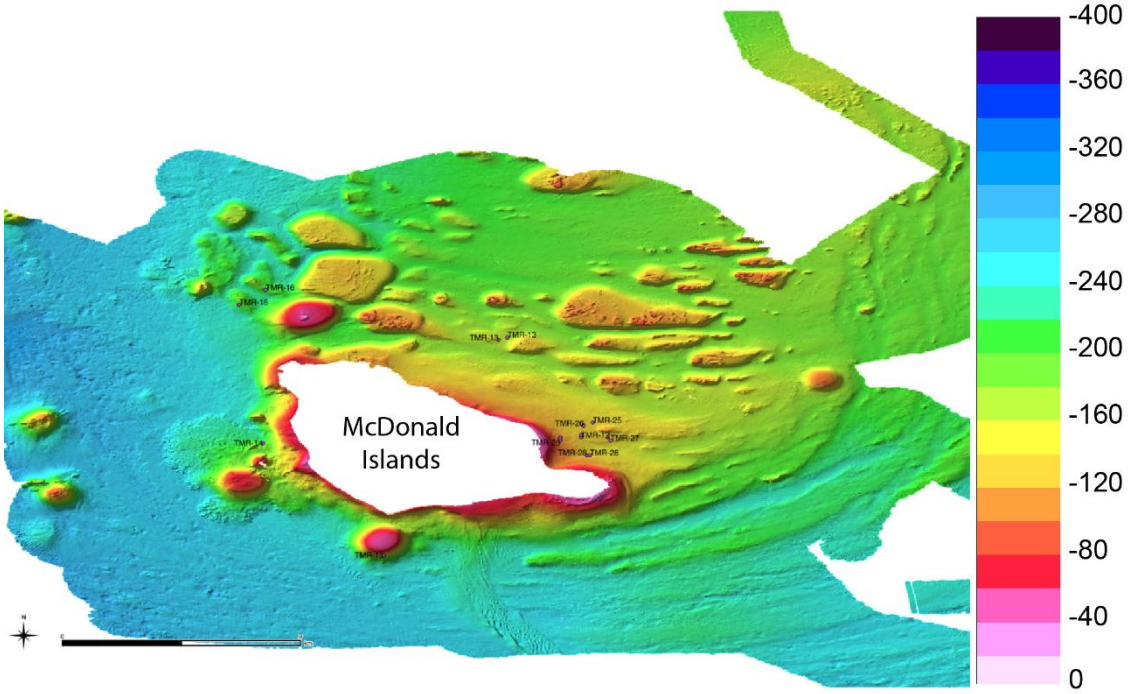

Figure 3.2. Sea knolls surrounding McDonald Islands, mapped using high resolution ship-board multi-beam sonar. Image courtesy of S. Watson, E. Spain and Marine National Facility, CSIRO.

Over 200 Acoustic anomalies, or 'flares', emanating from the seafloor were detected around HIMI, indicative of bubbles rising from the seafloor (Figure 3.3; Spain et al., 2018). Bubbles were confirmed to be emanating from the seafloor at several sites through direct observation by deep tow camera (Spain et al., 2018). Once sampling sites were located, a trace metal rosette was deployed and samples taken for DFe and DFe(II) were analysed in near real-time on-board as another potential tracer for hydrothermalism. Based on the results of these on-board analyses, one site at McDonald Islands (station TMR 12) and one site at Heard Island (station TMR 23) were revisited for further sampling. At each of these sites five further stations were sampled in a 'crosshair' pattern in an attempt to delineate the source of the elevated DFe and DFe(II) signals.

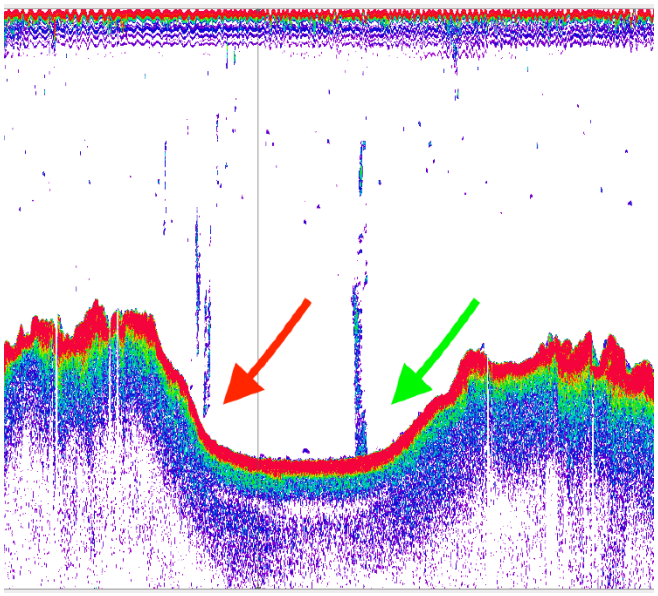

Figure 3.3. Example of acoustic anomalies ('flares') emanating from the seafloor during HEOBI, detected by ship-board multi-frequency echosounder. Image courtesy of E. Spain and the Marine National Facility, CSIRO.

3.2 Sampling

Once potential sites had been identified, samples were collected following protocols which have been developed over the last 30 years of trace metal research, designed to minimise the risk of contamination (Cutter et al., 2014). At each of the stations a standard conductivity-temperature-depth (CTD) rosette was initially deployed. Trace metal sample depths were chosen based on water masses identified using profiles collected by the CTD-mounted sensor package. In the absence of well-defined water masses, such as in well mixed waters near HIMI, sample depths were spaced across the water column with greater sample density near the surface and bottom of the profile, as these depths generally show the steepest gradients in trace metal concentrations.

Water for trace metal samples was collected using twelve, 12 L, Teflon-coated, Niskin-X bottles with external Teflon-coated spring closing mechanisms, specifically designed and modified for trace metal sampling. The Niskin-X bottles were mounted on a polyurethane powder-coated aluminium rosette frame (TMR, Sea-Bird Scientific) with programmable autonomous firing mechanism, also designed specifically for trace metal sampling (Figure 3.4). The TMR was

deployed using a Dyneema (polyethylene) line to minimise chance of contamination in the water column. The chosen depths were pre-programmed on the TMR, based on water column CTD profiles measured on the traditional CTD rosette. Once retrieved back on deck, Niskin bottles were transported as quickly as possible into a containerised trace metal clean laboratory, also located on the working deck, to minimise likelihood of contamination through airborne particulates.

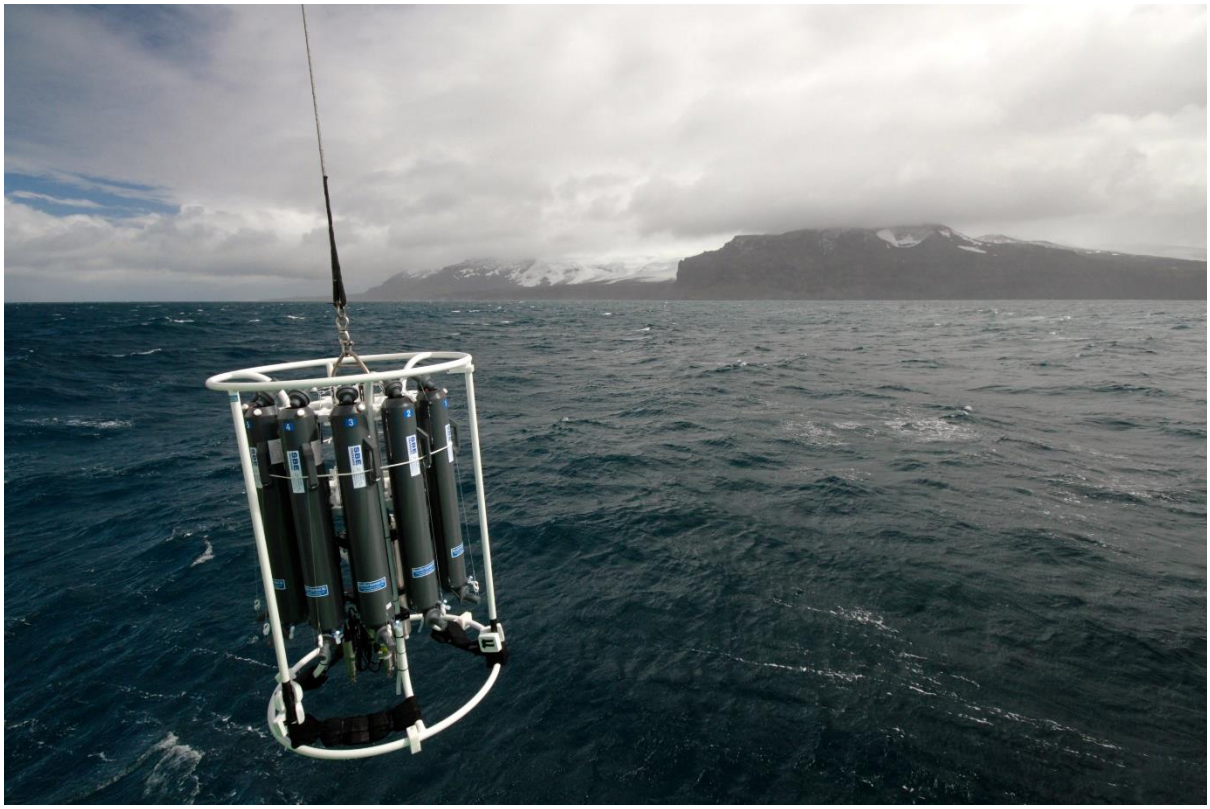

Figure 3.4. Deploying the trace metal clean rosette (TMR), with Heard Island seen in the background. Photo courtesy of Pete Harmsen.

The trace metal clean containerised laboratory is a modified shipping container, in which all surfaces are either plastic or sealed so that no metal is exposed. The container is under positive pressure supplied from an air conditioner via ISO 5 HEPA filters. The positive pressure inside the clean lab also minimises incoming unfiltered air when entering the container. There is an ante-room at the entrance of the container with plastic flaps to minimise incoming outside air and has a space to change into clean room attire: plastic Tyvek over suits and foam laboratory

shoes (Crocs; Figure 3.5). All equipment and sample handling was conducted wearing ultraclean nitrile gloves (cleanroom, Ansell). Niskin bottles were mounted in the trace metal clean container directly under the filtered air source during subsampling.

Subsamples were taken for DFe, DFe(II) and hydrogen peroxide (H_2O_2), which were analysed on-board using flow injection analysis chemiluminescence techniques (FIA-CL). Samples were collected in acid cleaned, low-density polyethylene (LDPE; DFe) or high-density polyethylene (HDPE; DFe(II) and H_2O_2), double bagged and transported to a second trace metal clean analysis container directly after sampling. Separate subsamples were also taken for a suite of trace metals, including DFe, for later land-based SeaFAST-ICP-MS analysis (Wuttig et al., 2019). The second trace metal clean container was a modified shipping container, similar to that already described. Within this container separate FIA-CL systems were set up for DFe, DFe(II) and H_2O_2 analysis. The DFe FIA-CL system, as the instrument most prone to possible contamination, was located directly under the ISO 5 HEPA filtered air source and partitioned off with plastic sheets to minimise risk of sample or reagent contamination by airborne particles.

3.3 Analysis

3.3.1 On-board FIA systems

The basic principle for each of the FIA-CL systems is the catalytic oxidation of luminol (5-Amino-2,3-dihydrophthalazine-1,4-dione) by the analyte under consideration (i.e. DFe, DFe(II) or H_2O_2). This reaction causes chemiluminescence, which is detected by a photomultiplier tube. The reaction is pH sensitive and maximum sensitivity is reached at slightly different pH for each of the three methods. The reagents used in each method buffer the solution, ensuring the correct pH range. DFe and DFe(II) systems both included solid phase extraction columns (8-hydroxyquinoline, hereafter 8HQ) to concentrate the analyte. Analyte adsorption to these

Figure 3.5. A/Prof. Zanna Chase and Manon Tonnard subsampling from the Niskin bottles in the trace metal clean container. Photo courtesy of Pete Harmsen.

columns is also pH sensitive, and so require buffering to the desired pH before preconcentration, followed by elution with HCl and then final reaction of analyte with luminol. Reagents and samples are pumped by peristaltic pumps through acid-cleaned Teflon tubing, while actuated solenoid valves are used to divert sample through preconcentration columns and inject sample into the flow stream.

DFe samples were analysed using an FIA-CL method adapted from de Jong et al., (1998) and Obata et al., (1993). This method relies on the preconcentration of DFe onto 8HQ immobilised on a vinyl copolymer resin and packed into a column, followed by elution off the column with 0.3 M distilled HCl (made from SeaStar Chemicals, Instrument Quality and tested for purity by ICP-MS prior to the voyage). The sample was buffered in-line to pH 3.5 – 4.0 with 0.2 M acetic acid/ammonia buffer (both SeaStar Chemicals, Baseline) for optimal column extraction efficiency. Eluted DFe was then injected into the flow stream, consisting of 0.2 mM luminol

(Sigma-Aldrich, HPLC grade), 0.5 M ammonia (SeaStar Chemicals, Baseline) and 0.1 M H_2O_2 (SeaStar Chemicals, Baseline), giving an optimal reaction pH of 9.3 – 9.5. The oxidation of luminol by DFe is catalysed by H_2O_2. This reaction is highly temperature sensitive, so the laboratory was tightly temperature controlled at ~25°C and reaction line was placed in a water bath at ~30°C, before reaching the detector (Figure 3.6).

Results were verified through regular analysis of characterised in-house seawater standards as well as periodic analysis of SAFe intercalibration standards. Mean DFe concentrations for SAFe seawater reference material 'S' were found to be 0.12 ± 0.04 nM (n = 8). These values lie within one standard deviation of the community consensus concentration of 0.095 ± 0.008 nM for SAFe 'S' (GEOTRACES, 2016). Blanks were obtained through analysis of characterised in-house low Fe seawater, acidified with HCl (Seastar Chemicals, Baseline). The detection limit of the DFe FIA-CL instrument was defined as the analyte concentration equivalent to three times the standard deviation of the blank peak (n=3; Bowie et al., 2004). During the HEOBI cruise the limit of detection was calculated each day and ranged from 0.02 to 0.20 nM with a mean of 0.09 nM (n = 20).

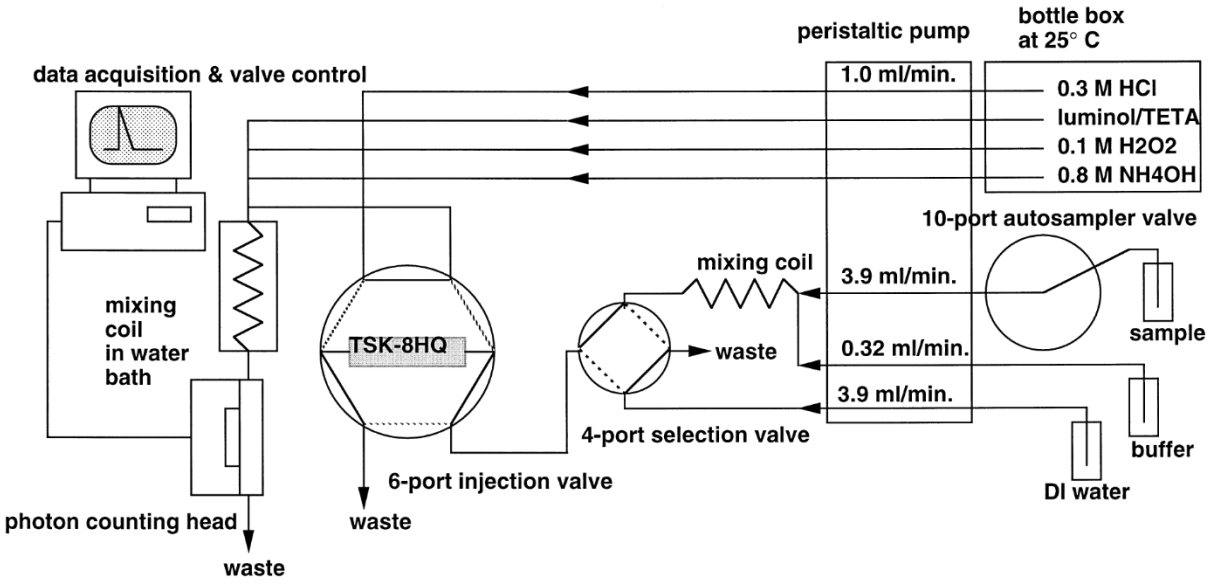

Figure 3.6. Schematic of the DFe FIA-CL system. Taken from de Jong et al., (1998).

Dissolved Fe(II) samples were analysed using an FIA-CL method adapted from the method of Bowie et al., (2005, 2002) and recently described by Sedwick et al., (2015). This method relies on the preconcentration of DFe(II) onto an 8HQ resin column, followed by elution with 0.06 M HCl (made from SeaStar Chemicals, Instrument Quality and tested for purity by ICP-MS prior to the voyage) before reaction with luminol (0.01 M, Sigma-Aldrich, HPLC grade). The sample is buffered in-line to pH 5.5 with a 0.4 M acetic acid/ammonia buffer (both SeaStar Chemicals, Baseline) for optimal column extraction efficiency. Iron(II) is then carried from the holding loop with 0.06 M HCl (made from SeaStar Chemicals, Instrument Quality and tested for purity by ICP-MS prior to the voyage) into the light-proof detector box where reaction with luminol takes place directly in front of the detector window at pH 10.2 (Figure 3.7).

The blank solution used for the DFe(II) FIA analysis consisted of low Fe seawater collected during the cruise, aged so that any Fe(II) in the solution had oxidised. Triplicate blank measurements were taken both before and after each analysis run. Analysis times were recorded for each sample. In instances where instrument signal drift was noted between the initial and final blank measurements, a blank value was calculated for each sample via linear interpolation.

The detection limit of the DFe(II) FIA-CL instrument was defined as the analyte concentration equivalent to three times the standard deviation of the blank peak (n=3) (Bowie et al., 2004). During the HEOBI voyage the detection limit was calculated each day and ranged from 0.02 to 0.16 nmol L^{-1} with a mean of 0.06 nmol L^{-1} (n = 17).

H_2O_2 samples were analysed using an FIA-CL method adapted from the method of Yuan and Shiller (1999). This method utilises cobalt to catalyse the oxidation of luminol by H_2O_2. This method requires no preconcentration, with sample being injected directly into a flow stream of mixed reagent for reaction with luminol at pH 10.15 (Figure 3.8). The mixed reagent solution consists of 0.576 g luminol (Sigma-Aldrich, HPLC grade) in 1000 mL of 0.1 M sodium carbonate

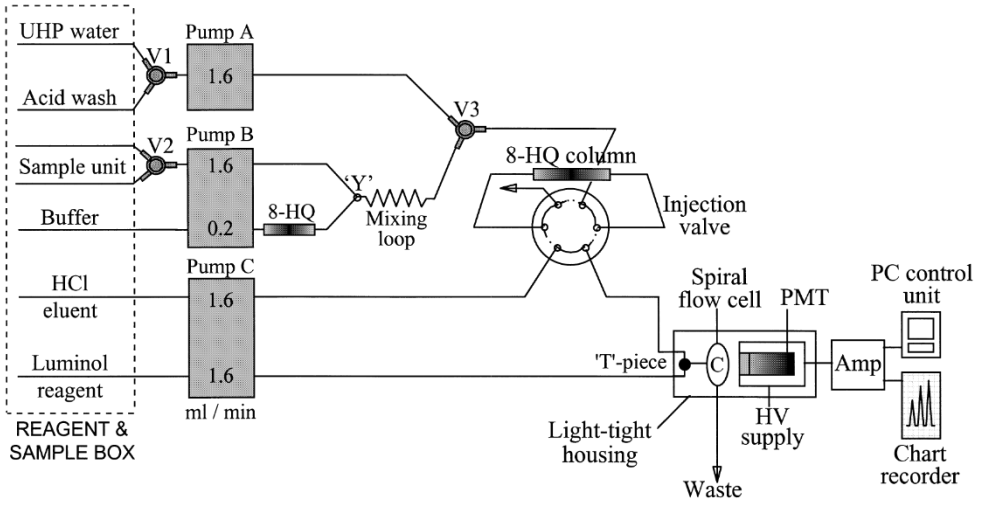

Figure 3.7. Schematic of the DFe(II) FIA-CL system. Taken from (Bowie et al., 1998).

solution (Merck, Suprapur). The pH is adjusted with 2 M HCl (made from SeaStar Chemicals, Instrument Quality and tested for purity by ICP-MS prior to the voyage) and spiked with Cobalt(II) (Sigma-Aldrich, AAS standard) to 60 μM. Each seawater sample was analysed at least four times with a typical precision of 3 – 5% through the concentration range 0.5 – 75 nmol L^{-1} and a typical detection limit (3σ) of 0.6 nmol L^{-1}.

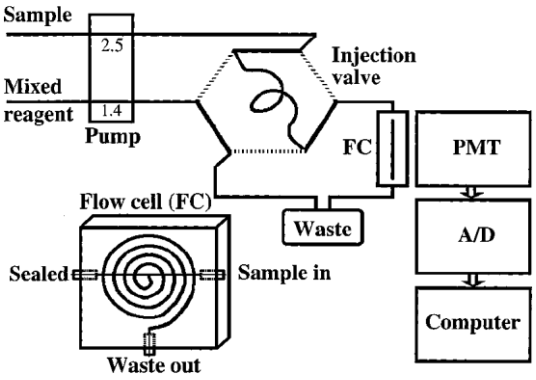

Figure 3.8. Schematic of the H_2O_2 FIA-CL system. Taken from Yuan and Shiller, (1999).

3.3.2 Laboratory based analysis

DFe samples were also analysed on-shore using a Sector Field Inductively Coupled Plasma Mass Spectrometer (SF-ICP-MS; Element 2 Thermo Fisher Scientific, Inc.) at the Central Science Laboratory (CSL), University of Tasmania. This instrument provides enhanced sensitivity with increased spectral resolution allowing elements of low atomic mass to be analysed interference

free (Townsend, 2000). Prior to analysis, samples were preconcentrated using a SeaFAST S2 pico (ESI, Elemental Scientific, USA) automated flow injection system with a Nobias Chelate-PA1 column. A detailed methodology and comparison between the SeaFAST-ICP-MS dataset and the FIA dataset is presented in Wuttig et al., (2019).

Data were blank-corrected by subtracting an average of at least three acidified ultra-high purity water (UHP) blanks that were treated in the same manner as the seawater samples. The DFe detection limit was calculated as 3x the standard deviation of the acidified UHP blank. Daily detection limits ranged from 0.006 to 0.062 nmol kg^{-1}, with a median of 0.022 nmol kg^{-1} (n=11). SAFe 'D1' and 'S', and GEOTRACES 'GD' community consensus samples were analysed in parallel with field samples and measured at 0.68 ± 0.04, 0.083 ± 0.020 and 1.02 ± 0.01 nmol kg^{-1} (n = 9, 5 and 6) respectively, in good agreement with consensus values (0.67 ± 0.04, 0.093 ± 0.008 and 1.00 ± 0.1).

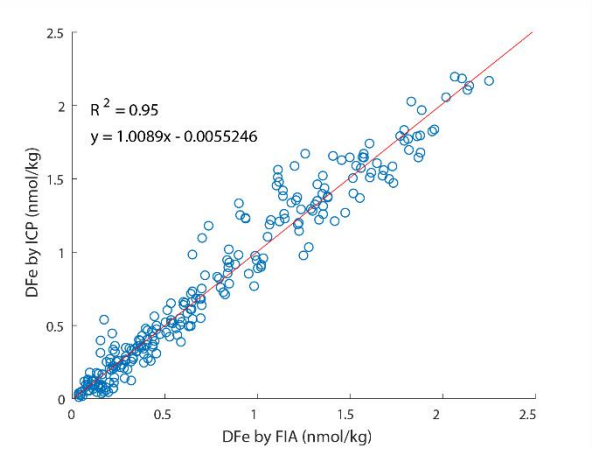

Figure 3.9. DFe analysed by SeaFAST-ICP-MS vs DFe analysed by FIA-CL.

Analyses performed for this thesis utilise the latter (SeaFAST-ICP-MS) dataset, as extensive method testing and validation was conducted in a separate study for this instrument (Wuttig et al., 2019). However, for analytical surety, the two Fe concentration datasets were compared and found to be in very close agreement (R^2 = 0.95, paired *t*-test, p >0.05, *n* = 244), demonstrating

the reliability of the analyses performed, and attesting to the quality of the sample collection and handling procedures undertaken during the voyage (Figure 3.9).

3.4 References

Beaman, R., O'Brien, P., 2011. Kerguelen Plateau Bathymetric Grid, November 2010.

Bowie, A.R., Achterberg, E.P., Mantoura, R.F.C., Worsfold, P.J., 1998. Determination of sub-nanomolar levels of iron in seawater using flow injection with chemiluminescence detection. Anal. Chim. Acta 361, 189–200. doi:10.1016/S0003-2670(98)00015-4

Bowie, A.R., Achterberg, E.P., Sedwick, P.N., Ussher, S., Worsfold, P.J., 2002. Real-Time Monitoring of Picomolar Concentrations of Iron (II) in Marine Waters Using Automated Flow Instrumentation. Environ. Sci. Technol. 36, 4600–4607. doi:10.1021/es020045v

Bowie, A.R., Achterberg, E.P., Ussher, S., Worsfold, P.J., 2005. Design of an automated flow injection-chemiluminescence instrument incorporating a miniature photomultiplier tube for monitoring picomolar concentrations of iron in seawater. J. Autom. Methods Manag. Chem. 2005, 37–43. doi:10.1155/JAMMC.2005.37

Bowie, A.R., Sedwick, P.N., Worsfold, P.J., 2004. Analytical intercomparison between flow injection-chemiluminescence and flow injection-spectrophotometry for the determination of picomolar concentrations of iron in seawater. Limnol. Oceanogr. Methods 2, 42–54. doi:10.4319/lom.2004.2.42

Coffin, M., 2016. HEOBI: Heard Earth-Ocean-Biosphere Interactions voyage summary. Hobart, Australia.

Cutter, G., Andersson, P., Codispoti, L., Croot, P., Francois, R., Lohan, M., Obata, H., Rutgers, M., 2014. Sampling and Sample-handling Protocols for GEOTRACES Cruises.

de Jong, J.T.., den Das, J., Bathmann, U., Stoll, M.H.., Kattner, G., Nolting, R.., de Baar, H.J..,

1998. Dissolved iron at subnanomolar levels in the Southern Ocean as determined by ship-board analysis. Anal. Chim. Acta 377, 113–124. doi:10.1016/S0003-2670(98)00427-9

GEOTRACES, 2016. Standards and Reference Materials [WWW Document]. URL http://www.geotraces.org/science/intercalibration/322-standards-and-reference-materials

Obata, H., Karatani, H., Nakayama, E., 1993. Automated determination of iron in seawater by chelating resin concentration and chemiluminescence detection. Anal. Chem. 65, 1524–1528.

Sedwick, P.., Sohst, B.M., Ussher, S.J., Bowie, A.R., 2015. A zonal picture of the water column distribution of dissolved iron(II) during the U.S. GEOTRACES North Atlantic transect cruise (GEOTRACES GA03). Deep Sea Res. Part II Top. Stud. Oceanogr. 116, 166–175. doi:10.1016/j.dsr2.2014.11.004

Spain, E., Johnson, S., Hutton, B., Whittaker, J., Lucieer, V., Watson, S., Fox, J., Coffin, M.F., 2018. Shallow seafloor gas emissions near Heard and McDonald islands on the Kerguelen Plateau, Southern Indian Ocean, in: Proceedings from the GeoHab: Marine Geological and Biological Habitat Mapping. Santa Barbara, p. 123.Sunda, W.G., Huntsman, S.A., 1997. Interrelated influence of iron, light and cell size on marine phytoplankton growth. Nature 390, 389–392. doi:10.1038/37093

Townsend, A.T., 2000. The accurate determination of the first row transition metals in water, urine, plant, tissue and rock samples by sector field ICP-MS. J. Anal. At. Spectrom. 15, 307–314. doi:10.1039/a904933i

Watson, S.J., Coffin, M.F., Whittaker, J.M., Lucieer, V., Fox, J.M., Carey, R., Arculus, R.J., Bowie, A.R., Chase, Z., Robertson, R., Martin, T., Cooke, F., 2016. Submarine geology and

geomorphology of active Sub-Antarctic volcanoes: Heard and McDonald Islands, in: AGU Fall Meeting Abstracts.

Wojtasiewicz, B., Trull, T.W., Davies, D.M., Schallenberg, C., Clementson, L., and Hardman-Mountford, N.J., 2018. Possible explanations for the unexpected lack of phytoplankton biomass in naturally iron fertilized waters near Heard and McDonald islands in the Southern Ocean. (In preparation).

Wuttig, K., Townsend, A.T., van der Merwe, P., Gault-Ringold, M., Holmes, T., Schallenberg, C., Latour, P., Tonnard, M., Rijkenberg, M.J.A., Lannuzel, D., Bowie, A.R., 2019. Critical evaluation of a seaFAST system for the analysis of trace metals in marine samples. Talanta 197, 653–668. doi:10.1016/j.talanta.2019.01.047

Yuan, J., Shiller, A.M., 1999. Determination of subnanomolar levels of hydrogen peroxide in seawater by reagent-injection chemiluminescence detection. Anal. Chem. 71, 1975–1980. doi:10.1021/ac981357c

Chapter 4

4 Iron availability influences nutrient drawdown in the Heard and McDonald Islands region, Southern Ocean

This chapter was published as an article under the same title in Marine Chemistry, 2019, by Elsevier Publishing, DOI: 10.1016/j.marchem.2019.03.002

Thomas M. Holmes[1,2], Kathrin Wuttig[1], Zanna Chase[2], Pier van der Merwe[1], Ashley T. Townsend[3] Christina Schallenberg[1], Manon Tonnard[1,2,4] and Andrew R. Bowie[1,2].

[1]Antarctic Climate and Ecosystems Cooperative Research Centre (ACE CRC), University of Tasmania, Hobart, Australia
[2]Institute for Marine and Antarctic Studies (IMAS), University of Tasmania, Hobart, Australia
[3]Central Science Laboratory (CSL), University of Tasmania, Hobart, Australia.
[4]Laboratoire des sciences de l'Environnement MARin (LEMAR) – CNRS UMR 6539 - Institut Universitaire Européen de la Mer (IUEM), Université de Bretagne Occidentale, Technopôle Brest-Iroise, rue Dumont d'Urville, 29280 Plouzané, France

4.1 Abstract

At the southern part of the northern Kerguelen Plateau (Southern Ocean) is an active volcanic hotspot, hosting volcanically active Heard Island and McDonald Islands (HIMI), the former of which is largely covered by glaciers. While offshore waters are persistently iron (Fe) limited, typical of the broader Southern Ocean, near shore waters over the Kerguelen plateau show variability in Fe distributions and support a high biomass of phytoplankton during austral spring-summer. This study investigates dissolved Fe (DFe) and macronutrient distributions in waters surrounding HIMI during the Heard Earth-Ocean-Biosphere Interactions (HEOBI) voyage in January-February 2016. Comparison of surface DFe with macronutrient concentrations shows that the majority of the plateau is Fe limited in late summer and, based on comparison with previous voyages, also Fe limited in different years and earlier in the bloom season. The distribution of DFe drawdown from estimated winter inventories to observed late summer inventories shows that DFe availability drives macronutrient uptake on the plateau. The drawdown of silicic acid decreases relative to nitrate drawdown in proximity to HIMI, in agreement with classical diatom nutrient uptake behaviour under iron replete conditions. Comparison of Fe:nitrate and Fe:phosphate drawdown ratios with expected uptake stoichiometry suggest that recycling of Fe increases with distance from Fe sources on the plateau. Lastly, comparison with data from previous voyages shows that DFe distribution varies inter-annually due to complex oceanographic conditions on the plateau, with greatest variability observed over the rough bathymetry and strongly tidally influenced region closest to HIMI. Together these data highlight the central role of Fe in driving nutrient uptake and stoichiometry in the HIMI region of the Kerguelen Plateau.

4.2 Introduction

Iron (Fe) is now recognised as a key limiting, or co-limiting, micronutrient for biological production in large parts of the ocean (Martin, 1990; Martin et al., 1990; Moore et al., 2013, 2009, 2001). When coupled with the inhibition of nitrogen fixation by microbes under low Fe conditions in low-latitude regions, Fe regulates biological productivity in as much as half the world's oceans (Moore et al., 2009, 2001). As such, Fe plays a key role in biogeochemical cycling and the drawdown of carbon from the atmosphere (Boyd et al., 2007; Boyd and Ellwood, 2010; Tagliabue et al., 2014). Areas of the ocean that are high in the macronutrients nitrogen (N) and phosphorous (P) but low in chlorophyll-producing organisms are known as high-nutrient, low-chlorophyll (HNLC) regions and cover approximately one third of the world's oceans (Boyd et al., 2007). The Southern Ocean (SO) is the largest of these HNLC regions (Boyd et al., 2012). Both artificial and natural Fe fertilisation produce large phytoplankton blooms in HNLC regions (e.g. Boyd et al., 2007; Morris and Charette, 2013). Islands in the SO naturally fertilise HNLC waters (Tyrrell et al., 2005) by supplying macro and micro-nutrients to waters typically depleted in Fe and silicic acid (Si; e.g. Blain et al., 2001). These island nutrient sources produce plumes of elevated phytoplankton biomass, such as the one formed over and downstream of the Kerguelen Plateau in the Indian sector of the SO in spring and early summer (Blain et al., 2007).

The Kerguelen plateau is shallow, is located directly in the path of strong currents associated with the Polar Front (Figure 4.1; Park et al., 2014) and hosts two active subaerial volcanic islands, Heard and McDonald Islands (HIMI). The shallow bathymetry of the plateau (<500 m at the HIMI Shoal) is characterised by many seamounts and ridges, which strongly constrain the two major currents (Park et al., 2008a). The Fawn Trough Current sweeps south of HIMI and follows the plateau bathymetry, then splits on the eastern side of the plateau where part of the flow heads in a NW direction to join the second major current, associated with the Polar Front, which sweeps just to the south of Kerguelen Islands (Park et al., 2014). These currents constrain

the shape and extent of the annual phytoplankton plume (Maraldi et al., 2009; Mongin et al., 2009).

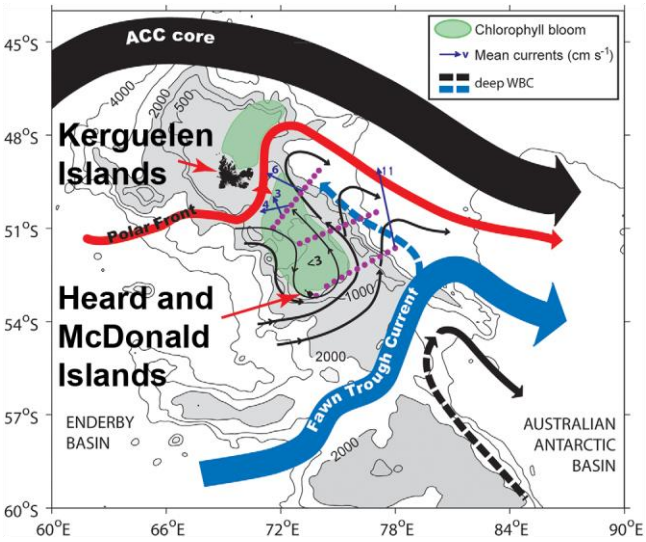

Figure 4.1 Schematic of the general circulation of the central to northern Kerguelen Plateau, with the polar front depicted in red and Fawn Trough Current in blue. Thin black arrows are subsurface western boundary currents (WBC). Purple dots are stations from KEOPS-1 voyage. Reproduced with permission from Park et al. (2008a).

Each summer, when photosynthesis is no longer light-limited, an Fe-fuelled phytoplankton plume covering thousands of square kilometres forms over and downstream of the Kerguelen Plateau (Blain et al., 2007). Previous studies conducted as part of the Kerguelen Ocean and Plateau Compared Study voyages (KEOPS-1, 19th January to 13th February 2005; KEOPS-2, 7th October to 30th November 2011) have attempted to characterise nutrient and dissolved Fe (DFe) sources and drawdown in the plume region between HIMI and Kerguelen Islands, which lies ~400 km to the north of HIMI (e.g. Blain et al., 2008a; Dehairs et al., 2015; Mosseri et al., 2008; Quéroué et al., 2015). These studies found that the bloom persisted even with surface waters both on and off the plateau containing low concentrations of DFe (0.090 ± 0.034 nmol L^{-1}; Blain et al., 2007), close to values known to be metabolically limiting for many phytoplankton (Blain et al., 2008a, 2007; Quéroué et al., 2015; Timmermans et al., 2001). This indicates that a continuous supply of Fe from the plateau along with efficient recycling of Fe within the mixed layer must sustain the bloom above the plateau during the growing season. A sediment supply of Fe to

bottom waters above the plateau, coupled with enhanced vertical mixing and deep winter mixing were cited as the main sources (Blain et al., 2008a, 2007; Bowie et al., 2015) with an additional DFe supply from particle dissolution required to reconcile calculated phytoplankton Fe demand (Blain et al., 2007; Bowie et al., 2015; van der Merwe et al., 2015). Previous studies also suggest that some of the iron supply must be sourced from further south on the plateau (Bowie et al., 2015; van der Merwe et al., 2015), with HIMI as a likely candidate (Bown et al., 2012). However, lack of data collected in the HIMI region has so far precluded definitive confirmation of HIMI as a major source.

Based on the high primary productivity observed in previous in situ and satellite studies of the region between HIMI and Kerguelen Islands (Blain et al., 2008a; Bowie et al., 2015; Mongin et al., 2008), we hypothesise in this study that supply of DFe from HIMI, and the plateau just to the north of HIMI, leads to greater drawdown of nutrients in the region, compared to surrounding SO waters. Here we report DFe, and macronutrient data collected during the Heard Earth-Ocean-Biosphere Interactions (HEOBI) voyage to the HIMI region in the austral summer of 2016. The distribution of DFe in relation to the estimated seasonal drawdown of macronutrients in this region of the Kerguelen Plateau is interpreted, in order to provide insight into biogeochemical cycling of key elements in this biological hotspot within the SO.

4.3 Methods

4.3.1 Sample collection

Sampling and shipboard analyses were carried out aboard R/V *Investigator* during the HEOBI voyage (GEOTRACES process study GIpr05) from January 8th to February 27th 2016 around Heard and McDonald Islands on the Kerguelen Plateau in the Indian sector of the SO. Thirty-six stations were successfully sampled for DFe in the study region, using a trace metal clean

rosette (TMR; Figure 4.2). The same locations were also occupied by conventional CTD casts, along with an additional thirteen conventional CTD only stations (not shown). Trace metal clean rosette deployments typically occurred within thirty minutes after conventional CTD retrieval. Sample stations were divided into 5 regions, Transect B, Transect C, Heard Island, McDonald Islands and reference stations. Transect B and Transect C are both oriented in a northeast-southwest direction. Transect B extends from off the plateau to a point on the plateau midway between Heard and Kerguelen Islands, broadly following the KEOPS-1 'B' transect (Figure 4.2; Blain et al., 2008a). Transect C extends from Heard Island towards Gunnari Ridge, along the same trajectory as the previous KEOPS-1 'C' transect (Figure 4.2; Blain et al., 2008a), though not reaching as far to the northeast as the previous transect, which extended off the plateau into waters >3500 m deep. Sampling station locations in the HIMI region were selected based on bathymetric features (Watson et al., 2016) and acoustic flare signals (indicators of bubbles rising from the sea floor) detected with shipboard echosounders (Spain et al., 2018) deemed indicative of potential hydrothermal activity. Two reference sites were sampled to the west and south of Heard Island. Station 11, ~80 km to the west of McDonald Islands, was expected to be located in HNLC waters, but observed shipboard underway fluorescence and chlorophyll biomass was relatively high (up to 2.1 mg m^{-3} Chl*a* in upper 200 m; Wojtasiewicz et al., in prep.). Station 18, ~100 km to the south of Heard Island, was located in waters more representative of HNLC conditions (max 0.81 mg m^{-3} Chl*a* in upper 200 m; Wojtasiewicz et al., in prep.).

Briefly, all water column samples were collected in 12 L, externally sprung, acid cleaned Niskin bottles (Ocean Test Equipment) modified for trace metal sampling, following well established trace metal sampling procedures (Bowie and Lohan, 2009; Cutter et al., 2014). These were deployed using the Australian Marine National Facility trace metal clean autonomous trace metal rosette (TMR) equipped with a Seabird CTD unit and attached to a Dyneema line. Once recovered, the Niskin bottles were rapidly transferred into a trace metal clean containerised laboratory for sub-sampling and sample processing. All sample manipulation and analysis was

conducted following GEOTRACES guidelines (Cutter et al., 2014) under ISO 5 HEPA filtered air within the containerised clean room. Dissolved iron samples were filtered through acid-washed Pall Acropak Supor capsule filters (0.2 μm), collected in acid-cleaned low-density polyethylene (LDPE) sample bottles and acidified immediately to pH 1.8 with 2 ‰ (v/v) ultrapure hydrochloric acid (Seastar Baseline), before double bagging in clean plastic bags and storage in the dark for subsequent laboratory-based analysis.

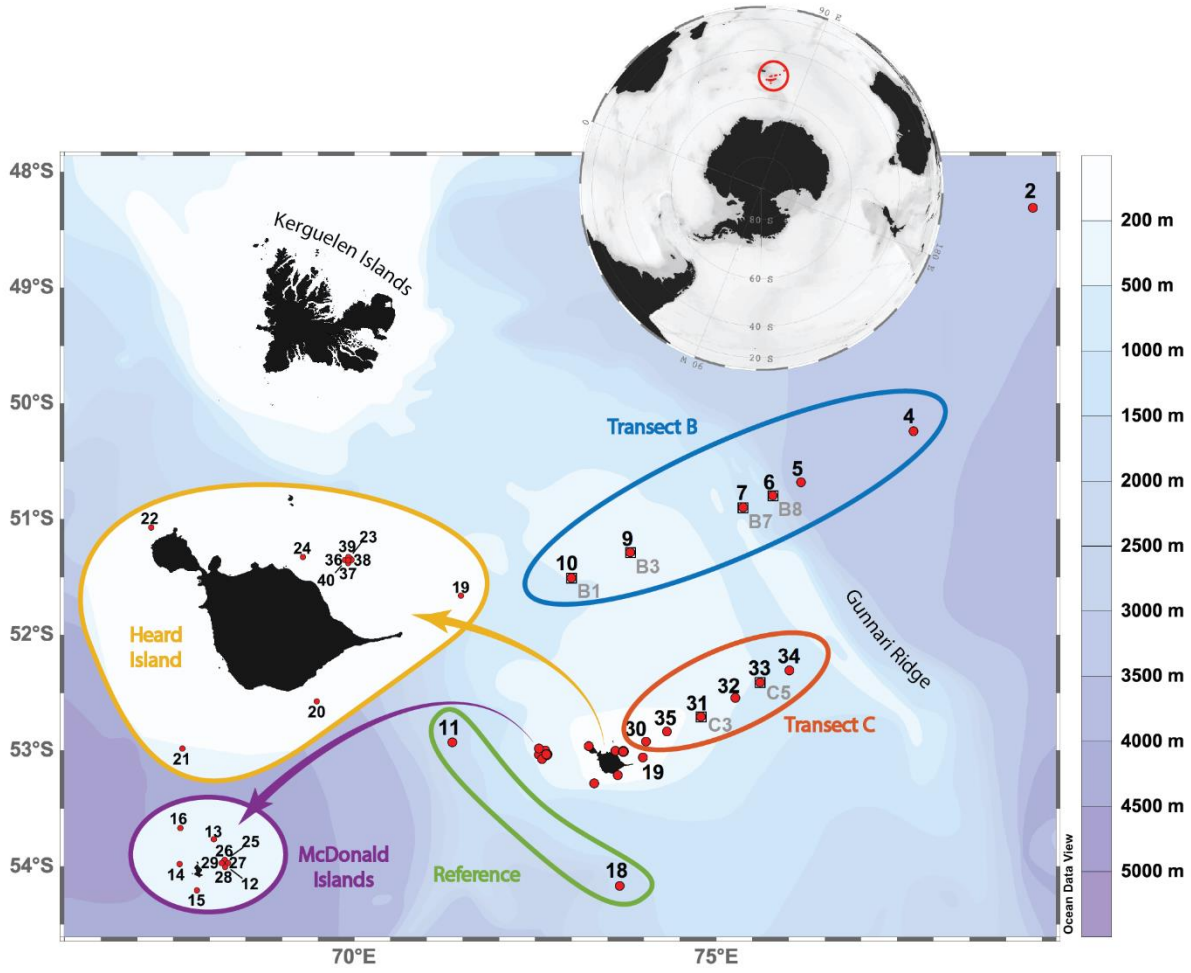

Figure 4.2 Sampling area with station locations. Heard and McDonald Islands are shown zoomed in inset. Transect B (blue) follows Kerguelen Ocean and Plateau Compared Study (KEOPS-1) transect B. Transect C (orange) follows the first 150 km of KEOPS-1 transect C. Square markers and grey station numbers show which KEOPS-1 stations were reoccupied. Heard Island (yellow) and McDonald Islands (purple) station locations were selected based on bathymetric features (Watson et al., 2016) and acoustic flares detected by shipboard echosounder (Spain et al., 2018). Reference stations (green) were located to the west and south of HIMI. Station 11 had higher than expected Fe and chl-a concentrations, but station 18 was located in HNLC waters.

4.3.2 Dissolved iron analysis

Dissolved Fe concentrations were determined using a sea*FAST* S2 pico (ESI, Elemental Scientific, USA) flow injection system with a Nobias Chelate-PA1 column (hereafter sea*FAST*), followed by analysis on a sector field inductively coupled plasma mass spectrometer (SF-ICP-MS, Element 2 Thermo Fisher Scientific, Inc.). Briefly, a sea*FAST* pre-concentration factor of 40 was used for this work and DFe was preconcentrated from 30 mL of sample onto a Nobias PA1 column followed by elution off the column in 750 μL of 1.7 M distilled HNO_3. Matrix-matched standards (internal standards) were gravimetrically prepared by adding DFe standard to aged and acidified Southern Ocean surface seawater and then processed using the same method as for samples. Multi-element standards over the same final concentration range as the internal standards were analysed directly on the SF-ICP-MS without pre-concentration on the sea*FAST* (external standards) to calculate recoveries off the column. A detailed methodology is described in Wuttig et al. (2019).

Data were blank-corrected by subtracting an average of at least three acidified ultra-high purity water (UHP) blanks that were treated in the same manner as the seawater samples. The DFe detection limit was calculated as 3x the standard deviation of the acidified UHP blank. Daily detection limits ranged from 0.006 to 0.062 nmol kg^{-1}, with a median of 0.022 nmol kg^{-1} (n=11). SAFe 'D1' and 'S', and GEOTRACES 'GD' community consensus samples were analysed in parallel with field samples and measured at 0.68 ± 0.04, 0.083 ± 0.020 and 1.02 ± 0.01 nmol kg^{-1} (n = 9, 5 and 6) respectively, in good agreement with consensus values (0.67 ± 0.04, 0.093 ± 0.008 and 1.00 ± 0.1).

To aid with strategic planning during the voyage, on-board near real-time analysis of DFe was also conducted on the full sample set, using flow injection analysis with luminol chemiluminescence detection (FIA-CL) and in-line preconcentration onto an 8-hydroxyquinoline (8-HQ) resin, adapted from the methods of de Jong et al., (1998) and Obata et al., (1993).

Excellent agreement between the two analytical methods was observed, with no significant difference between the sample sets (paired *t*-test, $p > 0.05$, $R^2 = 0.95$, n = 244; full data comparison in Wuttig et al., 2019). All figures and data discussed in this study utilise results from the laboratory-based sea*FAST*/SF-ICP-MS analyses. Dissolved Fe results for each sample are presented in appendix Table 4-1 and surface DFe and nutrient data for each station are presented in appendix Table 4-2. Nutrient data are available from the CSIRO data trawler website (https://www.cmar.csiro.au/data/trawler/survey_details.cfm?survey=IN2016_V01) and Fe data will be made available at the GEOTRACES International Data Assembly Centre (GDAC).

4.3.3 Fe* calculations

The Fe* tracer is based on the N* concept (Gruber and Sarmiento, 1997) and aids in determining which nutrient is most likely to be limiting, based on assumed consumption ratios. It is defined as the concentration of DFe minus the expected biological Fe consumption based on biological consumption of all ambient phosphate (PO_4^{3-}) (Fe*(P); equation 1) or NO_3^- (Fe*(N); equation 2) (Bowie et al., 2009; Parekh et al., 2005; Rijkenberg et al., 2014):

$$Fe^*(P) = [DFe] - \left(\left(\frac{Fe}{P}\right) algal\ uptake\ ratio\ \times [PO_4]\right) \quad (1)$$

$$Fe^*(N) = [DFe] - \left(\left(\frac{Fe}{N}\right) algal\ uptake\ ratio\ \times [NO_3]\right) \quad (2)$$

We calculated Fe* for all samples using the global average Fe/P algal uptake ratio of 0.47 (Parekh et al., 2005) or Fe/N algal uptake ratio of 0.039, derived from an assumed fixed stoichiometry based on the Redfield ratio of P:N = 1:12 (Anderson and Sarmiento, 1994; Parekh et al., 2005). Positive Fe* values indicate that DFe concentrations are theoretically sufficient to completely consume PO_4^{3-} or NO_3^- (i.e. a macronutrient limited system). Negative Fe* indicates insufficient DFe to completely consume PO_4^{3-} or NO_3^- (i.e. primary productivity is potentially Fe limited).

4.3.4 Macronutrients and CTD data

Temperature and salinity data were taken from Sea-Bird Electronics SBE3T and SBE4C sensors respectively, which were mounted on the primary CTD rosette. Nutrient samples were collected using the standard CTD rosette. Concentrations of NO_x (NO_3^- and NO_2^-), NO_2^-, SiO_4^- and PO_4^{3-} were analysed on-board using a SEAL AA3 HR AutoAnalyzer (Rees et al., 2018). Mixed layer depths (MLD) were calculated with the gsw_mlp package of the Gibbs-SeaWater (GSW) Oceanographic Toolbox (McDougall and Barker, 2011) using continuously measured CTD profile data. This package calculates the MLD based on a threshold method, defined as the depth where a change in density of 0.03 kg m^{-3} or change in temperature of 0.2 °C from a surface reference value is reached, as described in de Boyer Montégut et al. (2004).

Nutrient drawdown over the season was estimated by subtracting the summer nutrient inventory from the winter inventory over the depth range from surface to the depth of the temperature minimum (T_{min}; e.g. Sweeney et al., 2000; Trull et al., 2015). To calculate the winter nutrient inventory, the concentration of each nutrient (DFe, NO_3^-, PO_4^{3-} and Si) at the winter water (WW) T_{min} were multiplied by the depth of the T_{min}. To calculate the summer inventory, nutrient concentrations observed on the voyage were integrated to the depth of T_{min}. Integration was calculated using the trapezoidal numerical integration method. Continuously measured CTD profiles were used to estimate accurate T_{min} depths. The fraction of winter nutrient concentrations drawn down at each station was calculated by dividing the summer nutrient drawdown by the winter nutrient inventory. Drawdown could only be calculated at eight stations (stations 5 – 9, Transect B; stations 33 and 34, Transect C; 11 and 18, and Reference stations) due to the absence of a WW layer in the shallow and well-mixed stations near to HIMI (Figure 4.3b,g and 4.12). In order to investigate the effect of Fe inputs on drawdown at shallower stations closer to HIMI and where no WW layer was observed during the voyage, we used the average WW nutrient concentrations at the average WW depth (203 m) to calculate drawdown at

those stations. Where the station bottom depth was shallower than the average WW depth, the bottom depth was used as the WW depth for integrations.

4.4 Results

4.4.1 Regional Circulation

The HIMI region of the Kerguelen Plateau is characterised by a complex ocean circulation system, as observed during the HEOBI voyage and previous studies (Figure 4.1; Park et al., 2008b, 2008a; van Wijk et al., 2010). The circulation observed during HEOBI generally matched that encountered during KEOPS-1 (Park et al., 2008a). Slow mean currents were observed over the shallow plateau (~6 cm s^{-1}; R. Roberston, Pers. Comm.) flowing in a generally northeast direction, but these were influenced by strong (15 – 50 cm s^{-1}) tidal currents depending on depth. A strong north to north-eastward current (40 – 50 cm s^{-1}) was present at the edge of the eastern flank of the plateau on both transects, following bathymetry. A subsurface cold-water tongue present at stations 33 and 34 on Transect C was also observed during KEOPS-1 (Park et al., 2008a) (Figure 4.3g). Below the WW off-plateau, Upper Circumpolar Deep Water (UCDW), Lower Circumpolar Deep Water (LCDW) and Antarctic Bottom Water (AABW) water masses were identified. A cyclonic warm core eddy, which was associated with a strong southward current (R. Robertson, Pers. Comm.) and lower surface NO_3^- concentrations, affected the water column at station 4 of Transect B (Figure 4.3b). Temperature – salinity diagrams for all stations in each region are presented in appendix Figure 4.10.

4.4.2 Iron and macronutrients along Transects B and C

Transect B surface water DFe concentrations on and off the plateau were low and not significantly different (*t*-test, $p > 0.05$), with off-plateau and on-plateau mean mixed layer DFe concentrations of 0.11 ± 0.09 nmol L^{-1} and 0.08 ± 0.05 nmol L^{-1} (n = 13 and 16), respectively.

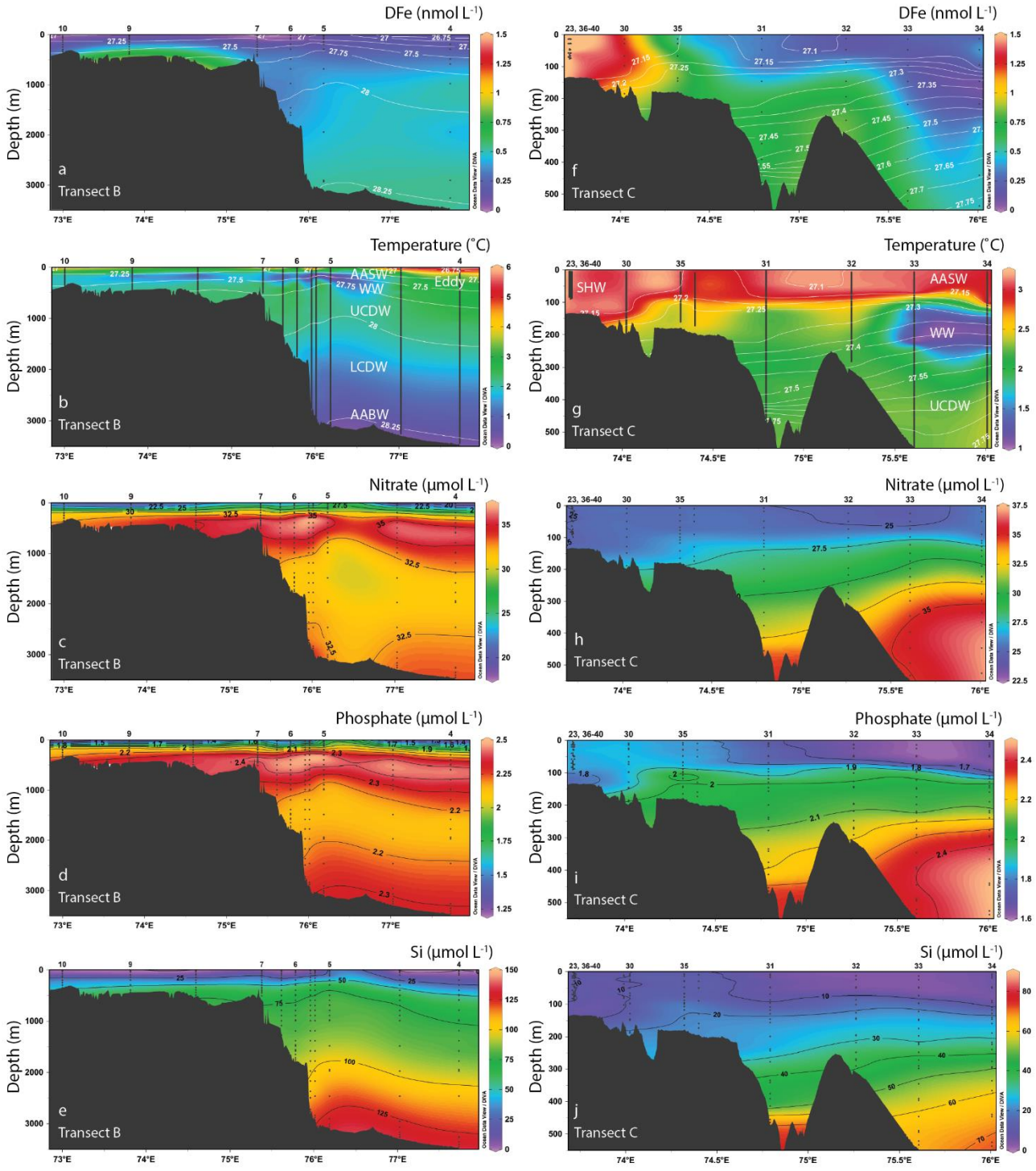

Figure 4.3 **a.** Transect B DFe concentration **b.** Transect B temperature **c.** Transect B nitrate **d.** Transect B phosphate **e.** Transect B Si **f.** Transect C DFe concentrations **g.** Transect C temperature **h.** Transect C nitrate **i.** Transect C phosphate and **j.** Transect C Si. Neutral density (γ^n) surfaces (white lines, calculated from continuous CTD data) have been overlaid on **a, b, f and g.** Water masses identified from T-S diagrams are annotated on the temperature transects **b** and **g** as follows: cyclonic warm core eddy (Eddy), Antarctic Surface Water (AASW), Winter Water (WW), Upper Circumpolar Deep Water (UCDW), Lower Circumpolar Deep Water (LCDW), Antarctic Bottom Water (AABW) and Shelf Water (SHW). Note that

temperature and depth scales differ between transects. Black dots represent sample locations. Station numbers for TMR deployments are shown above the top axis.

Concentrations of DFe increased with depth at all stations both on and off the plateau. The greatest concentration observed on transect B (0.77 nmol L^{-1}) was located approximately midway across the plateau at station 9, ~40 m above the seafloor (Figure 4.3a and 4.4a).

All Transect C stations were located above the plateau. The three most easterly stations (32, 33 and 34) had deep mixed layers, shoaling towards the east (285, 254 and 245 m, respectively). Surface DFe concentrations at the three easterly stations were low (mean upper 50 m, 0.24 nmol L^{-1}) relative to westerly stations (mean upper 50 m, 0.73 nmol L^{-1}), increasing with depth (Figures Figure 4.3f and 4.4b). Water masses at stations 33 and 34 were similar to those observed above the plateau on Transect B. Station 32 was located above a shallow ridge (305 m depth) and had a similar temperature-salinity profile to stations closer to Heard Island (Figure 4.10). Mixed layer DFe increased towards Heard Island with concentrations of 0.41, 0.73 and 1.2 nmol L^{-1} at stations 31, 35 and 30, respectively. Water column DFe profiles became increasingly homogenised towards Heard Island (Figure 4.3f).

Transect B mean NO_3^- concentrations in the upper 50 m ranged from 19.2 to 27.0 μmol L^{-1} (Figure 4.3c and 4.4a). Stations 5 to 9 decreased in surface concentrations from east to west. Station 4, at the east of the transect, was located in the middle of a cyclonic warm core eddy (Figure 4.3b; R. Roberston, Pers. Comm.) and exhibited the lowest NO_3^- surface concentrations on the transect (19.2 μmol L^{-1}). Station 5, just east of the shelf break, exhibited the highest NO_3^- concentration (27.0 μmol L^{-1}). Station 10, located further to the west on the plateau, was slightly higher in surface NO_3^- concentrations than station 9 (21.5 and 20.7 μmol L^{-1}, respectively). Nitrate concentrations increased with depth at all stations on Transect B, with off-plateau stations (stations 4-6) reaching maximum concentrations of around 35 μmol L^{-1} in UCDW, then decreasing to 31 μmol L^{-1} in LCDW before increasing slightly again in AABW (mean 33 μmol L^{-1}).

Surface PO_4^{3-} distributions over Transect B were similar to observed NO_3^- distributions, with concentrations from station 5 decreasing in a westward direction (with the exception of station 7 which was 0.03 μmol L^{-1} higher than station 6; Figure 4.3d and 4.4a). Mean PO_4^{3-} concentrations in the upper 50 m ranged between 1.30 and 1.83 nmol L^{-1}, with the lowest mean concentrations observed at stations 10 and 4 (1.30 and 1.34 μmol L^{-1}, respectively) and the highest mean concentration observed at station 5 (1.83 μmol L^{-1}). As with NO_3^-, PO_4^{3-} concentrations increased with depth, with off-plateau stations reaching maxima in UCDW, decreasing in the LCDW and increasing again in AABW (mean 2.41, 2.13 and 2.31 μmol L^{-1}, respectively).

Mean Si concentrations in the upper 50 m ranged from 0.8 to 5.6 μmol L^{-1}, with the exception of station 5, which had a much higher mean concentration (28.8 μmol L^{-1}), indicating upwelling was occurring at this station, close to the steep rise of the plateau (Figure 4.3e and 4.4a). Stations 6 and 7, on the plateau slope, had higher surface Si (4.0 and 5.6 μmol L^{-1}, respectively) than stations 9 and 10 on the plateau (1.6 and 2.3 μmol L^{-1}, respectively). Silicic acid concentrations increased with depth both on and off plateau, with concentrations reaching 130 μmol L^{-1} in AABW at off plateau stations, decreasing from east to west with 52.5 μmol L^{-1} at the bottom depth above the plateau at station 10.

Across Transect C, surface water NO_3^- concentrations were relatively constant in comparison to Transect B, ranging from 24.7 to 25.7 μmol L^{-1} mean in the upper 50 m (Figure 4.3h and 4.4b). Below the pycnocline, NO_3^- concentrations at deeper easterly stations increased with depth, reaching maxima in UCDW (35.5 and 37.0 μmol L^{-1} at stations 33 and 34, respectively) before decreasing slightly with depth to around 35 μmol L^{-1} at both stations (Figure 4.4b). Phosphate concentrations along Transect C ranged from 1.61 to 1.87 μmol L^{-1} in the upper 50 m, increasing towards Heard Island (Figure 4.3i and 4.4b). Phosphate concentrations also increased with depth past the pycnocline, becoming more homogenised over the water column towards Heard Island and reaching maxima in UCDW (2.40 and 2.50 μmol L^{-1} at stations 33 and 34, respectively).

Mean Si concentrations in the upper 50 m ranged from 3.9 – 6.1 μmol L^{-1} at stations 31 – 34, increasing to 10.9 μmol L^{-1} and 11.65 μmol L^{-1} at the two stations closest to Heard Island (stations 35 and 30, respectively). Like the other macronutrients, Si increased with depth below the pycnocline to a maximum of 84.3 in UCDW at station 34 and became more homogenised with surface concentrations towards HIMI as bottom depths decreased.

4.4.3 Heard and McDonald Islands

Waters surrounding HIMI were well mixed throughout the water column, with generally homogenous DFe, macronutrient, temperature and salinity profiles (Figure 4.4c, d). Depths were shallow, ranging from 56 to 216 m (mean 134 m). Mean DFe concentrations in the upper 50 m were greater around HIMI than elsewhere in the study region, with a mean of 1.34 nmol L^{-1} (Figures 4.3f and 4.4c,d). The mean NO_3^-, PO_4^{3-} and Si concentrations in the upper 50m at stations around HIMI (Figures 4.3h,i,j and 4.4c,d) were 24.9, 1.85 and 11.6 μmol L^{-1}, respectively.

4.4.4 Reference stations

Low surface DFe concentrations were observed at both reference stations (mean 0.12 nmol L^{-1} in the mixed layer at both stations 11 and 18). At station 11, CTD data showed evidence of an intrusion of warmer, saltier water at 120 – 210 m (R. Robertson, Pers. Comm.). Winter water DFe concentrations were low at both stations (0.22 and 0.04 nmol L^{-1} at stations 11 and 18, respectively). Below the WW, DFe concentrations increased to maxima of 0.65 nmol L^{-1} (at 690 m depth) at station 11 and 0.41 nmol L^{-1} (at 295 m depth) at station 18, before decreasing with depth at both stations (Figure 4.4e). Mean NO_3^-, PO_4^{3-} and Si concentrations in the upper 50m were 24.6, 1.55 and 0.9 μmol L^{-1}, respectively at station 11, and 25.8, 1.76 and 12.7 μmol L^{-1}, respectively at station 18 (Figure 4.4e). As previously mentioned, station 11 was not a true HNLC reference station, with relatively high Chl*a* (max 2.1 mg m^{-3} in upper 200 m; Wojtasiewicz et al., in prep.).

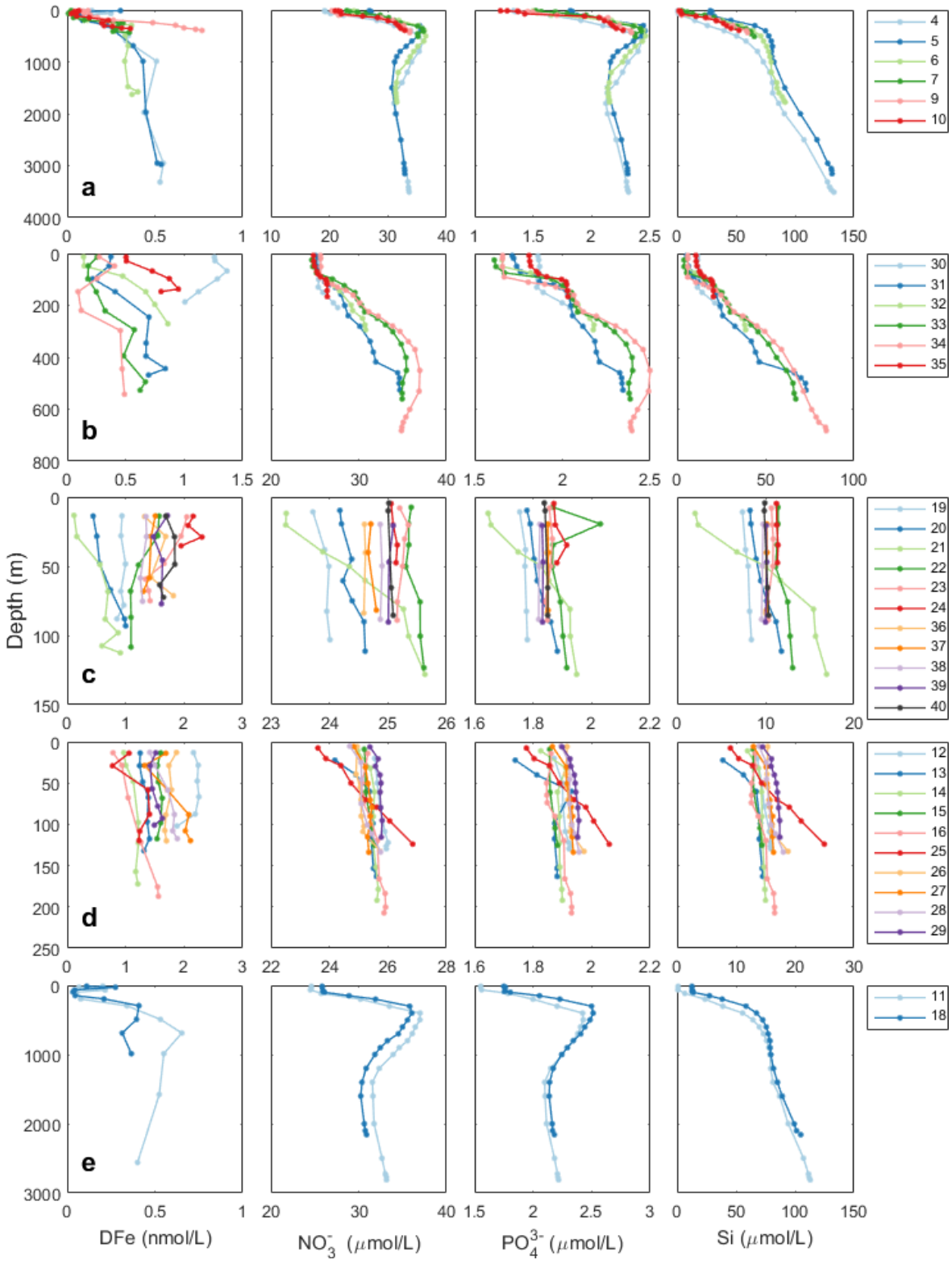

Figure 4.4 Profiles of DFe, NO_3^-, PO_4^{3-} and Si for **a.** Transect B, **b.** Transect C, **c.** Heard Island, **d.** McDonald Islands and **e.** Reference stations. Stations are colour coded and shown in legends on the right hand side of each region.

4.4.5 Fe*

Calculations of Fe* with respect to NO_3^- show, at least qualitatively, that the majority of the study region on the Kerguelen Plateau was limited by DFe in late summer, except for waters directly surrounding HIMI (Figure 4.5). Results were similar for Fe* calculated with respect to PO_4^{3-} (data not shown).

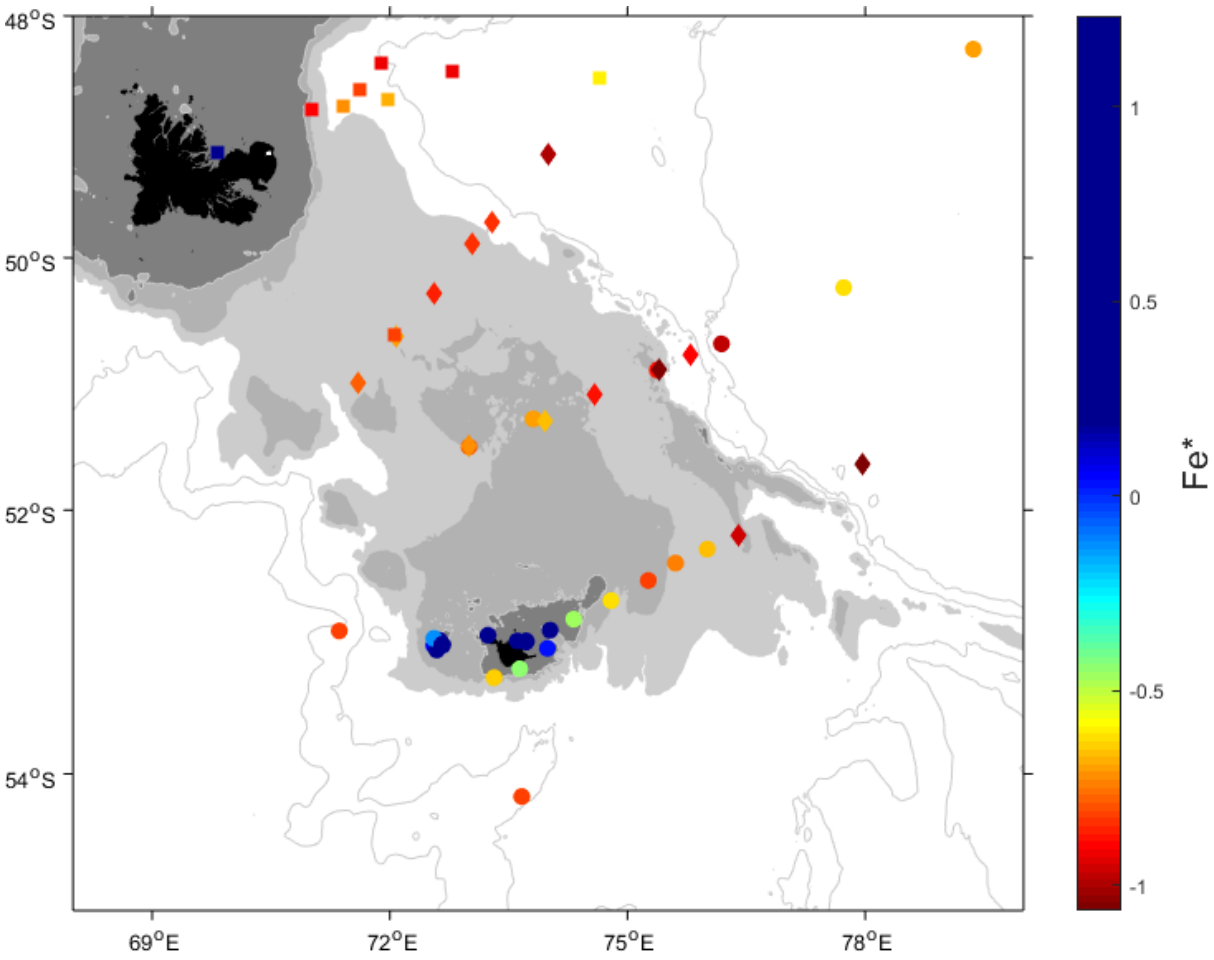

Figure 4.5 Mean Fe* in the upper 50m at each station sampled during HEOBI (circles), KEOPS-1 (diamonds) and KEOPS-2 (squares) voyages. Here, Fe* has been calculated with respect to N (Fe*(N) = [DFe] – ((Fe/N) algal uptake ratio x [NO3-])), due to better data availability. The (Fe/N) algal uptake ratio = 0.039 mmol/mol and was calculated from the updated Redfield ratio (P:N = 1:12 in the upper 3000m) (Anderson and Sarmiento, 1994). Waters are iron limited over most of the sampled area of the plateau, with the exception of stations directly surrounding Heard and McDonald Islands, and Kerguelen Islands. Bathymetric isobaths are shown, with seabed <200 m depth shaded dark grey, <500 m shaded lighter grey and <1000 m shaded lightest grey.

4.4.6 Nutrient Drawdown

Calculated drawdown was negative for DFe (i.e. higher surface than WW concentrations) at two stations (34 and 18), which were excluded from further analysis (Figure 4.6b; see Figure 4.2 for station locations). Station 11 showed the greatest DFe drawdown of all eight stations. Station 33, the only station on Transect C where a positive DFe drawdown was calculated, and station 9, with the largest DFe concentrations from the plateau on Transect B (Figure 4.6b), showed greater DFe drawdown relative to stations further east on Transect B. Fractions of winter DFe stock utilised over the season were highest at stations 6 and 7 (Transect B), followed by reference station 11 (Figure 4.6c). Station 5 (Transect B) showed the lowest utilisation, followed by station 33 (Transect C).

The greatest drawdown for NO_3^- and Si was calculated at stations 11 and 9, followed by 6, with drawdown at reference station 18 the lowest (Figure 4.6a). Drawdowns calculated at the rest of the stations (5, 7, 33 and 34) were somewhat similar, ranging from 680 – 540 mmol m^{-2} (NO_3^-) and 2960 – 2520 mmol m^{-2} (Si) with station 33 the maximum for both. The distribution of PO_4^{3-} drawdown was slightly different, with the greatest calculated at station 11, followed by stations 6 and 9 with drawdown at reference station 18 again the lowest (Figure 4.6b). Phosphate drawdown calculated at stations 5, 7, 33 and 34 was again similar, ranging from 44 – 50 mmol m^{-2}. Fractional drawdown was greatest at station 9 followed by 11 and 6 for NO_3^- and Si, while PO_4^{3-} fractional drawdown was greatest at station 6, closely followed by station 9 then 11. Fractional drawdown was lowest at stations 18 and 5 for NO_3^-, PO_4^{3-} and Si. At the remaining stations (7, 33 and 34), fractional drawdown ranged from 10 – 11%, 10 – 13% and 44 – 55% for NO_3^-, PO_4^{3-} and Si, respectively (Figure 4.6c).

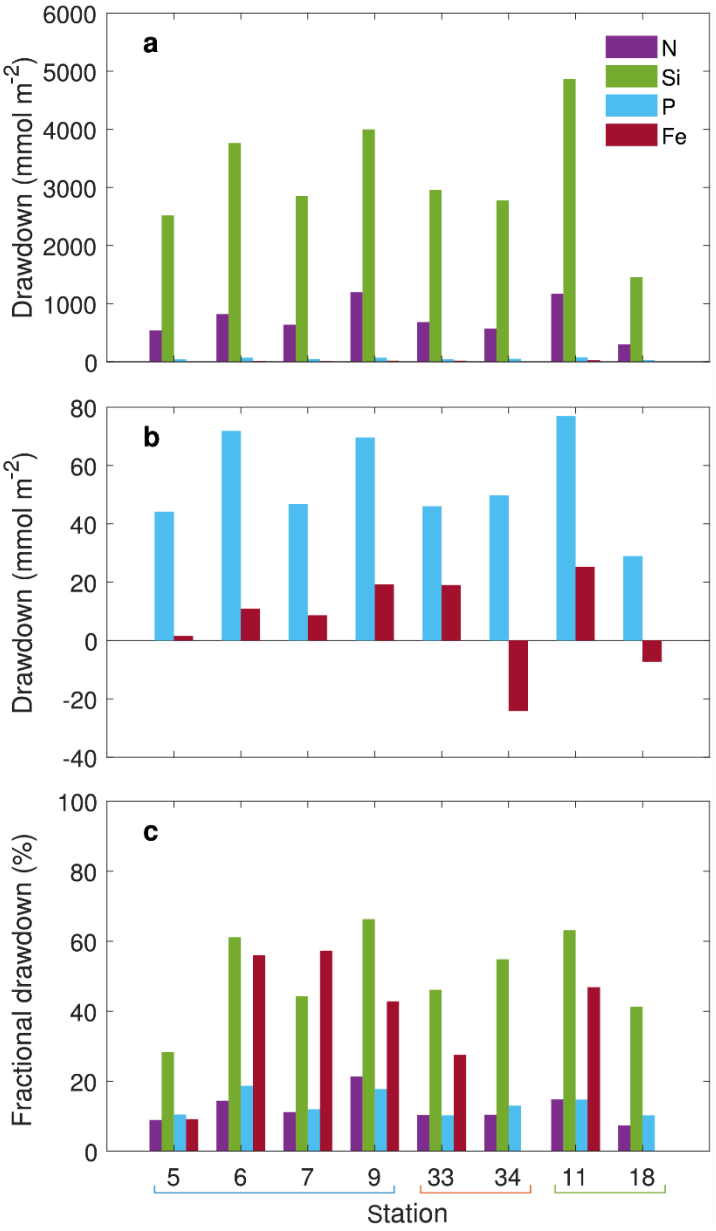

Figure 4.6 **a.** Drawdown of NO_3^-, Si, PO_4^{3-} and DFe at each station that had a WW temperature minimum (T_{min}), calculated by multiplying the DFe concentration at the T_{min} by the depth of the T_{min} to get the winter DFe inventory and integrated observed DFe concentrations to the depth of T_{min} for the summer inventory. We then subtracted the summer inventory from the winter inventory **b.** Drawdown of PO_4^{3-} and DFe at each station. **c.** Fraction of winter nutrient drawn down at each station ((winter – summer)/winter). Lines under station numbers indicate region, Transect B (blue), Transect C (orange) and reference stations (green).

4.5 Discussion

The impact of Fe availability on uptake of macronutrients, such as N and Si, by primary producers is well documented (Boyd et al., 2007; de Baar et al., 2005; Martin et al., 1990), but is not well constrained in the oceanographically and biologically complex HIMI region of the

Kerguelen Plateau. In order to interpret the impact of DFe distribution on the drawdown and cycling of macronutrients in this region, we (i) compare our results to the previous KEOPS-1 (January-February 2005) and KEOPS-2 (October-November 2011) voyages to explore inter-annual and inter-seasonal variability of DFe distribution in the region; (ii) use the tracer Fe* to investigate which areas of the northern Kerguelen Plateau might be Fe limited; (iii) explore the distribution of DFe drawdown in the study area; (iv) determine the influence of DFe availability on nutrient drawdown; (v) examine indicators of Fe recycling; and (vi) determine the influence of DFe availability on nutrient recycling by comparing nutrient drawdown ratios with expected uptake ratios.

4.5.1 Comparison of dissolved iron distributions between studies

To comprehensively explore how DFe impacts cycling of macronutrients in the study region, the variability of DFe concentrations between different voyages is first analysed. The KEOPS-1 voyage took place in 2005, 11 years prior to HEOBI. Both voyages took place during the summer season (January-February). Stations from the KEOPS-1 study which were reoccupied during HEOBI are shown in Figure 4.2. Comparison of stations occupied during both KEOPS-1 and HEOBI reveals that DFe concentrations were lower overall during KEOPS-1 (Figure 4.7). Considering HEOBI samples were measured using two independent methods, which showed excellent agreement (and of which one was a similar FIA-CL method to that used during KEOPS-1; Blain et al., 2008a; Wuttig et al., 2019), this variation is unlikely to be of an analytical nature. Instead, it may be due to differences in biological and physical processes between years, especially considering the dynamic oceanographic nature of the region (Park et al., 2008b, 2008a). Dissolved Fe concentrations at stations 6-10 (Transect B) were generally similar in surface waters before diverging with depth, while stations 31 and 33 (Transect C) differed between occupations over the entire water column (Figure 4.7a.). Calculating DFe inventories for each profile by integrating over the water column (for the depth range covered by samples

from both voyages), with errors propagated from the analytical error associated with each measurement (see caption to Figure 4.7), also shows a clear difference between the two voyages, well outside associated analytical uncertainties (Figure 4.7b.).

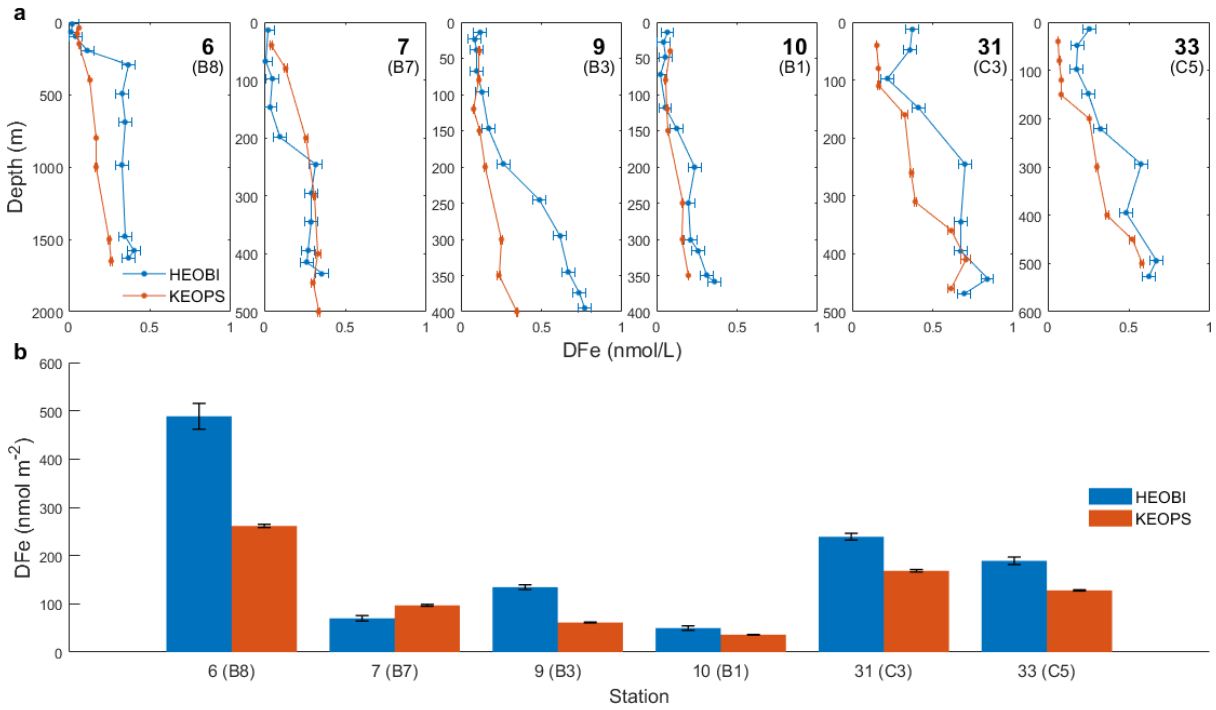

Figure 4.7 **a.** Dissolved Fe profiles at stations sampled during the KEOPS-1 voyage (orange) and revisited during HEOBI (blue). Station numbers are shown in the top right corner of each profile for both HEOBI (bold) and KEOPS-1 (bracketed) voyages. Stations 6-10 are located on Transect B and 31-32 on Transect C (see Figure 4.2). Error bars on the HEOBI ICP-MS data indicate instrumental precision for the dataset, based on the SD of in-house low-Fe seawater, analysed in triplicate during most analytical sequences (n = 25). Data obtained using ICP-MS and onboard FIA showed excellent agreement (paired t-test, $p > 0.05$, $R2 = 0.95$, n = 244; Wuttig et al., in review). Error bars on the KEOPS-1 FIA data are one SD of replicate measurements for each sample (n=3). **b.** Dissolved Fe inventories at each of the revisited stations from HEOBI and KEOPS-1, calculated by integrating DFe over the water column for the depth range covered by samples from both voyages. Error bars are propagated from the error of each data point on each profile.

The observed variation in profiles may be explained by considering regional current regimes, bathymetric features and phytoplankton bloom development at these stations. Profiles from both voyages are more similar in surface waters over the plateau on Transect B, where currents are slow (Park et al., 2008a; R. Robertson, pers. comm.) and biomass is high annually over summer (Mongin et al., 2008), keeping DFe at low and more homogeneous concentrations. Internal tides and vertical mixing (Park et al., 2008b) influence deeper waters over Transect B, which may explain differences observed between KEOPS-1 and HEOBI Fe concentrations at

depth. Stations 31 and 33 were located on either side of a shallow ridge, with strong northward currents, which fluctuated with time and were most likely tidally influenced (R. Robertson, pers. comm). Highly variable currents have been observed in this area previously (van Wijk et al., 2010) and comparing high resolution satellite mean daily sea surface temperature averaged over January to February between 2005 and 2016 adds further evidence to the variability of ocean currents in the region, with colder surface waters extending further north during KEOPS-1 in 2005 (Figure 4.11). These fluctuating currents, coupled with shallow bathymetric features, are likely to have influenced the supply of DFe through vertical mixing or lateral transport, and hence the variability in DFe concentrations observed at these locations. To summarise, comparison between HEOBI and KEOPS-1 data indicates that DFe concentrations may vary inter-annually in the HIMI region due to the complex oceanographic conditions, which likely influences the utilisation of other nutrients in the region, as shown below.

4.5.2 Fe*

The concept of Fe* has been used in previous studies to indicate whether primary productivity in surface waters may be limited by DFe concentrations (e.g. Blain et al., 2008b; Bowie et al., 2009; Parekh et al., 2005). While the Fe* concept includes caveats, mainly because cellular Fe:PO_4^{3-}, Fe:NO_3^- and Fe:C uptake ratios are not constant across all environments (Blain et al., 2008b; Ho et al., 2003; Sunda and Huntsman, 1995; Twining et al., 2004), we explore variability of Fe* between seasons and years using data from HEOBI, KEOPS-1 and KEOPS-2 voyages, as an indicator of Fe limitation.

Our Fe* calculations indicate that there was insufficient DFe to support full consumption of the available N and P during the HEOBI voyage, except for waters directly surrounding HIMI (Figure 4.5). Comparison of our Fe* results with those calculated for the KEOPS-1 and KEOPS-2 voyages indicates that the majority of surface waters on the northern plateau between

HIMI and Kerguelen Islands, as well as waters downstream of the plateau, are Fe limited both inter-annually and inter-seasonally with the exception of waters in direct proximity to HIMI and Kerguelen Islands (Figure 4.5). Iron budgets constructed for both KEOPS-1 (Blain et al., 2008a) and KEOPS-2 (Bowie et al., 2015) revealed that the DFe supply from the plateau (predominantly by winter mixing and vertical eddy diffusivity increased by large internal tides; Park et al., 2008b) was insufficient to meet the phytoplankton demand. This could only be met by invoking a dissolution of 2% - 2.5% of the particulate Fe (pFe) pool (Blain et al., 2007; Bowie et al., 2015). Since these Fe* calculations only take into account DFe, it's possible that the pFe pool over the plateau may influence the Fe limitation status of phytoplankton (van der Merwe et al., 2015). Indeed, results from HEOBI show that Heard Island is a strong source of labile pFe (discussed in more detail in van der Merwe et al., in prep.). While dissolution of pFe, and biological recycling of Fe (explored in more detail below) might alleviate some of the Fe limitation suggested by the Fe* calculations, we note that surface water DFe concentrations across Transect B and the four easterly stations of Transect C were close to values known to be growth rate limiting for some SO phytoplankton species (Blain et al., 2002; Timmermans et al., 2001). Furthermore, Fe limitation in regions of relatively high Fe supply has been demonstrated previously (Hutchins et al., 1998). In summary, Fe* calculations indicate that over much of the northern Kerguelen Plateau in mid to late summer, Fe is the ultimate limiting nutrient.

4.5.3 Dissolved iron drawdown distribution

Dissolved Fe drawdown calculations provide further support for the dominant role of Fe availability in shaping productivity in this region. Drawdown results indicate that areas of greater DFe supply on the plateau are associated with greater overall DFe drawdown (Figure 4.6b). Comparing DFe drawdown to winter DFe stocks gives a reasonably linear relationship for both HEOBI and KEOPS-1 data (Figure 4.8a). Stations with greater DFe supply, as indicated by a larger winter inventory of DFe, had a greater seasonal DFe drawdown. This indicates that Fe

concentration is the strongest limiting factor in the region, with phytoplankton drawing down DFe in proportion to its availability at the start of the growing season; if another environmental factor strongly influenced phytoplankton productivity, DFe drawdown should appear relatively constant, regardless of winter stocks.

The fraction of winter DFe stock drawn down, from winter water concentrations to those observed during the voyage in late summer, gives an indication of how much of the winter DFe reserves biota have utilised over the growing season. This varied from 9 to 57% (Figure 4.6c). The lowest fractional drawdown was calculated at station 5. However, this analysis assumes that vertical and lateral mixing in the WW and surface layers are small (Hoppe et al., 2017; Hoppema et al., 2000; Jennings et al., 1984). The very high surface Si concentrations indicate that upwelling affected surface waters at station 5, giving a smaller calculated drawdown for Fe. There was less utilisation of the winter stock at stations 9 (Transect B) and 33 (Transect C) compared to stations 6 and 7 (Transect B) off the plateau (Figure 4.6c). The lower fractional drawdown calculated at these stations is probably influenced by lateral or vertical supply of DFe from plateau sediments and HIMI.

Alternatively, or in addition, lower fractional drawdown at station 33 could be the result of a lateral intrusion of a relatively low DFe subsurface water mass. Dissolved Fe concentrations at Transect B stations increase between the surface and 100 m depth by a mean of 0.02 nmol L^{-1} while at station 33 the concentration decreases by 0.08 nmol L^{-1} (Figure 4.4). As further evidence for intrusion of a subsurface water mass, stations 34 and 18, which lie within the same circulation trajectory (Figure 4.1; Park et al., 2008a, 2014), also exhibit negative drawdown and show similar temperature-salinity profiles (Figure 4.10). Park et al. (2008a, 2014) showed that surface/subsurface currents sweep south of HIMI towards the east before turning northwest, closely following bathymetry before joining the Polar Front, which agrees with shipboard ADCP data (R. Robertson, Pers. Comm.) and temperature profiles (Figure 4.3g). The presence of this

lower DFe subsurface water mass drove WW DFe concentrations down at stations 18, 33 and 34, thus affecting drawdown calculations.

The large drawdown calculated for reference station 11 was also unexpected, as the station is located furthest to the west, off the plateau (Figure 4.2). The temperature-salinity profile reveals a thick intrusion of warmer water from 120 – 210 m depth at this station, just above the winter water layer. This suggests that an intrusion of DFe-enriched water from the plateau may have caused this anomaly, though lack of ADCP data from HEOBI precludes a definitive answer.

4.5.4 Influence of DFe availability on seasonal drawdown of nutrients in the region

To determine whether regions with higher Fe consumption show greater use of available macro-nutrients, we compared Fe drawdown with fractional drawdown of N and fractional drawdown of Si (Figure 4.8b,c). Both fractional N and fractional Si drawdown give a positive linear relationship with Fe drawdown for stations on Transect B, with the fraction of N and Si drawn down from winter stock concentrations increasing with increasing Fe drawdown (Figure 4.8b,c), indicating that Fe availability dictates the amount of macronutrients utilised. Fractional drawdown data from KEOPS-1 is more scattered, possibly indicating that plankton DFe utilisation, DFe supply or plateau currents differed during this year, again highlighting the dynamic nature of the region. Station 33 (Transect C) is offset from Transect B stations, with comparatively high DFe drawdown but lower fractional N and Si drawdown. This is due to a deeper mixed layer and temperature minimum at this station (see Table 4-2) compared with Transect B stations, resulting in a greater summer mixed layer N and Si inventory, which reduces the calculated drawdown. The relationship between fractional nutrient drawdown and Fe drawdown is consistent with Fe availability driving nutrient uptake.

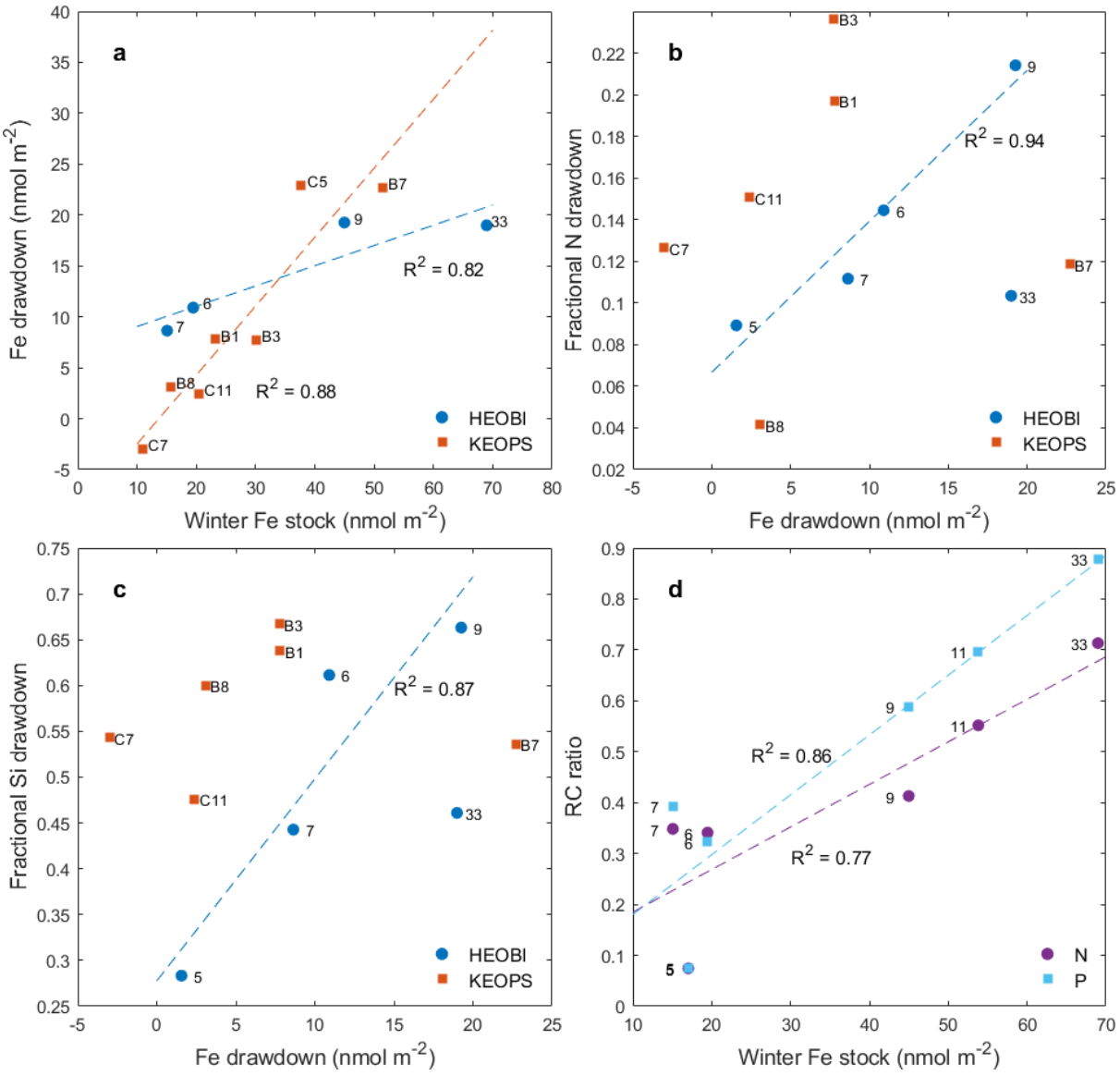

Figure 4.8 Dissolved Fe drawdown versus **a.** winter DFe stock **b.** fraction of N drawn down from winter stock **c.** fraction of Si drawn down from winter stock for stations where drawdown could be calculated from HEOBI (blue circles) and KEOPS-1 (orange squares) data and **d.** Quotient of Fe:N (purple) and Fe:P (blue) drawdown ratios to Redfield uptake ratios (RC ratio) versus winter DFe stock; see text for details. Dashed lines show linear regressions, with R^2 values annotated. Linear regressions in **b** and **c** are not shown for KEOPS-1 due to the spread of data and for HEOBI data only include stations from Transect B (5 – 9) as Transect C station (33) is clearly affected by different processes (discussed in text). Station numbers are annotated.

Plotting the distribution of Si:N drawdown using inferred WW depths and nutrient concentrations (see methods) shows that in close proximity to HIMI, Si uptake decreases relative to NO_3^- (Figure 4.9). This is likely a result of diatom nutrient uptake behaviour. Bottle enrichment experiments (Hutchins and Bruland, 1998; Takeda, 1998) and observations in HNLC waters (e.g. Brzezinski et al., 2003) have shown that Fe-stressed diatoms alter their nutrient

uptake ratios, increasing Si:C and Si:NO_3^- uptake, while diatoms growing under Fe replete conditions follow expected Redfield ratios close to 0.13 and 1, respectively (Brzezinski, 1985). The Si:N drawdown distribution observed in the HEOBI study area fits well with classical diatom nutrient uptake behaviour under Fe replete conditions, with ratios closer to 1 nearer to sediment sources above the plateau and around HIMI.

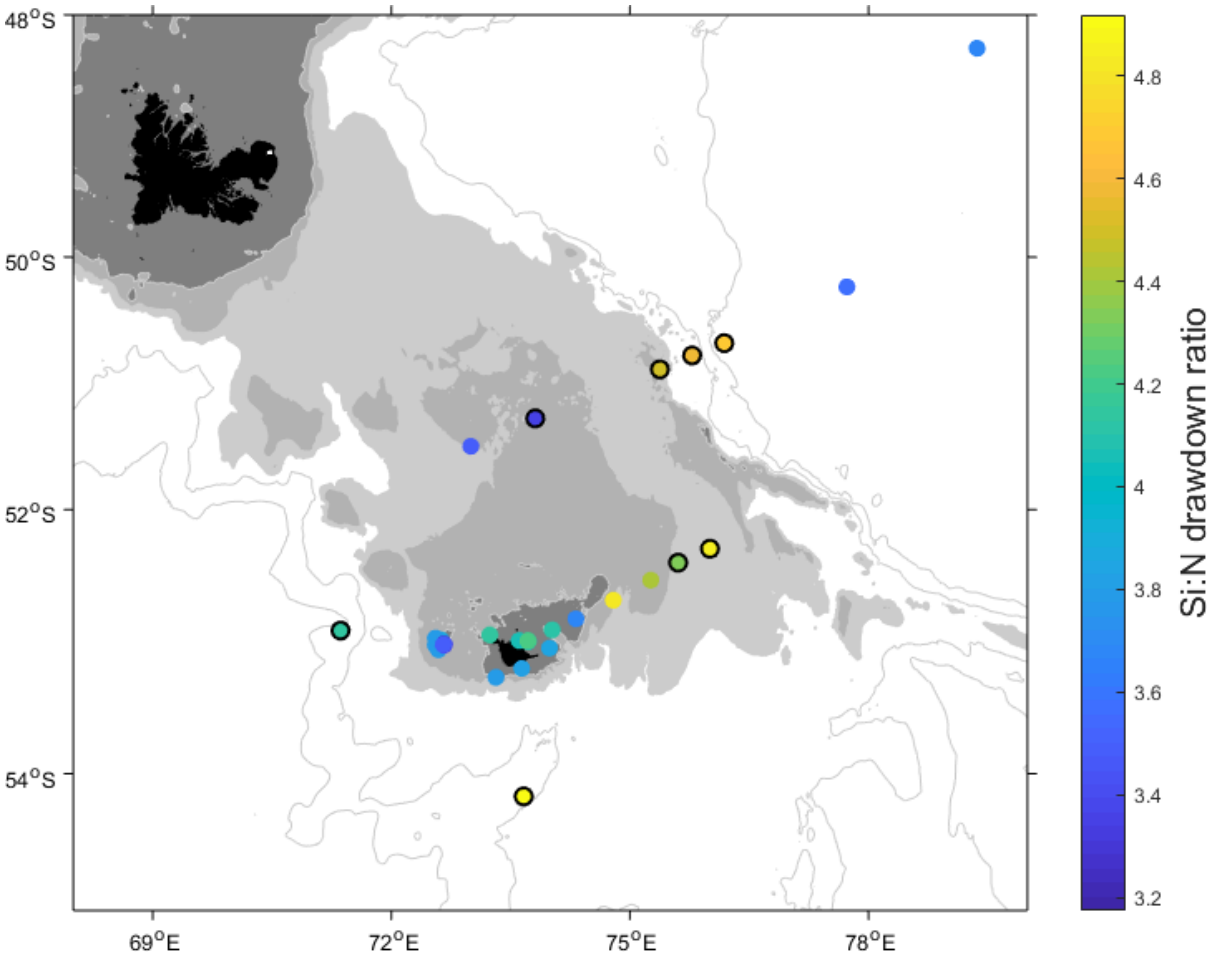

Figure 4.9 Si:N drawdown at each station sampled during HEOBI. Stations which had a defined WW layer, where drawdown could be calculated are circled in black. Drawdown at all other stations was calculated by using the average WW nutrient concentrations at the average WW depth (203 m). Where the station bottom depth was shallower than the average WW depth, the bottom depth was used instead as the WW depth for integrations.

4.5.5 Nutrient recycling

Biotic recycling of Fe has been identified as an important mechanism for retaining Fe in ocean surface waters (Boyd et al., 2017; Hutchins et al., 1993). While it has been shown that Fe

recycling is especially important for maintaining primary productivity in HNLC waters (Boyd et al., 2005), regeneration of Fe has also been demonstrated over the Kerguelen Plateau (Bowie et al., 2015; Sarthou et al., 2008). Iron budgets constructed from previous voyages found that regenerated Fe over the plateau played an increasingly important role in sustaining phytoplankton Fe requirements, with early season recycled Fe accounting for <8% of new supply (KEOPS2; Bowie et al., 2015) increasing to 42-61% of total Fe demand towards the end of the summer season (KEOPS1; Sarthou et al., 2008). As HEOBI also occurred during the end of the summer season, Fe recycling is further investigated here to determine its impact on observed nutrient drawdown ratios.

As an indicator of nutrient recycling during HEOBI, ratios of DFe drawdown to N and P drawdown were calculated and compared to expected phytoplankton uptake ratios. The expected Fe:P and Fe:N uptake ratios are 0.47 and 0.039 mmol:mol respectively (Anderson and Sarmiento, 1994; Parekh et al., 2005), as used for our Fe* calculations. However, mean calculated drawdown ratios of Fe:P and Fe:N were 0.21 and 0.014 respectively. It is unlikely these lower ratios reflect lower phytoplankton Fe requirements over the plateau, given the constant Fe supply (Blain et al., 2007), and considering Fe requirements of diatoms (the major contributor to phytoplankton biomass observed in the region previously (Obernosterer et al., 2008)) are demonstrated to be higher in regions of higher Fe supply than in HNLC waters (Twining and Baines, 2013). More likely, the low Fe:N and Fe:P drawdown ratios reflect greater recycling of DFe than of N and P. The same calculations cannot be relied upon for Si, due to the variable Si requirements of diatoms, depending on availability of Fe (Brzezinski et al., 2003). However, as suggested by Mosseri et al. (2008), low Si recycling can be inferred from the relatively large fractional drawdown for Si (median 50%) compared to N and P (Figure 4.6). This is consistent with previous studies in the region, which have found that in late summer, during the decline of the bloom, recycling of Si is low (Closset et al., 2014; Mosseri et al., 2008).

4.5.6 Influence of DFe availability on recycled nutrient uptake

To further investigate whether DFe availability influences nutrient recycling in the region, we calculated a Redfield comparison (RC) ratio as per equations 3 and 4:

$$RC\ ratio(N) = \frac{(Fe_{DD}: N_{DD})}{Redfield\ uptake(Fe: N)} \quad (3)$$

$$RC\ ratio(P) = \frac{(Fe_{DD}: P_{DD})}{Redfield\ uptake(Fe: P)} \quad (4)$$

Where Fe_{DD} is DFe drawdown, N_{DD} and P_{DD} are NO_3^- and PO_4^{3-} drawdown, respectively, and Redfield uptake (Fe:N and Fe:P) are expected Redfield uptake ratios of 0.039 and 0.47 mmol:mol (Anderson and Sarmiento, 1994; Parekh et al., 2005). It must be noted here that lateral inputs of 'new' DFe from the plateau over the growing season may have influenced calculated drawdown. Thus, our RC ratio does not allow for quantitative analysis of recycling, but rather provides a relative indication of recycling in the region.

Comparison of the RC ratio between stations shows that Fe:N and Fe:P drawdown ratios diverge away from the Redfield ratio, becoming smaller with decreasing winter DFe stock (Figure 4.8d). The RC ratio can reflect either a change in the uptake ratio of Fe:N (or Fe:P) or a change in the relative recycling of Fe:N (or Fe:P). The observed changes in drawdown ratio with Fe availability could thus be caused by greater Fe uptake by diatoms in regions of higher Fe supply, as mentioned above. While this interpretation is possible, we note that all of the Fe:N and Fe:P uptake ratios are lower than the expected Redfield uptake ratios, even close to HIMI where iron supply is large. This indicates Fe recycling is occurring, and we therefore suspect Fe recycling is the dominant influence on observed RC ratios in this region. Interpreted in this light, the RC ratio trend shows that further from DFe sources on the plateau, less of the DFe present in surface waters at the start of the growing season is drawn down relative to NO_3^- or PO_4^{3-}, indicating greater relative recycling of DFe with decreasing DFe availability.

Studies have shown that Fe regeneration plays an important role in sustaining biological productivity in areas of low DFe supply (Boyd et al., 2005), with less importance in regions of greater DFe supply, such as the Kerguelen Plateau (Bowie et al., 2015; Boyd et al., 2017; Sarthou et al., 2008), although we note the previously mentioned seasonality. Our results indicate that Fe recycling does play a role in biological productivity in the region, with increasing recycling with distance from areas of DFe supply. Station 33, the station closest to HIMI of the stations where drawdown could be calculated, has Fe:N and Fe:P drawdown ratios nearest to Redfield ratios. This indicates that less Fe recycling occurred close to HIMI. These results build on previous findings in the region and indicate that production and uptake of regenerated DFe become important processes with distance from DFe sources on the Kerguelen Plateau between HIMI and Kerguelen Islands.

4.6 Conclusions

We show that supply of DFe from HIMI, and the plateau just to the north of HIMI, leads to greater drawdown of nutrients in the region, compared to stations off the plateau. Dissolved Fe availability drives macronutrient uptake on the plateau, and Fe recycling off the plateau. In direct proximity to HIMI, Si:N drawdown ratios are lower, following classic diatom nutrient utilisation behaviour under Fe replete conditions (Takeda, 1998). These results highlight the importance of HIMI in contributing to the biogeochemical cycling and the annual phytoplankton bloom in the region.

The majority of the northern plateau between HIMI and Kerguelen Islands, as well as waters downstream of the plateau, are Fe limited, according to Fe* calculations, both inter-annually and inter-seasonally with the exception of waters in direct proximity to HIMI and Kerguelen Islands. These findings confirm previous studies indicating that DFe supply over the plateau is insufficient to supply phytoplankton needs without invoking a particle dissolution and/or Fe

recycling fraction (Blain et al., 2008a; Bowie et al., 2015). Although previous studies have suggested that Fe supply on the plateau is sufficient with the addition of particle dissolution (Blain et al., 2008a; Bowie et al., 2015), Fe limitation is likely a spectrum rather than a binary system (e.g. Hutchins et al., 1998), and our results show that phytoplankton still suffer from some Fe limitation on the plateau, indicated both by negative Fe* and recycling of Fe occurring to some degree both on and off the plateau.

Finally, comparison between HEOBI and KEOPS-1 data indicates that DFe distribution varies inter-annually due to the complex oceanographic conditions in the HIMI region, with less variability observed in surface waters over the plateau to the north of HIMI, where currents are more sluggish and biomass is higher, than observed deep in the water column over the plateau or over complex bathymetry to the east of HIMI.

4.7 Acknowledgements

The authors would like to thank the three anonymous reviewers for their attention to detail and numerous improvements to the final manuscript. We thank Melanie East (Antarctic Climate and Ecosystems Cooperative Research Centre: ACECRC) and Tom Trull (Commonwealth Scientific and Industrial Research Organisation: CSIRO) for their invaluable advice while preparing the manuscript and Lavenia Ratnarajah (ACECRC and Institute for Marine and Antarctic Studies: IMAS) for her assistance in collecting and filtering samples collected on the HEOBI voyage. We would like to thank Mark Rayner (CSIRO) and Kendall Sherrin (CSIRO) for their excellent hydrochemical analyses. We thank Sophie Bestley (IMAS, CSIRO) for her valuable analysis of SST data. We also thank the captain, officers and crew of the RV Investigator (HEOBI voyage) and Chief Scientist Mike Coffin for their support during the 53-day mission. We wish to acknowledge the Australian Research Council (DP150100345 and LE0989539), the Australian Antarctic Science Program (AAS4338) and the Australian Government Cooperative Research

Centres Program through ACECRC, who both provided project funding and PhD scholarship support.

4.8 Appendix

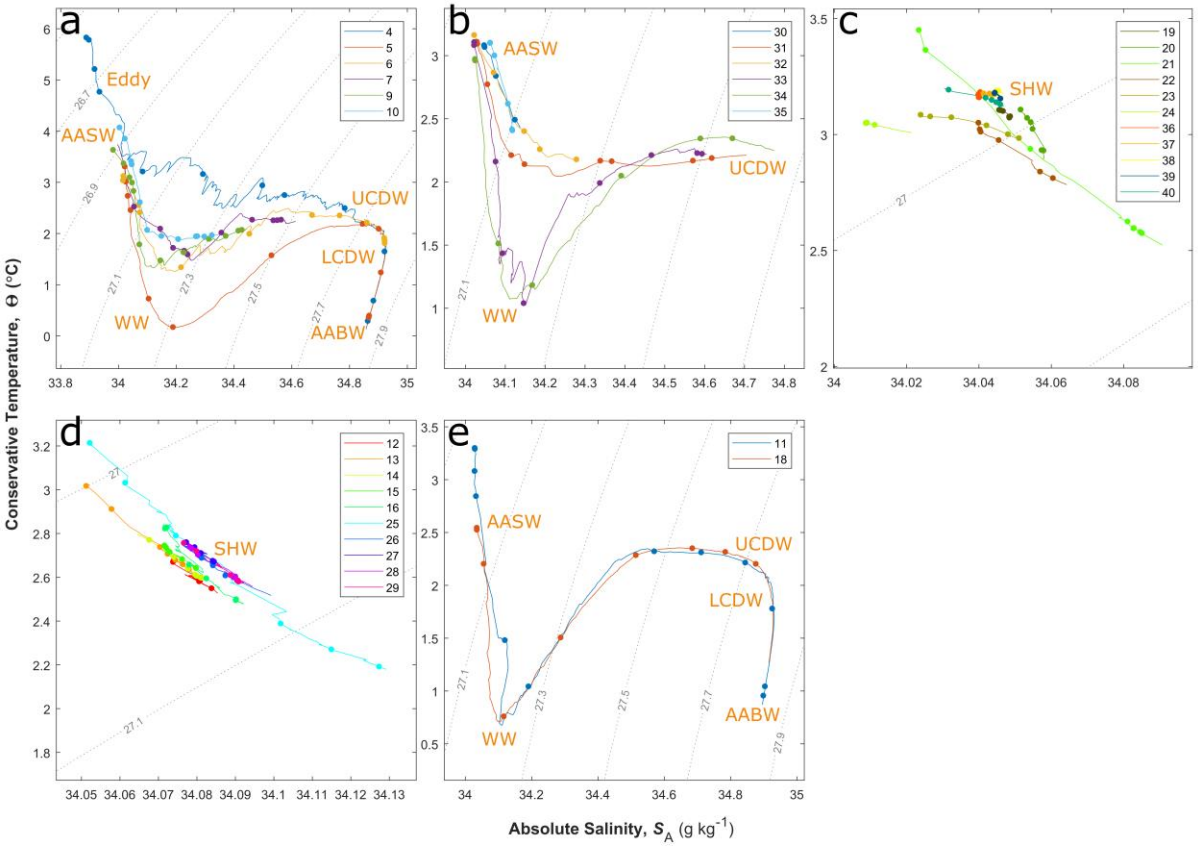

Figure 4.10 Absolute salinity (S_A) – Conservative Temperature (Θ) diagrams for stations within each region and with water masses and potential density isobars overlain. **(a)** Transect B **(b)** Transect C **(c)** Heard Island **(d)** McDonald Islands **(e)** Reference stations. Identified water masses are the cyclonic warm core eddy (Eddy), Antarctic Surface Water (AASW), Winter Water (WW), Upper Circumpolar Deep Water (UCDW), Lower Circumpolar Deep Water (LCDW) and Antarctic Bottom Water (AABW).

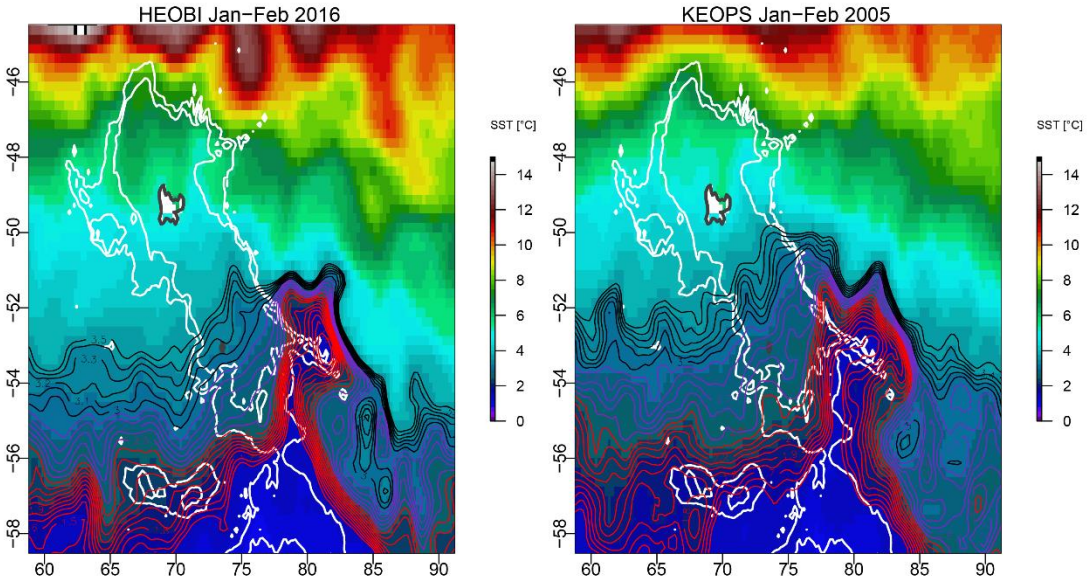

Figure 4.11 Mean daily sea surface temperature (SST) averaged over January to February for both 2016 (HEOBI) and 2005 (KEOPS-1). Countours showing SST from 1.5 – 2.5°C (red), 2.5 – 3°C (purple) and 3 – 3.5°C (black) have been added for clarity. This SST data was obtained from the Group for High Resolution Sea Surface Temperature analysis (NASA, 2002; GHRSST v4.1 Multiscale Ultrahigh Resolution L4 analysis, see http://data.nodc.noaa.gov/cgi-bin/iso?id=gov.noaa. nodc:GHRSST-MUR-JPL-L4-GLOB). The data was accessed using the libraries raadtools (Sumner, 2016) and roc (Sumner, 2017) for the freely available R software (R Core Team, 2016).

Table 4-1 Dissolved Fe data for all samples at each station occupied during the HEOBI voyage, analysed by SF-ICP-MS

Sample name	Station	Bottle	Depth (m)	SeaFAST date	DFe (nmol L^{-1})
26_HEOBI_st2_12_40x	2	12	13.9	20160801	0.17
25_HEOBI_st2_11_40x	2	11	28.6	20160801	0.09
24_HEOBI_st2_10_40x	2	10	49.0	20160801	0.05
23_HEOBI_st2_9_40x	2	9	68.7	20160801	0.26
22_HEOBI_st2_8_40x	2	8	98.5	20160801	0.07
21_HEOBI_st2_7_40x	2	7	148.3	20160801	0.11
20_HEOBI_st2_6_40x	2	6	198.4	20160801	0.18
19_HEOBI_st2_5_40x	2	5	298.3	20160801	0.28
18_HEOBI_st2_4_40x	2	4	498.0	20160801	0.43
17_HEOBI_st2_3_40x	2	3	697.8	20160801	0.46
16_HEOBI_st2_2_40x	2	2	998.7	20160801	0.56
15_HEOBI_st2_1_40x	2	1	1598.5	20160801	0.62
38_HEOBI_st4_12_40x	4	12	13.8	20160801	0.14
37_HEOBI_st4_11_40x	4	11	28.6	20160801	0.10
36_HEOBI_st4_10_40x	4	10	68.3	20160801	0.25
35_HEOBI_st4_9_40x	4	9	97.1	20160801	0.09
34_HEOBI_st4_8_40x	4	8	196.7	20160801	0.12

Sample name	Station	Bottle	Depth (m)	SeaFAST date	DFe (nmol L^{-1})
33_HEOBI_st4_7_40x	4	7	295.7	20160801	0.21
19_HEOBI_4_6	4	6	492.6	20161206	0.35
18_HEOBI_4_5	4	5	590.6	20161206	0.33
30_HEOBI_st4_4_40x	4	4	987.0	20160801	0.51
29_HEOBI_st4_3_40x	4	3	1971.3	20160801	0.44
28_HEOBI_st4_2_40x	4	2	2950.8	20160801	0.55
27_HEOBI_st4_1_40x	4	1	3317.0	20160801	0.53
50_HEOBI_st5_12_40x	5	12	13.6	20160801	NaN
49_HEOBI_st5_11_40x	5	11	28.0	20160801	0.08
48_HEOBI_st5_10_40x	5	10	68.4	20160801	0.07
47_HEOBI_st5_9_40x	5	9	98.1	20160801	0.08
46_HEOBI_st5_8_40x	5	8	147.8	20160801	0.08
45_HEOBI_st5_7_40x	5	7	196.9	20160801	0.09
44_HEOBI_st5_6_40x	5	6	294.9	20160801	0.23
43_HEOBI_st5_5_40x	5	5	690.0	20160801	0.38
42_HEOBI_st5_4_40x	5	4	986.2	20160801	0.43
41_HEOBI_st5_3_40x	5	3	1971.0	20160801	0.45
40_HEOBI_st5_2_40x	5	2	2951.1	20160801	0.51
39_HEOBI_st5_1_40x	5	1	2974.8	20160801	0.54
24_HEOBI_st6_12_40x	6	12	13.0	20160802	0.02
23_HEOBI_st6_11_40x	6	11	28.0	20160802	NaN
22_HEOBI_st6_10_40x	6	10	68.0	20160802	0.01
21_HEOBI_st6_9_40x	6	9	97.8	20160802	0.04
20_HEOBI_st6_8_40x	6	8	196.3	20160802	0.11
19_HEOBI_st6_7_40x	6	7	294.8	20160802	0.37
18_HEOBI_st6_6_40x	6	6	492.8	20160802	0.33
17_HEOBI_st6_5_40x	6	5	690.5	20160802	0.35
16_HEOBI_st6_4_40x	6	4	986.2	20160802	0.33
15_HEOBI_st6_3_40x	6	3	1479.4	20160802	0.35
20_HEOBI_6_2	6	2	1577.7	20161206	0.40
13_HEOBI_st6_1_40x	6	1	1627.8	20160802	0.37
21_HEOBI_7_12	7	12	13.8	20161206	0.02
35_HEOBI_st7_11_40x	7	11	27.6	20160802	NaN
34_HEOBI_st7_10_40x	7	10	67.6	20160802	0.01
33_HEOBI_st7_9_40x	7	9	97.7	20160802	0.05
32_HEOBI_st7_8_40x	7	8	147.0	20160802	0.04
31_HEOBI_st7_7_40x	7	7	197.8	20160802	0.10
30_HEOBI_st7_6_40x	7	6	246.0	20160802	0.32
29_HEOBI_st7_5_40x	7	5	295.0	20160802	0.29
28_HEOBI_st7_4_40x	7	4	345.1	20160802	0.29
27_HEOBI_st7_3_40x	7	3	394.0	20160802	0.27
26_HEOBI_st7_2_40x	7	2	414.2	20160802	0.26
25_HEOBI_st7_1_40x	7	1	434.6	20160802	0.35
48_HEOBI_st9_12_40x	9	12	14.1	20160802	0.12
47_HEOBI_st9_11_40x	9	11	23.8	20160802	0.09
46_HEOBI_st9_10_40x	9	10	38.7	20160802	0.10
45_HEOBI_st9_9_40x	9	9	67.5	20160802	0.10
44_HEOBI_st9_8_40x	9	8	96.8	20160802	0.13
43_HEOBI_st9_7_40x	9	7	146.7	20160802	0.17
42_HEOBI_st9_6_40x	9	6	195.7	20160802	0.26
41_HEOBI_st9_5_40x	9	5	245.6	20160802	0.49
40_HEOBI_st9_4_40x	9	4	295.4	20160802	0.62
39_HEOBI_st9_3_40x	9	3	345.2	20160802	0.67
38_HEOBI_st9_2_40x	9	2	373.9	20160802	0.73

Sample name	Station	Bottle	Depth (m)	SeaFAST date	DFe (nmol L^{-1})
37_HEOBI_st9_1_40x	9	1	394.9	20160802	0.77
26_HEOBI_st10_12_40x	10	12	13.9	20160804	0.07
25_HEOBI_st10_11_40x	10	11	27.6	20160804	0.04
24_HEOBI_st10_10_40x	10	10	48.3	20160804	0.05
23_HEOBI_st10_9_40x	10	9	72.3	20160804	0.02
22_HEOBI_st10_8_40x	10	8	118.0	20160804	0.05
21_HEOBI_st10_7_40x	10	7	146.9	20160804	0.13
20_HEOBI_st10_6_40x	10	6	200.3	20160804	0.24
19_HEOBI_st10_5_40x	10	5	250.0	20160804	0.20
18_HEOBI_st10_4_40x	10	4	300.9	20160804	0.21
17_HEOBI_st10_3_40x	10	3	316.1	20160804	0.26
16_HEOBI_st10_2_40x	10	2	349.3	20160804	0.31
15_HEOBI_st10_1_40x	10	1	358.4	20160804	0.36
46_HEOBI_11_12	11	12	13.1	20170602	0.20
45_HEOBI_11_11	11	11	28.6	20170602	0.07
44_HEOBI_11_10	11	10	67.8	20170602	0.22
43_HEOBI_11_9	11	9	98.1	20170602	0.05
42_HEOBI_11_8	11	8	197.2	20170602	0.08
41_HEOBI_11_7	11	7	295.4	20170602	0.34
40_HEOBI_11_6	11	6	493.1	20170602	0.53
39_HEOBI_11_5	11	5	689.4	20170602	0.65
38_HEOBI_11_4	11	4	986.5	20170602	0.55
37_HEOBI_11_3	11	3	1577.8	20170602	0.52
36_HEOBI_11_2	11	2	2559.8	20170602	0.40
35_HEOBI_11_1	11	1	2658.5	20170602	NaN
21_HEOBI_st12_6_40x	12	6	13.1	20161012	2.16
20_HEOBI_st12_5_40x	12	5	28.3	20161012	2.24
19_HEOBI_st12_4_40x	12	4	47.5	20161012	2.22
18_HEOBI_st12_3_40x	12	3	66.6	20161012	2.25
17_HEOBI_st12_2_40x	12	2	87.5	20161012	2.19
16_HEOBI_st12_1_40x	12	1	102.1	20161012	1.88
28_HEOBI_st13_10_40x	13	10	13.6	20161012	1.25
27_HEOBI_st13_9_40x	13	9	28.9	20161012	1.24
26_HEOBI_st13_8_40x	13	8	48.6	20161012	1.29
25_HEOBI_st13_7_40x	13	7	67.4	20161012	1.39
24_HEOBI_st13_6_40x	13	6	96.9	20161012	1.37
23_HEOBI_st13_2_40x	13	2	117.6	20161012	1.41
22_HEOBI_st13_1_40x	13	1	132.1	20161012	1.31
35_HEOBI_st14_7_40x	14	7	13.2	20161012	0.97
34_HEOBI_st14_6_40x	14	6	28.6	20161012	1.00
33_HEOBI_st14_5_40x	14	5	47.8	20161012	1.13
32_HEOBI_st14_4_40x	14	4	97.6	20161012	1.22
31_HEOBI_st14_3_40x	14	3	122.5	20161012	1.22
30_HEOBI_st14_2_40x	14	2	157.2	20161012	1.17
29_HEOBI_st14_1_40x	14	1	172.2	20161012	1.21
41_HEOBI_st15_6_40x	15	6	13.5	20161012	1.60
40_HEOBI_st15_5_40x	15	5	28.6	20161012	1.54
39_HEOBI_st15_4_40x	15	4	48.5	20161012	1.56
38_HEOBI_st15_3_40x	15	3	68.2	20161012	1.62
37_HEOBI_st15_2_40x	15	2	98.3	20161012	1.60
36_HEOBI_st15_1_40x	15	1	117.5	20161012	1.54
47_HEOBI_st16_6_40x	16	6	13.3	20161012	0.79
46_HEOBI_st16_5_40x	16	5	28.4	20161012	0.94
45_HEOBI_st16_4_40x	16	4	67.9	20161012	1.04

Table 4-1 Continued

Sample name	Station	Bottle	Depth (m)	SeaFAST date	DFe (nmol L^{-1})
44_HEOBI_st16_3_40x	16	3	121.7	20161012	1.26
43_HEOBI_st16_2_40x	16	2	175.8	20161012	1.55
42_HEOBI_st16_1_40x	16	1	187.2	20161012	1.56
16_HEOBI_18_12	18	12	12.6	20170603	0.11
17_HEOBI_18_11	18	11	27.8	20170603	0.28
18_HEOBI_18_10	18	10	67.8	20170603	0.04
19_HEOBI_18_9	18	9	96.9	20170603	0.03
20_HEOBI_18_8	18	8	147.6	20170603	0.05
21_HEOBI_18_7	18	7	197.0	20170603	0.21
22_HEOBI_18_6	18	6	294.5	20170603	0.41
23_HEOBI_18_5	18	5	491.8	20170603	0.40
24_HEOBI_18_4	18	4	690.6	20170603	0.31
25_HEOBI_18_3	18	3	987.4	20170603	0.37
21_HEOBI_st19_6_40x	19	6	13.6	20161013	0.94
20_HEOBI_st19_5_40x	19	5	28.1	20161013	0.92
19_HEOBI_st19_4_40x	19	4	48.4	20161013	1.00
18_HEOBI_st19_3_40x	19	3	68.1	20161013	0.92
17_HEOBI_st19_2_40x	19	2	78.2	20161013	0.97
16_HEOBI_st19_1_40x	19	1	88.0	20161013	0.85
27_HEOBI_st20_6_40x	20	6	13.8	20161013	0.44
26_HEOBI_st20_5_40x	20	5	28.4	20161013	0.51
25_HEOBI_st20_4_40x	20	4	47.9	20161013	0.55
24_HEOBI_st20_3_40x	20	3	67.2	20161013	0.74
23_HEOBI_st20_2_40x	20	2	88.1	20161013	0.98
22_HEOBI_st20_1_40x	20	1	93.1	20161013	1.00
23_HEOBI_st21_8_40x	21	8	13.3	20160809	0.12
22_HEOBI_st21_7_40x	21	7	28.7	20160809	0.17
21_HEOBI_st21_6_40x	21	6	48.8	20160809	0.56
20_HEOBI_st21_5_40x	21	5	68.3	20160809	0.70
19_HEOBI_st21_4_40x	21	4	88.3	20160809	0.65
18_HEOBI_st21_3_40x	21	3	98.1	20160809	0.87
17_HEOBI_st21_2_40x	21	2	107.5	20160809	0.60
16_HEOBI_st21_1_40x	21	1	112.6	20160809	0.91
33_HEOBI_st22_6_40x	22	6	13.8	20161013	1.57
32_HEOBI_st22_5_40x	22	5	28.0	20161013	1.55
31_HEOBI_st22_4_40x	22	4	49.1	20161013	1.22
30_HEOBI_st22_3_40x	22	3	68.0	20161013	1.08
29_HEOBI_st22_2_40x	22	2	86.9	20161013	1.09
28_HEOBI_st22_1_40x	22	1	108.4	20161013	1.09
27_HEOBI_st23_6_40x	23	6	14.4	20161017	2.05
26_HEOBI_st23_5_40x	23	5	28.2	20161017	1.95
25_HEOBI_st23_4_40x	23	4	48.1	20161017	1.66
24_HEOBI_st23_3_40x	23	3	59.3	20161017	1.34
23_HEOBI_st23_2_40x	23	2	67.7	20161017	1.39
22_HEOBI_st23_1_40x	23	1	75.0	20161017	1.42
31_HEOBI_st24_4_40x	24	4	13.9	20161017	2.15
30_HEOBI_st24_3_40x	24	3	20.5	20161017	2.07
29_HEOBI_st24_2_40x	24	2	28.9	20161017	2.30
28_HEOBI_st24_1_40x	24	1	35.3	20161017	1.95
17_HEOBI_st25_6_40x	25	6	13.9	20161014	1.06
16_HEOBI_st25_5_40x	25	5	29.1	20161014	0.78
34_HEOBI_st25_4_40x	25	4	58.1	20161017	1.38
33_HEOBI_st25_3_40x	25	3	87.7	20161017	1.41
32_HEOBI_st25_2_40x	25	2	108.2	20161017	1.24

Sample name	Station	Bottle	Depth (m)	SeaFAST date	DFe (nmol L^{-1})
15_HEOBI_st25_1_40x	25	1	119.6	20161014	1.23
40_HEOBI_st26_6_40x	26	6	12.9	20161017	1.87
39_HEOBI_st26_5_40x	26	5	28.7	20161017	1.74
38_HEOBI_st26_4_40x	26	4	58.0	20161017	1.78
37_HEOBI_st26_3_40x	26	3	88.5	20161017	1.69
36_HEOBI_st26_2_40x	26	2	107.5	20161017	1.67
35_HEOBI_st26_1_40x	26	1	120.0	20161017	1.70
23_HEOBI_st27_6_40x	27	6	13.9	20161014	1.69
22_HEOBI_st27_5_40x	27	5	28.7	20161014	1.32
21_HEOBI_st27_4_40x	27	4	58.3	20161014	1.71
20_HEOBI_st27_3_40x	27	3	88.3	20161014	2.08
19_HEOBI_st27_2_40x	27	2	107.9	20161014	2.02
18_HEOBI_st27_1_40x	27	1	119.7	20161014	2.11
29_HEOBI_st28_6_40x	28	6	12.7	20161014	1.41
28_HEOBI_st28_5_40x	28	5	28.5	20161014	1.50
27_HEOBI_st28_4_40x	28	4	58.7	20161014	1.72
26_HEOBI_st28_3_40x	28	3	88.0	20161014	1.83
25_HEOBI_st28_2_40x	28	2	107.8	20161014	1.80
24_HEOBI_st28_1_40x	28	1	117.3	20161014	1.88
35_HEOBI_st29_6_40x	29	6	13.4	20161014	1.52
34_HEOBI_st29_5_40x	29	5	29.0	20161014	1.42
33_HEOBI_st29_4_40x	29	4	56.9	20161014	1.46
32_HEOBI_st29_3_40x	29	3	78.1	20161014	1.55
31_HEOBI_st29_2_40x	29	2	92.9	20161014	1.63
30_HEOBI_st29_1_40x	29	1	101.0	20161014	1.49
29_HEOBI_st30_6_40x	30	6	13.9	20160809	1.26
28_HEOBI_st30_5_40x	30	5	28.2	20160809	1.26
27_HEOBI_st30_4_40x	30	4	67.5	20160809	1.37
26_HEOBI_st30_3_40x	30	3	98.3	20160809	1.28
25_HEOBI_st30_2_40x	30	2	147.4	20160809	1.12
24_HEOBI_st30_1_40x	30	1	186.9	20160809	1.01
38_HEOBI_st31_9_40x	31	9	12.6	20160809	0.37
37_HEOBI_st31_8_40x	31	8	48.3	20160809	0.36
36_HEOBI_st31_7_40x	31	7	97.4	20160809	0.22
35_HEOBI_st31_6_40x	31	6	147.4	20160809	0.41
34_HEOBI_st31_5_40x	31	5	245.2	20160809	0.70
33_HEOBI_st31_4_40x	31	4	345.0	20160809	0.68
32_HEOBI_st31_3_40x	31	3	395.4	20160809	0.67
31_HEOBI_st31_2_40x	31	2	443.7	20160809	0.84
30_HEOBI_st31_1_40x	31	1	468.6	20160809	0.70
22_HEOBI_32_6	32	6	12.9	20170602	0.14
21_HEOBI_32_5	32	5	47.9	20170602	0.15
20_HEOBI_32_4	32	4	87.5	20170602	0.48
19_HEOBI_32_3	32	3	147.4	20170602	0.67
18_HEOBI_32_2	32	2	196.4	20170602	0.75
17_HEOBI_32_1	32	1	271.0	20170602	0.86
28_HEOBI_33_9	33	9	14.2	20170602	0.26
27_HEOBI_33_8	33	8	48.3	20170602	0.18
26_HEOBI_33_7	33	7	97.7	20170602	0.18
25_HEOBI_33_6	33	6	148.0	20170602	0.25
24_HEOBI_33_5	33	5	221.2	20170602	0.32
23_HEOBI_33_4	33	4	294.0	20170602	0.57
27_HEOBI_33_3	33	3	394.9	20161206	0.48
26_HEOBI_33_2	33	2	494.6	20161206	0.67

Table 4-1 Continued

Sample name	Station	Bottle	Depth (m)	SeaFAST date	DFe (nmol L^{-1})
25_HEOBI_33_1	33	1	526.8	20161206	0.62
34_HEOBI_34_9	34	9	13.5	20170602	0.27
33_HEOBI_34_8	34	8	48.1	20170602	0.40
32_HEOBI_34_7	34	7	96.1	20170602	0.25
31_HEOBI_34_6	34	6	147.5	20170602	0.09
30_HEOBI_34_5	34	5	219.6	20170602	0.12
29_HEOBI_34_4	34	4	296.8	20170602	0.45
29_HEOBI_34_3	34	3	444.7	20161206	0.47
28_HEOBI_34_2	34	2	542.6	20161206	0.49
36_HEOBI_35_6	35	6	13.6	20161206	0.50
35_HEOBI_35_5	35	5	28.7	20161206	0.51
34_HEOBI_35_4	35	4	68.1	20161206	0.73
33_HEOBI_35_3	35	3	97.4	20161206	0.87
32_HEOBI_35_2	35	2	137.3	20161206	0.95
31_HEOBI_35_1	35	1	146.7	20161206	0.80
39_HEOBI_st36_4_40x	36	4	14.1	20161014	1.33
38_HEOBI_st36_3_40x	36	3	28.5	20161014	1.69
37_HEOBI_st36_2_40x	36	2	58.3	20161014	1.43
36_HEOBI_st36_1_40x	36	1	71.3	20161014	1.82
43_HEOBI_st37_4_40x	37	4	13.7	20161014	1.51
42_HEOBI_st37_3_40x	37	3	28.5	20161014	1.43
41_HEOBI_st37_2_40x	37	2	58.5	20161014	1.40
40_HEOBI_st37_1_40x	37	1	68.2	20161014	1.30
47_HEOBI_st38_4_40x	38	4	14.1	20161014	1.35
46_HEOBI_st38_3_40x	38	3	28.6	20161014	1.36
45_HEOBI_st38_2_40x	38	2	58.5	20161014	1.25
44_HEOBI_st38_1_40x	38	1	75.4	20161014	1.29
37_HEOBI_39_4	39	4	13.5	20161206	1.71
50_HEOBI_st39_3_40x	39	3	28.7	20161014	1.47
49_HEOBI_st39_2_40x	39	2	45.6	20161014	1.63
48_HEOBI_st39_1_40x	39	1	77.2	20161014	1.61
45_HEOBI_st40_5_40x	40	5	13.8	20161017	1.69
44_HEOBI_st40_4_40x	40	4	28.8	20161017	1.84
43_HEOBI_st40_3_40x	40	3	48.6	20161017	1.84
42_HEOBI_st40_2_40x	40	2	63.4	20161017	1.58
41_HEOBI_st40_1_40x	40	1	72.4	20161017	1.65

Table 4-2 Mean concentrations of dissolved iron (DFe), nitrate (NO_3^-) and phosphate (PO_4^{3-}) in the mixed layer (ML) and upper 50 m for stations in each region.

Region	Station	Day	Lat (°N)	Lon (°E)	ML (m)	DFe (nM)		NO3 (µM)		PO4 (µM)		Si (µM)	
						ML	50 m	ML	50 m	ML	50 m	ML	50 m
Transect B	2	16	-48.2798	79.36634	98	0.14	0.11	20.4	20.6	1.40	1.41	1.80	2.05
	4	18	-50.24	77.72869	128	0.15	0.12	20.3	19.2	1.44	1.34	1.66	0.75
	5	19	-50.691	76.18671	154	0.08	0.08	27.2	27.0	1.86	1.83	29.03	28.81
	6	20	-50.7888	75.78225	189	0.03	0.02	24.8	24.2	1.55	1.51	5.81	4.06
	7	20	-50.8996	75.37746	123	0.03	0.02	25.2	23.7	1.70	1.59	10.69	5.61
	9	21	-51.2871	73.80983	181	0.12	0.10	22.5	20.8	1.63	1.44	7.12	1.59
	10	21	-51.5064	72.99996	187	0.06	0.05	23.4	21.5	1.55	1.29	8.52	2.32
	Mean					0.09	0.07	23.4	22.4	1.59	1.49	9.23	6.45
	±1sd					0.05	0.04	2.5	2.7	0.16	0.18	9.34	9.99
Transect C	30	39	-52.922	74.02227	203	1.22	1.26	25.7	25.4	1.88	1.86	13.23	11.65
	31	40	-52.6964	74.79167	331	0.41	0.37	26.8	25.1	1.91	1.73	15.41	5.86
	32	41	-52.5428	75.26237	285	0.51	0.14	27.6	24.8	1.96	1.66	21.57	4.15
	33	41	-52.4092	75.60666	254	0.24	0.22	28.3	24.7	1.93	1.61	20.02	3.91
	34	41	-52.302	76.00671	245	0.23	0.34	27.9	25.7	1.90	1.66	17.67	6.06
	35	42	-52.8381	74.32217	162	0.73	0.50	25.6	24.9	1.91	1.81	15.34	10.90
	Mean					0.56	0.47	27.0	25.1	1.92	1.72	17.21	7.09
	±1sd					0.37	0.41	1.1	0.4	0.03	0.10	3.15	3.36

Table 4-2 Continued

Region	Station	Day	Lat (°N)	Lon (°E)	ML (m)	DFe (nM)		NO3 (µM)		PO4 (µM)		Si (µM)	
						ML	50 m	ML	50 m	ML	50 m	ML	50 m
Heard Island	19	34	-53.0599	73.98966	100	0.93	0.95	23.9	23.8	1.77	1.76	7.84	7.57
	20	34	-53.2133	73.63984	112	0.71	0.50	24.4	24.3	1.82	1.79	9.73	8.51
	21	34	-53.2808	73.31556	124	0.57	0.28	24.3	23.5	1.80	1.68	9.14	3.73
	22	34	-52.9604	73.23888	124	1.27	1.45	25.4	25.4	1.91	1.92	11.95	11.38
	23	35	-53.0059	73.72118	88	1.63	1.88	25.2	25.3	1.86	1.86	10.68	10.78
	24	35	-53.0037	73.60683	48	2.12	2.12	25.1	25.1	1.89	1.89	11.32	11.32
	36	42	-53.0077	73.70902	84	1.57	1.51	24.6	24.6	1.85	1.85	10.04	10.04
	37	42	-53.0118	73.71645	82	1.41	1.47	24.7	24.7	1.85	1.85	10.15	10.16
	38	42	-53.0074	73.72444	88	1.31	1.35	24.9	24.9	1.82	1.82	9.69	9.69
	39	42	-53.0027	73.71675	90	1.61	1.60	25.1	25.1	1.83	1.83	10.10	10.10
	40	43	-53.0076	73.7161	85	1.72	1.79	25.0	25.0	1.84	1.84	10.00	9.89
	Mean					1.35	1.36	24.8	24.7	1.84	1.83	10.06	9.38
	±1sd					0.46	0.57	0.5	0.6	0.04	0.06	1.07	2.18

Table 4-2 Continued

Region	Station	Day	Lat (°N)	Lon (°E)	ML (m)	DFe (nM)		NO3 (µM)		PO4 (µM)		Si (µM)	
						ML	50 m	ML	50 m	ML	50 m	ML	50 m
McDonald Islands	12	27	-53.0323	72.65818	122	2.16	2.21	25.7	25.6	1.90	1.89	14.59	13.96
	13	28	-52.9988	72.62552	166	1.32	1.26	25.2	24.5	1.86	1.78	12.78	9.52
	14	29	-53.0351	72.55227	190	1.13	1.03	25.5	25.2	1.88	1.87	14.09	12.87
	15	29	-53.0726	72.5929	124	1.58	1.57	25.3	25.2	1.86	1.86	13.23	12.92
	16	29	-52.9846	72.55511	207	1.19	0.86	25.4	25.3	1.88	1.86	14.14	13.23
	25	37	-53.035	72.66254	121	1.18	0.92	24.8	24.2	1.89	1.83	14.82	11.66
	26	37	-53.0288	72.66081	133	1.74	1.80	25.1	24.9	1.93	1.91	16.05	15.31
	27	37	-53.0334	72.66873	132	1.82	1.51	25.3	25.0	1.92	1.89	15.41	14.04
	28	37	-53.0387	72.66159	133	1.69	1.46	25.1	25.0	1.92	1.91	15.40	14.73
	29	38	-53.0337	72.65347	114	1.51	1.47	25.7	25.6	1.94	1.92	16.44	15.75
	Mean					1.53	1.41	25.3	25.0	1.90	1.87	14.70	13.40
	±1sd					0.33	0.41	0.3	0.4	0.03	0.04	1.17	1.83
Reference	11	23	-52.9275	71.36159	282	0.12	0.14	25.9	24.6	1.69	1.55	6.56	0.87
	18	31	-54.1674	73.66494	202	0.12	0.19	27.2	25.8	1.87	1.76	18.63	12.66
	Mean					0.12	0.16	26.6	25.2	1.78	1.65	12.59	6.77
	±1sd					0.00	0.04	0.9	0.9	0.13	0.14	8.54	8.34

4.9 References

Anderson, L.A., Sarmiento, J.L., 1994. Redfield ratios of remineralization determined by nutrient data analysis. Global Biogeochem. Cycles 8, 65–80. doi:10.1029/93GB03318

Blain, S., Bonnet, S., Guieu, C., 2008b. Dissolved iron distribution in the tropical and sub tropical South Eastern Pacific. Biogeosciences 5, 269–280. doi:10.5194/bgd-4-2845-2007

Blain, S., Quéguiner, B., Armand, L., Belviso, S., Bombled, B., Bopp, L., Bowie, A., Brunet, C., Brussaard, C., Carlotti, F., Christaki, U., Corbière, A., Durand, I., Ebersbach, F., Fuda, J.-L., Garcia, N., Gerringa, L., Griffiths, B., Guigue, C., Guillerm, C., Jacquet, S., Jeandel, C., Laan, P., Lefèvre, D., Lo Monaco, C., Malits, A., Mosseri, J., Obernosterer, I., Park, Y.-H., Picheral, M., Pondaven, P., Remenyi, T., Sandroni, V., Sarthou, G., Savoye, N., Scouarnec, L., Souhaut, M., Thuiller, D., Timmermans, K., Trull, T., Uitz, J., van Beek, P., Veldhuis, M., Vincent, D., Viollier, E., Vong, L., Wagener, T., 2007. Effect of natural iron fertilization on carbon sequestration in the Southern Ocean. Nature 446, 1070–4. doi:10.1038/nature05700

Blain, S., Sarthou, G., Laan, P., 2008a. Distribution of dissolved iron during the natural iron-fertilization experiment KEOPS (Kerguelen Plateau, Southern Ocean). Deep Sea Res. Part II Top. Stud. Oceanogr. 55, 594–605. doi:10.1016/j.dsr2.2007.12.028

Blain, S., Sedwick, P.N., Griffiths, F.B., Quéguiner, B., Bucciarelli, E., Fiala, M., Pondaven, P., Tréguer, P., 2002. Quantification of algal iron requirements in the Subantarctic Southern

Ocean (Indian sector). Deep. Res. Part II Top. Stud. Oceanogr. 49, 3255–3273. doi:10.1016/S0967-0645(02)00082-6

Blain, S., Tréguer, P., Belviso, S., Bucciarelli, E., Denis, M., Desabre, S., Fiala, M., Martin Jézéquel, V., Le Fèvre, J., Mayzaud, P., Marty, J.-C., Razouls, S., 2001. A biogeochemical study of the island mass effect in the context of the iron hypothesis: Kerguelen Islands, Southern Ocean. Deep Sea Res. Part I Oceanogr. Res. Pap. 48, 163–187. doi:10.1016/S0967-0637(00)00047-9

Bowie, A.R., Lannuzel, D., Remenyi, T. a., Wagener, T., Lam, P.J., Boyd, P.W., Guieu, C., Townsend, A.T., Trull, T.W., 2009. Biogeochemical iron budgets of the Southern Ocean south of Australia: Decoupling of iron and nutrient cycles in the subantarctic zone by the summertime supply. Global Biogeochem. Cycles 23, n/a-n/a. doi:10.1029/2009gb003500

Bowie, A.R., Lohan, M.C., 2009. Analysis of iron in seawater, in: Wurl, O. (Ed.), Practical Guidelines for the Analysis of Seawater. Taylor and Francis, Boca Raton, Fla., pp. 235–257.

Bowie, A.R., van der Merwe, P., Quéroué, F., Trull, T., Fourquez, M., Planchon, F., Sarthou, G., Chever, F., Townsend, A.T., Obernosterer, I., Sallée, J.-B., Blain, S., 2015. Iron budgets for three distinct biogeochemical sites around the Kerguelen archipelago (Southern Ocean) during the natural fertilisation experiment KEOPS-2. Biogeosciences Discuss. 11, 17861–17923. doi:10.5194/bgd-11-17861-2014

Bown, J., Boye, M., Laan, P., Bowie, A.R., Park, Y.-H., Jeandel, C., Nelson, D.M., 2012. Imprint of a dissolved cobalt basaltic source on the Kerguelen Plateau. Biogeosciences 9, 5279–

5290. doi:http://dx.doi.org/10.5194/bg-9-5279-2012

Boyd, P.W., Arrigo, K.R., Strzepek, R., van Dijken, G.L., 2012. Mapping phytoplankton iron utilization: Insights into Southern Ocean supply mechanisms. J. Geophys. Res. 117, C06009. doi:10.1029/2011JC007726

Boyd, P.W., Ellwood, M.J., 2010. The biogeochemical cycle of iron in the ocean. Nat. Geosci. doi:10.1038/ngeo964

Boyd, P.W., Ellwood, M.J., Tagliabue, A., Twining, B.S., 2017. Biotic and abiotic retention, recycling and remineralization of metals in the ocean. Nat. Geosci. 10, 167–173. doi:10.1038/ngeo2876

Boyd, P.W., Jickells, T., Law, C.S., Blain, S., Boyle, E. a, Buesseler, K.O., Coale, K.H., Cullen, J.J., de Baar, H.J.W., Follows, M., Harvey, M., Lancelot, C., Levasseur, M., Owens, N.P.J., Pollard, R., Rivkin, R.B., Sarmiento, J., Schoemann, V., Smetacek, V., Takeda, S., Tsuda, a, Turner, S., Watson, a J., 2007. Mesoscale iron enrichment experiments 1993-2005: synthesis and future directions. Science 315, 612–7. doi:10.1126/science.1131669

Boyd, P.W., Law, C.S., Hutchins, D. a., Abraham, E.R., Croot, P.L., Ellwood, M., Frew, R.D., Hadfield, M., Hall, J., Handy, S., Hare, C., Higgins, J., Hill, P., Hunter, K. a., LeBlanc, K., Maldonado, M.T., McKay, R.M., Mioni, C., Oliver, M., Pickmere, S., Pinkerton, M., Safi, K., Sander, S., Sanudo-Wilhelmy, S. a., Smith, M., Strzepek, R., Tovar-Sanchez, a., Wilhelm, S.W., 2005. FeCycle: Attempting an iron biogeochemical budget from a mesoscale SF6 tracer experiment in unperturbed low iron waters. Global Biogeochem. Cycles 19, 1–13. doi:10.1029/2005GB002494

Brzezinski, M.A., 1985. The Si: C: N ratio of marine diatoms: interspecific variability and the effect of some environmental variables. J. Phycol. 21, 347–357. doi:10.1111/j.0022-3646.1985.00347.x

Brzezinski, M.A., Dickson, M.-L., Nelson, D.M., Sambrotto, R., 2003. Ratios of Si, C and N uptake by microplankton in the Southern Ocean. Deep. Res. Part II Top. Stud. Oceanogr. 50, 619–633. doi:https://doi.org/10.1016/S0967-0645(02)00587-8

Closset, I., Lasbleiz, M., Leblanc, K., Quéguiner, B., Cavagna, a.-J., Elskens, M., Navez, J., Cardinal, D., 2014. Seasonal evolution of net and regenerated silica production around a natural Fe-fertilized area in the Southern Ocean estimated with Si isotopic approaches. Biogeosciences 11, 5827–5846. doi:10.5194/bg-11-5827-2014

Cutter, G., Andersson, P., Codispoti, L., Croot, P., Francois, R., Lohan, M., Obata, H., Rutgers, M., 2014. Sampling and Sample-handling Protocols for GEOTRACES Cruises.

de Baar, H.J.W., Boyd, P.W., Coale, K.H., Landry, M.R., Tsuda, A., Assmy, P., Bakker, D.C.E., Bozec, Y., Barber, R.T., Brzezinski, M. a., Buesseler, K.O., Boyé, M., Croot, P.L., Gervais, F., Gorbunov, M.Y., Harrison, P.J., Hiscock, W.T., Laan, P., Lancelot, C., Law, C.S., Levasseur, M., Marchetti, A., Millero, F.J., Nishioka, J., Nojiri, Y., van Oijen, T., Riebesell, U., Rijkenberg, M.J. a, Saito, H., Takeda, S., Timmermans, K.R., Veldhuis, M.J.W., Waite, A.M., Wong, C.S., 2005. Synthesis of iron fertilization experiments: From the iron age in the age of enlightenment. J. Geophys. Res. C Ocean. 110, 1–24. doi:10.1029/2004JC002601

de Boyer Montégut, C., Madec, G., Fischer, A.S., Lazar, A., Iudicone, D., 2004. Mixed layer

depth over the global ocean: An examination of profile data and a profile-based climatology. J. Geophys. Res. C Ocean. 109, 1–20. doi:10.1029/2004JC002378

de Jong, J.T.., den Das, J., Bathmann, U., Stoll, M.H.., Kattner, G., Nolting, R.., de Baar, H.J.., 1998. Dissolved iron at subnanomolar levels in the Southern Ocean as determined by ship-board analysis. Anal. Chim. Acta 377, 113–124. doi:10.1016/S0003-2670(98)00427-9

Dehairs, F., Fripiat, F., Cavagna, A.-J., Trull, T.W., Fernandez, C., Davies, D., Roukaerts, A., Fonseca Batista, D., Planchon, F., Elskens, M., 2015. Nitrogen cycling in the Southern Ocean Kerguelen Plateau area: evidence for significant surface nitrification from nitrate isotopic compositions. Biogeosciences 12, 1459–1482. doi:10.5194/bg-12-1459-2015

Gruber, N., Sarmiento, J.L., 1997. Global patterns of marine nitrogen fixation and denitrification. Global Biogeochem. Cycles 11, 235–266. doi:10.1029/97GB00077

Ho, T.-Y., Quigg, A., Finkel, Z. V., Milligan, A.J., Wyman, K., Falkowski, P.G., Morel, F.M.M., 2003. The elemental composition of some marine phytoplankton. J. Phycol. 39, 1145–1159. doi:10.1111/j.0022-3646.2003.03-090.x

Hoppe, C.J.M., Klaas, C., Ossebaar, S., Soppa, M.A., Cheah, W., Laglera, L.M., Santos-Echeandia, J., Rost, B., Wolf-Gladrow, D.A., Bracher, A., Hoppema, M., Strass, V., Trimborn, S., 2017. Controls of primary production in two phytoplankton blooms in the Antarctic Circumpolar Current. Deep. Res. Part II Top. Stud. Oceanogr. 138, 63–73. doi:10.1016/j.dsr2.2015.10.005

Hoppema, M., Goeyens, L., Fahrbach, E., 2000. Intense nutrient removal in the remote area off Larsen Ice Shelf (Weddell Sea). Polar Biol. 23, 85–94. doi:10.1007/s003000050012

Hutchins, D.A., Bruland, K.W., 1998. Iron-limited diatom growth and Si:N uptake ratios in a coastal upwelling regime. Nature 393, 561–564. doi:10.1038/31203

Hutchins, D.A., DiTullio, G.R., Zhang, Y., Bruland, K.W., 1998. An iron limitation mosaic in the Californian upwelling regime. Limnol. Oceanogr. 43, 1037–1054.

Hutchins, D.A., DiTullio, G.R., Burland, K.W., 1993. Iron and regenerated production: Evidence for biological iron recycling in two marine environments. Limnol. Oceanogr. 38, 1242–1255. doi:10.4319/lo.1993.38.6.1242

Jennings, J.C., Gordon, L.I., Nelson, D.M., 1984. Nutrient depletion indicates high primary productivity in the Weddell Sea. Nature 309, 51–54. doi:10.1038/309051a0

Maraldi, C., Mongin, M., Coleman, R., Testut, L., 2009. The influence of lateral mixing on a phytoplankton bloom: Distribution in the Kerguelen Plateau region. Deep Sea Res. Part I Oceanogr. Res. Pap. 56, 963–973. doi:10.1016/J.DSR.2008.12.018

Martin, J., 1990. Glacial-interglacial CO2 change: The iron hypothesis. Paleoceanography 5, 1–13.

Martin, J.H., Gordon, R.M., Fitzwater, S.E., 1990. Iron in Antarctic waters. Nature 345, 156–158. doi:10.1038/345156a0

McDougall, T.J., Barker, P.M., 2011. Getting started with TEOS-10 and the Gibbs Seawater (GSW) Oceanographic Toolbox. Scor/Iapso Wg127, ISBN 978-0-646-55621-5.

Mongin, M., Molina, E., Trull, T.W., 2008. Seasonality and scale of the Kerguelen plateau phytoplankton bloom: A remote sensing and modeling analysis of the influence of natural iron fertilization in the Southern Ocean. Deep Sea Res. Part II Top. Stud. Oceanogr. 55, 880–892. doi:10.1016/j.dsr2.2007.12.039

Mongin, M.M., Abraham, E.R., Trull, T.W., 2009. Winter advection of iron can explain the summer phytoplankton bloom that extends 1000 km downstream of the Kerguelen Plateau in the Southern Ocean. J. Mar. Res. 67, 225–237. doi:10.1357/002224009789051218

Moore, C.M., Mills, M.M., Achterberg, E.P., Geider, R.J., LaRoche, J., Lucas, M.I., McDonagh, E.L., Pan, X., Poulton, A.J., Rijkenberg, M.J. a., Suggett, D.J., Ussher, S.J., Woodward, E.M.S., 2009. Large-scale distribution of Atlantic nitrogen fixation controlled by iron availability. Nat. Geosci. 2, 867–871. doi:10.1038/ngeo667

Moore, C.M., Mills, M.M., Arrigo, K.R., Berman-Frank, I., Bopp, L., Boyd, P.W., Galbraith, E.D., Geider, R.J., Guieu, C., Jaccard, S.L., Jickells, T.D., La Roche, J., Lenton, T.M., Mahowald, N.M., Maranon, E., Marinov, I., Moore, J.K., Nakatsuka, T., Oschlies, A., Saito, M.A., Thingstad, T.F., Tsuda, A., Ulloa, O., 2013. Processes and patterns of oceanic nutrient limitation. Nat. Geosci 6, 701–710. doi:10.1038/ngeo1765

Moore, J.K., Doney, S.C., Glover, D.M., Fung, I.Y., 2001. Iron cycling and nutrient-limitation patterns in surface waters of the world ocean. Deep. Res. Part II Top. Stud. Oceanogr. 49,

463–507. doi:10.1016/S0967-0645(01)00109-6

Morris, P.J., Charette, M.A., 2013. A synthesis of upper ocean carbon and dissolved iron budgets for Southern Ocean natural iron fertilisation studies. Deep Sea Res. Part II Top. Stud. Oceanogr. 90, 147–157. doi:10.1016/j.dsr2.2013.02.001

Mosseri, J., Quéguiner, B., Armand, L., Cornet-Barthaux, V., 2008. Impact of iron on silicon utilization by diatoms in the Southern Ocean: A case study of Si/N cycle decoupling in a naturally iron-enriched area. Deep. Res. Part II Top. Stud. Oceanogr. 55, 801–819. doi:10.1016/j.dsr2.2007.12.003

NASA, 2002. Jet Propulsion Laboratory, Physical Oceanography Distributed Active Archive Center (JPL PO.DAAC). GHRSST Level 4 MUR Global Foundation Sea Surface Temperature Analysis (v4.1) (GDS versions 1 and 2). National Oceanographic Data Center, NOAA. (Accessed 20 November 2018).

Obata, H., Karatani, H., Nakayama, E., 1993. Automated determination of iron in seawater by chelating resin concentration and chemiluminescence detection. Anal. Chem. 65, 1524–1528. doi:10.1021/ac00059a007

Obernosterer, I., Christaki, U., Lefèvre, D., Catala, P., Van Wambeke, F., Lebaron, P., 2008. Rapid bacterial mineralization of organic carbon produced during a phytoplankton bloom induced by natural iron fertilization in the Southern Ocean. Deep Sea Res. Part II Top. Stud. Oceanogr. 55, 777–789. doi:10.1016/j.dsr2.2007.12.005

Parekh, P., Follows, M.J., Boyle, E.A., 2005. Decoupling of iron and phosphate in the global ocean. Global Biogeochem. Cycles 19, 1–16. doi:10.1029/2004GB002280

Park, Y.-H., Fuda, J.-L., Durand, I., Naveira Garabato, A.C., 2008b. Internal tides and vertical mixing over the Kerguelen Plateau. Deep Sea Res. Part II Top. Stud. Oceanogr. 55, 582–593. doi:10.1016/j.dsr2.2007.12.027

Park, Y.-H., Roquet, F., Durand, I., Fuda, J.-L., 2008a. Large-scale circulation over and around the Northern Kerguelen Plateau. Deep Sea Res. Part II Top. Stud. Oceanogr. 55, 566–581. doi:10.1016/j.dsr2.2007.12.030

Park, Y.Y.-H., Durand, I., Kestenare, E., Rougier, G., Zhou, M., d'Ovidio, F., Cotté, C., Lee, J.-H., 2014. Polar Front around the Kerguelen Islands: An up-to-date determination and associated circulation of surface/subsurface waters. J. Geophys. Res. Ocean. 1–18. doi:10.1002/2014JC010061.Received

Quéroué, F., Sarthou, G., Planquette, H.F., Bucciarelli, E., Chever, F., van der Merwe, P., Lannuzel, D., Townsend, A.T., Cheize, M., Blain, S., D'Ovidio, F., Bowie, A.R., 2015. High variability in dissolved iron concentrations in the vicinity of the Kerguelen Islands (Southern Ocean). Biogeosciences 12, 3869–3883. doi:10.5194/bg-12-3869-2015

Rees, C., Pender, L., Sherrin, K., Schwanger, C., Hughes, P., Tibben, S., Marouchos, A., Rayner, M., 2018. Methods for reproducible shipboard SFA nutrient measurement using RMNS and automated data processing. Limnol. Oceanogr. Methods lom3.10294. doi:10.1002/lom3.10294

Sarthou, G., Vincent, D., Christaki, U., Obernosterer, I., Timmermans, K.R., Brussaard, C.P.D., 2008. The fate of biogenic iron during a phytoplankton bloom induced by natural fertilisation: Impact of copepod grazing. Deep Sea Res. Part II Top. Stud. Oceanogr. 55, 734–751. doi:10.1016/j.dsr2.2007.12.033

Rijkenberg, M.J.A., Middag, R., Laan, P., Gerringa, L.J.A., van Aken, H.M., Schoemann, V., de Jong, J.T.M., de Baar, H.J.W., 2014. The distribution of dissolved iron in the west atlantic ocean. PLoS One 9, e101323. doi:10.1371/journal.pone.0101323

R Core Team, 2016. R: A Language and Environment for Statistical Computing Version 3.3.2. R Foundation for Statistical Computing, Vienna, Austria (URL). ⟨https://www. R-project.org/⟩.

Spain, E., Johnson, S., Hutton, B., Whittaker, J., Lucieer, V., Watson, S., Fox, J., Coffin, M.F., 2018. Shallow seafloor gas emissions near Heard and McDonald islands on the Kerguelen Plateau, Southern Indian Ocean, in: Proceedings from the GeoHab: Marine Geological and Biological Habitat Mapping. Santa Barbara, p. 123.Sunda, W.G., Huntsman, S.A., 1997. Interrelated influence of iron, light and cell size on marine phytoplankton growth. Nature 390, 389–392. doi:10.1038/37093

Sumner, M.D.S., 2016. raadtools: Tools for Synoptic Environmental Spatial Data. R package version 0.4.0.9001. URL ⟨https://github.com/AustralianAntarcticDivision/ raadtools⟩.

Sumner, M.D.S., 2017. roc: Working With Ocean Colour Data. R package version 0.0.8. 9001. URL ⟨https://github.com/mdsumner/roc⟩.

Sunda, W.G., Huntsman, S.A., 1995. Iron uptake and growth limitation in oceanic and coastal phytoplankton. Mar. Chem. 50, 189–206. doi:10.1016/0304-4203(95)00035-P

Sweeney, C., Hansell, D.A., Carlson, C.A., Codispoti, L.A., Gordon, L.I., Marra, J., Millero, F.J., Smith, W.O., Takahashi, T., 2000. Biogeochemical regimes, net community production and carbon export in the Ross Sea, Antarctica. Deep. Res. Part II Top. Stud. Oceanogr. 47, 3369–3394. doi:10.1016/S0967-0645(00)00072-2

Tagliabue, A., Aumont, O., Bopp, L., 2014. The impact of different external sources of iron on the global carbon cycle. Geophys. Res. Lett. 41, 10.1002/2013GL059059. doi:10.1002/2013GL059059.Received

Takeda, S., 1998. Influence of iron availability on nutrient consumption ratio of diatoms in oceanic waters. Nature 393, 774–777. doi:10.1038/31674

Timmermans, K.R., Gerringa, L.J.A., de Baar, H.J.W., van der Wagt, B., Veldhuis, M.J.W., de Jong, J.T.M., Croot, P.L., Boye, M., 2001. Growth rates of large and small Southern Ocean diatoms in relation to availability of iron in natural seawater. Limnol. Oceanogr. 46, 260–266. doi:10.4319/lo.2001.46.2.0260

Trull, T.W., Davies, D.M., Dehairs, F., Cavagna, A.-J., Lasbleiz, M., Laurenceau-Cornec, E.C., D'Ovidio, F., Planchon, F., Leblanc, K., Quéguiner, B., Blain, S., 2015. Chemometric perspectives on plankton community responses to natural iron fertilisation over and downstream of the Kerguelen Plateau in the Southern Ocean. Biogeosciences 12, 1029–1056. doi:10.5194/bg-12-1029-2015

Twining, B.S., Baines, S.B., 2013. The trace metal composition of marine phytoplankton. Ann. Rev. Mar. Sci. 5, 191–215. doi:http://dx.doi.org/10.1146/annurev-marine-121211-172322

Twining, B.S., Baines, S.B., Fisher, N.S., Landry, M.R., 2004. Cellular iron contents of plankton during the Southern Ocean Iron Experiment (SOFeX). Deep. Res. Part I Oceanogr. Res. Pap. 51, 1827–1850. doi:10.1016/j.dsr.2004.08.007

Tyrrell, T., Merico, A., Waniek, J.J., Wong, C.S., Metzl, N., Whitney, F., 2005. Effect of seafloor depth on phytoplankton blooms in high-nitrate, low-chlorophyll (HNLC) regions. J. Geophys. Res. Biogeosciences 110, n/a-n/a. doi:10.1029/2005JG000041

van der Merwe, P., Bowie, A.R., Quéroué, F., Armand, L., Blain, S., Chever, F., Davies, D., Dehairs, F., Planchon, F., Sarthou, G., Townsend, A.T., Trull, T.W., 2015. Sourcing the iron in the naturally fertilised bloom around the Kerguelen Plateau: particulate trace metal dynamics. Biogeosciences 12, 739–755. doi:10.5194/bg-12-739-2015

van der Merwe, P., Wuttig, K., Holmes, T., Chase, Z., Trull, T., Bowie, A.R., 2018. High Fe lability of particles sourced from glacial erosion, Heard Island, Southern Ocean. (In preparation).

van Wijk, E.M., Rintoul, S.R., Ronai, B.M., Williams, G.D., 2010. Regional circulation around Heard and McDonald Islands and through the Fawn Trough , central Kerguelen Plateau. Deep. Res. Part I 57, 653–669. doi:10.1016/j.dsr.2010.03.001

Watson, S.J., Coffin, M.F., Whittaker, J.M., Lucieer, V., Fox, J.M., Carey, R., Arculus, R.J., Bowie,

A.R., Chase, Z., Robertson, R., Martin, T., Cooke, F., 2016. Submarine geology and geomorphology of active Sub-Antarctic volcanoes: Heard and McDonald Islands, in: AGU Fall Meeting Abstracts.

Wojtasiewicz, B., Trull, T.W., Davies, D.M., Schallenberg, C., Clementson, L., and Hardman-Mountford, N.J., 2018. Possible explanations for the unexpected lack of phytoplankton biomass in naturally iron fertilized waters near Heard and McDonald islands in the Southern Ocean. (In preparation).

Wuttig, K., Townsend, A.T., van der Merwe, P., Gault-Ringold, M., Holmes, T., Schallenberg, C., Latour, P., Tonnard, M., Rijkenberg, M.J.A., Lannuzel, D., Bowie, A.R., 2019. Critical evaluation of a seaFAST system for the analysis of trace metals in marine samples. Talanta 197, 653–668. doi:10.1016/j.talanta.2019.01.047

Chapter 5

5 Glacial and hydrothermal sources of dissolved iron(II) in Southern Ocean waters surrounding Heard and McDonald Islands

This chapter has been prepared for submission as an article in Earth and Planetary Science Letters

Thomas M. Holmes[1,2], Kathrin Wuttig[1], Zanna Chase[2], Christina Schallenberg[1], Pier van der Merwe[1], Ashley T. Townsend[3] and Andrew R. Bowie[1,2].

[1]Antarctic Climate and Ecosystems Cooperative Research Centre (ACE CRC), University of Tasmania, Hobart, Australia
[2]Institute for Marine and Antarctic Studies (IMAS), University of Tasmania, Hobart, Australia
[3]Central Science Laboratory (CSL), University of Tasmania, Hobart, Australia.

5.1 Abstract

The Southern Ocean is the largest body of water in which iron limits the growth of phytoplankton. However, a phytoplankton bloom on the order of thousands of square kilometres forms each spring-summer in the Indian sector of the Southern Ocean, both above and to the west of the Kerguelen Plateau. In the central region of the Kerguelen plateau is an active volcanic hotspot, hosting two subaerial volcanically active islands, Heard and McDonald (HIMI), the former of which is largely covered by glaciers. In the absence of detailed biogeochemical studies near HIMI, we hypothesise that these two islands play a key role in supplying iron to the region.

Dissolved iron(II) (DFe(II)) is the short lived, potentially more bioavailable oxidation state of Fe in the ocean. Concentrations of DFe(II) in the surface ocean are inversely correlated to the concentration of reactive oxygen species such as hydrogen peroxide (H_2O_2), which decrease DFe(II) half-life. Here we report measurements of the transient species DFe(II) and H_2O_2 in the HIMI region of the Kerguelen Plateau. Surface DFe(II) concentrations at the open ocean reference station were generally very low (<0.09 nmol L^{-1}), while stations near Heard Island and McDonald Islands showed elevated concentrations over the entire water column (mean 0.24 nmol L^{-1} and 0.36 nmol L^{-1}, respectively). At Heard Island, the greatest DFe(II) concentrations (max 0.57 nmol L^{-1}) were detected north of the island, and an inverse correlation of DFe(II) concentrations with salinity suggest the origin is from a sea-terminating glacier on the island. At McDonald Islands, the greatest DFe(II) concentrations (1.01 nmol L^{-1}) were detected east of the island which, based on DFe(II) profiles from five targeted stations, appears likely to originate from shallow diffuse hydrothermalism. DFe(II):DFe(total) percentages at the sites of high DFe(II) concentrations at Heard and Mcdonald Islands (25% and 37%, respectively) adds further evidence that strong, but different reducing sources of Fe exist at each of the islands.

H_2O_2 and irradiance data suggests that over the plateau near HIMI, DFe(II) concentrations are more strongly governed by strong DFe(II) sources rather than by H_2O_2 and irradiance.

5.2 Introduction

Iron (Fe) is a key limiting, or co-limiting, micronutrient for biological production (Martin et al., 1990; Moore et al., 2013) in as much as half of the world's oceans (Moore et al., 2009, 2001) with important implications for biogeochemical cycling and the drawdown of carbon from the atmosphere (Boyd and Ellwood, 2010; Tagliabue et al., 2014). The most energetically stable form of Fe in the oxygenated ocean, Fe(III), has low solubility. The reduced form of Fe, Fe(II), is more soluble in seawater and should be kinetically more bioavailable to phytoplankton (Shaked et al., 2005). However, Fe(II) is only present as a transient species in the oxygenated ocean, generally existing in vanishingly low concentrations (picomolar or less) due to rapid (minutes to days) oxidation by oxygen (O_2) and hydrogen peroxide (H_2O_2) in surface waters (Millero et al., 1987).

Nevertheless, continuous production of Fe(II) by several processes in the ocean can lead to measurable quantities in both the surface ocean and deeper waters. In the surface ocean, concentrations of Fe(II) are increased by photochemical reduction of organic-Fe(III) complexes (Barbeau et al., 2001; Rijkenberg et al., 2005), wet and dry atmospheric deposition (Croot and Heller, 2012), glacial melt in higher latitudes (Hawkings et al., 2018; Hopwood et al., 2014) and biological production by processes such as, for example, viral lysis of cells and grazing (Hansard et al., 2009 and references therein). In the deeper ocean and on continental shelves, sources include benthic fluxes from anoxic sediments (Lohan and Bruland, 2008), hydrothermal fluids (Holmes et al., 2017; Kleint et al., 2017; Sedwick et al., 2015) and redox cycling induced by oxygen minimum zones (Lohan and Bruland, 2008). Thus, given the rapid transformation of

Fe(II) in oxygenated seawater, measurements of Fe speciation can be used as a near-field tracer of processes and sources of Fe biogeochemistry in the ocean (Holmes et al., 2017).

The oxidation kinetics of Fe(II) in seawater are complex depending on many factors including pressure, temperature, salinity, O_2 concentration, H_2O_2 concentration and pH (Millero et al., 1987; Millero and Sotolongo, 1989; Moffett and Zika, 1987; Santana-Casiano et al., 2006). At the pH of seawater, the oxidation rate of Fe(II) is heavily dependent on O_2 and H_2O_2 concentrations, with the relative influence of each species dependent on its concentration (Santana-Casiano et al., 2006). Therefore, it is important to consider both of these oxidants when analysing Fe(II) cycling. Rainwater and biological production can contribute to the H_2O_2 inventory (Croot et al., 2004). Rainwater scavenges H_2O_2 from the atmosphere (Cohan et al., 1999), increasing surface ocean concentrations through direct deposition; however, this process is more prevalent in lower latitudes (Weller and Schrems, 1993). Studies have also demonstrated biological production of H_2O_2 in the water column (Palenik and Morel, 1988); however, the major source of H_2O_2 in the ocean is through photochemical reactions involving dissolved organic matter and O_2 (Croot et al., 2004).

The Southern Ocean (SO) is the largest region of Fe deficiency in the oceans (Boyd et al., 2007). However, within the Indian sector of the SO there is an oasis of relatively Fe rich waters overlaying the Kerguelen Plateau. At the southern part of the central Kerguelen plateau is an active volcanic hotspot, hosting two active subaerial volcanic islands, Heard and McDonald (HIMI), the former of which is largely covered by glaciers. Waters in the region are subject to an intense mixing regime, caused by strong winds, shallow bathymetry characterised by many seamounts and ridges, and the location of the plateau in the path of strong currents associated with the polar front to the north and Fawn Trough Current to the south of HIMI (Figure 5.1; Park et al., 2014). Fed by the Fe rich waters formed on the plateau, a plankton bloom on the order of thousands of square kilometres forms over and downstream of the plateau annually

each summer (Blain et al., 2007). In the austral summer of 2016, the first voyage to focus on biogeochemical cycling in the HIMI region was undertaken: Heard Earth-Ocean-Biosphere Interactions (HEOBI). With our studies centred around hydrothermalism, we utilise DFe(II) and H_2O_2 data to uncover which sources and processes are important for the distribution and oxidation kinetics of DFe(II) around HIMI, with implications for Fe bioavailability and transport of Fe to the northern plateau.

5.3 Methods

5.3.1 Study area

Sampling and shipboard analyses were carried out aboard R/V *Investigator* during the HEOBI voyage (GEOTRACES process study GIpr05) from January 8th to February 27th 2016 around Heard and McDonald Islands (HIMI) on the Kerguelen Plateau in the Indian sector of the SO. Twenty-seven stations were successfully sampled for both DFe(II) and H_2O_2 (Figure 5.1), with an extra four stations sampled for H_2O_2 only (not shown). The same locations were also occupied by CTD casts, along with an additional 22 CTD only stations (not shown). Sample stations were divided into 4 regions: Transect C, Heard Island, McDonald Islands and reference stations. Transect C was oriented in a northeast-southwest direction, with the aim of highlighting the near shore to deep water gradient in biogeochemical tracers. Transect C extends from Heard Island across Gunnari Ridge towards Shell Bank, crossing almost perpendicular to the prevailing current, which flows northward along the plateau. This transect followed the same trajectory as the previous KEOPS-1 'C' transect (Blain et al., 2008), though not reaching as far to the northeast as the previous transect, which extended off the plateau into waters >3500 m deep.

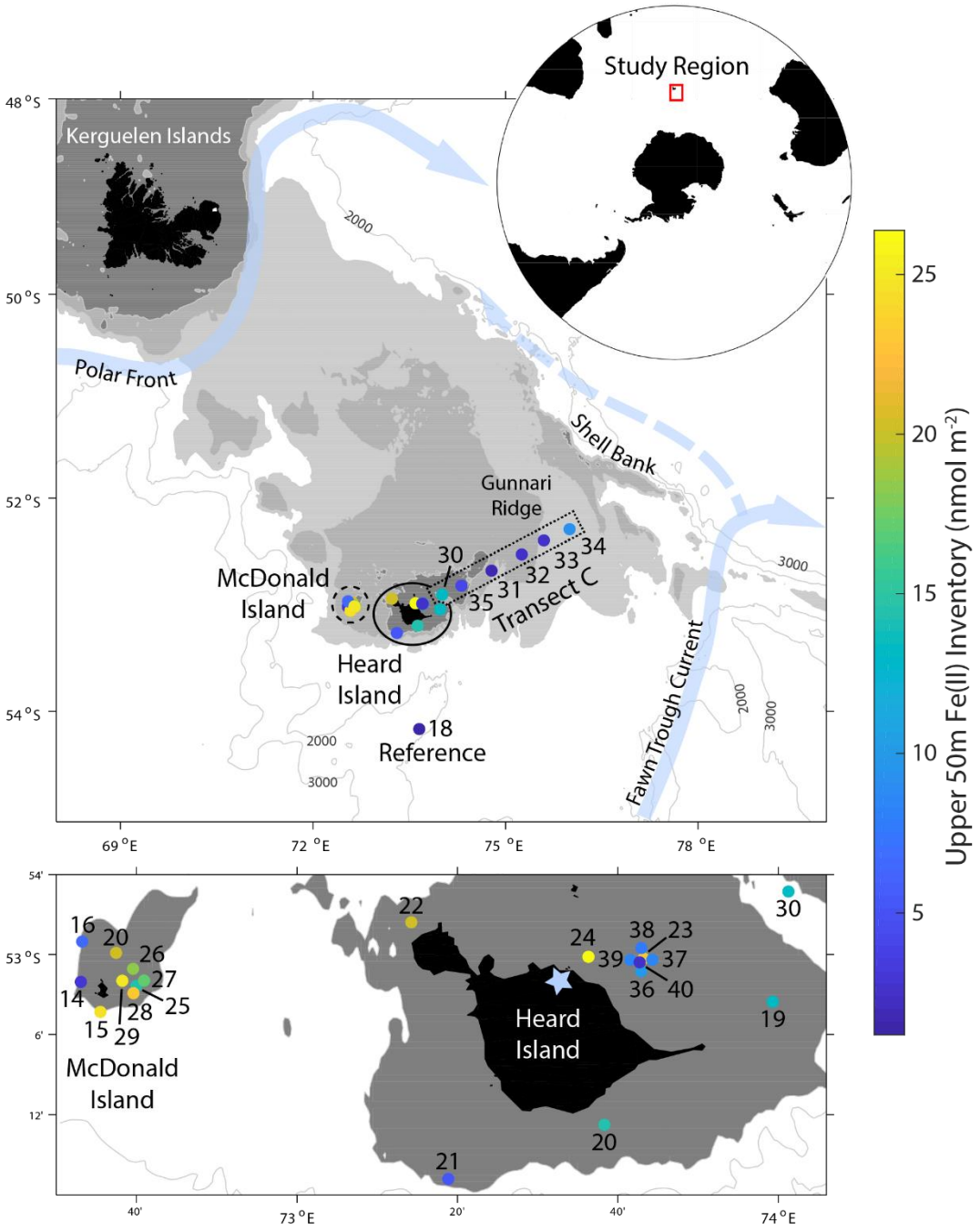

Figure 5.1. DFe(II) integrated inventory in the upper 50 m at each station sampled for DFe(II) during HEOBI. Concentrations indicated by colour bar. TMR Station numbers and regions are annotated. Location of study region is shown in top inset. Heard and McDonald Islands are shown zoomed in bottom inset. Transect C (dotted square) follows the first 150 km of 'Transect C' from a previous voyage (Kerguelen Ocean and Plateau Compared Study: KEOPS-1; Blain et al., 2008). The reference station was located to the south of HIMI in high-nutrient, low chlorophyll (HNLC) waters. Bathymetric isobaths are shown, with seabed <200 m depth shaded dark grey, <500 m shaded lighter grey and <1000 m shaded lightest grey. Major currents are shown in light blue arrows, adapted from Park et al., *(2014)*. Downes and Ealey marine terminating glaciers are marked by a blue star on Heard Island.

Sampling station locations in the HIMI region were selected based on bathymetric features (Watson et al., 2016) and acoustic flare signals detected with shipboard echosounders (Spain et al., 2018) deemed indicative of potential hydrothermal activity (see section 3.1). Acoustic flare signals had distinct characteristics when caused by seafloor gas seepage (Spain et al., 2018). Two reference sites were sampled to the west and south of Heard Island. Station 11 (not shown), ~80 km to the west of McDonald Islands, was expected to be located in HNLC waters, but observed shipboard underway fluorescence and chlorophyll biomass was relatively high (up to 2.1 mg m^{-3} Chl*a* in upper 200 m; B. Wojtasiewicz, pers. comm.). Conversely, station 18, ~100 km to the south of Heard Island, was located in waters more representative of HNLC conditions (max 0.81 mg m^{-3} Chl*a* in upper 200 m; B. Wojtasiewicz, pers. comm.). Mean currents at this station are associated with the Fawn Trough Current, and so move from west (open ocean) to east (plateau; Figure 5.1; Park et al., 2014). Hereafter 'reference' data refers only to data from station 18.

5.3.2 Sample collection

Briefly, all water column samples were collected in 12 L Niskin bottles modified for trace metal sampling, deployed using the Australian Marine National Facility trace-metal-clean rosette (TMR) equipped with a Seabird CTD unit and attached to a Dyneema rope. Once recovered, the Niskin bottles were rapidly transferred into a trace-metal-clean containerised laboratory for sub-sampling and sample processing. All sample manipulation and analysis was conducted following GEOTRACES guidelines (Cutter et al., 2014) under ISO 5 HEPA filtered air within the containerised clean room. DFe(II) samples were filtered through acid-washed Pall Acropak Supor capsule filters (0.2 μm) into acid-cleaned bottles without head space. Unfiltered H_2O_2 samples were collected into acid-cleaned bottles without head space. Both DFe(II) and H_2O_2 samples were collected in acid-cleaned, dark brown (low-light transmittance), high-density polyethylene (Nalgene) sample bottles, double bagged and put directly on ice. Samples were then transported into a separate trace metal clean analytical container for immediate analysis (DFe(II)

within 1 hour, H_2O_2 within 2 hours). To ensure that any oxidation of DFe(II) which occurred between subsampling and analysis was consistent, every effort was made to keep the time between subsampling and analysis as consistent as possible at each station.

5.3.3 Dissolved iron(II) analyses

Dissolved Fe(II) samples were analysed using chemiluminescence flow injection analysis (FIA-CL) with in-line preconcentration onto an 8-HQ resin adapted from the method of Bowie et al., (2005, 2002) and recently described by Sedwick et al., (2015). Briefly, a 0.02 M DFe(II) stock solution was prepared before the voyage by dissolving trace metal grade ammonium iron(II) sulfate hexahydrate (Aldrich) in 0.1 M ultrapure hydrochloric acid (Seastar Baseline) solution. The stock solution was kept in darkness for the duration of the voyage. Working solutions of 200 μmol L^{-1} and 200 nmol L^{-1} concentrations were prepared daily via serial dilution. All DFe(II) stock solutions contained sodium sulphite as a stabilising agent. Calibration standards were also prepared daily from the stock solution, in aged low-Fe seawater, buffered with 0.4 M ammonium acetate to a pH of ~6. Calibration standards covered a concentration range of 0 – 1.2 nmol L^{-1}, which was adequate for the majority of samples collected. Calibrations were run before each block of samples from individual stations.

The blank solution used for the DFe(II) FIA analysis consisted of low Fe seawater collected during the cruise, aged so that any Fe(II) in the solution had oxidised. Triplicate blank measurements were taken both before and after each analysis run. Analysis times were recorded for each sample. In instances where instrument signal drift was noted between the initial and final blank measurements, a blank value was calculated for each sample via linear interpolation.

The detection limit of the DFe(II) FIA-CL instrument was defined as the analyte concentration equivalent to three times the standard deviation of the blank peak (n=3) (Bowie et al., 2004).

During the HEOBI voyage the detection limit was calculated each day and ranged from 0.02 to 0.16 nmol L^{-1} with a mean of 0.06 nmol L^{-1} (n = 17).

5.3.4 Dissolved hydrogen peroxide analyses

Dissolved H_2O_2 samples were analysed using a FIA-CL reagent injection method (Yuan and Shiller, 1999). Briefly, H_2O_2 catalyses the chemiluminescence of luminol in the presence of Co^{2+} at alkaline pH. H_2O_2 standards were made by serial dilution from a 30% stock solution (Seastar Baseline) and were determined by spectrophotometric measurements with a 10 cm Liquid Waveguide Capillary Flow Cell (LWCC, World Precision Instruments, ε = 40.9 mol L^{-1} cm^{-1}; Hwang and Dasgupta, 1985). Each seawater sample was analysed at least four times with a typical precision of 3 – 5% through the concentration range 0.5 – 75 nmol L^{-1} and a typical detection limit (3σ) of 0.6 nmol L^{-1}.

5.3.5 Modelling dissolved iron(II) half-lives

Shipboard pH data was unavailable during HEOBI. Therefore using in-situ oxygen (O_2), H_2O_2, salinity, temperature and depth data we have modelled expected Fe(II) half-lives over a pH range of 7.1 – 8.2 (the pH range of historical observations in the region, taken from the World Ocean Database; Tanhua et al., 2013) using a method modified from Hansard et al. (2009). The overall rate of oxidation of Fe(II) is given by:

$$\frac{-dFe(II)}{dt} = k_{app,O_2}[Fe(II)][O_2] + k_{app,H_2O_2}[Fe(II)][H_2O_2] \quad (1)$$

where $k_{app,O2}$ and $k_{app,H2O2}$ are the apparent rate constants (M^{-1} min^{-1}) for oxidation by O_2 and H_2O_2, respectively. When oxidants are in excess, the reaction is pseudo first-order, and is given by:

$$\frac{-dFe(II)}{dt} = (k'_{O_2} + k'_{H_2O_2})[Fe(II)] \quad (2)$$

where k'_{O2} (min^{-1}) = $k_{app,O2}[O_2]$ and $k'_{[H2O2]}$ (min^{-1}) = $k_{app,h2O2}[H_2O_2]$. The overall half-life with respect to oxidation is:

$$T_{half} = 0.693(k'_{O_2} + k'_{H_2O_2})^{-1} \quad (3)$$

The k'_{O2} value was calculated following Millero et al. (1987) as follows:

$$\frac{-dFe(II)}{dt} = k'_{O_2}[Fe(II)] \quad (4)$$

where

$$k'_{O_2} = k[OH]^2[O_2] \quad (5)$$

The rate constant k can be calculated for a given temperature and ionic strength (see equations in Millero et al., 1987). Similarly, k'_{H2O2} was calculated according to Millero and Sotolongo (1989), with some assumptions:

$$\frac{-dFe(II)}{dt} = k'_{H_2O_2}[Fe(II)] \quad (6)$$

where

$$k'_{H_2O_2} = k[H_2O_2][OH^-] \quad (7)$$

These calculations assume that $[H_2O_2]$>>[Fe(II)], which makes the oxidation of Fe(II) by H_2O_2 pseudo-first order.

5.3.6 CTD data

Temperature, salinity, pressure and oxygen data were taken from Sea-Bird Electronics SBE3T, SBE4C, SBE9plus and SBE43 sensors respectively, which were mounted on the primary Conductivity-Temperature-Depth (CTD) rosette.

5.4 Results

5.4.1 Dissolved Fe(II) distribution

5.4.1.1 Transect C

All Transect C stations were located above the plateau. The three most easterly stations (32, 33 and 34) had deep mixed layers, shoaling towards the east (285, 254 and 245 m, respectively). Surface DFe(II) concentrations were low (mean upper 50 m concentrations, ≤ 0.15 nmol L^{-1}) compared to stations 30 and 23 at the western end of the transect (closer to HIMI), increasing to 0.29 and 0.44 nmol L^{-1} mean in the upper 50 m, respectively (Figure 5.2). A subsurface DFe(II) maximum was observed at Stations 31 – 34. Concentrations in the maximum layer decreased

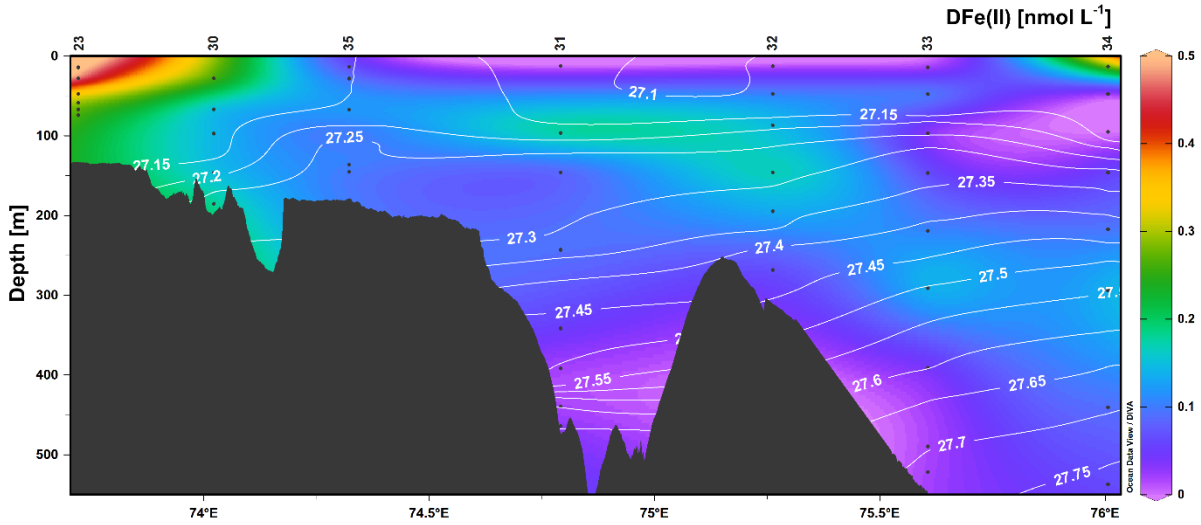

Figure 5.2. Transect C DFe(II) concentrations, with neutral density (γ^n; kg m^{-2}) surfaces overlaid (white lines, calculated from continuous CTD data). Black dots represent sample locations. Station numbers for TMR deployments are shown above the top axis.

from 0.21 to 0.15 nmol L^{-1} between stations 31 to 34, while the depth of the layer increased from 97 to 297 m (Figure 5.2). The full DFe(II) and H_2O_2 dataset is available in supplementary Table 5-1.

5.4.1.2 Heard and McDonald Islands

Concentrations of DFe(II) were elevated around HIMI relative to transect and reference stations, with relatively homogeneous profiles throughout the water column (Figure 5.4). McDonald Islands had a significantly higher mean DFe(II) concentration (mean 0.36 nmol L^{-1}, σ = 0.16, n = 56) compared to Heard Island (0.24 nmol L^{-1}, σ = 0.14, n = 57; t-test, $p<0.01$). At Heard Island, the maximum DFe(II) concentration (0.57 nmol L^{-1}) was located at station 24, north of the island and near Downes and Ealey marine-terminating glaciers. At McDonald Islands, the maximum DFe(II) concentration (1.01 nmol L^{-1}) was located to the west of the island. DFe(II) inventories calculated in the upper 50 m (minimum station depth at HIMI was ~48 m, measured at station 24) are shown in Figure 5.1, along with arrows showing general circulation features, adapted from (Park et al., 2014). Stations to the south and east of Heard Island had lower DFe(II) inventories than stations to the north of Heard Island. Stations to the west of McDonald Islands had lower DFe(II) inventories than stations to the east of McDonald Islands. This distribution corresponds to higher concentrations on the shallower, plateau side of the islands.

5.4.1.3 Reference station

Surface DFe(II) concentrations were very low at reference station 18 (measured 0.03 nmol L^{-1} mean in the upper 100m, though all but two samples were below detection limit), increasing to a maximum (0.10 nmol L^{-1}) at 197 m before decreasing with depth (Figure 5.4).

5.4.2 Dissolved H_2O_2 distribution

5.4.2.1 Transect C

Greater surface concentrations of H_2O_2 were observed at stations 31 – 34 (>48 nmol L^{-1}) towards the east of transect C compared to stations 35, 30 and 23 (41.9 – 25.3 nmol L^{-1}) towards the west of the transect, with the lowest surface concentration observed closest to HIMI at station 23 (Figure 5.3). The distribution of H_2O_2 closely followed density layers, with concentrations at stations 31 – 34 decreasing with depth, while stations 35, 30 and 23 became increasingly homogenised over the water column towards HIMI.

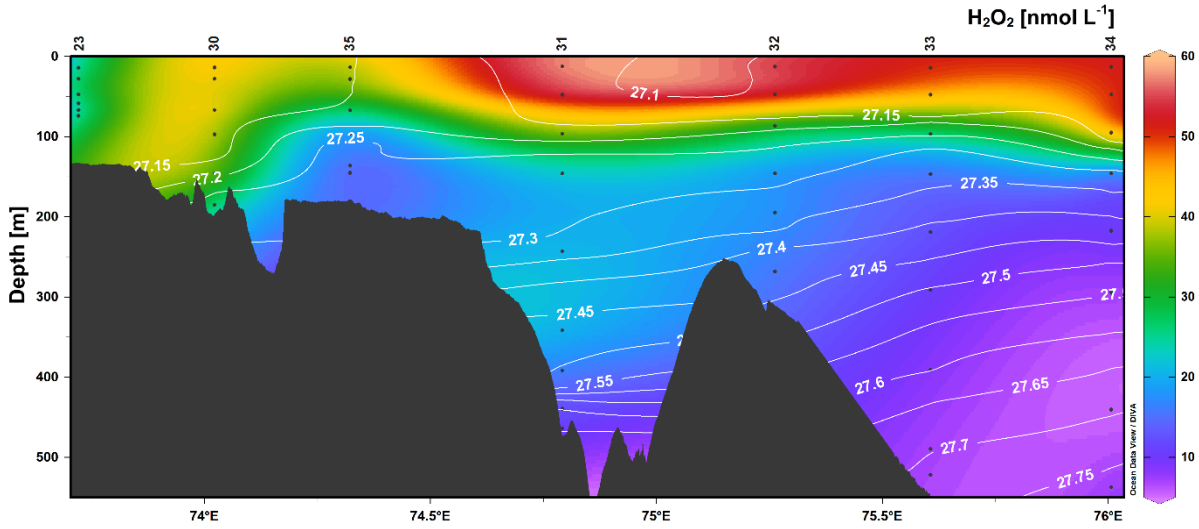

Figure 5.3. Transect C H_2O_2 concentrations, with neutral density (γ^n; kg m^{-2}) surfaces overlaid (white lines, calculated from continuous CTD data). Black dots represent sample locations. Station numbers for TMR deployments are shown above the top axis.

5.4.2.2 Heard and McDonald Islands

Surface concentrations of H_2O_2 around HIMI were highest at stations most likely affected by open ocean waters flowing along the western edge of the plateau and associated with the Fawn Trough Current: station 16, northwest of McDonald, and stations 20 and 21 south of HIMI. All other stations had homogeneous H_2O_2 profiles, with surface concentrations ranging between 13.5 – 31.0 nmol L^{-1} at McDonald Islands and 20.8 – 29.3 nmol L^{-1} at Heard Island (Figure 5.4).

5.4.2.3 Reference station

The mean surface H_2O_2 concentration in the upper 100 m was 30.6 nmol L^{-1}, decreasing with depth (Figure 5.4).

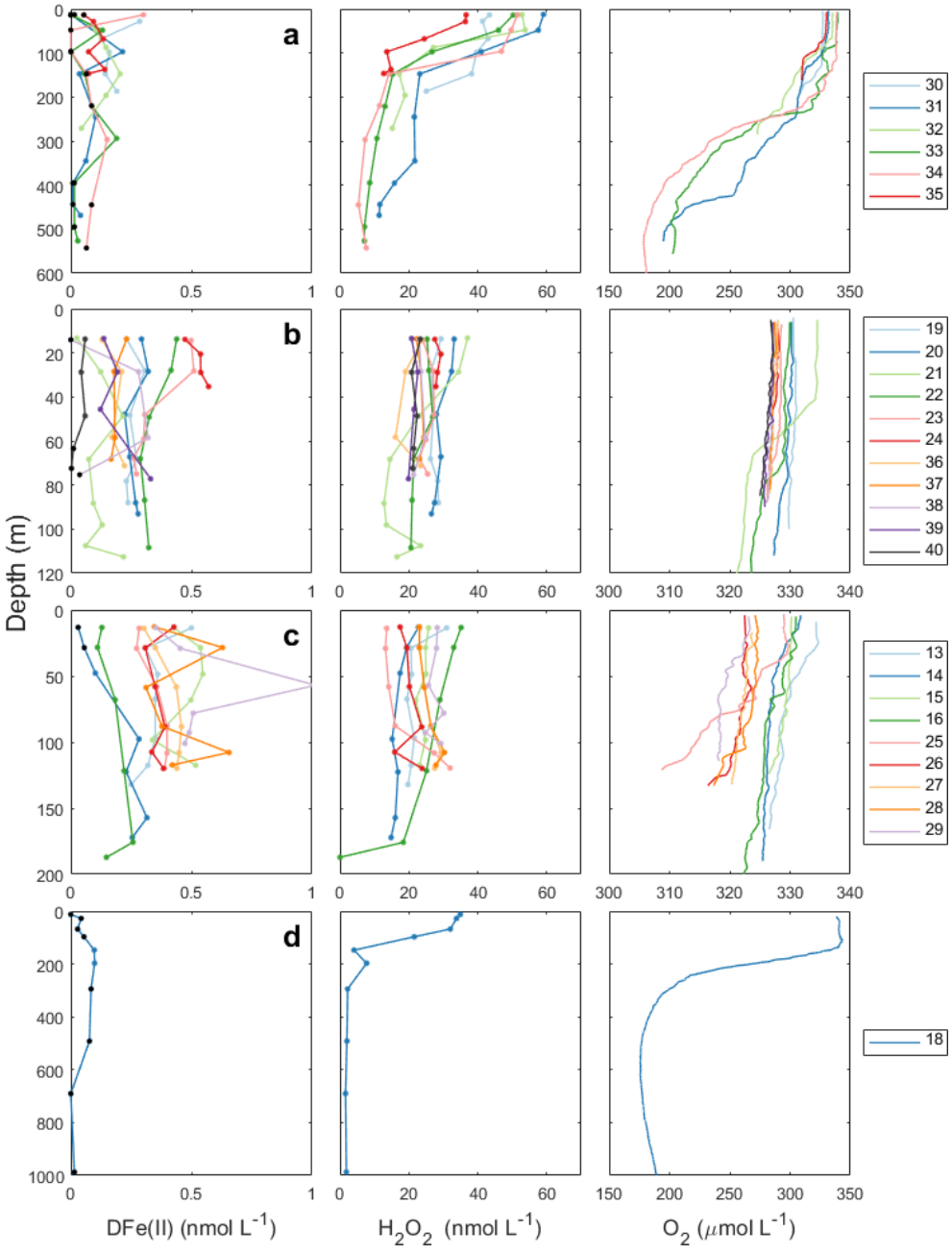

Figure 5.4. Profiles of DFe(II), H_2O_2 and O_2 for **a.** Transect C, **b.** Heard Island, **c.** McDonald Islands, and **d.** Reference station. Stations are colour coded and shown in legends on the right hand side of each region. Samples that were below the calculated detection limit for each station are shown in black. Note that O_2 x-axis scales vary.

5.4.3 Modelled DFe(II) half-lives

Modelled DFe(II) half-lives show that within the pH range 7.1 – 8.2 (the pH range of historical observations in the region, taken from the World Ocean Database; Tanhua et al., 2013), we can expect the DFe(II) half-life to range between 30 minutes – 172 hours, decreasing with increasing pH (Figure 5.5).

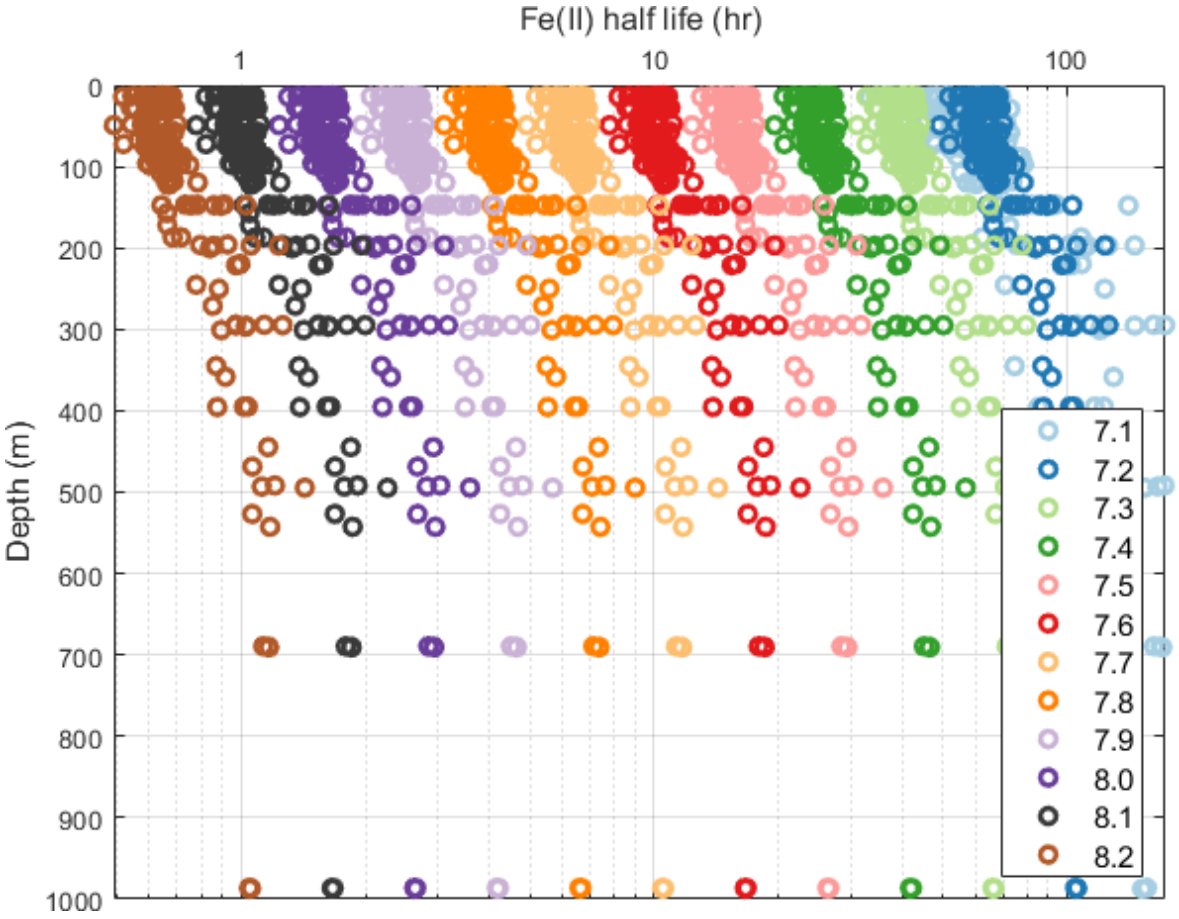

Figure 5.5. Scatter plot of all Fe(II) samples showing effect of pH on Fe(II) half-life, calculated from in-situ DFe(II), H_2O_2 and O_2 measurements. The pH range reflects upper and lower bounds of observations made during historical hydrographic voyages in the region, taken from the World Ocean Database *(Tanhua et al., 2013)*.

5.5 Discussion

Dissolved Fe(II) concentrations as high as 0.57 nmol L^{-1} were measured in waters north of Heard Island and 1.01 nmol L^{-1} to the east of McDonald Islands. These concentrations are elevated above most existing DFe(II) measurements in open Southern Ocean surface waters,

which are generally below 0.03 nmol L^{-1} (Bowie et al., 2002; Sarthou et al., 2011). H_2O_2 concentrations around HIMI (13.5 – 31.0 nmol L^{-1}), were low relative to concentrations found in lower latitude regions of the ocean (e.g. 300 nmol L^{-1}; Yuan and Shiller, 2001), but consistent with other Southern Ocean observations taken ~700 km west of the Kerguelen Plateau (4.9 – 20.2 nmol L^{-1}; Sarthou et al., 1997).

Sources of DFe(II) near HIMI may include benthic fluxes from anoxic sediments (Lohan and Bruland, 2008), hydrothermal fluids (Kleint et al., 2017), glacial runoff (Hopwood et al., 2014) and atmospheric deposition of aerosols (Croot and Heller, 2012). Additional production mechanisms of DFe(II) in the surface ocean include photochemistry, through the breakdown and reduction of Fe(III)-ligand complexes (Barbeau et al., 2001; Rijkenberg et al., 2005) and biological production, through bioreduction of Fe(III)-ligand complexes, grazing or viral lysis of cells (Hansard et al., 2009). We now discuss each of these potential sources in relation to data collected during the HEOBI voyage in order to identify respective influences on the elevated Fe(II) concentrations observed in the region.

5.5.1 Glacial runoff

Glacial erosion and melting results in runoff enriched with DFe (Annett et al., 2017, 2015; Bhatia et al., 2013) and fine particles ('glacial flour'), including Fe(II)-enriched nanoparticles (Hawkings et al., 2018; Shoenfelt et al., 2017), from which DFe(II) may be released and stabilised by ligands (Hawkings et al., 2018; Hopwood et al., 2014) or potentially consumed directly from particles (Shoenfelt et al., 2017). Heard Island is heavily glaciated, while McDonald Islands is ice-free. Comparing DFe(II) concentrations with salinity at stations north of Heard Island suspected of being influenced by glacial processes (stations 24, 23 and 36 – 40) shows a significant inverse correlation at Heard Island ($R^2 = 0.57$, $P < 0.01$; Figure 5.6). Samples taken at the station in front of Downes and Ealey marine terminating glaciers (station 24) are clearly set apart from the other

Heard Island samples, with lower salinities (mean 33.85) and higher DFe(II) concentrations (mean 0.53 nmol L^{-1}) compared to nearby stations (mean salinity 33.88 and mean DFe(II) 0.18 nmol L^{-1} at stations 36 – 40). This is strong evidence that the elevated DFe(II) signal at station 24 originates from Heard Island glacial meltwaters.

DFe(II) concentrations at the Heard Island station closest to Downes and Ealey glaciers (24) were an order of magnitude higher than those observed at the reference station (below detection – 0.05 nmol L^{-1} range in the upper 100 m), i.e. regional open ocean conditions (Figure 5.4). The percentage of DFe(II) relative to DFe(total) can indicate the presence of a strong Fe(II) source (e.g. Sedwick et al., 2015). Mean DFe(II) percentage over the water column at station 24 was also high at 25% (Figure 5.7; DFe(total) measured on-shore using Sector Field ICP-MS; data presented in Holmes et al. (2019)). Clearly this data suggests that there was a strong DFe(II) source adjacent to the glacial outflow, which supported the elevated concentrations observed during HEOBI in well oxygenated waters (median 328 μmol L^{-1} O_2).

High DFe(II) (0.44 nmol L^{-1}) and DFe (1.88 nmol L^{-1}) concentrations were also observed in the upper 30 m downstream to the east (7 km) of station 24 (station 23, Figure 5.4), where targeted sampling was undertaken based on a large acoustic plume (Spain et al., 2018). This area was later revisited and sampled in a crosshair pattern (stations 36 – 40) in an attempt to delineate the signal source. However, these crosshair stations yielded lower DFe(II) and DFe concentrations (mean 0.15 and 1.53 nmol L^{-1}, respectively) compared to the elevated samples observed previously (station 23) or further to the west, towards the glacier terminus (station 24). The two samples in the upper 30 m of station 23 are also associated with water that was lower in salinity and higher in DFe(II) than revisited crosshair stations 36 – 40, but slightly lower in DFe(II) than station 24 samples. This is likely laterally advected, glacially influenced surface water that has diluted with distance from the Heard Island source. Indeed, particle laden waters advecting away from Heard Island are visible in satellite imagery of the region (van der Merwe et al., 2018).

Suspended particulate analysis from the HEOBI voyage provides additional evidence that waters to the north of Heard Island are influenced by glacial runoff (van der Merwe et al., 2018). Immediately adjacent to the large marine terminating glacier on the north of Heard Island, suspended particles were found to be highly labile, biogenic nanoparticles, in contrast to lithogenic, less-labile Fe bearing mineral particles observed at McDonald Islands (van der Merwe et al., 2018). Exchange between labile particulates and dissolved Fe fractions has been shown as a mechanism contributing to DFe and DFe(II) concentrations (Achterberg et al., 2018; Fitzsimmons et al., 2017). This could also be an important mechanism in maintaining the observed DFe(II) and DFe enrichment at Heard Island.

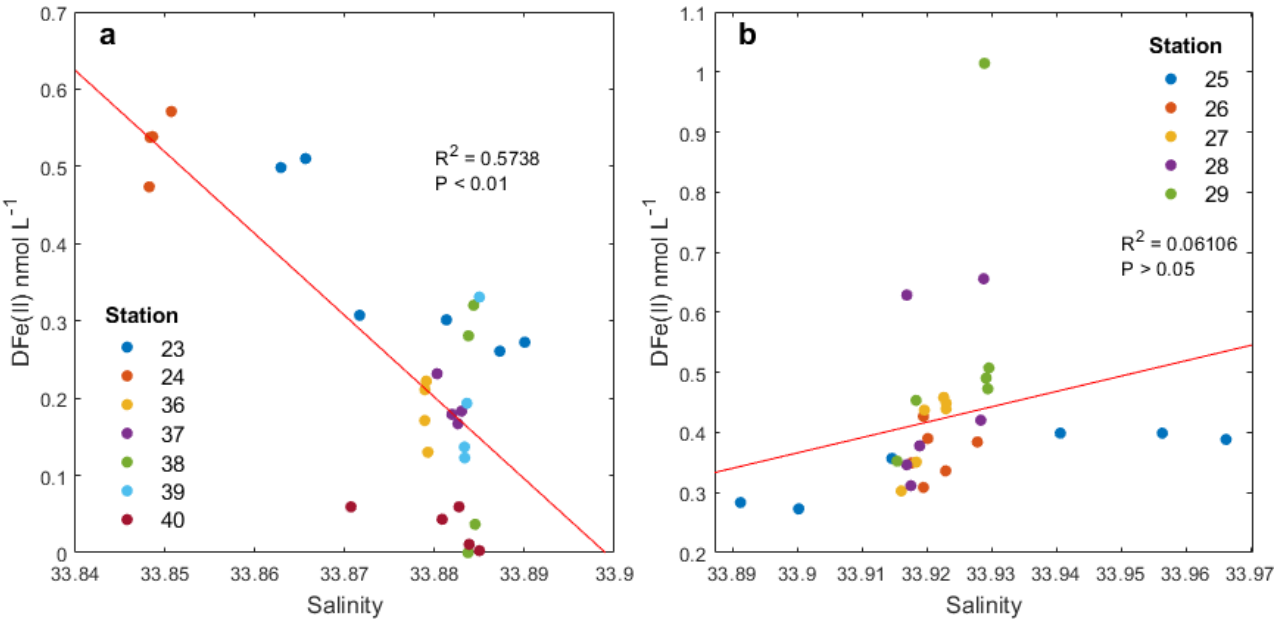

Figure 5.6. DFe(II) versus Salinity at **a.** Heard Island station 24 and crosshair stations 23, 36 – 40 and **b.** McDonald Islands crosshair stations 25 – 29. Station numbers are annotated.

5.5.2 Sedimentary and hydrothermal sources

Sediments on continental shelves have been identified as strong DFe(II) sources, especially in the presence of hypoxic bottom waters (Lohan and Bruland, 2008). In the presence of oxygenated bottom waters, the upper layer of sediment tends to form an oxidising barrier, meaning relatively little DFe(II) can penetrate into the overlying water column (Homoky et al.,

2016; Pakhomova et al., 2007). However, an example of benthic flux of Fe(II) to oxygenated bottom waters has been observed in a region of hydrothermal activity in the Bransfield Straight, Southern Ocean (Aquilina et al., 2014). This flux was attributed to infaunal tubeworms, the remains of which provided conduits for subsurface fluid to bypass the upper sediment layer (Aquilina et al., 2014). Though few tubeworms were observed during the HEOBI voyage (there was no biologically focused sampling program), bioturbation of surface sediments is likely due to the shallow bathymetry and biological productivity in the region, including a rich diversity of benthic species (Améziane et al., 2011). In addition, wind-driven mixing events often reached the seafloor around HIMI during the voyage (R. Robertson, pers. comm.), which could disturb upper oxidising sediment layers, resuspending sediments and potentially allowing the escape of Fe(II) from underlying anoxic sediments (e.g. Elrod et al., 2004).

Alternatively, or in addition, hydrothermalism is a potential source of DFe(II) in the region. Deep sea hydrothermal vents emit fluids containing DFe(II) up to millimolar concentrations (Holmes et al., 2017; Von Damm, 1995). A large fraction of this DFe(II) is quickly oxidised upon mixing with ambient seawater (German et al., 1991; Rudnicki and Elderfield, 1993). However, concentrations elevated over ambient seawater concentrations can persist in the plume over hundreds of kilometres (Sedwick et al., 2015), stabilised in the water column by organic ligands (Daugherty et al., 2017) or within nanoparticles (Gartman et al., 2014; Sedwick et al., 2015; Yücel et al., 2011). Shallow hydrothermalism generally results in lower temperatures (due to lower pressure) and therefore lower metal concentrations than deep-sea systems (Holmes et al., 2017). However, in the HNLC Southern Ocean, even relatively small Fe inputs in the euphotic zone may have large impacts on primary productivity (Hawkes et al., 2014). Numerous acoustic flare signals detected by ship-board echosounder and footage of bubbles emanating from the seafloor, which were captured by deep tow camera (Figure 5.9) at several locations around HIMI, were clues that hydrothermal vents are present in the region. The presence of localised elevated DFe(II) maximum concentrations (Figure 5.4), elevated DFe(II) to DFe(total) ratios (Figure 5.7)

and sharp DFe(II) spikes in the water column (Figure 5.8) along with observations of excess ^{3}He with clear hydrothermal origins (Lupton et al., 2017), indicate that shallow water (<200 m) hydrothermalism was a likely source of DFe(II) at stations west of McDonald Islands, as detailed below.

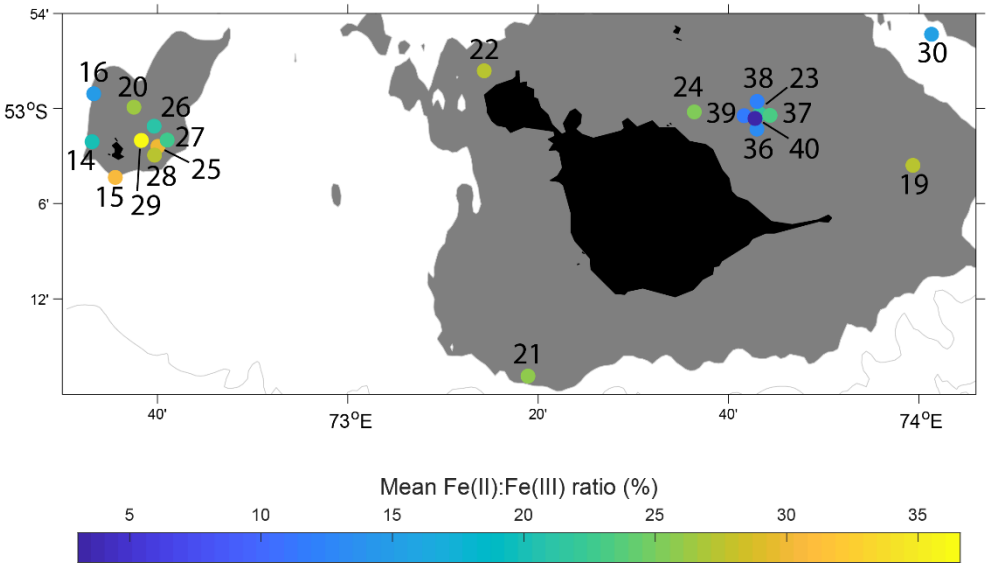

Figure 5.7. Mean Fe(II) to Fe(III) percentage over the water column for each station near Heard and McDonald Islands. Note that station 20 is omitted as data are at detection limits, giving a false high ratio.

The first clue that hydrothermalism may be a source of DFe(II) at McDonald Islands is the presence of localised elevated DFe(II) maximum concentrations. Five stations (25 – 29) were sampled to the east of McDonald Islands in a 'crosshair' pattern (Figure 5.1). These sampling locations were selected in an attempt to further delineate elevated DFe concentrations detected at a previous station (station 12; Holmes et al., 2019) and acoustic flare signals (Spain et al., 2018). The station at the western side of the crosshair (29), closest to McDonald Islands, had the greatest DFe(II) concentration and DFe(II):DFe(total) percentage observed during HEOBI (1.01 nmol L^{-1} and 37%, respectively; Figure 5.7). The next highest maximum DFe(II) concentration (0.66 nmol L^{-1}) was observed at the southernmost crosshair station (28). These stations were separated by a distance of 780 m and ~1.5 hours between sampling. The spikes in maximum DFe(II) concentrations were unusual compared to other stations around HIMI (Figure 5.4, 5.8). The other three stations of the crosshair (25, 26 and 27; 630 m east-southeast,

730 m northeast and 1040 m east from station 29, respectively) had lower overall DFe(II) concentrations and were more homogeneous over the water column (0.27 – 0.40, 0.31 – 0.43 and 0.30 – 0.46 nmol L^{-1}, respectively). The transition from profiles with pronounced spikes in DFe(II) concentrations to homogenous DFe(II) profiles between the closely spaced crosshair stations may attest to the turbulent mixing and rapidly oxidising conditions in the region and indicates that the DFe(II) originates from a point source(s) such as a diffuse vent or patch, rather than a larger area of the seafloor, such as might be expected from benthic flux.

The shape of individual DFe(II) profiles over the water column from McDonald crosshair stations also provides an indication of a dynamic DFe(II) source at this location. Profiles of the two elevated DFe(II) stations (28, 29) show increased variability and high DFe(II) spikes at different depths compared to other stations on the McDonald Islands crosshair (25 – 27) and to the Heard Island crosshair stations (36 – 40; Figure 5.8). The presence of DFe(II) peaks at different depths in the water column at the two elevated stations (28, 29) could indicate that TMR casts intercepted point source plumes as the ship and/or rising plumes moved laterally with currents (e.g Bennett et al., 2009). Due to the turbulent nature of waters surrounding HIMI, and the point source nature of the observed elevated DFe(II) concentrations at the McDonald Islands crosshair stations, it is unlikely that a TMR cast would stay within a plume for the duration of the cast (~1 hour). A DFe(II) point source would also make sampling directly above the source challenging without a remotely operated vehicle. If the source of elevated DFe(II) at the McDonald crosshair stations was sedimentary in origin, we would expect to see an increase in concentrations towards the seafloor over a larger area (Lohan and Bruland, 2008), which was not observed during HEOBI.

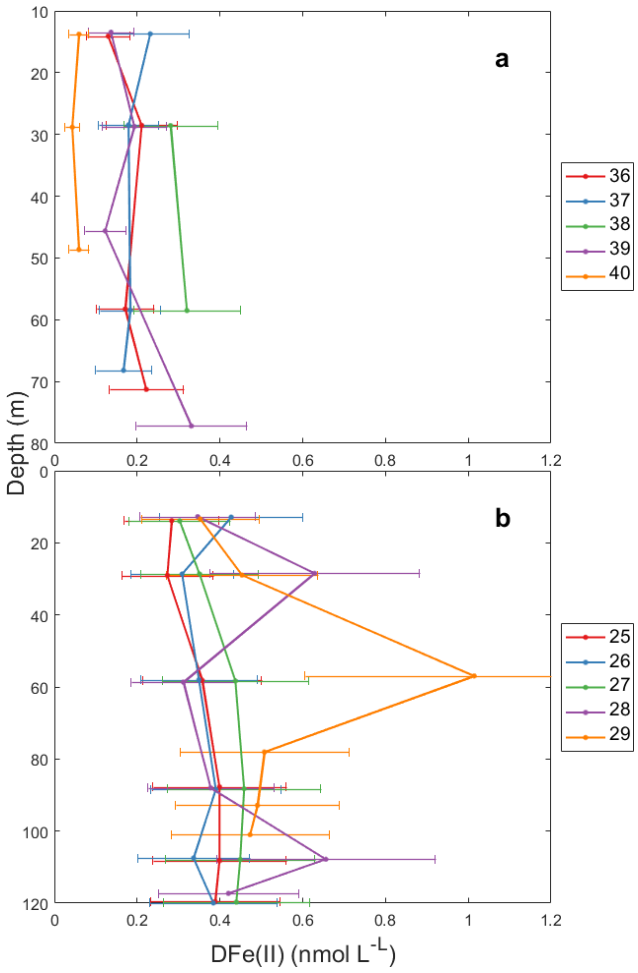

Figure 5.8. DFe(II) versus depth at **a.** Heard Island crosshair stations (36 – 40) and **b.** McDonald Islands crosshair stations 25 – 29. Station numbers are annotated. Note that due to analytical constraints, replicate measurements were unavailable for some samples. Therefore, as a conservative estimate of the error associated with these measurements, uncertainty was derived from the relative standard deviation between samples at each of the crosshair stations, which due to their spatial and temporal proximity essentially represented replicate measurements, though likely overestimate error.

Numerous observations via deep tow camera of bubbles emitted from seafloor vents scattered around the entire region during the HEOBI voyage (Figure 5.9) and recent δ^3He anomaly data (an unequivocal tracer of hydrothermalism; Lupton et al., 2017; Lupton and Craig, 1981) add further evidence that diffuse hydrothermal venting is a likely source of DFe(II) at McDonald Islands. The greatest δ^3He enrichment (10.1%) in the region was observed in the vicinity of the crosshair station group near McDonald Islands, compared to 1.7% close to station 37, near the northeast of Heard Island (Lupton et al., 2017). Acoustic flares, detected by the shipboard echosounder, were observed at both Heard and McDonald Islands (Spain et al., 2018). This could mean that while there were stronger glacial sources of DFe(II) at Heard Island,

hydrothermalism may have contributed to elevated background concentrations observed around both islands, along with sedimentary and other sources (discussed below).

Figure 5.9. Bubbles rising from the seafloor at a site NE of Heard Island, captured using deep tow camera during the HEOBI voyage. No bubble plumes were captured on camera near McDonald Islands. Photo courtesy of the Marine National Facility, CSIRO.

5.5.3 Other DFe(II) sources and sinks

Photochemical processes, H_2O_2 concentrations, atmospheric deposition of wet and dry aerosols, biological processes and variation in pH all represented potential sources and sinks in the HIMI region during HEOBI. Production of Fe(II) through photochemical processes did not appear to be the strongest influence of DFe(II) concentrations around HIMI, as comparison of shipboard surface photosynthetically active radiation (PAR) observations with surface DFe(II) concentrations showed no correlation (Figure SF1). Surface H_2O_2 concentrations also showed no correlation with PAR (Figure SF1); however, concentrations in surface waters were correlated with distance from land ($R^2 = 0.70$, $P < 0.01$), with greatest surface H_2O_2 observed at stations furthest from HIMI (i.e. stations 9 and 10 on the central northern plateau and 30 – 35 on transect C; Figure 5.3, 5.4). These stations were deeper and could thus form a stratified surface mixed layer, allowing H_2O_2 to accumulate above the pycnocline. Surface H_2O_2 showed no correlation with surface DFe(II) concentrations (Figure SF2). The low H_2O_2 concentrations and

lack of correlation between DFe(II) and either H_2O_2 or PAR around HIMI suggests that on-plateau DFe(II) distributions are predominantly governed by strong external DFe(II) sources.

Atmospheric deposition did not appear to be a major source of dissolved or particulate Fe during HEOBI, and therefore not a major source of DFe(II), as DFe(II) represents a fraction of total Fe. Precipitation was minimal during HEOBI, so wet deposition of DFe(II) and H_2O_2 was not apparent (Figure SF1). The mean aerosol soluble Fe observed during HEOBI (0.30±0.12 ng m^{-3}; M. Perron, pers. comm.) was on the same order as values found near Kerguelen Island to the north (0.29±0.14 ng m^{-3}; Blain et al., 2008), which were not deemed to be a significant source of DFe to that region (Blain et al., 2008). These values also fall in the range of baseline Southern Ocean aerosol soluble Fe (0.01 – 0.3 ng m^{-3}; Winton et al., 2015), where surface concentrations of DFe(II) are reported to range from below detection to 30 pmol L^{-1}. Thus, we can assume that the contribution of dry deposition aerosols to DFe(II) is probably minor; however, further research is required to confirm this.

No direct observations were taken to enable an estimate of the biological production of DFe(II) during HEOBI; however, it can be inferred that biological production was not a major source of elevated DFe(II) observed near Heard or McDonald Islands, as chlorophyll *a* (and thus biomass) concentrations were relatively low in general around HIMI (B. Wojtasiewicz, pers. comm).

In addition, pH and temperature conditions should be considered in relation to Fe(II) half-life in the HIMI region. Low temperatures, such as those found in waters around HIMI, extend Fe(II) half-life in high-latitude waters by slowing oxidation reactions (Croot et al., 2001). Our modelling results show that pH has a significant impact on Fe(II) half-life (Figure 5.5). Using in-situ observations of variables required in the equations and changing pH in steps of 0.1 units shows the strong dependence of Fe(II) half-life on pH. The well-mixed nature of the water column around HIMI probably indicates that input of low pH fluids from diffuse hydrothermal sources

would not have a major impact on regional pH, but could dramatically impact Fe(II) speciation and half-life close to vent sources.

Aerosol deposition, biological production and photochemical processes were not the strongest sources of DFe(II) in the HIMI region; however, it is likely that these sources, coupled with low water temperature and possibly lower pH in areas of the region, contributed to the overall elevated DFe(II) concentrations observed at stations in the HIMI region.

5.5.4 Fe(II) transport

Using current velocities observed during HEOBI and previous voyages (Park et al., 2008), and our modelled Fe(II) half-lives, a rough estimate of the distance Fe(II) might travel from HIMI can be calculated. Modelled half-lives ranged from 30 minutes to 172 hours. Current velocities over the plateau were slow (~6 cm s^{-1}), while currents to the east of Heard Island were stronger (~40 cm s^{-1}) in agreement with previous observations (Park et al., 2008). Both currents over the plateau and to the east of Heard Island flowed in a northerly direction. Using these figures, the distance Fe(II) could theoretically travel in one half-life over the plateau ranges from ~100 m to ~37 km. If Fe(II) reached the stronger currents to the east of Heard Island, in one half-life Fe(II) could theoretically travel between ~700 m and ~250 km. Considering that the greatest observed Fe(II) concentration observed at HIMI (~1 nmol L^{-1}) will take approximately 5 half-lives to reach surface Southern Ocean background concentrations (~0.03 nmol L^{-1}; Sarthou et al., 2011), it is plausible that Fe(II) from hydrothermal and glacial sources at HIMI could travel the distances required to fertilise the phytoplankton plume that forms over the plateau annually. This may have implications for future Fe supply to the northern plateau, since under warming climate conditions melting glacial waters will increase, increasing the supply of DFe(II), but then rapidly decrease once glaciers have melted.

5.6 Conclusion

We show that the strongest sources of DFe(II) differ between adjacent, volcanically active Heard and McDonald Islands. Maximum DFe(II) concentrations and varying mid-depth maxima in the water column at adjacent, targeted stations at McDonald Islands suggest that hydrothermalism is the strongest DFe(II) source there. At Heard Island, the strongest DFe(II) source correlates with low salinity waters and is near a marine-terminating glacier, suggesting that glacial meltwater (and possibly associated glacial flour) are the major source of DFe(II) there. Revisited stations to the east of the strongest signal showed a temporary freshwater and elevated DFe(II) signal, which suggests that glacially fertilised waters may be transported offshore from Heard Island. These results are in agreement with preliminary δ^3He (Lupton et al., 2017) and particulate Fe data (van der Merwe et al., in prep.) also collected during the HEOBI voyage.

Peroxide and PAR data helps to resolve which DFe(II) cycling processes are important in regulating decay and production rates in the HIMI region. Our data shows that neither H_2O_2 or PAR correlate with DFe(II) concentrations around HIMI, which suggests that on-plateau DFe(II) concentrations are predominantly governed by strong DFe(II) sources. Preliminary aerosol data collected during the HEOBI voyage confirms that soluble aerosol concentrations were low. The homogenous nature of most DFe(II) and H_2O_2 profiles around HIMI highlights the strong mixing regime in the region but obscures some features that would allow direct attribution to a source. Further research is necessary to determine exact mechanisms of decay and/or consumption. In addition to the strong sources from hydrothermal and glacial inputs identified in this study, the overall elevated concentrations of DFe(II) around HIMI are likely to be an accumulation of multiple sources (sedimentary resuspension, surface irradiance, biological production and atmospheric deposition), in addition to opposing controls on DFe(II) half-life from low temperature, highly oxygenated waters and potentially lower pH, which have all been homogenised in the well mixed water column. The elevated concentrations of DFe(II) around

HIMI, a highly labile and bioavailable form of Fe, may increase Fe availability for biota in the region. High DFe(II) concentrations may also indicate slower oxidation kinetics in the region, which has implications for transport of Fe away from the islands to the broader northern Kerguelen Plateau where the annual plankton bloom is strongest.

5.7 Acknowledgements

The authors would like to thank Rob Middag (Royal Netherlands Institute for Sea Research: NIOZ) for supplying the H_2O_2 FIA-CL instrument that was used to analyse samples during the voyage, Manon Tonnard (Laboratoire des sciences de l'Environnement MARin: LEMAR) and Lavenia Ratnarajah (Antarctic Climate and Ecosystems Cooperative Research Centre and Institute for Marine and Antarctic Studies: ACECRC, IMAS) for their assistance in collecting and filtering samples collected on the HEOBI voyage. We would like to thank Mark Rayner and Kendall Sherrin for their excellent hydrochemical analyses. We also thank the captain, officers and crew of the RV Investigator (HEOBI voyage) and Chief Scientist Mike Coffin for their support during the 53-day expedition. We wish to acknowledge the Australian Research Council (DP150100345 and LE0989539), the Australian Antarctic Science Program (AAS4338) and the Australian Government Cooperative Research Centres Program through the Antarctic Climate and Ecosystems CRC, who provided project funding and PhD scholarship support.

5.8 Appendix

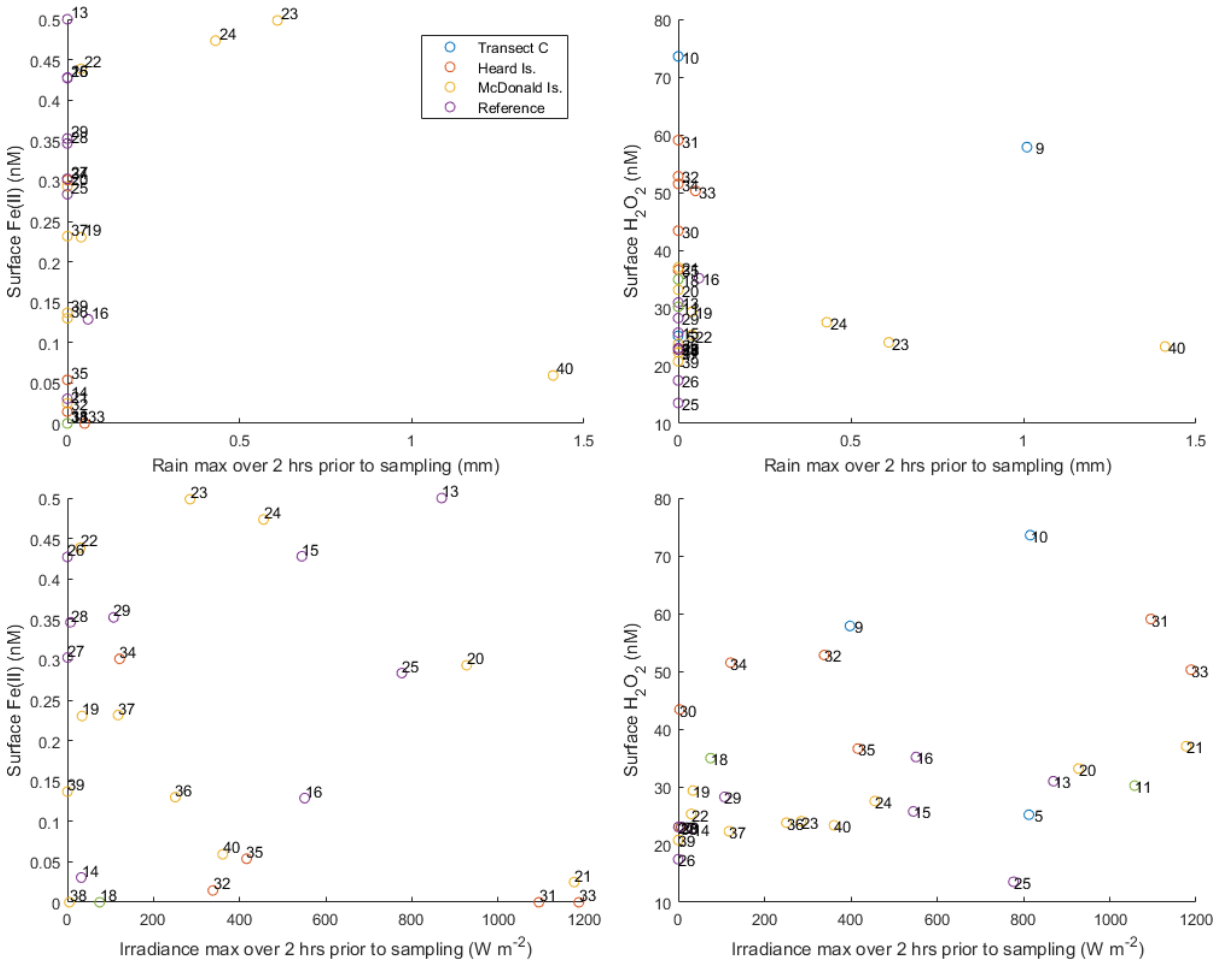

Figure 5.10 Surface DFe(II) and H_2O_2 vs maximum rainfall and maximum irradiance (PAR) over the 2 hours prior to sampling. Stations are annotated and colour coded by region.

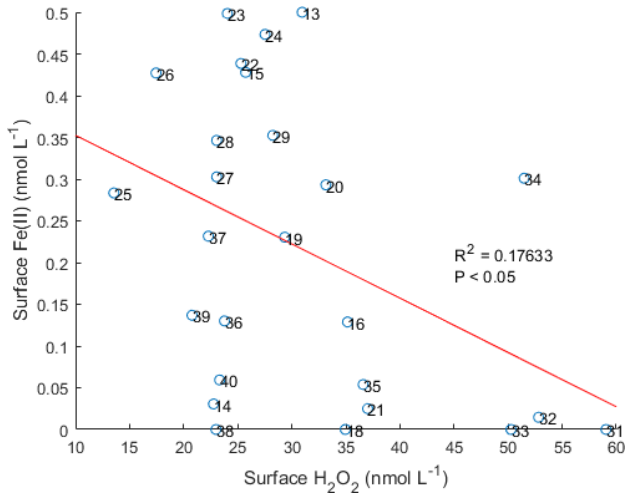

Figure 5.11 Surface DFe(II) vs surface H_2O_2 at all stations. Station numbers annotated.

Table 5-1 Dissolved iron(II) and hydrogen peroxide concentrations for all stations where this data was available during the HEOBI voyage, analysed during the voyage by FIA-CL.

Station	Bottle	Latitude	Longitude	Depth (m)	Fe(II) (nM)	H2O2 (nM)
2	12	-48.2798	79.36634	13.883	NaN	NaN
2	11	-48.2798	79.36634	28.616	NaN	NaN
2	10	-48.2798	79.36634	48.989	NaN	NaN
2	9	-48.2798	79.36634	68.699	NaN	NaN
2	8	-48.2798	79.36634	98.519	NaN	NaN
2	7	-48.2798	79.36634	148.284	NaN	NaN
2	6	-48.2798	79.36634	198.38	NaN	NaN
2	5	-48.2798	79.36634	298.326	NaN	NaN
2	4	-48.2798	79.36634	498.029	NaN	NaN
2	3	-48.2798	79.36634	697.813	NaN	NaN
2	2	-48.2798	79.36634	998.671	NaN	NaN
2	1	-48.2798	79.36634	1598.464	NaN	NaN
4	12	-50.24	77.72869	13.75	NaN	NaN
4	11	-50.24	77.72869	28.632	NaN	NaN
4	10	-50.24	77.72869	68.256	NaN	NaN
4	9	-50.24	77.72869	97.122	NaN	NaN
4	8	-50.24	77.72869	196.741	NaN	NaN
4	7	-50.24	77.72869	295.724	NaN	NaN
4	6	-50.24	77.72869	492.59	NaN	NaN
4	5	-50.24	77.72869	590.592	NaN	NaN
4	4	-50.24	77.72869	987.013	NaN	NaN
4	3	-50.24	77.72869	1971.293	NaN	NaN
4	2	-50.24	77.72869	2950.791	NaN	NaN
4	1	-50.24	77.72869	3317.002	NaN	NaN
5	12	-50.691	76.18671	13.572	NaN	25.15892
5	11	-50.691	76.18671	27.986	NaN	35.59774
5	10	-50.691	76.18671	68.373	NaN	22.25919
5	9	-50.691	76.18671	98.086	NaN	20.04955
5	8	-50.691	76.18671	147.752	NaN	10.99818
5	7	-50.691	76.18671	196.864	NaN	7.585468
5	6	-50.691	76.18671	294.875	NaN	2.922109
5	5	-50.691	76.18671	690.015	NaN	1.790626
5	4	-50.691	76.18671	986.243	NaN	1.253079
5	3	-50.691	76.18671	1970.959	NaN	1.333103
5	2	-50.691	76.18671	2951.099	NaN	1.633958
5	1	-50.691	76.18671	2974.75	NaN	0.252053
6	12	-50.7888	75.78225	12.99	NaN	NaN
6	11	-50.7888	75.78225	28.012	NaN	NaN
6	10	-50.7888	75.78225	67.962	NaN	NaN
6	9	-50.7888	75.78225	97.807	NaN	NaN
6	8	-50.7888	75.78225	196.296	NaN	NaN
6	7	-50.7888	75.78225	294.808	NaN	NaN
6	6	-50.7888	75.78225	492.79	NaN	NaN
6	5	-50.7888	75.78225	690.474	NaN	NaN
6	4	-50.7888	75.78225	986.176	NaN	NaN
6	3	-50.7888	75.78225	1479.401	NaN	NaN
6	2	-50.7888	75.78225	1577.708	NaN	NaN
6	1	-50.7888	75.78225	1627.844	NaN	NaN
7	12	-50.8996	75.37746	13.768	NaN	NaN
7	11	-50.8996	75.37746	27.59	NaN	NaN
7	10	-50.8996	75.37746	67.576	NaN	NaN

Station	Bottle	Latitude	Longitude	Depth (m)	Fe(II) (nM)	H2O2 (nM)
7	9	-50.8996	75.37746	97.671	NaN	NaN
7	8	-50.8996	75.37746	147.009	NaN	NaN
7	7	-50.8996	75.37746	197.766	NaN	NaN
7	6	-50.8996	75.37746	246.005	NaN	NaN
7	5	-50.8996	75.37746	295.014	NaN	NaN
7	4	-50.8996	75.37746	345.101	NaN	NaN
7	3	-50.8996	75.37746	394.025	NaN	NaN
7	2	-50.8996	75.37746	414.187	NaN	NaN
7	1	-50.8996	75.37746	434.647	NaN	NaN
9	12	-51.2871	73.80983	14.116	NaN	57.85064
9	11	-51.2871	73.80983	23.794	NaN	50.71496
9	10	-51.2871	73.80983	38.729	NaN	16.72643
9	9	-51.2871	73.80983	67.481	NaN	15.7856
9	8	-51.2871	73.80983	96.781	NaN	16.74272
9	7	-51.2871	73.80983	146.734	NaN	14.39615
9	6	-51.2871	73.80983	195.713	NaN	11.57648
9	5	-51.2871	73.80983	245.553	NaN	7.712186
9	4	-51.2871	73.80983	295.364	NaN	6.42497
9	3	-51.2871	73.80983	345.164	NaN	5.673204
9	2	-51.2871	73.80983	373.865	NaN	6.234043
9	1	-51.2871	73.80983	394.853	NaN	6.83727
10	12	-51.5064	72.99996	13.926	NaN	73.57338
10	11	-51.5064	72.99996	27.638	NaN	45.6466
10	10	-51.5064	72.99996	48.288	NaN	33.8083
10	9	-51.5064	72.99996	72.306	NaN	28.22148
10	8	-51.5064	72.99996	118.034	NaN	15.29694
10	7	-51.5064	72.99996	146.932	NaN	10.52844
10	6	-51.5064	72.99996	200.319	NaN	5.792809
10	5	-51.5064	72.99996	249.995	NaN	3.52822
10	4	-51.5064	72.99996	300.868	NaN	4.624608
10	3	-51.5064	72.99996	316.094	NaN	4.71675
10	2	-51.5064	72.99996	349.314	NaN	NaN
10	1	-51.5064	72.99996	358.374	NaN	3.004176
11	12	-52.9275	71.36159	13.106	NaN	30.19517
11	11	-52.9275	71.36159	28.641	NaN	33.39405
11	10	-52.9275	71.36159	67.823	NaN	32.64753
11	9	-52.9275	71.36159	98.108	NaN	17.73527
11	8	-52.9275	71.36159	197.196	NaN	6.01594
11	7	-52.9275	71.36159	295.385	NaN	2.746298
11	6	-52.9275	71.36159	493.073	NaN	1.413807
11	5	-52.9275	71.36159	689.369	NaN	1.94688
11	4	-52.9275	71.36159	986.512	NaN	1.447222
11	3	-52.9275	71.36159	1577.817	NaN	1.453966
11	2	-52.9275	71.36159	2559.788	NaN	1.347548
11	1	-52.9275	71.36159	2658.453	NaN	1.158779
12	6	-53.0323	72.65818	13.138	NaN	NaN
12	5	-53.0323	72.65818	28.272	NaN	NaN
12	4	-53.0323	72.65818	47.471	NaN	NaN
12	3	-53.0323	72.65818	66.55	NaN	NaN
12	2	-53.0323	72.65818	87.496	NaN	NaN
12	1	-53.0323	72.65818	102.059	NaN	NaN
13	10	-52.9988	72.62552	13.573	0.5	30.9583
13	9	-52.9988	72.62552	28.897	0.31	20.60596
13	8	-52.9988	72.62552	48.619	0.36	20.7981
13	7	-52.9988	72.62552	67.37	0.35	19.42686
13	6	-52.9988	72.62552	96.928	0.35	21.55899

Station	Bottle	Latitude	Longitude	Depth (m)	Fe(II) (nM)	H2O2 (nM)
13	2	-52.9988	72.62552	117.577	0.32	20.66585
13	1	-52.9988	72.62552	132.135	0.25	19.7409
14	7	-53.0351	72.55227	13.189	0.03057	22.7589
14	6	-53.0351	72.55227	28.556	0.056044	19.31646
14	5	-53.0351	72.55227	47.805	0.101899	17.45076
14	4	-53.0351	72.55227	97.631	0.282769	15.14302
14	3	-53.0351	72.55227	122.492	0.229272	16.82578
14	2	-53.0351	72.55227	157.154	0.315886	16.06095
14	1	-53.0351	72.55227	172.227	0.254746	14.83105
15	6	-53.0726	72.5929	13.53	0.427981	25.73479
15	5	-53.0726	72.5929	28.565	0.537465	24.82952
15	4	-53.0726	72.5929	48.532	0.547418	24.93982
15	3	-53.0726	72.5929	68.211	0.497653	21.98645
15	2	-53.0726	72.5929	98.274	0.338404	24.81739
15	1	-53.0726	72.5929	117.496	0.517559	23.09538
16	6	-52.9846	72.55511	13.3	0.128819	35.1506
16	5	-52.9846	72.55511	28.356	0.110417	33.03102
16	4	-52.9846	72.55511	67.882	0.184028	29.02345
16	3	-52.9846	72.55511	121.723	0.220833	25.11476
16	2	-52.9846	72.55511	175.822	0.257639	18.38147
16	1	-52.9846	72.55511	187.19	0.147222	0
18	12	-54.1674	73.66494	12.621	-3.43E-17	34.94551
18	11	-54.1674	73.66494	27.79	0.042798	33.83229
18	10	-54.1674	73.66494	67.787	0.027984	32.01916
18	9	-54.1674	73.66494	96.889	0.054321	21.55846
18	8	-54.1674	73.66494	147.647	0.097119	4.046461
18	7	-54.1674	73.66494	197.004	0.098765	7.756472
18	6	-54.1674	73.66494	294.459	0.083951	2.209019
18	5	-54.1674	73.66494	491.785	0.077366	2.004212
18	4	-54.1674	73.66494	690.635	-0.01152	1.602537
18	3	-54.1674	73.66494	987.414	0.014815	1.8537
19	6	-53.0599	73.98966	13.634	0.230366	29.34913
19	5	-53.0599	73.98966	28.061	0.307155	26.43874
19	4	-53.0599	73.98966	48.381	0.244328	27.07139
19	3	-53.0599	73.98966	68.133	0.272251	26.25336
19	2	-53.0599	73.98966	78.164	0.230366	28.38649
19	1	-53.0599	73.98966	88.034	0.237347	28.59244
20	6	-53.2133	73.63984	13.756	0.293194	33.14566
20	5	-53.2133	73.63984	28.439	0.321117	32.40409
20	4	-53.2133	73.63984	47.896	0.223386	27.98615
20	3	-53.2133	73.63984	67.178	0.244328	29.29488
20	2	-53.2133	73.63984	88.051	0.268761	27.47886
20	1	-53.2133	73.63984	93.088	0.279232	26.53593
21	8	-53.2808	73.31556	13.271	0.024931	37.01473
21	7	-53.2808	73.31556	28.651	0.124098	34.44433
21	6	-53.2808	73.31556	48.765	0.215488	22.88427
21	5	-53.2808	73.31556	68.321	0.074794	14.49503
21	4	-53.2808	73.31556	88.306	0.093742	12.79084
21	3	-53.2808	73.31556	98.136	0.130142	13.49046
21	2	-53.2808	73.31556	107.543	0.06183	23.37634
21	1	-53.2808	73.31556	112.6	0.218399	16.53867
22	6	-52.9604	73.23888	13.757	0.438672	25.29686
22	5	-52.9604	73.23888	27.955	0.415584	25.80142
22	4	-52.9604	73.23888	49.145	0.325156	26.9169
22	3	-52.9604	73.23888	68.045	0.2886	21.43639
22	2	-52.9604	73.23888	86.872	0.305916	20.9332

Station	Bottle	Latitude	Longitude	Depth (m)	Fe(II) (nM)	H2O2 (nM)
22	1	-52.9604	73.23888	108.445	0.323232	20.60044
23	6	-53.0059	73.72118	14.402	0.498551	24.04201
23	5	-53.0059	73.72118	28.24	0.510145	27.07191
23	4	-53.0059	73.72118	48.053	0.307246	27.38061
23	3	-53.0059	73.72118	59.322	0.301449	24.98825
23	2	-53.0059	73.72118	67.7	0.26087	23.05525
23	1	-53.0059	73.72118	75.02	0.272464	25.44332
24	4	-53.0037	73.60683	13.901	0.473491	27.52554
24	3	-53.0037	73.60683	20.519	0.537533	29.27902
24	2	-53.0037	73.60683	28.885	0.538583	28.27456
24	1	-53.0037	73.60683	35.27	0.571129	27.81576
25	6	-53.035	72.66254	13.872	0.283465	13.54655
25	5	-53.035	72.66254	29.071	0.272966	13.22903
25	4	-53.035	72.66254	58.134	0.356955	14.14021
25	3	-53.035	72.66254	87.731	0.39895	16.02761
25	2	-53.035	72.66254	108.245	0.39895	27.36035
25	1	-53.035	72.66254	119.586	0.388451	31.96008
26	6	-53.0288	72.66081	12.864	0.427142	17.44573
26	5	-53.0288	72.66081	28.669	0.308532	19.442
26	4	-53.0288	72.66081	58.001	0.349281	20.15696
26	3	-53.0288	72.66081	88.469	0.390031	23.70023
26	2	-53.0288	72.66081	107.496	0.336183	15.88943
26	1	-53.0288	72.66081	119.969	0.38421	23.84019
27	6	-53.0334	72.66873	13.921	0.302711	23.04924
27	5	-53.0334	72.66873	28.669	0.350737	23.0427
27	4	-53.0334	72.66873	58.347	0.437329	24.48343
27	3	-53.0334	72.66873	88.273	0.458432	26.38703
27	2	-53.0334	72.66873	107.923	0.448972	29.35477
27	1	-53.0334	72.66873	119.736	0.439512	27.47414
28	6	-53.0387	72.66159	12.73	0.346371	23.04924
28	5	-53.0387	72.66159	28.458	0.628707	23.0427
28	4	-53.0387	72.66159	58.665	0.311543	24.48343
28	3	-53.0387	72.66159	88.021	0.377837	26.38703
28	2	-53.0387	72.66159	107.833	0.655835	30.31347
28	1	-53.0387	72.66159	117.306	0.420439	27.87476
29	6	-53.0337	72.65347	13.39	0.352406	28.24213
29	5	-53.0337	72.65347	28.975	0.453477	28.03404
29	4	-53.0337	72.65347	56.947	1.014404	25.67791
29	3	-53.0337	72.65347	78.064	0.507424	30.14941
29	2	-53.0337	72.65347	92.863	0.490539	24.73785
29	1	-53.0337	72.65347	101.019	0.472865	29.28149
30	6	-52.922	74.02227	13.878	5.173907	43.38744
30	5	-52.922	74.02227	28.235	0.285676	41.37166
30	4	-52.922	74.02227	67.518	0.126967	42.97981
30	3	-52.922	74.02227	98.262	0.158709	39.67458
30	2	-52.922	74.02227	147.422	0.142838	38.21724
30	1	-52.922	74.02227	186.937	0.190451	25.03412
31	9	-52.6964	74.79167	12.603	-0.00447	59.0513
31	8	-52.6964	74.79167	48.258	5.418345	57.53533
31	7	-52.6964	74.79167	97.416	0.214765	40.96099
31	6	-52.6964	74.79167	147.418	0.035794	23.17195
31	5	-52.6964	74.79167	245.205	0.102908	21.56045
31	4	-52.6964	74.79167	345.04	0.06264	21.72319
31	3	-52.6964	74.79167	395.434	0.008949	15.81971
31	2	-52.6964	74.79167	443.703	0.008949	11.57393
31	1	-52.6964	74.79167	468.562	0.040268	11.38487

Station	Bottle	Latitude	Longitude	Depth (m)	Fe(II) (nM)	H2O2 (nM)
32	6	-52.5428	75.26237	12.871	0.014625	52.81464
32	5	-52.5428	75.26237	47.889	0.102377	53.72495
32	4	-52.5428	75.26237	87.467	0.146252	27.12847
32	3	-52.5428	75.26237	147.438	0.204753	17.14814
32	2	-52.5428	75.26237	196.365	0.146252	18.88747
32	1	-52.5428	75.26237	271.03	0.043876	15.17406
33	9	-52.4092	75.60666	14.22	0	50.26546
33	8	-52.4092	75.60666	48.259	0.131627	46.00405
33	7	-52.4092	75.60666	97.726	0	26.69294
33	6	-52.4092	75.60666	148.04	0.058501	15.31341
33	5	-52.4092	75.60666	221.234	0.087751	13.07136
33	4	-52.4092	75.60666	293.952	0.190128	10.73295
33	3	-52.4092	75.60666	394.851	0.014625	8.649526
33	2	-52.4092	75.60666	494.551	0.014625	7.107548
33	1	-52.4092	75.60666	526.794	0.02925	7.067597
34	9	-52.302	76.00671	13.47	0.301075	51.48856
34	8	-52.302	76.00671	48.05	0	49.68593
34	7	-52.302	76.00671	96.09	0	46.84237
34	6	-52.302	76.00671	147.486	0.064516	14.18614
34	5	-52.302	76.00671	219.642	0.086022	11.46784
34	4	-52.302	76.00671	296.809	0.150538	7.291876
34	3	-52.302	76.00671	444.724	0.086022	5.358688
34	2	-52.302	76.00671	542.576	0.064516	7.641063
35	6	-52.8381	74.32217	13.648	0.053872	36.59579
35	5	-52.8381	74.32217	28.746	0.094276	36.38404
35	4	-52.8381	74.32217	68.064	0.13468	24.47819
35	3	-52.8381	74.32217	97.401	0.074074	13.58863
35	2	-52.8381	74.32217	137.334	0.141414	14.78911
35	1	-52.8381	74.32217	146.741	0.074074	12.68924
36	4	-53.0077	73.70902	14.094	0.13001	23.77608
36	3	-53.0077	73.70902	28.533	0.210981	19.01267
36	2	-53.0077	73.70902	58.272	0.171065	16.10411
36	1	-53.0077	73.70902	71.277	0.222059	23.41104
37	4	-53.0118	73.71645	13.71	0.23165	22.28596
37	3	-53.0118	73.71645	28.479	0.179125	23.42051
37	2	-53.0118	73.71645	58.461	0.183165	24.30983
37	1	-53.0118	73.71645	68.211	0.167003	23.10616
38	4	-53.0074	73.72444	14.088	-0.00458	22.98903
38	3	-53.0074	73.72444	28.569	0.280673	23.51511
38	2	-53.0074	73.72444	58.511	0.320269	24.6925
38	1	-53.0074	73.72444	75.355	0.036633	21.34652
39	4	-53.0027	73.71675	13.46	0.136835	20.77638
39	3	-53.0027	73.71675	28.716	0.193346	22.57333
39	2	-53.0027	73.71675	45.62	0.122696	21.4729
39	1	-53.0027	73.71675	77.198	0.330879	19.88652
40	5	-53.0076	73.7161	13.771	0.059379	23.32216
40	4	-53.0076	73.7161	28.819	0.043185	20.80127
40	3	-53.0076	73.7161	48.649	0.059379	22.35696
40	2	-53.0076	73.7161	63.429	0.010796	21.3951
40	1	-53.0076	73.7161	72.432	0.002699	21.16987

5.9 References

Achterberg, E.P., Steigenberger, S., Marsay, C.M., Lemoigne, F.A.C., Painter, S.C., Baker, A.R., Connelly, D.P., Moore, C.M., Tagliabue, A., Tanhua, T., 2018. Iron Biogeochemistry in the High Latitude North Atlantic Ocean. Sci. Rep. 8, 1–15. doi:10.1038/s41598-018-19472-1

Améziane, N., Eléaume, M., Hemery, L.G., Monniot, F., Hemery, A., Hautecoeur, M., Dettaï, A., 2011. Biodiversity of the benthos off Kerguelen Islands : overview and perspectives. Kerguelen Plateau Mar. Ecosyst. Fish. 157–167.

Annett, A.L., Fitzsimmons, J.N., Séguret, M.J.M., Lagerström, M., Meredith, M.P., Schofield, O., Sherrell, R.M., 2017. Controls on dissolved and particulate iron distributions in surface waters of the Western Antarctic Peninsula shelf. Mar. Chem. 196, 81–97. doi:10.1016/j.marchem.2017.06.004

Annett, A.L., Skiba, M., Henley, S.F., Venables, H.J., Meredith, M.P., Statham, P.J., Ganeshram, R.S., 2015. Comparative roles of upwelling and glacial iron sources in Ryder Bay, coastal western Antarctic Peninsula. Mar. Chem. 176, 21–33. doi:10.1016/j.marchem.2015.06.017

Aquilina, A., Homoky, W.B., Hawkes, J.A., Lyons, T.W., Mills, R.A., 2014. Hydrothermal sediments are a source of water column Fe and Mn in the Bransfield Strait, Antarctica. Geochim. Cosmochim. Acta 137, 64–80. doi:10.1016/j.gca.2014.04.003

Barbeau, K., Rue, E.L., Bruland, K.W., Butler, A., 2001. Photochemical cycling of iron in the surface ocean mediated by microbial iron(III)-binding ligands. Nature 413, 409–413. doi:10.1038/35096545

Bennett, S.A., Rouxel, O., Schmidt, K., Garbe-Schönberg, D., Statham, P.J., German, C.R., 2009. Iron isotope fractionation in a buoyant hydrothermal plume, 5°S Mid-Atlantic Ridge. Geochim. Cosmochim. Acta 73, 5619–5634. doi:10.1016/j.gca.2009.06.027

Bhatia, M.P., Kujawinski, E.B., Das, S.B., Breier, C.F., Henderson, P.B., Charette, M.A., 2013. Greenland meltwater as a significant and potentially bioavailable source of iron to the ocean. Nat. Geosci. 6, 274–278. doi:10.1038/ngeo1746

Blain, S., Quéguiner, B., Armand, L., Belviso, S., Bombled, B., Bopp, L., Bowie, A., Brunet, C., Brussaard, C., Carlotti, F., Christaki, U., Corbière, A., Durand, I., Ebersbach, F., Fuda, J.-L., Garcia, N., Gerringa, L., Griffiths, B., Guigue, C., Guillerm, C., Jacquet, S., Jeandel, C., Laan, P., Lefèvre, D., Lo Monaco, C., Malits, A., Mosseri, J., Obernosterer, I., Park, Y.-H., Picheral, M., Pondaven, P., Remenyi, T., Sandroni, V., Sarthou, G., Savoye, N., Scouarnec, L., Souhaut, M., Thuiller, D., Timmermans, K., Trull, T., Uitz, J., van Beek, P., Veldhuis, M., Vincent, D., Viollier, E., Vong, L., Wagener, T., 2007. Effect of natural iron fertilization on carbon sequestration in the Southern Ocean. Nature 446, 1070–4. doi:10.1038/nature05700

Blain, S., Sarthou, G., Laan, P., 2008. Distribution of dissolved iron during the natural iron-fertilization experiment KEOPS (Kerguelen Plateau, Southern Ocean). Deep Sea Res. Part II Top. Stud. Oceanogr. 55, 594–605. doi:10.1016/j.dsr2.2007.12.028

Bowie, A.R., Achterberg, E.P., Sedwick, P.N., Ussher, S., Worsfold, P.J., 2002. Real-Time Monitoring of Picomolar Concentrations of Iron (II) in Marine Waters Using Automated Flow Instrumentation. Environ. Sci. Technol. 36, 4600–4607. doi:10.1021/es020045v

Bowie, A.R., Achterberg, E.P., Ussher, S., Worsfold, P.J., 2005. Design of an automated flow injection-chemiluminescence instrument incorporating a miniature photomultiplier tube for monitoring picomolar concentrations of iron in seawater. J. Autom. Methods Manag. Chem. 2005, 37–43. doi:10.1155/JAMMC.2005.37

Bowie, A.R., Sedwick, P.N., Worsfold, P.J., 2004. Analytical intercomparison between flow injection-chemiluminescence and flow injection-spectrophotometry for the determination

of picomolar concentrations of iron in seawater. Limnol. Oceanogr. Methods 2, 42–54. doi:10.4319/lom.2004.2.42

Boyd, P.W., Ellwood, M.J., 2010. The biogeochemical cycle of iron in the ocean. Nat. Geosci. doi:10.1038/ngeo964

Boyd, P.W., Jickells, T., Law, C.S., Blain, S., Boyle, E. a, Buesseler, K.O., Coale, K.H., Cullen, J.J., de Baar, H.J.W., Follows, M., Harvey, M., Lancelot, C., Levasseur, M., Owens, N.P.J., Pollard, R., Rivkin, R.B., Sarmiento, J., Schoemann, V., Smetacek, V., Takeda, S., Tsuda, a, Turner, S., Watson, a J., 2007. Mesoscale iron enrichment experiments 1993-2005: synthesis and future directions. Science 315, 612–7. doi:10.1126/science.1131669

Cohan, D.S., Schultz, M.G., Jacob, D.J., Heikes, B.G., Blake, D.R., 1999. Convective injection and photochemical decay of peroxides in the tropical upper troposphere: Methyl iodide as a tracer of marine convection. J. Geophys. Res. Atmos. 104, 5717–5724. doi:10.1029/98JD01963

Croot, P.L., Bowie, A.R., Frew, R.D., Maldonado, M.T., Hall, J.A., Safi, K.A., La Roche, J., Boyd, P.W., Law, C.S., 2001. Retention of dissolved iron and Fe II in an iron induced Southern Ocean phytoplankton bloom. Geophys. Res. Lett. 28, 3425–3428. doi:10.1029/2001GL013023

Croot, P.L., Heller, M.I., 2012. The importance of kinetics and redox in the biogeochemical cycling of iron in the surface ocean. Front. Microbiol. 3, 219. doi:10.3389/fmicb.2012.00219

Croot, P.L., Streu, P., Peeken, I., Lochte, K., Baker, A.R., 2004. Influence of the ITCZ on H2O2 in near surface waters in the equatorial Atlantic Ocean. Geophys. Res. Lett. 31, 1–4. doi:10.1029/2004GL020154

Cutter, G., Andersson, P., Codispoti, L., Croot, P., Francois, R., Lohan, M., Obata, H., Rutgers,

M., 2014. Sampling and Sample-handling Protocols for GEOTRACES Cruises.

Daugherty, E.E., Gilbert, B., Nico, P.S., Borch, T., 2017. Complexation and Redox Buffering of Iron(II) by Dissolved Organic Matter. Environ. Sci. Technol. 51, 11096–11104. doi:10.1021/acs.est.7b03152

Elrod, V. a., Berelson, W.M., Coale, K.H., Johnson, K.S., 2004. The flux of iron from continental shelf sediments: A missing source for global budgets. Geophys. Res. Lett. 31, n/a-n/a. doi:10.1029/2004GL020216

Fitzsimmons, J.N., John, S.G., Marsay, C.M., Hoffman, C.L., Nicholas, S.L., Toner, B.M., German, C.R., Sherrell, R.M., Ho, C.L., Nicholas, S.L., Toner, B.M., German, C.R., Sherrell, R.M., 2017. Iron persistence in a distal hydrothermal plume supported by dissolved-particulate exchange. Nat. Geosci. 10, 195–201. doi:10.1038/NGEO2900

Gartman, A., Findlay, A.J., Luther, G.W., 2014. Nanoparticulate pyrite and other nanoparticles are a widespread component of hydrothermal vent black smoker emissions. Chem. Geol. 366, 32–41. doi:10.1016/j.chemgeo.2013.12.013

German, C., Campbell, A., Edmond, J., 1991. Hydrothermal scavenging at the Mid-Atlantic Ridge: modification of trace element dissolved fluxes. Earth Planet. Sci. Lett. 107, 101–114.

Hansard, S.P., Landing, W.M., Measures, C.I., Voelker, B.M., 2009. Dissolved iron(II) in the Pacific Ocean: Measurements from the PO2 and P16N CLIVAR/CO_2 repeat hydrography expeditions. Deep. Res. Part I Oceanogr. Res. Pap. 56, 1117–1129. doi:10.1016/j.dsr.2009.03.006

Hawkes, J.J.A., Connelly, D.P., Rijkenberg, M.J.A., Achterberg, E.P., 2014. The importance of shallow hydrothermal island arc systems in ocean biogeochemistry. Geophys. Res. Lett. 41, 942–947. doi:10.1002/2013GL058817

Hawkings, J.R., Benning, L.G., Raiswell, R., Kaulich, B., Araki, T., Abyaneh, M., Stockdale, A., Koch-müller, M., Wadham, J.L., Tranter, M., 2018. Biolabile ferrous iron bearing nanoparticles in glacial sediments. Earth Planet. Sci. Lett. 493, 92–101. doi:10.1016/j.epsl.2018.04.022

Holmes, T.M., Chase, Z., Van Der Merwe, P., Townsend, A.T., Bowie, A.R., 2017. Detection, dispersal and biogeochemical contribution of hydrothermal iron in the ocean. Mar. Freshw. Res. 68, 2184–2204. doi:10.1071/MF16335

Holmes, T.M., Wuttig, K., Chase, Z., van der Merwe, P., Townsend, A.T., Schallenberg, C., Tonnard, M., Bowie, A.R., 2019. Iron availability influences nutrient drawdown in the Heard and McDonald Islands region, Southern Ocean. Mar. Chem. 211, 1–14. doi:10.1016/j.marchem.2019.03.002

Homoky, W.B., Weber, T., Berelson, W.M., Conway, T.M., Henderson, G.M., van Hulten, M., Jeandel, C., Severmann, S., Tagliabue, A., 2016. Quantifying trace element and isotope fluxes at the ocean–sediment boundary: a review, Philosophical Transactions of the Royal Society A: Mathematical, Physical and Engineering Sciences. doi:10.1098/rsta.2016.0246

Hopwood, M.J., Statham, P.J., Tranter, M., Wadham, J.L., 2014. Glacial flours as a potential source of Fe(II) and Fe(III) to polar waters. Biogeochemistry 118, 443–452. doi:10.1007/s10533-013-9945-y

Hwang, H., Dasgupta, P.K., 1985. Thermodynamics of the hydrogen peroxide-water system. Environ. Sci. Technol. 19, 255–258. doi:10.1021/es00133a006

Kleint, C., Pichler, T., Koschinsky, A., 2017. Geochemical characteristics, speciation and size-fractionation of iron (Fe) in two marine shallow-water hydrothermal systems, Dominica, Lesser Antilles. Chem. Geol. 454, 44–53. doi:10.1016/j.chemgeo.2017.02.021

Lohan, M.C., Bruland, K.W., 2008. Elevated Fe(II) and dissolved Fe in hypoxic shelf waters off Oregon and Washington: An enhanced source of iron to coastal upwelling regimes. Environ. Sci. Technol. 42, 6462–6468. doi:10.1021/es800144j

Lupton, J.E., Arculus, R.J., Coffin, M., Bradney, A., Baumberger, T., Wilkinson, C., 2017. Hydrothermal venting on the flanks of Heard and McDonald islands, southern Indian Ocean, in: AGU Fall Meeting Abstracts. p. V51F–0435.

Lupton, J.E., Craig, H., 1981. A Major Helium-3 Source at 15°S on the East Pacific Rise. Science (80-.). 214, 13–8. doi:10.1126/science.214.4516.13

Martin, J.H., Gordon, R.M., Fitzwater, S.E., 1990. Iron in Antarctic waters. Nature 345, 156–158. doi:10.1038/345156a0

Millero, F.J., Sotolongo, S., 1989. The oxidation of Fe(II) with H2O2 in seawater. Geochim. Cosmochim. Acta 53, 1867–1873. doi:10.1016/0016-7037(89)90307-4

Millero, F.J., Sotolongo, S., Izaguirre, M., 1987. The oxidation kinetics of Fe(II) in seawater. Geochim. Cosmochim. Acta 51, 793–801. doi:10.1016/0016-7037(87)90093-7

Moffett, J.W., Zika, R.G., 1987. Reaction kinetics of hydrogen peroxide with copper and iron in seawater. Environ. Sci. Technol. 21, 804–810. doi:10.1021/es00162a012

Moore, C.M., Mills, M.M., Achterberg, E.P., Geider, R.J., LaRoche, J., Lucas, M.I., McDonagh, E.L., Pan, X., Poulton, A.J., Rijkenberg, M.J. a., Suggett, D.J., Ussher, S.J., Woodward, E.M.S., 2009. Large-scale distribution of Atlantic nitrogen fixation controlled by iron availability. Nat. Geosci. 2, 867–871. doi:10.1038/ngeo667

Moore, C.M., Mills, M.M., Arrigo, K.R., Berman-Frank, I., Bopp, L., Boyd, P.W., Galbraith, E.D., Geider, R.J., Guieu, C., Jaccard, S.L., Jickells, T.D., La Roche, J., Lenton, T.M., Mahowald, N.M., Maranon, E., Marinov, I., Moore, J.K., Nakatsuka, T., Oschlies, A., Saito,

M.A., Thingstad, T.F., Tsuda, A., Ulloa, O., 2013. Processes and patterns of oceanic nutrient limitation. Nat. Geosci 6, 701–710. doi:10.1038/ngeo1765

Moore, J.K., Doney, S.C., Glover, D.M., Fung, I.Y., 2001. Iron cycling and nutrient-limitation patterns in surface waters of the world ocean. Deep. Res. Part II Top. Stud. Oceanogr. 49, 463–507. doi:10.1016/S0967-0645(01)00109-6

Pakhomova, S. V., Hall, P.O.J., Kononets, M.Y., Rozanov, A.G., Tengberg, A., Vershinin, A. V., 2007. Fluxes of iron and manganese across the sediment-water interface under various redox conditions. Mar. Chem. 107, 319–331. doi:10.1016/j.marchem.2007.06.001

Palenik, B., Morel, F.M.M., 1988. Dark production of H2O2 in the Sargasso Sea. Limnol. Oceanogr. 33, 1606–1611. doi:10.4319/lo.1988.33.6part2.1606

Park, Y.Y.-H., Durand, I., Kestenare, E., Rougier, G., Zhou, M., d'Ovidio, F., Cotté, C., Lee, J.-H., 2014. Polar Front around the Kerguelen Islands: An up-to-date determination and associated circulation of surface/subsurface waters. J. Geophys. Res. Ocean. 1–18. doi:10.1002/2014JC010061.Received

Park, Y.-H., Roquet, F., Durand, I., Fuda, J.-L., 2008. Large-scale circulation over and around the Northern Kerguelen Plateau. Deep Sea Res. Part II Top. Stud. Oceanogr. 55, 566–581. doi:10.1016/j.dsr2.2007.12.030

Rijkenberg, M.J.A., Fischer, A.C., Kroon, J.J., Gerringa, L.J.A., Timmermans, K.R., Wolterbeek, H.T., De Baar, H.J.W., 2005. The influence of UV irradiation on the photoreduction of iron in the Southern Ocean. Mar. Chem. 93, 119–129. doi:10.1016/j.marchem.2004.03.021

Rudnicki, M.D., Elderfield, H., 1993. A chemical model of the buoyant and neutrally buoyant plume above the TAG vent field, 26 degrees N, Mid-Atlantic Ridge. Geochim. Cosmochim. Acta 57, 2939–2957. doi:10.1016/0016-7037(93)90285-5

Santana-Casiano, J.M., González-Dávila, M., Millero, F.J., 2006. The role of Fe(II) species on the oxidation of Fe(II) in natural waters in the presence of O_2 and H_2O_2. Mar. Chem. 99, 70–82. doi:10.1016/j.marchem.2005.03.010

Sarthou, G., Bucciarelli, E., Chever, F., Hansard, S.P., González-Dávila, M., Santana-Casiano, J.M., Planchon, F., Speich, S., 2011. Labile Fe(II) concentrations in the Atlantic sector of the Southern Ocean along a transect from the subtropical domain to the Weddell Sea Gyre. Biogeosciences 8, 2461–2479. doi:10.5194/bg-8-2461-2011

Sarthou, G., Jeandel, C., Brisset, L., Amouroux, D., Besson, T., Donard, O.F.X., 1997. Fe and H2O2 distributions in the upper water column in the Indian sector of the Southern Ocean. Earth Planet. Sci. Lett. 147, 83–92. doi:10.1016/S0012-821X(97)00004-6

Sedwick, P.., Sohst, B.M., Ussher, S.J., Bowie, A.R., 2015. A zonal picture of the water column distribution of dissolved iron(II) during the U.S. GEOTRACES North Atlantic transect cruise (GEOTRACES GA03). Deep Sea Res. Part II Top. Stud. Oceanogr. 116, 166–175. doi:10.1016/j.dsr2.2014.11.004

Shaked, Y., Kustka, A.B., Morel, M.M., 2005. A general kinetic model for iron acquisition by eukaryotic phytoplankton. Limnol. Oceanogr. 50, 872–882.

Spain, E., Johnson, S., Hutton, B., Whittaker, J., Lucieer, V., Watson, S., Fox, J., Coffin, M.F., 2018. Shallow seafloor gas emissions near Heard and McDonald islands on the Kerguelen Plateau, Southern Indian Ocean, in: Proceedings from the GeoHab: Marine Geological and Biological Habitat Mapping. Santa Barbara, p. 123.Sunda, W.G., Huntsman, S.A., 1997. Interrelated influence of iron, light and cell size on marine phytoplankton growth. Nature 390, 389–392. doi:10.1038/37093

Tagliabue, A., Aumont, O., Bopp, L., 2014. The impact of different external sources of iron on the global carbon cycle. Geophys. Res. Lett. 41, 10.1002/2013GL059059.

doi:10.1002/2013GL059059.Received

Tanhua, T., Olsen, A., Hoppema, M., Jutterström, S., Schirnick, C., van Heuven, S.M.A.C., Velo, A., Lin, X., Kozyr, A., Álvarez, M., Bakker, D.C.E., Brown, P.J., Falck, E., Jeansson, E., Lo Monaco, C., Ólafsson, J., Pérez, F.F., Pierrot, D., Ríos, A.F., Sabine, C.L., Schuster, U., Steinfeldt, R., Stendardo, I., Anderson, L.G., Bates, N., Bellerby, R.G.J., Blindheim, J., Bullister, J.L., Gruber, N., Ishii, M., Johannessen, T., Jones, E.P., Köhler, J., Körtzinger, A., Metzl, N., Murata, A., Musielewicz, S., Omar, A.M., Olsson, K.A., de la Paz, M., Pfeil, B., Rey, F., Rhein, M., Skjelvan, I., Tilbrook, B., Wanninkhof, R., Mintrop, L., Wallace, D.W.R., Key, R.M., 2013. Dissolved inorganic carbon, alkalinity, pH, temperature, salinity, and other variables collected from profile observations using CTD, discrete bottles, and other instruments from October 7, 1977 to March 11, 2006 [WWW Document]. URL https://www.nodc.noaa.gov/OC5/SELECT/dbsearch/dbsearch.html (accessed 7.18.18).

van der Merwe, P., Wuttig, K., Holmes, T.M., Chase, Z., Trull, T., Bowie, A.R., 2018. High Fe lability of particles sourced from glacial erosion, Heard Island, Southern Ocean. In Prep.

Von Damm, K.L., 1995. Controls on the Chemistry and Temporal Variability of Seafloor Hyrdrothermal Fluids, in: Humphris, S.E., Zierenberg, R.A., Mullineaux, L.S., Thomson, R.E. (Eds.), Seafloor Hydrothermal Systems: Physical, Chemical, Biological, and Geological Interactions, Geophysical Monograph Series. American Geophysical Union, Washington, D. C., pp. 222–247. doi:10.1029/GM091

Watson, S.J., Coffin, M.F., Whittaker, J.M., Lucieer, V., Fox, J.M., Carey, R., Arculus, R.J., Bowie, A.R., Chase, Z., Robertson, R., Martin, T., Cooke, F., 2016. Submarine geology and geomorphology of active Sub-Antarctic volcanoes: Heard and McDonald Islands, in: AGU Fall Meeting Abstracts.

Weller, R., Schrems, O., 1993. H2O2 in the marine troposphere and seawater of the Atlantic Ocean (48°N - 63°S). Geophys. Res. Lett. 20, 125–128. doi:10.1029/93GL00065

Winton, V.H.L., Bowie, A.R., Edwards, R., Keywood, M., Townsend, A.T., van der Merwe, P., Bollhöfer, A., 2015. Fractional iron solubility of atmospheric iron inputs to the Southern Ocean. Mar. Chem. 177, 20–32. doi:10.1016/j.marchem.2015.06.006

Yuan, J., Shiller, A.M., 2001. The distribution of hydrogen peroxide in the southern and central Atlantic ocean 48, 2947–2970.

Yuan, J., Shiller, A.M., 1999. Determination of subnanomolar levels of hydrogen peroxide in seawater by reagent-injection chemiluminescence detection. Anal. Chem. 71, 1975–1980. doi:10.1021/ac981357c

Yücel, M., Gartman, A., Chan, C.S., Luther, G.W., 2011. Hydrothermal vents as a kinetically stable source of iron-sulphide-bearing nanoparticles to the ocean. Nat. Geosci. 4, 367–371. doi:10.1038/ngeo1148

Chapter 6

6 Summary and future directions

This thesis was originally titled 'The impact of hydrothermalism on trace metal biogeochemistry in the Southern Ocean', but like most studies of natural systems, the findings turned out to be complex, new research questions presented themselves, and the focus was adjusted in response. Thus, the hypothesis put forward in this research is that *volcanism* impacts trace metal biogeochemistry in the Southern Ocean. This study has focused on aspects of both the impact of hydrothermalism and the impact of subaerial volcanic islands on water column Fe distribution and cycling in the Southern Ocean.

The role of the trace metal iron (Fe) in limiting primary productivity in vast regions of the ocean is now well established (Tagliabue et al., 2017), as is the importance of the Southern Ocean in absorbing CO_2 from the atmosphere and thus regulating the Earth's climate (Takahashi et al., 2002). The Southern Ocean is also known to be the largest area of Fe-limited waters in the ocean (Boyd et al., 2012). However, due to the inaccessibility and remoteness of the Southern Ocean, there are still many unanswered questions regarding the biogeochemical cycling of Fe in this region (Tagliabue et al., 2017). For example, spatial and temporal variations in the distribution of Fe in the Southern Ocean need to be further resolved (Tagliabue et al., 2017). Understanding the distribution and cycling of Fe is especially important in regions of the Southern Ocean with increased biological activity (biological 'hotspots'), because these areas can sequester large quantities of carbon to the ocean interior and sediments (Blain et al., 2007). In order to address the proposed hypothesis, the framework of this dissertation begins broadly, examining current knowledge of hydrothermally derived Fe in the ocean, and narrows quickly to an important biological hotspot in the Southern Ocean, and the location of two subaerial volcanoes: Heard and McDonald Islands. Three questions are addressed in the course of the research:

1. What is the impact of hydrothermalism on Fe distribution in the ocean, and especially in the Southern Ocean?
2. What impact does Fe from Heard and McDonald Islands have on nutrient cycling in the central Kerguelen Plateau region of the Southern Ocean?
3. What does Fe speciation reveal about the sources and cycling of Fe at each of Heard and McDonald Islands?

6.1 Summary of key results

The findings for the three key questions are presented within the three main chapters of this thesis respectively. All three studies indicate that there is an important role for volcanism in supplying Fe to the Southern Ocean.

The major findings for each of the three studies are:

Chapter 2: Detection, dispersal and biogeochemical contribution of hydrothermal iron in the ocean.

A compilation of Fe measurements from both hydrothermal plumes and end-member vent fluids was analysed and revealed the small fraction of hydrothermal vents discovered south of 30°S (72 of 631 globally discovered vents). Given the ~20,000 km of circumpolar plate boundary, much of which is unexplored, it is likely many vents remain undiscovered in the Southern Ocean. The review highlights recent discoveries that Fe in hydrothermal plumes may travel for thousands of kilometres. This distal transport of Fe, coupled with upwelling in the Southern Ocean, means that Southern Ocean hydrothermal vents have greater chance of influencing surface water Fe concentrations, and thus primary productivity, than in other regions of the ocean.

Chapter 3: Iron availability influences nutrient drawdown in the Heard and McDonald Islands region, Southern Ocean.

In the region surrounding Heard and McDonald active volcanic islands (HIMI) on the Kerguelen Plateau in the Southern Ocean, Fe is shown to play a central role in the biogeochemical cycling of nitrate, phosphate and silicic acid (Si). DFe availability drives macronutrient uptake on the plateau, which is somewhat surprising, given the low concentrations of Si in the region (another limiting factor in large regions of the Southern Ocean). Comparing seasonal depletion ratios of Fe:N and Fe:P with the Redfield ratio indicates that recycling of Fe decreases in proximity to HIMI, indicating that Fe limitation is alleviated close to the islands. These results highlight the important role HIMI plays in supplying DFe to this biological hotspot in the Southern Ocean.

Chapter 4: Glacial and hydrothermal sources of dissolved iron(II) in Southern Ocean waters surrounding Heard and McDonald Islands.

Concentrations of dissolved Fe(II) (DFe(II)), the reduced and short-lived oxidation state of Fe in the ocean, at Heard and McDonald Islands indicate strong sources of reduced Fe at both islands. At Heard Island, the highest concentrations were inversely correlated to salinity. This correlation, coupled with proximity to a marine-terminating glacier, and results from suspended particulate matter analysis, indicate that the strongest DFe(II) source at Heard Island is glacially derived. At McDonald Islands, the highest concentrations most likely originated from shallow diffuse hydrothermalism, based on water column profiles from five closely spaced targeted stations and ^{3}He data (an unequivocal tracer of hydrothermalism). The generally elevated DFe(II) concentrations around HIMI, relative to regional open ocean concentrations, were most likely the result of a combination of the strong glacial and hydrothermal influences, along with sources that could not be isolated due to the well mixed nature of the water column such as sedimentary resuspension and aerosol deposition. These results highlighted the importance of multiple

sources of Fe, including processes related to the subaerial volcanic islands, within the water column and hydrothermal activity in maintaining the elevated concentrations observed in the region.

6.2 Implications of this research

6.2.1 Southern Ocean volcanism

The compilation of global hydrothermal measurements highlighted a dearth of studies conducted in the Southern Ocean but also indicated that, given upwelling water masses in the Southern Ocean, and the discovery of 16 hydrothermal vents in the upper 1000 m at the time of the research, hydrothermalism could be an important contributor of Fe to surface waters in some regions south of 30°S. Even if hydrothermal contribution represents a smaller fraction of Fe supply directly to Southern Ocean surface waters than other sources such as sea ice, aerosols, margin sediments or island mass effects, the hydrothermally derived Fe supply to the deep ocean is probably a large contributor to the elevated Fe concentrations of upwelled deep waters in the Southern Ocean (Tagliabue et al., 2017) and represents a stable source of Fe over longer timescales, which should be incorporated into changing climate projections. Even if the ~20,000 km of unsurveyed circumpolar plate boundary yields relatively few hydrothermal sources of Fe that could contribute directly to surface waters, there are regions of the Southern Ocean where volcanism may have a stronger impact on Fe cycling in surface waters.

The focus of this PhD was originally on the impact of hydrothermalism on biogeochemistry in the Southern Ocean, because it was expected that hydrothermal activity should be a major contributor of DFe close to HIMI, known to be highly active volcanic islands. However, conditions observed during the Heard Earth-Ocean-Biosphere Interactions (HEOBI) voyage showed stark contrast to the focused, high temperature vent systems found on mid-ocean ridges,

where most of the measurements assimilated in chapter 2 were collected. Instead, hundreds of plumes of gas bubbles emitted from the seafloor were detected by shipboard echosounder and several were observed directly by deep-tow camera (Coffin, 2016). The presence of a major exsolved gas phase is characteristic of shallow hydrothermal venting (Prol-Ledesma et al., 2005), as are lower temperatures and metal concentrations (Holmes et al., 2017). However, diffuse hydrothermal fluids generally contain much higher concentrations of organics than high-temperature vent systems, and have been proposed as a source of Fe-stabilising ligands (e.g. Hawkes et al., 2013), which can aid in the transport of Fe and increase bioavailability (Gledhill and Buck, 2012). The chemical and physical water column properties observed in the HIMI region during the HEOBI voyage were far more complex than expected and the data indicates that multiple sources of Fe, including these shallow hydrothermal systems, are likely to have contributed to the Fe cycling in the region. The impact of these volcanic islands on Fe and nutrient cycling over the central Kerguelen Plateau, and likely sources of Fe around the islands is demonstrated in chapters three and four of this dissertation.

6.2.2 Central Kerguelen Plateau

Previous studies on the Kerguelen Plateau suggested that phytoplankton in the region were unlikely to be Fe-limited and that DFe and PFe supply from vertical flux and sediment resuspension may be enough to supply the large phytoplankton bloom that forms over and in the lee of the plateau each spring/summer season (Blain et al., 2008; Bowie et al., 2015). DFe and nutrient data collected in the HIMI region for this study indicates that biota probably do suffer from some form of Fe limitation, at least in late summer, over the plateau. DFe and nutrient data in the HIMI region also indicate that Fe recycling decreases towards HIMI, which means that Fe limitation is probably alleviated near the islands. This is an indication that HIMI is a strong source of Fe in the region, which may play a role in supplying Fe to the bloom further to the north.

6.2.3 Heard and McDonald Islands

This study highlighted the complex nature of Fe supply and cycling processes at Heard and McDonald Islands. Elevated concentrations of DFe(II), the most labile and probably bioavailable form of Fe in the ocean, were produced by multiple sources including glacial melt and hydrothermal activity in the HIMI region. The almost ubiquitous elevated DFe(II) near the islands may increase the bioavailability of Fe for phytoplankton. High DFe(II) concentrations around the islands might also indicate that oxidation kinetics are slower in the region, which may have implications for transport of Fe away from the islands towards the northern plateau where the annual plankton bloom is strongest.

The discovery of multiple sources of DFe(II) around HIMI may also have implications for future Fe supply in this region. For instance, under warming climate conditions melting glacial waters will increase, increasing the supply of Fe(II) laden nanoparticles and DFe(II), but then rapidly decrease once glaciers have melted. Hydrothermal input should stay more or less constant, at least on shorter geological timescales, unless there's a subsurface eruption event. Furthermore, the impact of changing climate conditions on biological production, aerosol deposition and sediment resuspension cannot be predicted unless the magnitude of each of these other potential sources of DFe(II) is further resolved in the region.

6.3 Future directions

Much progress has been made in identifying the longevity of Fe in hydrothermal plumes since their discovery some forty years ago, with the contribution of hydrothermal Fe flux to the global ocean now widely accepted (Conway and John, 2014; Holmes et al., 2017; Resing et al., 2015; Tagliabue et al., 2010). However, vast stretches of the plate boundaries, including the remote Antarctic plate boundary, remain under-surveyed. Detailed surveying of the circumpolar plate boundary needs to be undertaken to identify undiscovered hydrothermal systems, so that the

contribution of hydrothermalism to the Southern Ocean Fe inventory can be accurately constrained. Due to the logistically challenging nature of this undertaking, the most plausible solution is through the use of autonomous underwater vehicles (AUV), which can survey vast regions in high detail and relatively quickly (Baker, 2017; Matsuda et al., 2016; Petillo and Schmidt, 2012).

The data presented in chapter 4 of this dissertation indicate that nutrient limitation and recycling increase with distance from HIMI based on comparisons with Redfield ratios. However, analysis of phytoplankton cellular nutrient concentrations, physiological signs of nutrient limitation and species composition are recommended to further resolve and confirm these findings.

Data collected near McDonald Islands indicated that hydrothermalism was the most likely source of DFe(II). However, it is likely that the elevated DFe(II) concentrations associated with hydrothermalism at McDonald Islands were only detected in samples of diluted hydrothermal input rising through the water column. In order to further resolve the impact of hydrothermalism on Fe speciation and distribution in the region, escaping gases and fluids need to be sampled directly at the seafloor source. In order to locate the seafloor venting present in the well mixed, turbid waters near McDonald Islands locating and sampling these vents will require the use of a remotely operated vehicle (ROV), which has been demonstrated in previous studies (e.g. Passaro et al., 2016).

Accurate prediction of Fe supply from the region under future climate change scenarios should take into account the impact of glacial melt from Heard Island. In order to achieve this, it will be necessary to measure the rate of glacial retreat on the island, along with further resolving the magnitude of Fe input and cycling associated with glacial meltwaters. Furthermore, resolution of DFe(II) cycling and input from biological production, aerosol deposition and sediment resuspension in the region is also required for more accurate modelling of Fe supply from HIMI.

This thesis has examined the impact of volcanism on the Southern Ocean at three different scales. At the broadest scale, we have shown that a great deal more information, in the form of hydrothermal surveys and tracing of hydrothermal inputs, is required in order to accurately assess the impact of hydrothermalism on surface Fe distributions and primary productivity in the Southern Ocean. At the regional scale, we have shown that Fe inputs increase nutrient drawdown in the vicinity of two volcanically active islands in the Southern Ocean. And at a more local scale, we show that multiple sources of DFe(II) exist at Heard and McDonald Islands, including both hydrothermal sources and sources associated with the subaerial landmass of the volcanoes. Overall, this thesis has put forward a strong case that volcanism does indeed impact biogeochemical cycling at the regional scale, and has also posed many further questions about the role of volcanism in biogeochemical cycling in the Southern Ocean as a whole.

6.4 References

Baker, E.T., 2017. Exploring the ocean for hydrothermal venting: New techniques, new discoveries, new insights. Ore Geol. Rev. 86, 55–69. doi:10.1016/j.oregeorev.2017.02.006

Blain, S., Quéguiner, B., Armand, L., Belviso, S., Bombled, B., Bopp, L., Bowie, A., Brunet, C., Brussaard, C., Carlotti, F., Christaki, U., Corbière, A., Durand, I., Ebersbach, F., Fuda, J.-L., Garcia, N., Gerringa, L., Griffiths, B., Guigue, C., Guillerm, C., Jacquet, S., Jeandel, C., Laan, P., Lefèvre, D., Lo Monaco, C., Malits, A., Mosseri, J., Obernosterer, I., Park, Y.-H., Picheral, M., Pondaven, P., Remenyi, T., Sandroni, V., Sarthou, G., Savoye, N., Scouarnec, L., Souhaut, M., Thuiller, D., Timmermans, K., Trull, T., Uitz, J., van Beek, P., Veldhuis, M., Vincent, D., Viollier, E., Vong, L., Wagener, T., 2007. Effect of natural iron fertilization on carbon sequestration in the Southern Ocean. Nature 446, 1070–4. doi:10.1038/nature05700

Blain, S., Sarthou, G., Laan, P., 2008. Distribution of dissolved iron during the natural iron-

fertilization experiment KEOPS (Kerguelen Plateau, Southern Ocean). Deep Sea Res. Part II Top. Stud. Oceanogr. 55, 594–605. doi:10.1016/j.dsr2.2007.12.028

Bowie, A.R., van der Merwe, P., Quéroué, F., Trull, T., Fourquez, M., Planchon, F., Sarthou, G., Chever, F., Townsend, A.T., Obernosterer, I., Sallée, J.-B., Blain, S., 2015. Iron budgets for three distinct biogeochemical sites around the Kerguelen archipelago (Southern Ocean) during the natural fertilisation experiment KEOPS-2. Biogeosciences Discuss. 11, 17861–17923. doi:10.5194/bgd-11-17861-2014

Boyd, P.W., Arrigo, K.R., Strzepek, R., van Dijken, G.L., 2012. Mapping phytoplankton iron utilization: Insights into Southern Ocean supply mechanisms. J. Geophys. Res. 117, C06009. doi:10.1029/2011JC007726

Coffin, M., 2016. HEOBI: Heard Earth-Ocean-Biosphere Interactions voyage summary. Hobart, Australia.

Conway, T., John, S., 2014. Quantification of dissolved iron sources to the North Atlantic Ocean. Nature 511, 212–215. doi:10.1038/nature13482

Gledhill, M., Buck, K.N., 2012. The organic complexation of iron in the marine environment: a review. Front. Microbiol. 3, 69. doi:10.3389/fmicb.2012.00069

Hawkes, J.A., Connelly, D.P., Gledhill, M., Achterberg, E.P., 2013. The stabilisation and transportation of dissolved iron from high temperature hydrothermal vent systems. Earth Planet. Sci. Lett. 375, 280–290. doi:10.1016/j.epsl.2013.05.047

Holmes, T.M., Chase, Z., Van Der Merwe, P., Townsend, A.T., Bowie, A.R., 2017. Detection, dispersal and biogeochemical contribution of hydrothermal iron in the ocean. Mar. Freshw. Res. 68, 2184–2204. doi:10.1071/MF16335

Matsuda, T., Maki, T., Sato, Y., Sakamaki, T., 2016. Sea experiments and tank tests on alternating

landmark navigation using multiple AUVs: Towards accurate and efficient survey of seafloor by AUVs, in: 2016 IEEE/OES Autonomous Underwater Vehicles (AUV). IEEE, pp. 213–221. doi:10.1109/AUV.2016.7778674

Passaro, S., Tamburrino, S., Vallefuoco, M., Tassi, F., Vaselli, O., Giannini, L., Chiodini, G., Caliro, S., Sacchi, M., Rizzo, A.L., Ventura, G., 2016. Seafloor doming driven by degassing processes unveils sprouting volcanism in coastal areas. Sci. Rep. 6, 22448. doi:10.1038/srep22448

Petillo, S.M., Schmidt, H., 2012. Autonomous and Adaptive Underwater Plume Detection and Tracking with AUVs: Concepts, Methods, and Available Technology. IFAC Proc. Vol. 45, 232–237. doi:10.3182/20120919-3-IT-2046.00040

Prol-Ledesma, R.M., Dando, P.R., de Ronde, C.E.J., 2005. Special issue on "shallow-water hydrothermal venting." Chem. Geol. 224, 1–4. doi:10.1016/j.chemgeo.2005.07.012

Resing, J. a., Sedwick, P.N., German, C.R., Jenkins, W.J., Moffett, J.W., Sohst, B.M., Tagliabue, A., 2015. Basin-scale transport of hydrothermal dissolved metals across the South Pacific Ocean. Nature 523, 200–203. doi:10.1038/nature14577

Tagliabue, A., Bopp, L., Dutay, J.-C., Bowie, A.R., Chever, F., Jean-Baptiste, P., Bucciarelli, E., Lannuzel, D., Remenyi, T., Sarthou, G., Aumont, O., Gehlen, M., Jeandel, C., 2010. Hydrothermal contribution to the oceanic dissolved iron inventory. Nat. Geosci. 3, 252–256. doi:10.1038/ngeo818

Tagliabue, A., Bowie, A.R., Boyd, P.W., Buck, K.N., Johnson, K.S., Saito, M.A., 2017. The integral role of iron in ocean biogeochemistry. Nature 543, 51–59. doi:10.1038/nature21058

Takahashi, T., Sutherland, S.C., Sweeney, C., Poisson, A., Metzl, N., Tilbrook, B., Bates, N., Wanninkhof, R., Feely, R.A., Sabine, C., Olafsson, J., Nojiri, Y., 2002. Global sea–air CO_2 flux based on climatological surface ocean pCO2, and seasonal biological and temperature

effects. Deep Sea Res. Part II Top. Stud. Oceanogr. 49, 1601–1622. doi:10.1016/S0967-0645(02)00003-6

Finished!